Passive Earth Pressure under Shock-Type Loads

vorgelegt von
Dipl.-Ing.
Tudor Saidel

an der Fakultät VI – Planen Bauen Umwelt
der Technischen Universität Berlin
zur Erlangung des akademischen Grades

Doktor der Ingenieurwissenschaften
- Dr.-Ing. –

genehmigte Dissertation

Promotionsausschuss:

Vorsitzender: Univ.-Prof. Dr.-Ing. Yuri Petryna
Gutachter: Univ.-Prof. Dr.-Ing. Frank Rackwitz
Gutachter: Univ.-Prof. Dr.-Ing. habil. Christos Vrettos
Gutachter: Univ.-Prof. Dr.-Ing. Stavros Savidis

Tag der wissenschaftlichen Aussprache: 15. Oktober 2018

Berlin 2020

Foreword

My first thought and my deepest gratitude goes to prof. D.Eng. A. Marcu, who developed my interest in the geotechnics and foundations field during my university years at the Faculty of Hydrotechnics at the Technical University of Civil Engineering Bucharest. I sincerely thank prof. Marcu for being a role model.

I first began studying soil dynamics in 1996 as a TEMPUS exchange student to prepare the graduation thesis at the Department of Geotechnics and Foundations of the Technical University in Berlin under the guidance of prof. D.Eng. S. Savidis and prof. D.Eng. C. Vrettos, thesis which I finished at the Technical University of Civil Engineering Bucharest under the guidance of prof. D.Eng. Marcu. With the kind recommendation of prof. D.Eng. I. Manoliu, I obtained a DAAD scholarship from the German government to further study soil dynamics during an academic year at the Department of Geotechnics and Foundations of the Technical University in Berlin.

The subject of this research paper was given by prof. D.Eng. S. Savidis, who also guided me in developing the "Passiver Erddruck auf Stützkonstruktionen bei stoßartiger Belastung" paper, published by the Fraunhofer Institut with the IRB publishing company in 2000. I want to thank prof. D.Eng. S. Savidis for the tireless requirements he asked for in developing the mathematical model for the passive earth pressure under shock-type loads, as well as in using thorough scientific language. I thank D.Eng. J. Mittag for his assistance during editing the published paper, whose results were partially incorporated in the provisions of the DIN 1054:2005 German standard.

Due to the NaFöG scholarship obtained from the German government for two and a half years, I had the opportunity to continue the research for the doctoral dissertation. I thank prof. Savidis for offering me the chance to continue the research for the doctoral dissertation, and at the same time to take part in other interesting projects during another two years as a researcher under his and prof. Vrettos's guidance.

I thank Mr. G. Spengler for his support and encouragement given at making the mechanical components of the experimental stand and Mrs. Eng. R. Kauther from the Bundesanstalt für Wasserbau for the scientific debates and for generously providing the high-speed recording and

processing system, thanks to which I added valuable information to my research.

I sincerely thank Mr. D.Eng. U. Holzlöhner from the Bundesanstalt für Materialprüfung for his in-depth explanation of the model developed by him, for his generous guidance in dimensional analysis and for his granted confidence.

Mr. Eng. M. Ionescu, Mr. Eng. M. Stăruș and D.Eng. D. Cvaci I thank for their generous support given to conduct several tests on physical models during their studies at the TU Berlin.

I thank my colleagues at the Department of Geotechnics and Foundations of the Technical University in Berlin, D.Eng. W. Scheppers, D.Eng. R. Hirschauer, Eng. Y. Zahng, Eng. M. Römer and prof. D.Eng. F. Rackwitz for their friendly help and productive scientific dialog.

I thank Mr. D.Eng. S. Georgescu for the corrections of the numerical calculation program of the passive pressure under dynamic shock-type loads.

My colleague Eng. V. Boureanu I thank him for his generous support given at editing the final draft of the paper and at the English corrections.

I sincerely thank prof. Vrettos for the scientific guidance he continuously provided throughout the research, for initiating me in the soil dynamics field during the Bachelor's degree, for his vision that guided my professional development, as well as for his friendship.

To my wife Ioana I am grateful for her love, patience and confidence that she supported me with ever since my university years and substituting me in educating our sons, Victor and Theodor.

I am grateful to my parents Dr. Alice Saidel and Eng. Ștefan Saidel for their unconditional love, for the professional passion and for their example that it is never too late to accomplish something.

In the end I want to express my gratitude for the knowledge acquired, as well for completing the paper, to everyone I have met and learned from, my teachers and professors, as well as to the authors of the cited publications.

Tudor Saidel

TABLE OF CONTENTS

TABLE OF FIGURES

LIST OF TABLES

Chapter 1. Introduction

The subject of the thesis is in the soil dynamics field. Firstly, the paper proposes to examine the basis of passive resistance mobilization under static loads, relying on reduced scale models. An own mathematical model is calibrated, based on these results. The model is then extended to the dynamic case by including the inertial forces generated by a shock-type load applied on the retaining wall.

The mathematical model is validated so it can be used in current design practice, for the case of accidental actions generated by the collision of vehicles with earth retaining structures. The validation of the mathematical model is based on own dynamic tests, carried out under the same boundary conditions as the static ones.

As an alternative, the physical tests are also analysed by finite element method, using the PLAXIS 2D software package. The tests are simulated using the simplified approach of plane strain models. The obtained satisfactory results are presented, as well as the potential development of FEM models to be safely used for this purpose.

Finally, practical examples of applying the mathematical model developed by the author are presented. The examples consist of passive earth pressure calculations, in case several common transportation vehicles collide with retaining walls.

Furthermore, a simplified preliminary analysis is recommended, in order to identify the design cases in which the dynamic response may lead to the system’s loss of stability.

For the safe design of earth retaining structures exposed to risk of vehicle impact, the amount of passive earth pressure that can be considered in design is needed to be known. Neither the Romanian norms nor the international ones provide any guidance regarding the passive earth pressure under impact generated loads.

The aim of the research is to develop a simple verified model to calculate the passive earth pressure on flat, vertical and rigid retaining structures subjected to shock-type loads. For this purpose, the author conducted tests on models in a glazed channel, which pursued the direct comparison of passive earth pressure mobilization on reduced scale models, under both static and

dynamic loading with a transitory shock-type load. Phenomenological comparison was made not only by using the electronic transducers method, but also by applying optical methods, adapting the use of image analysis techniques for the first time in soil dynamics, in order to define the mechanism of passive earth pressure mobilization under dynamic loads.

The developed mathematical model is based on the simplifying assumptions of Coulomb's theory (1776), but introduces deformation elements by considering the prism mobilization proportional with the wall displacement. This defines the term of compressible monolith. This hypothesis, formulated by Holzlöhner (1994 and 1995), was confirmed on physical models by analysing the recorded images during static passive earth pressure mobilization. Similar own analyses, made under dynamic loads, have not revealed a definite significant variation of the inclination of the failure plane with the acceleration applied to the soil prism. The static mathematical model was calibrated based on the static tests performed on experimental models. For the basic research of the mechanism of passive earth pressure mobilization under static and shock-type dynamic loads, a non-cohesive, dry and thus drained sand was used, so the friction angle determined by static tests could also be considered for calculation of the dynamic tests.

The results obtained using the mathematical model have been confirmed by the recordings made. For a simplified practical approach, in case of a preliminary design analysis, the author proposes a series of simplified graphs to evaluate the wall displacement, when the characteristics of the impact force can be estimated as input data. The use of the mathematical model, developed through the present research, is recommended in current design practice.

In special case of high importance projects, complex numerical models can be employed. The parameters and constitutive models used for the numerical analyses need to be calibrated and validated by centrifuge or real scale tests.

It is increasingly common to build different types of retaining structures near the transportation ways, thereby exposing them to vehicle collision risks.

The impact of the retaining wall takes it out of the static equilibrium state and pushes it towards the retained soil. Opposing the movement, the passive earth pressure is mobilized as a reaction. In this case of impact load a dynamic soil-structure interaction occurs.

The passive pressure is usually used in the engineering design of the retaining structures as the most important variable. For this purpose, taking into

account the dependency of the passive pressure on the allowable displacement of the wall is of the utmost importance, since the pressure has a supporting effect on the wall.

All the calculations of the earth pressure are approximations. This is not only valid for the passive pressure and for the practical case of the passive resistance, obtained by integrating the pressure on the wall height, but also for the probable distribution of the pressure.

Several authors, starting with Okabe (1926) and Manonobe & Matsuo (1929), studied the passive earth pressure under indirect dynamic loads generated by earthquakes. The effects of the earth acceleration and inertial forces of the wall are often simulated using quasi-static forces, for example in Stanciu & Lungu (2006).

In the case of retaining structures, under a vehicle impact loading, a nonlinear dynamic reaction of the ground is obtained, which cannot be effortlessly modelled using the currently available numerical software and constitutive laws. Therefore, appears the necessity to develop a design method to verify the overall stability (ULS) and displacement (SLS) of the retaining walls loaded by dynamic forces due to the impact of vehicles. In this context, geotechnical investigations need to provide information regarding the failure mechanism and the interaction between the structure and the ground. Since testing on real scale models is an extremely costly method, reduced scale models were used. This offers the possibility to study the influence of different parameters, by varying them, on the dynamic behaviour of ground-structure interaction. Some of these parameters include the density index of the tested sand, the characteristics of the impact force, wall geometry etc.

Based on experimental test results obtained from the laboratory model, a proposed mathematical model will be calibrated and validated considering a wide range of relevant parameters. The model is intended to be used for the determination of the passive earth pressure under dynamic shock-type loads. After applying this model, if the overall stability (ULS) and displacement (SLS) of the retaining wall subjected to dynamic shock-type loads are verified, its simplification will be attempted, in order to provide a calculation method usable in engineering practice.

The collision of a vehicle with a structure occurs after the control of the vehicle is lost during movement. This impact process is complex, equivalent to traffic accidents. This type of incident must be considered as a high intensity short-term load, with a low probability of occurrence. It can result in collapse of the structure or structural members, or they stop functioning under normal use.

Permanent retaining structures and bridge abutments are usually built as planar profiles of cast-in-place reinforced concrete walls. Embedded walls are wall-like retaining structures that maintain the stability of different levels, when they are not supported by slopes. Various types of embedded walls can be employed, varying their dimensions, support type and materials, resulting in different bending stiffness. Their bending stiffness and resistance is the main factor of supporting the different levels of the soil, while their weight is insignificant. The calculation of the static stability of the walls and of the static passive earth pressure is done in accordance with the principles described in SR EN 1997-1:2004 and with the regulations of the NP113:2004 and NP120:2014 norms. The embedded walls are considered flexible to bending in their static design at ultimate limit states. Despite this, in order to study the basic principles of passive resistance mobilization during impact loads, in the present paper an ideal wall with rigid bending stiffness and with one degree of freedom (horizontal displacement) was adopted.

At the moment of impact, the ideal wall is in equilibrium and it is subjected to the at-rest earth pressure, as represented in Figure 1-1.

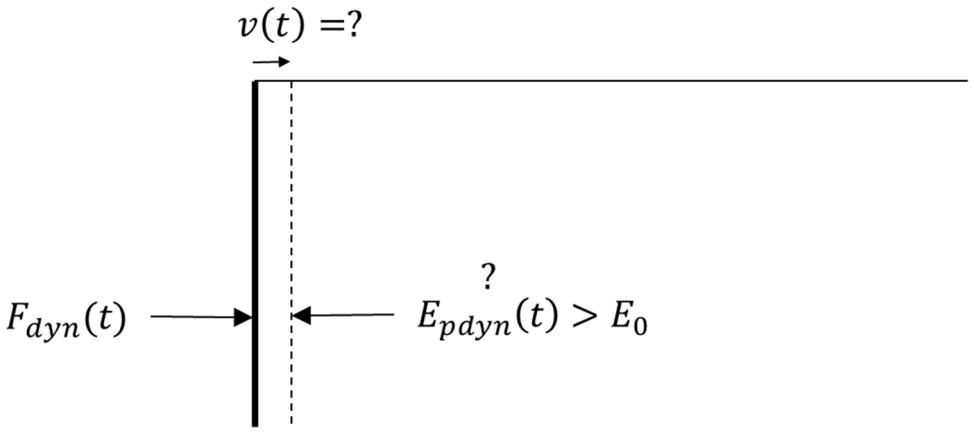

Figure 1-1: Basic representation of the stresses acting on the ideal wall at the moment of impact

Among all types of vehicles, like motor vehicles, rolling stock, river and sea vessels or aircraft, the first ones present the highest collision probability with earth retaining structures. Figure 1-2 and Figure 1-3 present possible real case scenarios of passive earth pressure mobilization in case of a motor vehicle colliding with retaining walls and a structure having a shallow or a deep foundation.

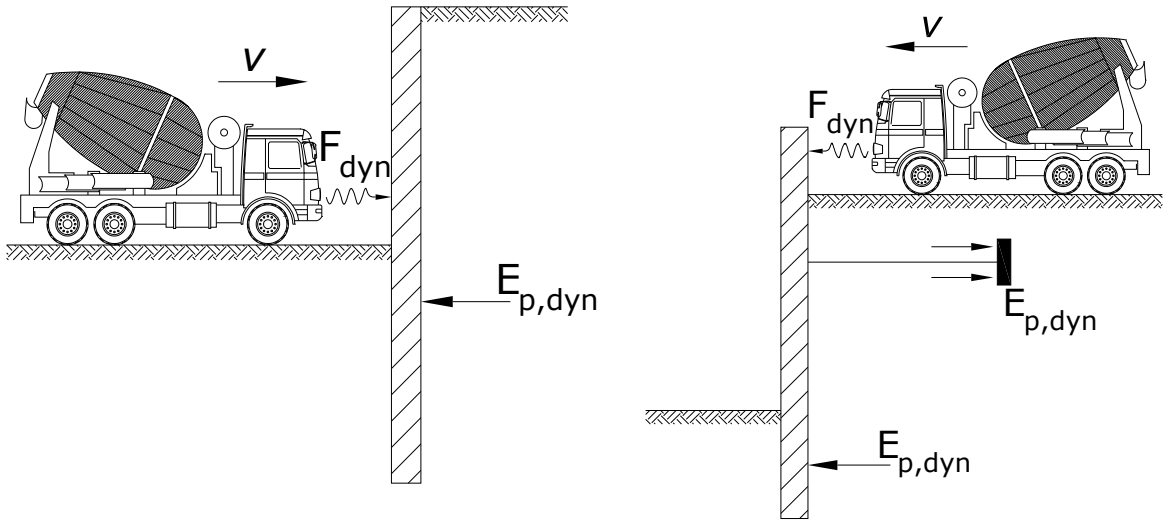

Figure 1-2: Possible real case scenarios of passive earth pressure mobilization in case of a motor vehicle colliding a retaining wall

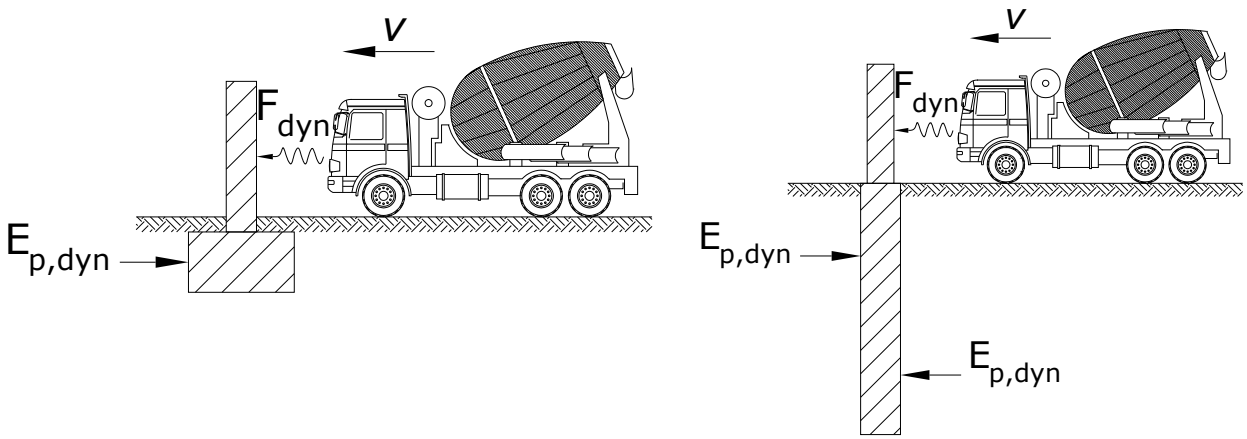

Figure 1-3: Possible real case scenarios of passive earth pressure mobilization in case of a motor vehicle colliding a structure having a shallow or a deep foundation

The most common heavy vehicles driving on public roads are lorries and construction equipment. Due to the low traffic of the heavy haulers or army armoured vehicles, the probability of their impact with retaining structures near the roads is extremely low. Hence, taking these type of vehicle into account is only justifiable for high importance structures. The trucks used to move goods over long distances present the highest risk of collision with retaining structures, due to their large mass and relatively high velocities.

Chapter 2. Experimental equipment

2.1 General information

In order to study the passive earth pressure under shock-type loads, experimental testing is a sine qua non condition. For this purpose, 1g model test, centrifuge test or full-scale tests may be considered. Due to the study's budget restraints, the 1g model testing technique was chosen to analyse the phenomenon.

The purposes of the reduced scale model tests were not only to obtain qualitative results regarding the passive earth pressure under shock-type loads, but also to obtain quantitative comparisons with static passive earth pressure.

The first own experimental tests were conducted on the physical model in static conditions. They served to validate and calibrate the mathematical model for static passive earth resistance mobilization, presented in 3.5. The equipment acquired for the static tests was used for conducting the more complex dynamic tests on the physical model. These were performed in the same conditions as the static ones. Based on the results obtained by dynamic tests on the reduced scale model, the mathematical model for passive earth resistance mobilization in static conditions was further developed for the calculation of the passive earth resistance under shock-type dynamic loads. The mathematical model for the calculation of passive earth resistance in dynamic conditions is presented in Chapter 4.

2.2 The own experimental stand

The real retaining structures endangered by collision are not rigid to bending and they have finite dimensions, in order to study the basics of the phenomenon and to facilitate the comparison between the static and dynamic case, in this paper, a wall stiff to bending and a plane strain condition are considered.

In order to perform the model tests, the author conceived a complete experimental stand (see Figure 2-1), which was built in the testing facility of the geotechnical and foundation department of the Technical University of Berlin. The experimental stand is mainly made out of a glazed channel filled with sand, two parts of equipment to apply loads, one for each type of load, static and dynamic, a container for pluviometrically laying the sand and electronic equipment to record the measured values.

The glazed channel has a solid steel frame. The channel is also provided with a guiding device, which ensures the horizontal displacement of the measuring wall, when subjected to loads.

To more precisely include the influence of side friction, as well as the scale of the physical model, the glazed channel has a modular design, in order to effortlessly modify it to double its internal width by comparison with the initial one. The same components were used for both widths of the glazed channel, besides the measuring wall, the base plate, the side plate behind and the connection between the side walls. The guiding device, the loading equipment and the side glass walls remain the same.

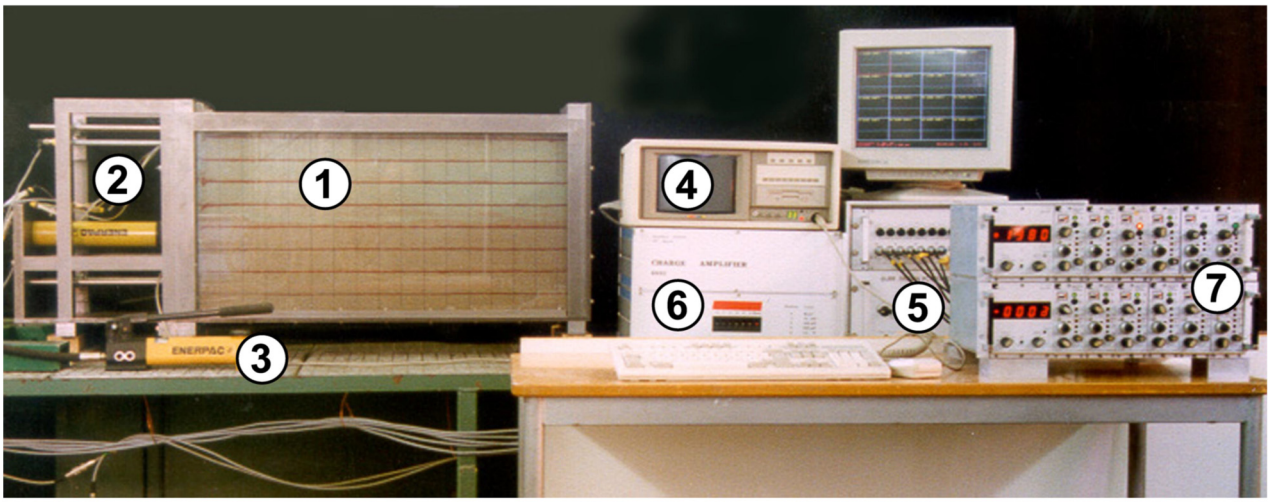

Figure 2-1: Preliminary experimental stand: (1) glazed channel filled with sand; (2) guiding device of the mobile wall; (3) hydraulic loading equipment for static tests; (4) equipment to record the measured values with a computer measurement data acquisition board; (5) analogue/digital converter; (6) amplifier for accelerometers and (7) universal amplifier for displacement, force and pressure transducers

The glazed channel has a nominal 16 cm width, a 45 cm height and an 82 cm length for the narrow series of tests, respectively 32 cm for the wider ones (see Figure 2-2).

Legend:

1 Mobile measuring wall
2 Stiffening corner steel
3 Guiding axle
4 Fixed support
5 Glazed lateral walls
6 Inductive displacement transducer
7 Trial sand
8 Load cell
9 Bottom plate
h Sand height in the glazed channel

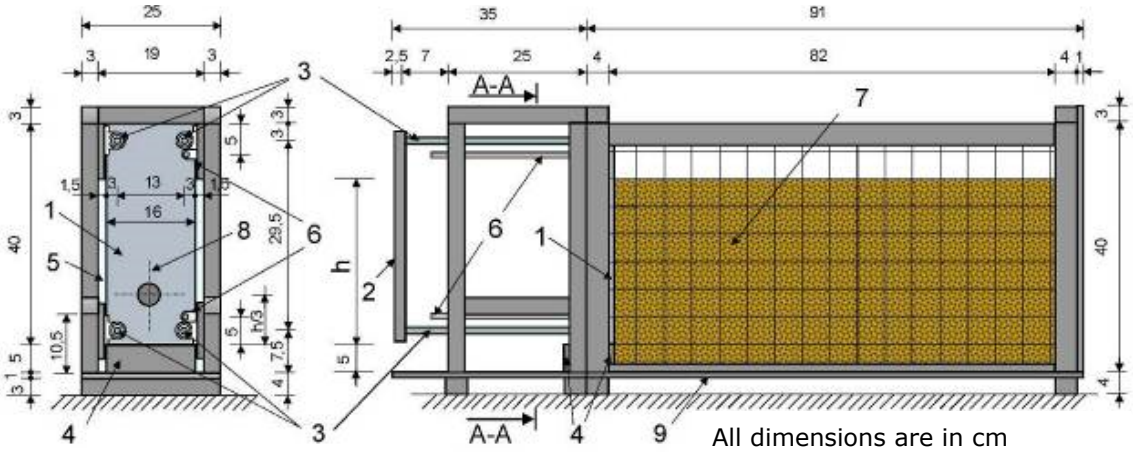

Figure 2-2: Schematic representation of the glazed channel for the narrow series of tests, without the loading equipment

Initially it was considered to use two different scales in order to obtain relations that define a model group with the scale factor 1/2, but this did not lead to directly usable results, therefore this was no longer pursued.

The static, respectively the dynamic tests were conducted under the same conditions, in terms of mobile wall, side walls and sliding device friction with the sand, by using the same measuring mobile wall and by changing the loading device. This fact eased the direct comparison of the results obtain for both static and dynamic load cases.

The mobile measuring wall has an area of 40 x 32/16 cm and it is supported by the guiding device at 5 cm above the base plate of the glazed channel. Between the base plate and the lower edge of the mobile wall, a fixed restraint was introduced, having a 5 cm height and the side facing the glazed channel aligned under the one of the mobile wall. In order to prevent any sand leaks during its displacement towards the inside of the channel, a thin L aluminium profile with a 4 cm side, was fixed on the outer side of the mobile wall. The inner side of the profile is horizontal, at the level of the mobile's wall lower edge and it gradually slides on the upper side of the fixed restraint. In this way, the glazed channel was sealed against sand leaks near the lower edge of the mobile wall during its displacement. Due to the resulting space between the

lower level of the mobile wall and the base of the glazed channel, the failure surface can develop freely, even in the case of circular surfaces which would extend under the base of the wall. On the upper side of the glazed channel's base sand was glued to create a rough surface, which ensured that the failure surface would develop inside the glazed channel and the mobilized soil body did not slide on the base plate of the glazed channel. The mobile wall, made of S235 steel with a 1 cm thickness and a 40 cm height, can be considered for the purpose of the present research as being rigid, comparing its displacements with the ones of the sand body. The wall is also stiffened by the guiding device. The latter is made of four horizontal round steel bars, with a 12 mm diameter, which are fixed on the mobile wall. The bars slide through bearing fixed on the rigid frame of the guiding device (see Figure 2-2). The bars are joined in pairs at the other end by vertical L profiles, with a 2 cm side, providing an added stiffness to the mobile wall – guiding device assembly. Being thus stiffened and guided, the mobile wall has only one degree of freedom, the horizontal displacement. It was wanted to build the mobile wall's assembly as stiff and light as possible. Its mass is not influencing the static tests, but in the dynamic ones it intervenes to the dynamic equilibrium of the wall through the inertial forces. During the acceleration of the mobile wall, the mass-dependent inertial force act as a resistance, opposing the movement, and during its deceleration it act for continuing the movement. A viable measurement of the vertical component of the passive earth resistance to determine the mobilization of the wall's friction angle with its displacement was aborted, since it would have increased the unfavourable effect of the wall's mass.

To determine the boundary conditions of the model, both static and dynamic preliminary tests have been conducted. For the static preliminary tests, a hydraulic equipment was used to apply the loads, made of a hydraulic cylinder and a manual pump (see Figure 2-1). The gradual displacement of the wall, imposed by manual pumping did not result in a uniform mobilization of the passive earth resistance (see Figure 2-3). The test represented was conducted for the wall with a 16 cm width, a 16 cm height of the sand column inside the channel and a density index of D=0.7.

In order to obtain more accurate results, the loading hydraulic equipment was replaced with and electro-mechanical one, which was used for all the static tests (see Figure 2-4). This is made of an electric engine with gearbox, having the velocity electronically adjusted. It was able to continuously move the mobile

wall in front of it towards the sand body with adjustable velocity steps varying between 0.0001 and 1.33 mm/min. The maximum displacement from the initial position w is 4 cm, corresponding to a w/h=16.7% relationship for the height of the wall h=24 cm. The electric engine with gearbox can apply a constant velocity to the mobile wall, overcoming resistance forces of up to 10 kN. In Figure 2-5 quasi-uniform mobilization of the passive earth resistance can be seen, for a constant velocity of 1.33 mm/min imposed by the electric engine device on the mobile wall with a 32 cm width, the a 24 cm height of the soil column inside the glazed channel, and the density index D=0.7.

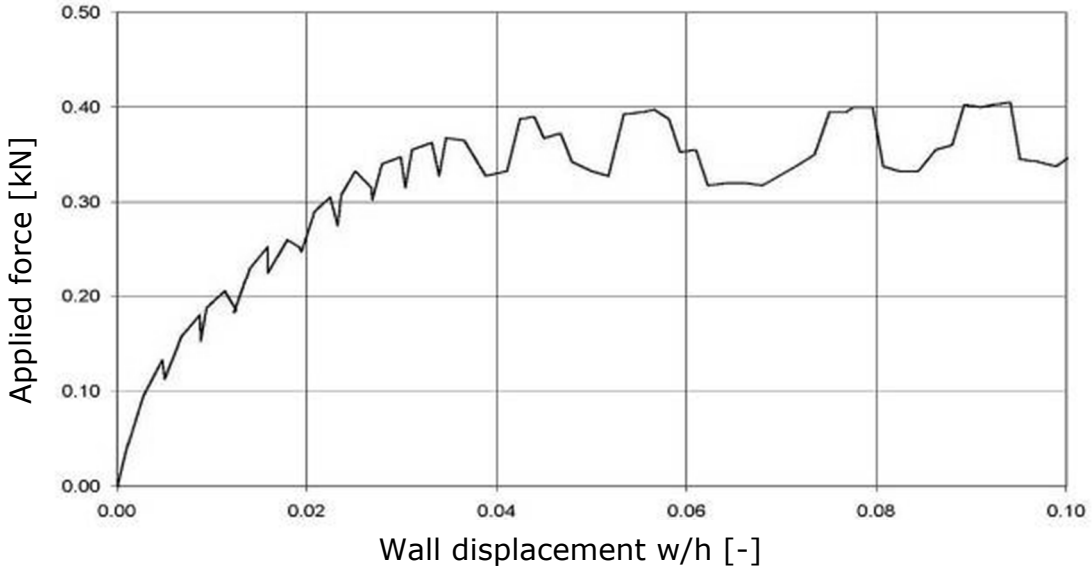

Figure 2-3: The gradual displacement with the hydraulic equipment with a manual pump leads to an irregular mobilization of the passive earth resistance

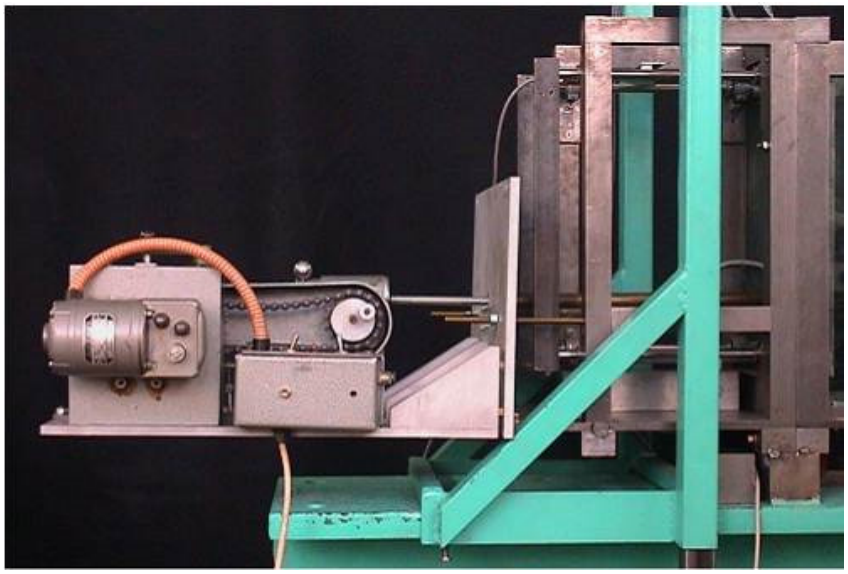

Figure 2-4: The equipment with an electric motor and a reducer, for applying a constant displacement speed of the measuring wall, for static tests

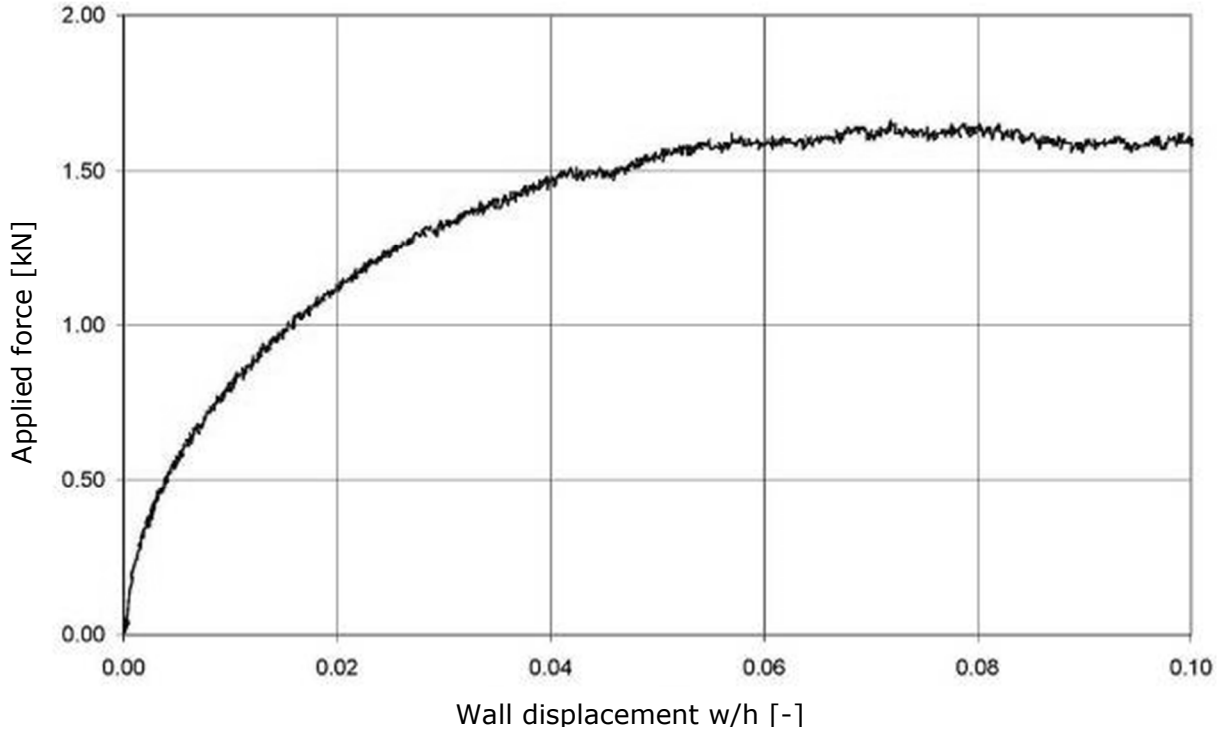

Figure 2-5: The constant speed-rate displacement of the mobile wall leads to a quasi-uniform mobilization of the passive earth resistance

In order to apply a dynamic shock-type load that reproduces the vehicle collision on the measuring wall, different equipment was considered. The first version used a hammer with impulse, which is usually used for a wide range of application to establish certain dynamic parameters, to apply impulses to foundations and other structures, as well for studying the wave velocities through soil. For shock-type loading of piles during centrifuge tests done by other authors Kotthaus (1992) and Jessberger and Latolzke (1998) pre-stressed spring equipment and elastic collision bodies have been developed. The testing techniques used in seismic engineering and for vehicle collision simulations, recorded accelerograms are reproduced with high precision using electronically controlled hydraulic equipment. Due to the low budget of the research project and the wider characteristics of the shock-type dynamic loads, a complex equipment to apply the dynamic load was not chosen.

In order to thoroughly study the phenomenon with the limited available means, at conducting the own tests a hammer, set as a pendulum, was used. An overall photo of the experimental stand, ready for static tests can be seen in Figure 2-6. The pendulum-hammer can be seen above the mobile wall.

Figure 2-6: The 32 cm wide glazed channel filled with sand, ready for a static passive earth pressure mobilization test; behind the experimental stand, the mobile container for pluviometrically laying the sand and on the right there are the amplifiers for accelerometers, displacement, force and pressure transducers

In order to ensure repeatable tests in terms of speed, angle and collision surface on the wall, a guiding frame was built for the loading hammer (see Figure 2-7). The vertical steel frame is mounted on a HE800A steel beam, which also supports the glazed channel. The vertical steel frame is able to slide horizontally along the steel beam. Therefore, the horizontal position of the frame can be continuously adjusted, depending on the length of the impact cap, with four adjustable screws, so the wall is in contact with the impact hammer while it is at rest. The hammer was mounted on the guiding frame by a rotating shaft fixed on circular rolling bearings. It was mounted parallel with the measuring wall, therefore freely oscillating in the vertical plane. In the following paragraphs, the hammer assembly will be referred to as an impact pendulum. The repeatability of the shock-type loading of the measuring wall was done by the free-falling of the pendulum from a predetermined height. The impact load could be varied within a wide range by using different falling heights, masses and lengths of the pendulum, as well as by using impact caps with different elastic properties. To ensure different masses and collision velocities, the hammer was replaced with

lighter and longer pendulums. Therefore, the time dependency of the collision force was measured, in the same manner as for the static tests, with a strain gauge load cell mounted on the outer side of the mobile wall (see Figure 2-8). The accuracy of force measurements in the dynamic case was successfully checked with parallel measurement with the impulse hammer.

To determine the mass that acts at the collision with the wall, the pendulum was moved in horizontal position. The mass was measured by supporting the impact cap on an electronic scale. The height of the rotation axis could be continuously adjusted, in order to maintain the impact point at approximately one third of the fill height behind the wall. The purpose of applying the shock-type load as close as possible to the position of the resultant force of the passive pressure was to minimize the overturning moment of the mobile wall and implicitly the stresses developed in the guiding device. The experience acquired from the first tests proved the measuring difficulty of the earth pressure, which has also been found by other authors. For the first glazed channel, this was done using three small pressure sensors with a flexible membrane and a diameter of only 16 mm, which are usually used the measure fluid pressure. The small-area pressure sensors proved to be sensitive at the soil's lack of homogeneity and to the shocks transferred to the wall during dynamic tests. Also, the bending of the membrane while subjected to pressure leads to arching effects and thus to a possible uncertainty of the results, therefore the pressure sensors for fluids were not used. In order to minimize the measurement errors of the earth pressure, measurements needed to be done on a larger surface. For this purpose, five independent deformable steel plates were fixed on the inner surface of the wall (see Figure 2-9), on which strain gauges were set. Even minimal bending of the plates, having insignificant deformations by comparison with the displacement of the wall, modify the electrical resistivity of the strain gauges, registered by the electronic measuring device. The pressure sensors of own design and execution were calibrated using a soft rubber container filled with water. Over the container set on the base of the glazed channel, the mobile wall was overlain with the flexible plates facing downwards, and making contact with the container on their entire surface. Using a hydraulic cylinder a quasi-linear vertical increasing load was applied, which was measured with an electric pressure cell. During the calibration procedure, the variation of the strain gauges' resistivity mounted on the flexible plates was measured. Thus, the five measuring plates of the earth pressure on different depth levels were calibrated.

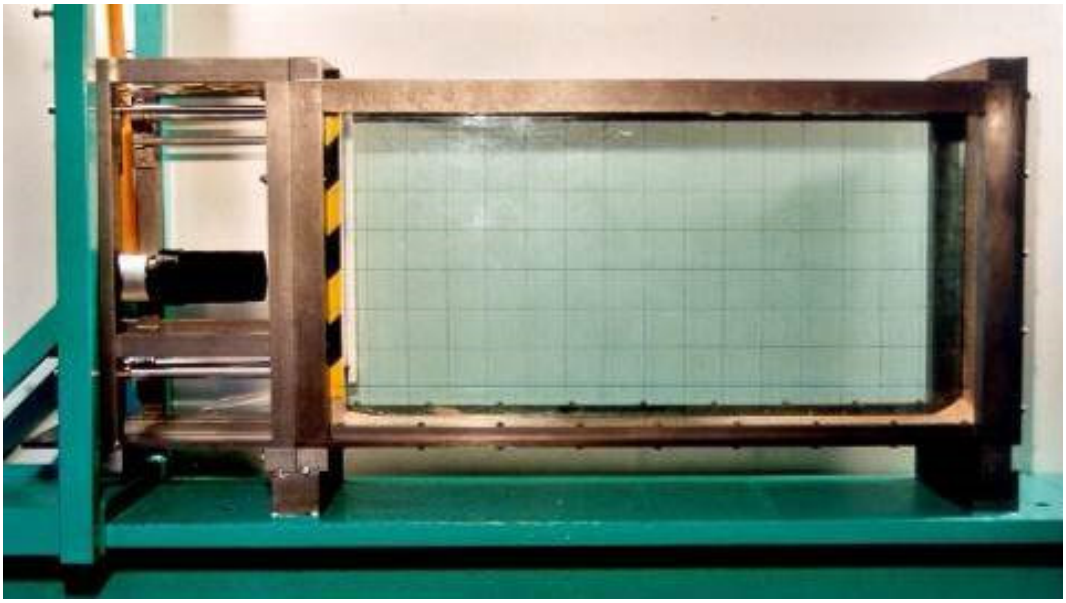

Figure 2-7: The empty glazed channel mounted on the HE-A steel beam, with the guiding frame and the impact pendulum that applies the load on the measuring wall

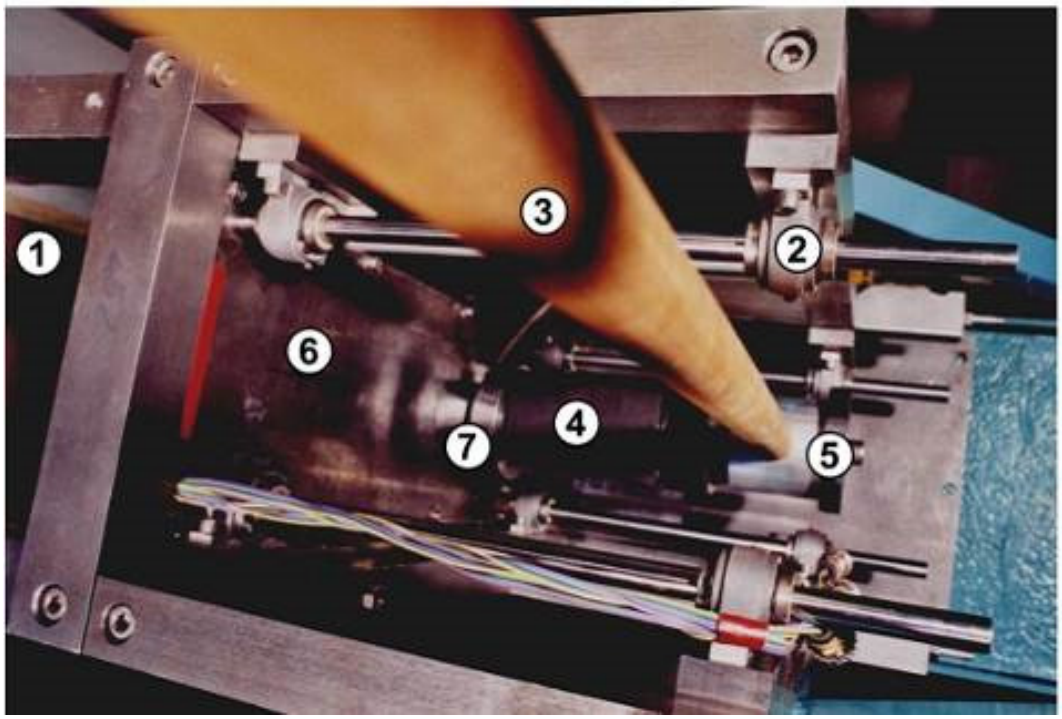

Figure 2-8: Top view of the guiding system fixed on circular rolling bearings (1); steel shafts (2) that allow a horizontal displacement of the measuring wall; impact pendulum (3) with a soft impact cover (4) and an additional mass (5); outer face of the measuring wall (6) with a strain gauge load cell (7)

For building the second measuring wall with a 32 cm width the use of flexible plates with strain gauges was no longer viable, since for a double width of the wall meant that their thickness needed to be doubled, in order to maintain the same bending sagging, therefore would unwantedly increase the mobile

wall's mass. Thus, in order to measure the earth pressure on the mobile wall at different depth levels, a successful attempt of measurements with resistive pressure sensors was made (see Figure 2-9). This was performed for the first time worldwide for tests in soil mechanics, by the knowledge of the author. These pressure sensors type FSR-154 made by IEE (International Electronics & Engineering) perform measurements by modifying the electrical resistivity of an internal semi-conductive polymer layer when pressed. The type used has a square active area of 37.7 x 37.7 mm, for a total area of 45.7 x 45.7 mm. Their thickness is only 0.4 mm, making them ideal for measurements on the inner surface of the wall.

After building the glazed channel, the author built and adjusted a complete assembly to record data for numerous sensors. Since the existing measuring equipment did not correspond to the high data acquisition frequencies needed to record the sudden value variations during the dynamic tests, data acquisition cards and a specialized software made by BMC-Systeme, were installed on a new computer. The MAD 12f data acquisition card has 16 input channels, 12 bit resolution, a measurement range of +/-10 V and a total data acquisition frequency of 333 kHz, being able to record 10,000 values per second for each input channel. It converts the pre-amplified input analogue signals in digital format, which are simultaneously measured, viewed and stored in ASCII format. The recorded data is interpreted with tabular calculation software. The following physical quantities have been recorded: forces with the type HBM C2 strain gauge dynamometer, displacements with the inductive displacement sensors, accelerations with capacitive sensors based on piezo-crystals and pressures with strain gauges and resistive pressure sensors.

The output signals of the dynamometers and of the inductive displacement sensors were amplified using a universal amplifier with 12 channels, type KWS 3073, made by Hottinger Baldwin Meßtechnik. For the acceleration sensors, two capacitive amplifiers have been used (type 2635 made by Brüel & Kjaer with 3 channels and type 0028 made by RFT with 4 channels). The resistive pressure sensors were charged and amplified with a self-made amplifier and then calibrated in a pressurized container. The pressurized calibration done was successfully verified in an oedometer test using the trial sand.

Figure 2-9: View of the measuring wall from the inside of the glazed channel and a typical layout of the resistive pressure sensors for the test series with narrow mobile wall

2.3 The trial sand and laying it in the physical model

2.3.1 The grain size distribution curve and specific weight

A fine to medium quartz sand was used as a trial soil, with a poorly graded grain size distribution curve (coefficient of uniformity $U = d_{60}/d_{10} = 1.8$). The grain size distribution curve of the trial sand is presented in Figure 2-10 ($d_{50} = 0.35$ mm) and it is representative for the standard trial soil, named in the scientific literature "Karlsruhe sand". This is a sand with a uniform grain size distribution curve and is used as trial material for scale tests in various geotechnical laboratories within Germany. The geotechnical tests to determine the sand parameters were conducted after the preliminary model tests. The smallest particles might have been removed during the repeated laying of the sand with the pluviometric method. The grain size distribution tests were conducted in accordance with DIN 18123 (2011) on three random soil samples.

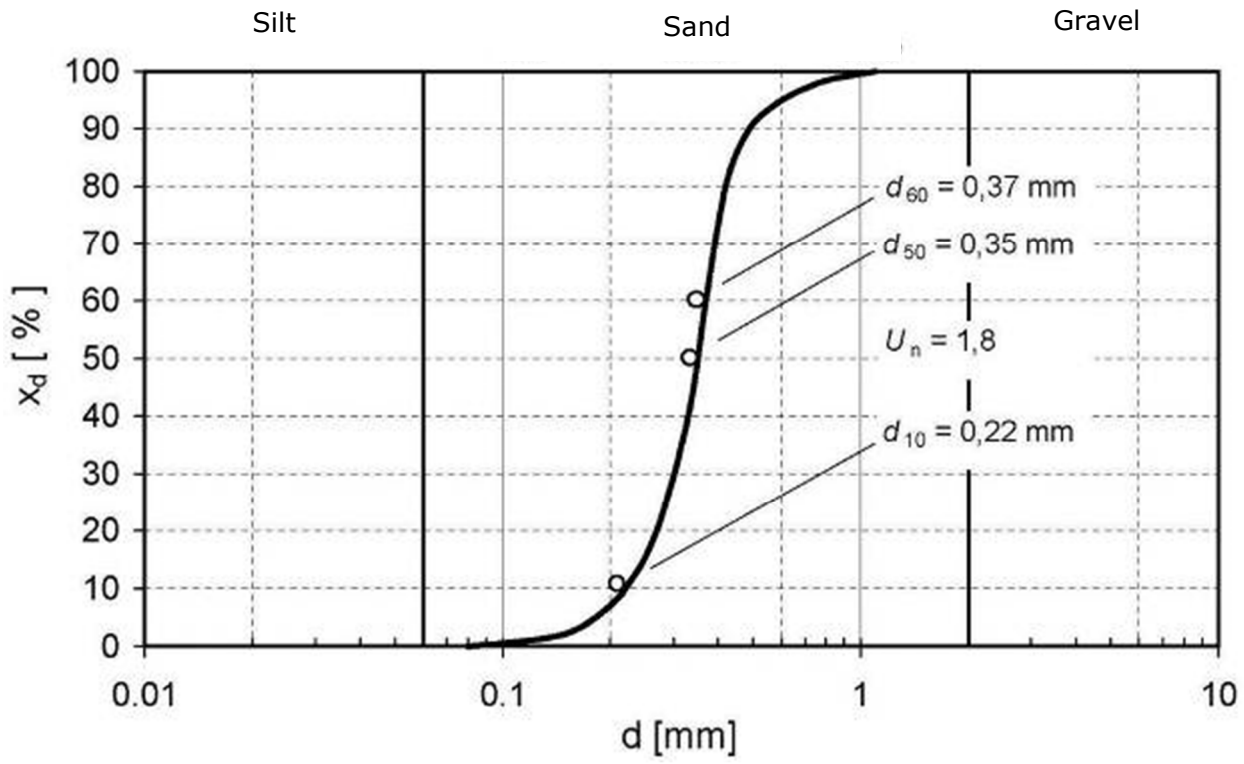

Figure 2-10: The grain size distribution curve of the trial sand

After several model tests, the sand was analysed again and no changes of the grain size distribution curve were identified. This indicates that no relevant particle crushing occurred and the grain size distribution remained unchanged during the whole test period.

The unit weight of the solid particles $\gamma_s = 26{,}6\frac{kN}{m^3}$ was determined in the laboratory on three samples according to DIN 18124 (2011). A reference value of the gravitational acceleration g = 10 m/s^2 was considered for the tests and within the whole paper. The unit weight for dry sand γ_d was done in accordance with DIN 18125-1 (1997). The dry unit weight and the void ratio were determined for the lowest and highest density indexes on four samples according to DIN 18126 (1996). The tests found the dry unit weight for the lowest density index $\gamma_{d,\min} = 14{,}7\frac{kN}{m^3}$ and the void ratio $e_{\max}$ = 0,45 and for the highest density index $\gamma_{d,\max} = 17{,}2\frac{kN}{m^3}$ and $e_{\min}$ = 0,36.

2.3.2 Shear strength of the trial sand

Since the influence of the density index on the passive earth resistance needed to be analysed on model tests, the influence of the density index on the friction angle needed to also be evaluated. In the present paper the density index is used as

$$D = \frac{\gamma - \gamma_{d,\min}}{\gamma_{d,\max} - \gamma_{d,\min}} \tag{2-1}$$

instead of the usually employed relative density index $D_r = I_d$ because the density index D is defined as a function of the dry unit weight γ_d, while the D_r index is obtained based on the void ratio e.

Since the assessment of the passive earth pressure is related to the measuring wall of the glazed channel, which practically corresponds to a plane strain state, the friction angle φ' must be calculated in accordance with EAU 2004 (2009) for similar strain states. This requirement is met in the direct shear test. Direct shear tests were performed in accordance with DIN 18137-3 (2002) in order to determine the friction angle for three different density indexes (D), of 0.25, 0.75 and 0.9. For each different density index, three confining stresses (σ) were applied, of 100 kN/m^2, 200 kN/m^2 and 300 kN/m^2. The needed density index was obtained by pluviometrically laying the sand in the shear box according to the method described in chapter 2.3.4. Each test was performed three times. The average peak values for each different density index and confining stress, obtained by shear tests, are presented in Figure 2-11.

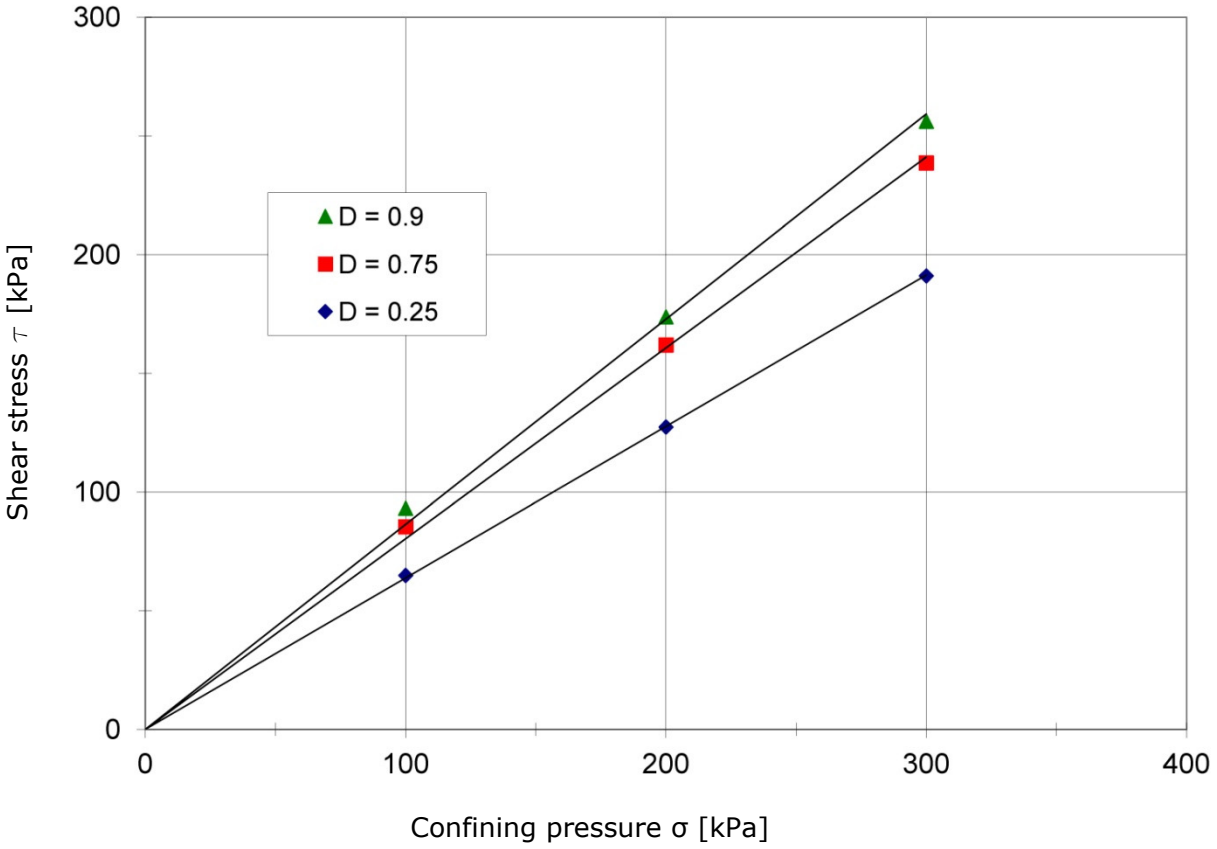

Figure 2-11: The shear strength τ, plotted on the confining stress σ for each one of the three different density indexes D

The friction angles obtained for each density index by linear regression are presented in Table 2-1. The effective friction angle φ' will be reffered to as φ in the following paragraphs, since in this case undrained soils are not being analyzed. The maximum shear strength was used to obtain the friction angle.

Table 2-1. Maximum friction angle dependent on the density index

D [-]	0,25	0,75	0,9
φ [°]	32,5	38,8	40,8

Once the density index *D* is increased, the shear strength also increases. From the values above, the following dependency of the friction angle on the density index is obtained by linear regression Figure 2-11.

$$\varphi = 30^{\circ} + 12 \cdot D \qquad (2\text{-}2)$$

This relationship is also confirmed by results obtained by other authors on the same sand (for comparison see Weißenbach (1961) and Mao (1993)). From equation (2-2) results the critical friction angle $\varphi_{min} = 30°$ for a minimum density index $D = 0$.

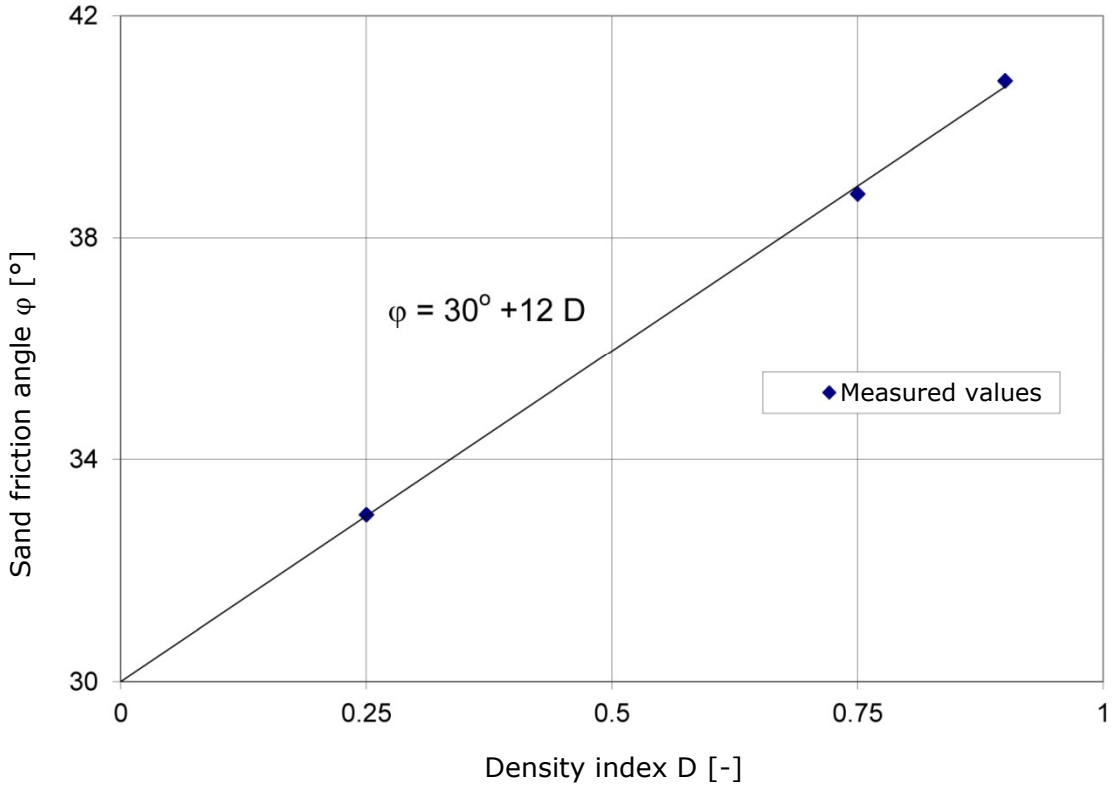

Figure 2-12: The measured friction angle φ plotted on the initial density index $\boldsymbol{D}$

A first recalculation of the passive earth resistance measured during the static tests according to Müller-Breslau (1947) using the values of the friction angle in Table 2-1 resulted in significantly lower values of the passive earth pressure coefficient.

Numerous authors, as Hettler (1997) and Walz&Kremer (1997), state that the friction angle φ is dependent on the confining pressure σ, which has a significant influence on the value of the passive earth pressure force in the case of low stresses developed within the 1 g models. Knowing the relationship between φ and σ helps to correctly evaluate the effective friction angle, needed to asses and recalculate the scale tests.

If the friction angle of the trial sand is no longer calculated by linear regression, independently from the confining stress, but is directly obtained for each pair of shear strength – stress values (in Figure 2-11), a friction angle

value dependent on the density index and the confining stress can be obtained. These values are presented in Table 2-2.

Table 2-2. Maximum friction angle dependent on the density index and the confining stress

σ [kN/m²]	φ		
	D = 0.25	D = 0.75	D = 0.9
100	33°	40.5°	43°
200	32.5	39°	41°
300	32.5°	38.5°	40.5°

Hettler (1997) describes the dependency of the friction angle on the confining stress, obtained by direct shear tests, as an exponential function:

$$\tan\varphi = \left(\frac{\sigma_0}{\sigma}\right)^{\varepsilon} \cdot \tan\varphi_0 \tag{2-3}$$

Herein, φ_0 is the measured friction angle for the σ_0 confining stress and φ is the friction angle for the σ confining stress. The ε exponent depends on the density index and has been analysed by Bauer (1995) and Wu (1992) for the Karlsruhe sand, used for the performed tests. These resulted with a $\varepsilon = 0{,}08$ for a very dense soil, whereas a value of $\varepsilon = 0{,}03$ was obtained for medium dense ones. For a loose soil, ε tends to become null. Based on these values, in the present paper, the following simplified linear relation between the ε exponent and the density index *D* was adopted:

$$\varepsilon = 0.1 \cdot D \tag{2-4}$$

Equation (2-2) and (2-4) are introduced in equation (2-3), and the following relation results:

$$\tan\varphi = \left(\frac{\sigma_0}{\sigma}\right)^{0{,}1\cdot D} \cdot \tan\left(30^o + 12 \cdot D\right) \tag{2-5}$$

where $\sigma_0 = 100\ kPa$.

If the (2-5) equation is evaluated for a confining stress σ equal with the average stress developed within the physical model (2 kPa), up to a real stress

level of 500 kPa and for the entire range of values of the density index, the graphs presented in Figure 2-13 result for the $\varphi(\sigma, D)$ dependency.

Equation (2-5) is confirmed by the measured values and presented in Table 2-2, for the confining stress range from 100 up to 300 kPa, determined in optimal conditions for the present research, using common available direct shear test apparatuses.

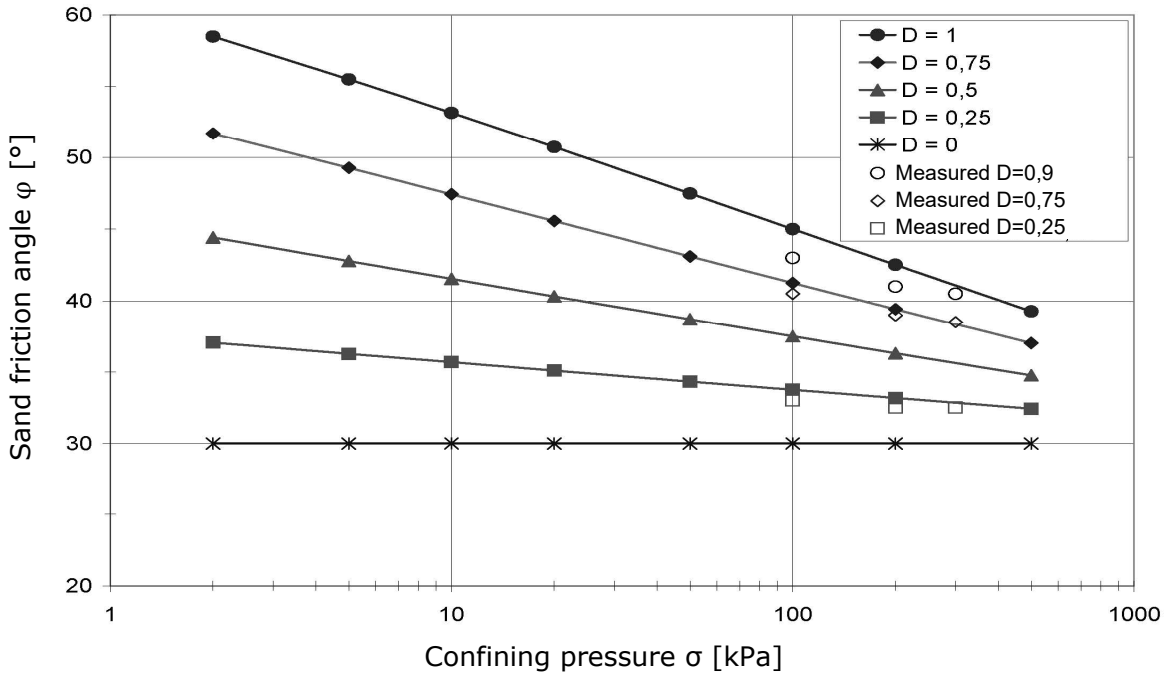

Figure 2-13: The calculated and approximated density index (*D*) – confining stress (*σ)* dependency of the friction angle (φ)

Walz and Kremer (1997) summarised the direct shear tests performed by different authors and concluded that for a maximum density index of a sand overlaid pluviometrically "mathematical" friction angles of up to $\varphi = 60°$ can be encountered under a low confining pressure (about σ = 5 kN/m²).

For a high and very high density index, soil resistance to shearing occurs from particle resistance to movement in a dense particle grid – "grip strength" or "structural resistance" – and form the Coulombian "actual" friction dependent on the confining stress. The high friction angle obtained for a low confining stress is firstly due to "grip strength", which is divided by the low confining stress to obtain the "mathematical" friction angle.

For the extreme case, $\sigma \to 0$, the "mathematical" friction angle increases to infinity, because a certain structural resistance exists, which is divided by a confining pressure. With an increased value of the confining pressure the relation between the "actual" friction and the "grip strength" is amplified until the percentage of the "grip strength" from the total shear strength is lowered to zero.

2.3.3 Measuring wall and side wall friction

Theoretically a sand-wall interface friction angle $\delta = 0$ was employed, because for this case most theories for calculating the passive earth pressure are unanimous (for comparison see Weißenbach (1983)), assessment of the passive earth resistance is thus made less ambiguous. Since an absolutely plane wall $\delta = 0$ is not technically achievable, the condition $\delta = 0$ is fulfilled only when the load is horizontal, the wall moves freely along the vertical axis and its weight is balanced.

These requirements can only be fulfilled by an elaborate mechanical design. A structure like this, which would need to be supported on round bearings, would increase the total mass of the wall together with the mobile part of the guiding device. In the dynamic case the ratio between the inertial masses of the wall and the ones of the foundation would have unallowable high values. Therefore, the possibility of movement of the wall along the vertical axis was no longer considered and a guiding device that allows the movement along the horizontal axis was conceived.

To determine the structure-ground interface friction angle (δ), on which the relation between the passive earth pressure and the wall displacement is depended, either the vertical component of the passive earth pressure (E_{pv}), or the interface shear stresses (τ) must be measured on the contact surface. Each of the two requirements would have unwantedly led to a considerable increase of the wall's mass and thus it would have increased the contribution of its force of inertia to the total inertial forces of the moving soil prism – mobile wall system. In order to keep the system fit for dynamic impact, the structure-ground interface friction angle measurements were discarded.

Since several series of tests were conducted, the wall's surface was covered with a plastic sheet in order to obtain a similar surface roughness. It was changed periodically after a few tests, before its roughness would have

changed. The adhesive sheet used has the advantage that it can stick on the side seals of the wall and on the earth pressure measuring sensors, creating a smooth wall surface. In case of damage it can be partially replaced.

In order to measure both the sand–measuring wall interface friction angle and the sand–glass wall one, a number of modified direct shear tests were performed. The bottom frame of the shear box was either replaced with a plastic foil-wrapped steel sheet or with a glass plate. The direct shear tests were performed in both cases, for two density indexes (D = 0.5 and D = 0.9) and three confining stresses (σ = 100 kN/m^2, σ = 200 kN/m^2 and σ = 300 kN/m^2).

The tests revealed a value of the sand–glass wall interface friction angle independent from density index:

$$\delta_s = 8,5^o = \frac{\phi}{4} \div \frac{\phi}{5} \tag{2-6}$$

which will be referred to as the side friction angle.

In the case of the plastic foil-wrapped steel sheet, the direct shear tests revealed a linear relationship between the interface friction angle δ and the density index D, but independent of the applied stress range of 100 up to 300 kN/m^2.

$$\delta = 9 + 12,5 \cdot D \tag{2-7}$$

Since the plastic foil wrapping was used to cover the wall for all the tests, the symbol δ will be referred to as the sand-mobile wall interface friction angle.

In order to make visual observations of the deformations within the soil body, the sand had to be in contact with the glass walls. Therefore the unwanted friction between the sand and the glass wasn't decreased as other authors did. Direct measurement of the side pressure in order to accurately calculate the interface friction angle with justifiable costs and with the available resources was not possible.

Jaeger (1931) thoroughly studied the influence of side walls on the passive earth resistance using high model scales. After his research, he proposed for the side walls a simplified empiric relation:

$$R_s = \frac{2}{3} \cdot \frac{h}{b} \cdot E_{ph} \cdot \tan \delta_s \tag{2-8}$$

The sand-glass wall interface friction angle $\delta_s = 8{,}5^o$ was found to remain constant and independent from the density index. If this value is introduced in equation (2-8), the ration between the friction force with the side walls and the passive earth resistance has the following domain, for the ratio height-width $\frac{h}{b} = 0{,}5 \div 2$ of the wall:

$$R_s \cong \frac{2}{3} \cdot (0{,}5 \div 2) \cdot E_{ph} \cdot 0{,}15 = (0{,}05 \div 0{,}20) \cdot E_{ph} \tag{2-9}$$

After assessing the own tests in static condition a light dependency of the total passive resistance, which include the side friction, on the ratio height-width of the wall, but a proportionality like the one in equation (2-8) was not found for the given testing condition.

All the friction angle values listed above are peak values. Although the values vary with the relative displacement between the trial sand and the sliding surface, in order to focus on the main variables, the peak values are used in this paper.

According to Mao's assumptions (1993), for similar model tests, the total side friction force R_s, corresponding to the passive earth pressure mobilization in a rigid box, can be approximated, in a simplified but sufficiently accurate manner, by using the at-rest earth pressure coefficient K_0, as specified below in the empirical equation:

$$R_s \cong 2 \cdot E_{ph} \cdot K_0 \cdot \tan \delta_s \tag{2-10}$$

If the side friction angle $\delta_s = 8{,}5^o$, determined to be independent from the density index and the internal friction angle of the sand $\varphi = 37° \div 45°$, are introduced in (2-10), the following equation results:

$$R_s \cong 2 \cdot E_{ph} \cdot K_0 \cdot \tan \delta_s \cong 2 \cdot E_{ph} \cdot (0{,}3 \div 0{,}4) \cdot 0{,}15 = (0{,}09 \div 0{,}12) \cdot E_{ph} \tag{2-11}$$

The total side friction force R_s is plausible and is considered an acceptable disturbance, since it only amounts about 10 % of the horizontal component of the passive earth resistance E_{ph}. In order to evaluate the test results on models in static conditions, described in Chapter 3 and dynamic ones, described in Chapter 4, as well as input data for the mathematical calculations made, the side friction will be approximated using EC 2 – 10.

However, it is not subtracted from the measured passive earth resistance for a uniform comparison, less influenced by approximations of the static and dynamic cases.

The side friction obtained with equation (2-10) is a good approximation, considering the uncertainty and simplifications of own models. Considering this approximation allows to assimilate the tests on physical models as a plane strain state.

2.3.4 Laying the sand

The own preliminary tests proved that neither the manual laying of the sand with later increasing the density index by pressing or vibrating, nor by pluviometrically laying it through a single horizontal mobile hole, falling from a predefined height above the sand level in the box, could obtain repeatable measured values of the passive earth resistance. This is due to the local variation of the density index of the sand in the glazed channel, which influence the mobilization of the passive resistance, despite having a uniform index on average. Thus the pluviometric method was opted for.

By pluviometrically laying the sand, it falls in the glazed channel at a constant speed, from a predetermined height. Therefore a homogenous density index of the sand volume can be obtained (see Walz et al. (1975)). From a container above the glazed channel, the sand fall through a sieve made of a cut steel sheet. The needed density index was obtained by either varying the free-falling height or the sieve size. The flowing intensity depends on the size and density of the sieve. With smaller sieve sizes, indirectly small flowing intensity, and a higher free-falling height a higher density index can be obtained.

After several tests to obtain a repeatable value of the density index, a sieve with a fixed size was built. While pluviometrically laying the sand, the container was hanged above the glazed channel with a crane. The distance h_R from the sieves at the bottom of the container and the surface of the laid sand was kept constant by continuously lifting the container. After several tests to obtain the optimal sieve diameter and the distance between the holes, a d = 5 mm diameter was obtained and a l = 30 mm distance between holes were found to be able to reproduce the wanted range of density indexes, with a convenient fill time and free-falling height. After several tests with various values of the height h_R, the results presented in Figure 2-15 were obtained. The

values lead for the range considered here to the following empiric relation between the density index and the falling height:

$$D = 0{,}42 \cdot \ln\left(h_R\right) - 1{,}04 \tag{2-12}$$

In case of intense falling, vibrations occur in the side walls of the container, resulting in disturbances of the density index. For this reason two tests were conducted for the falling heights h_R = 70 cm and h_R = 90 cm with five containers on the bottom of the glazed channel to check the uniformity of the resulted density indexes. Therefore the containers were filled using the pluviometric method, and by weighting the total sand volume an average and local values of the density index were obtained. No remarkable variation was found.

The trial sand was pluviometrically laid and the free-falling height was determined for the needed density according to equation (2-12). The preliminary tests revealed that a low density index at the base of the volume is difficult to obtain due to a low free-falling height and the base is more fragile to vibrations that may occur. They also showed that neither limit values of the passive earth resistance, nor reproducible failure surface can be observed even if a compaction occurs during wall displacement. Moreover, the limit value of the passive earth pressure and the geotechnical parameters for an initial state with a low density index are inaccurate. Therefore, the tests were conducted on a medium to very dense sand – $D = 0.5 \div 0.9$.

Figure 2-14: Pluviometrically laying the sand in the 16 cm wide glazed channel, in order to obtain a reproducible an homogenous density index

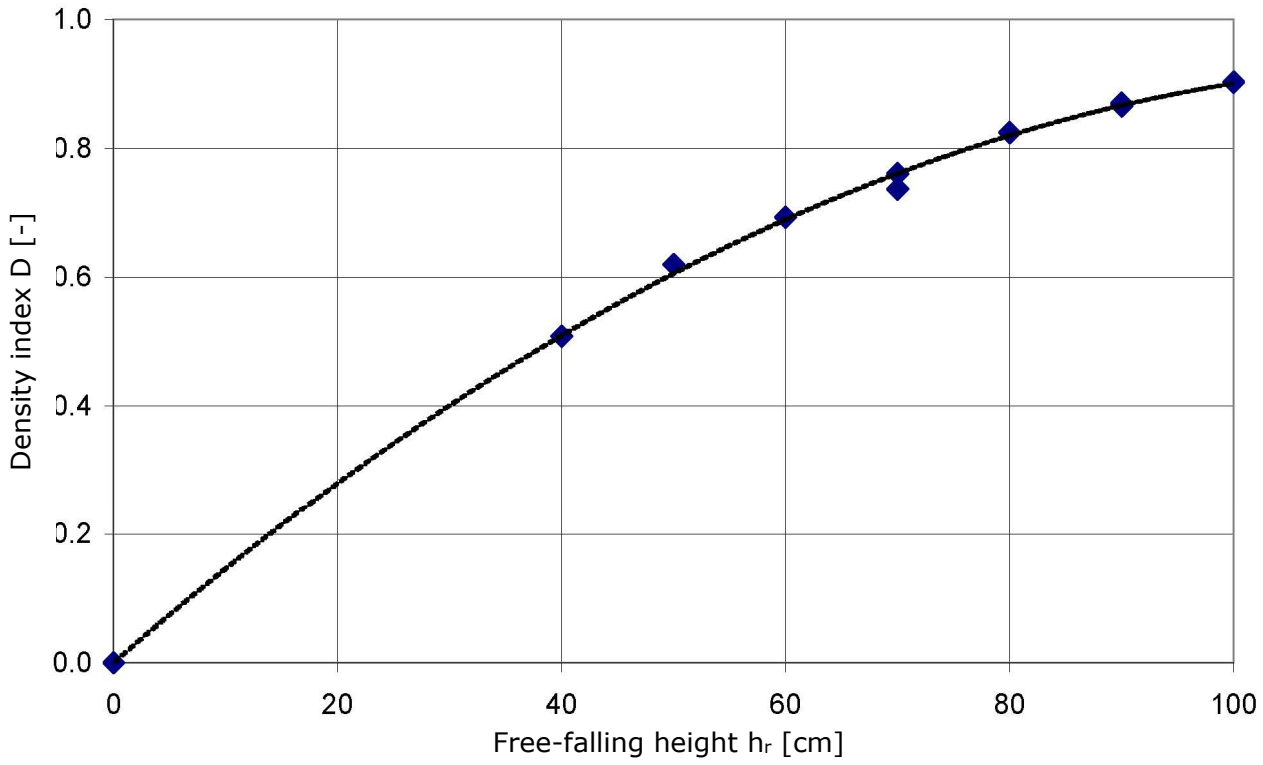

Figure 2-15: Density index plotted on the free-falling height; measured values and regression curve

2.4 Optical analysis method

2.4.1 Limitation and boundary conditions

Visual observations of the trial sand displacement during tests were made through the side glass walls.

For the first tests, the sand was laid with alternate thin layers of coloured black sand, in order to provide a better view of the displacements (see Figure 2-16). Moreover, for the first tests a square grid spaced 5 cm was drawn on the glass surface.

Visual observations could not be made during the dynamic tests, since displacement of both the wall and sand would stop after a short period of time (about 0.1 seconds). Instead, a photographic observation of the phenomena was attempted. This method obtained unsatisfactory results as it mainly recorded the displacement of the active prism, corresponding to the returning movement of the wall towards its original position (see Figure 2-17).

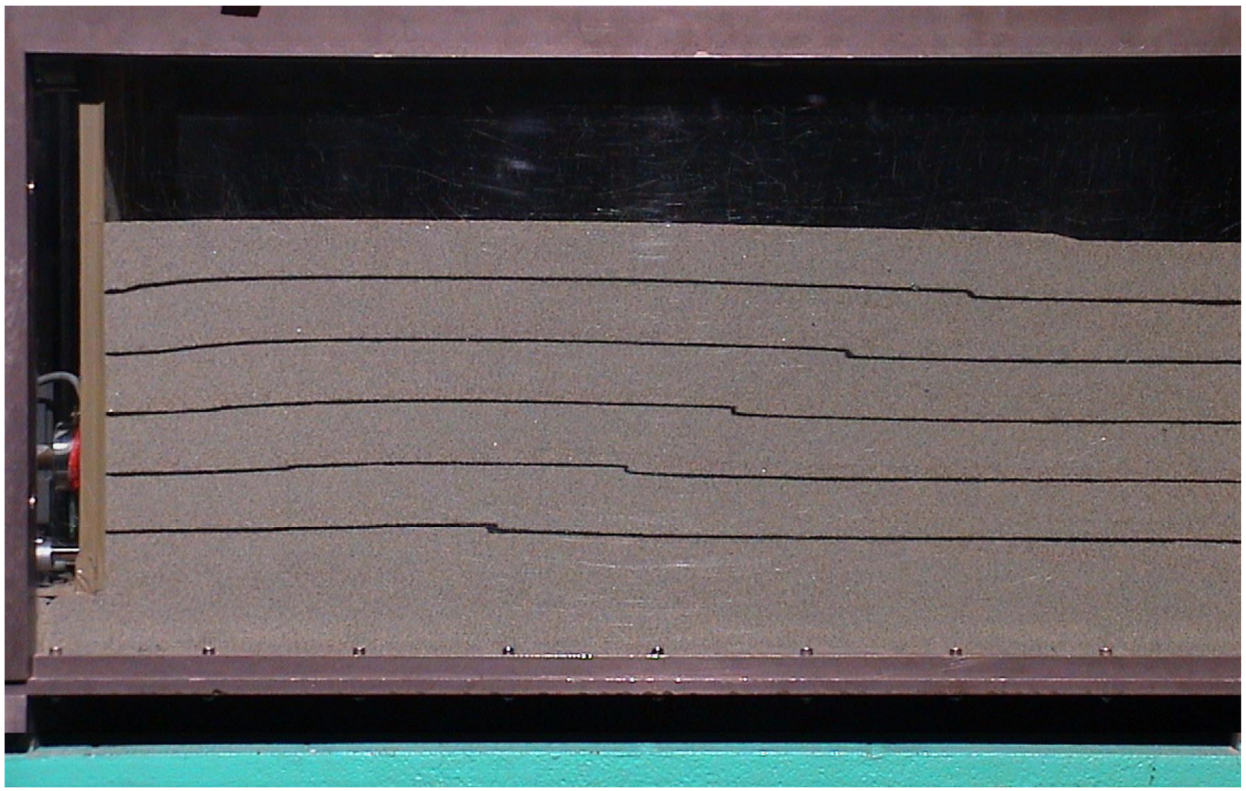

Figure 2-16: Static passive earth resistance mobilization for sand laid with contrast layers

For several dynamic tests long exposure photos (f = 1/8 up to 1/15 s) were taken. These were triggered by an electric circuit before the impact of the pendulum with the wall, thus synchronizing the photo with the impact. It is expected for moved area to be unclear, having the opportunity to identify the failure surfaces in this manner. To better identify the failure surface for the dynamic tests, horizontal layers of black sand were introduced. Since the exposure time could only be doubled or halved, a time-displacement variation of the wall could not be determined (see Figure 2-17).

As a result, a timeline of the observed displacements could not be established, and it could not be determined whether the high deformations of the sand near the wall appear before or after the maximum wall displacement.

To establish a timeline of the displacements, a usual video camera S-VHS with a recording frequency of 25 frames per second was used. It proved to be useless after several tests for the dynamic condition, due to the low recording frequency.

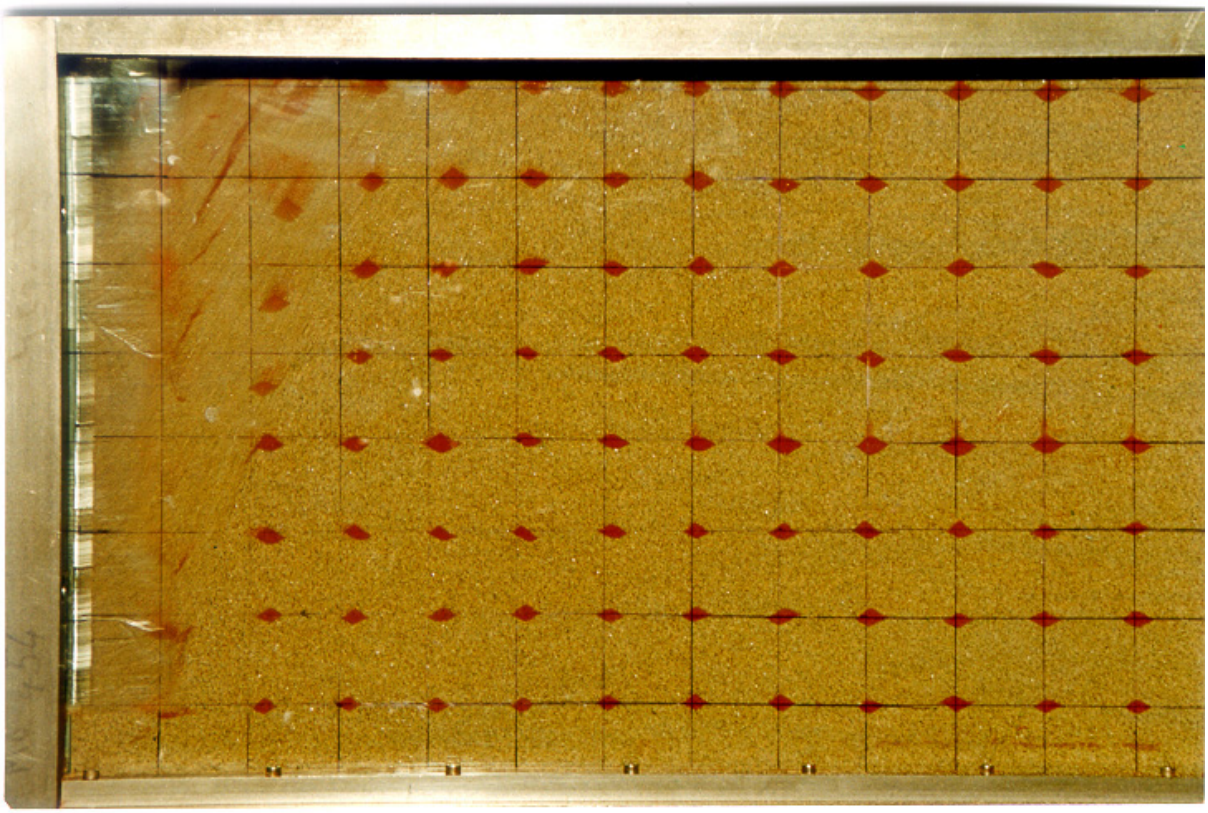

Figure 2-17: Sand displacement under a shock-type load; blurry image of the failure surface or with high displacements; shutter speed f=1/8 s

As the only adequate optical recording method, a high-speed camera was used, which found an increasingly wider applicability in the recent years, which started with the automotive crash tests. A collaboration with the German federal institute for hydraulic structures (Bundesanstalt für Wasserbau) resulted with the possibility of using a device capable of recording 1000 frames per second. The SpeedCAM PRO device, made by Weinberger, consists of an 8 bit (black and white) CCD camera with a square pixel frame (Charged-Coupled-Device) (see Figure 2-18) and hardware devices to store and process the recorded data (see Figure 2-19). For a data transfer rate of 256 MB/s corresponding to 1000 frames/s and a maximum resolution of 512x512 pixels, the memory for 128 Mb images is enough for a 0.5 s video record. Longer records are only possible at lower frame rate frequencies or lower resolution. The recording is triggered by the falling pendulum, before colliding with the mobile wall, by operating a laser barrier. After this, the video images are converted as individual digital images in TIFF format and stored on the hard disk drive. High-rate frame per second recordings and converting videos in individual digital images allowed an accurate time lapse observation of the phenomenon. The recorded images

were analysed using the Particle-Image-Velocimetry (PIV) optical method. In order to compare the dynamic deformations of the trial sand under shock-type loads, obtained with the image analysis, a similar observational method needed to be used for the static tests. For this purpose, the static passive earth pressure mobilization was recorded with a digital remote controlled camera with a resolution of 1152 x 864 pixels. During a slow and constant displacement speed of the wall, images were recorded at predefined 30 second time intervals. For each recorded static test, a series of digital images has been store, which has been processed and evaluated as the ones recorded during dynamic tests.

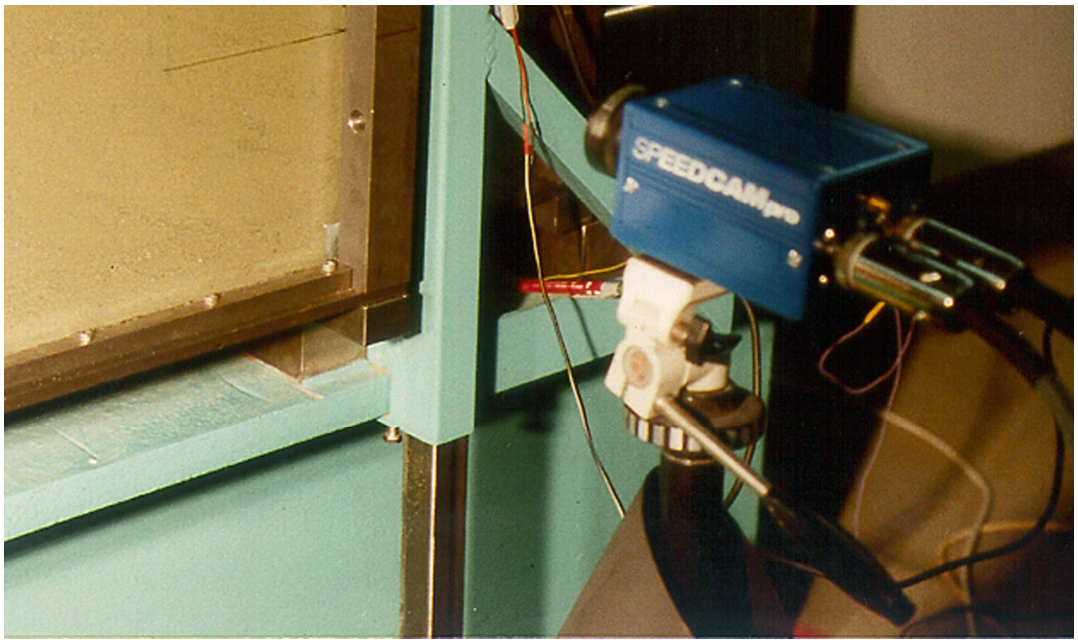

Figure 2-18: High-speed camera set in front of the glazed channel

Figure 2-19: The computer used to process and analyse the data recorded with the high speed camera (left) and the one used to process and analyse the recording made with the sensors (right)

For the PIV analysis of the model tests with video and photo recordings, the sand was laying with intermediate coloured layers was proved to be inappropriate due to the coarse grid. For a better contrast on the entire contact surface of the sand with the glass walls, approximately 1% of the total sand volume (the upper domain of the grain size distribution) was coloured in black, as can be seen in Figure 2-20. By colouring the larger particles a good contrast and resolution of the recorded images was obtained. By playing the images with a convenient time step, the deformation of the sand and failure surface can be easily observed on the interface. Using the PIV method, the displacements of the sand were transformed in a field of vector displacements between two successive images. The author elaborated an own algorithm to derive the field of vector displacements to obtain their local gradient. By doing this, the mobilized soil prism and the failure surface were further highlighted.

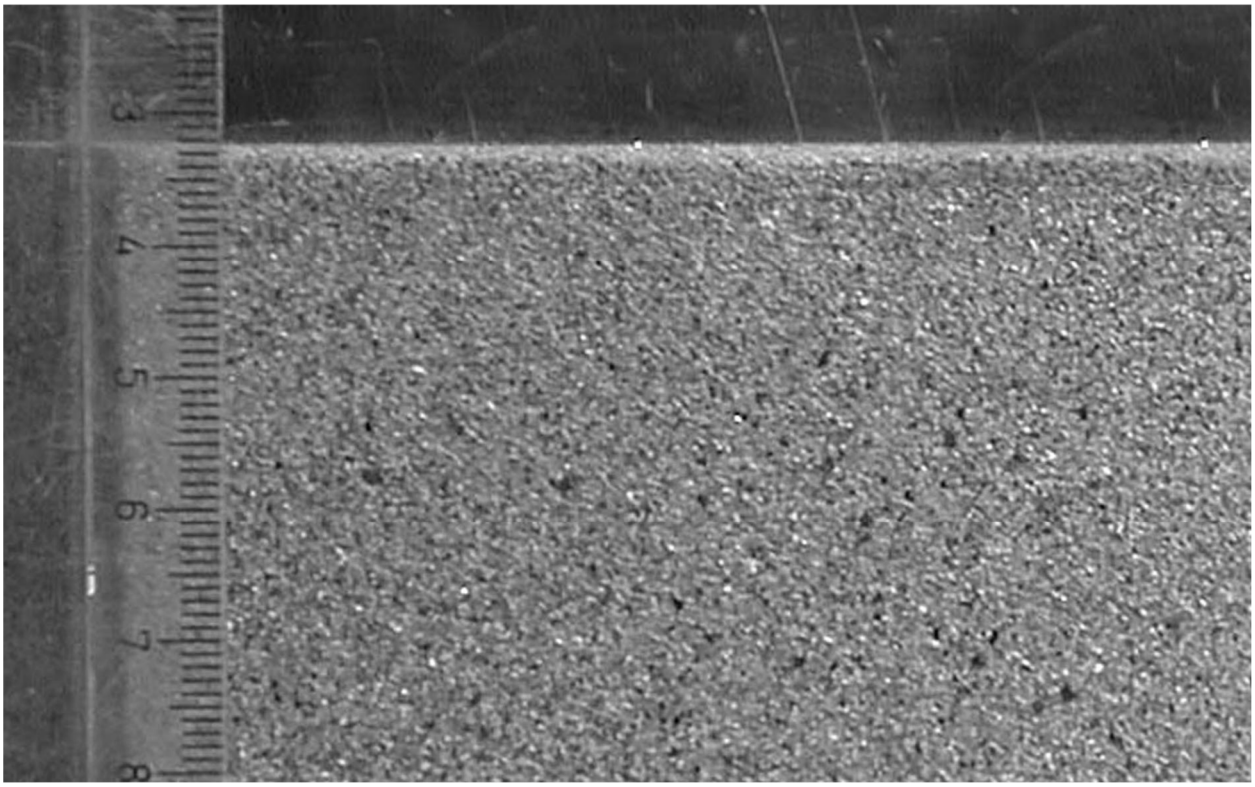

Figure 2-20: Photo of the sand particles coloured in black

In Chapter 3 and Chapter 4 the results obtained using the digital video analysis of the tests in static and dynamic conditions will be presented, proving the applicability of this new method for geotechnical analyses, mainly for soil dynamics.

The digital video analysis method and the algorithms for obtaining the field of vector displacements and their derivatives are presented in Keane and Adrian

(1992). Paikowsky and Xi (2000) did experimental tests to study the development of failure area in granular materials by processing the recorded high resolution images and by applying the evaluation algorithms on a 2D physical model made of round artificial particles. The method offers a unique possibility to analyse the deformation mechanisms of granular materials with a relatively low effort.

2.4.2 PIV analysis method

The Particle-Image-Velocimetry (PIV) is and optical method used to analyse and calculate the field of vector velocities in successive images to study the flow of fluids. It has been developed approximately 20 years ago. A thorough description of the method is done by Raffel et al. (1998). For the majority of the problems, the velocity inside the fluid is determined using particles introduced in it, which are lightened with a bright intermittent laser light. Since the trial sand is an opaque material, the recordings of its displacement were done through the glass walls of the glazed channel.

The first step of the PIV analysis method consists of dividing the images into small individual "interrogation cells". The images recorded with the high speed camera during the dynamic tests have a 512 x 512 pixel resolution, and those recorded with camera during the static tests have one of 1027 x 780 pixel. For the analyses performed, the interrogation cells used had a resolution between 64 x64 pixels and 4 x 4 pixels. These values have corresponding dimensions of about 30 x 30 mm up to 2 x 2 mm of the physical model, depending on the size of the image (Figure 2-21).

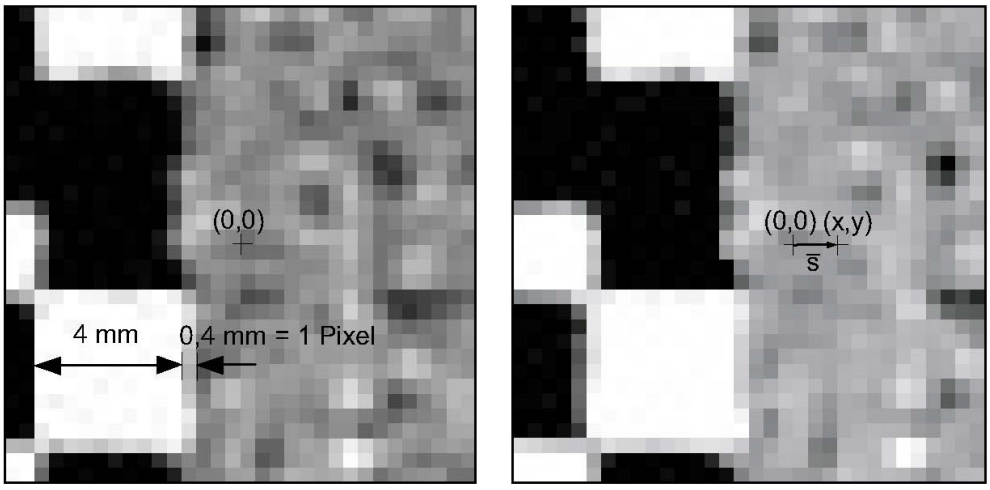

Figure 2-21: Interrogation cell with 32 x 32 pixels from two photos of the static tests, made at a time step of 60 s; in the left side of the photos one can see the edge of the mobile wall on which a 4 mm sized square grid was drawn

The PIV algorithm operates with light intensity within an interrogation cell. By applying a cross correlation (see Keane şi Adrian (1992)) the value and direction of the velocity is computed as a corresponding vector in each interrogation cell for two images Figure 2-22.

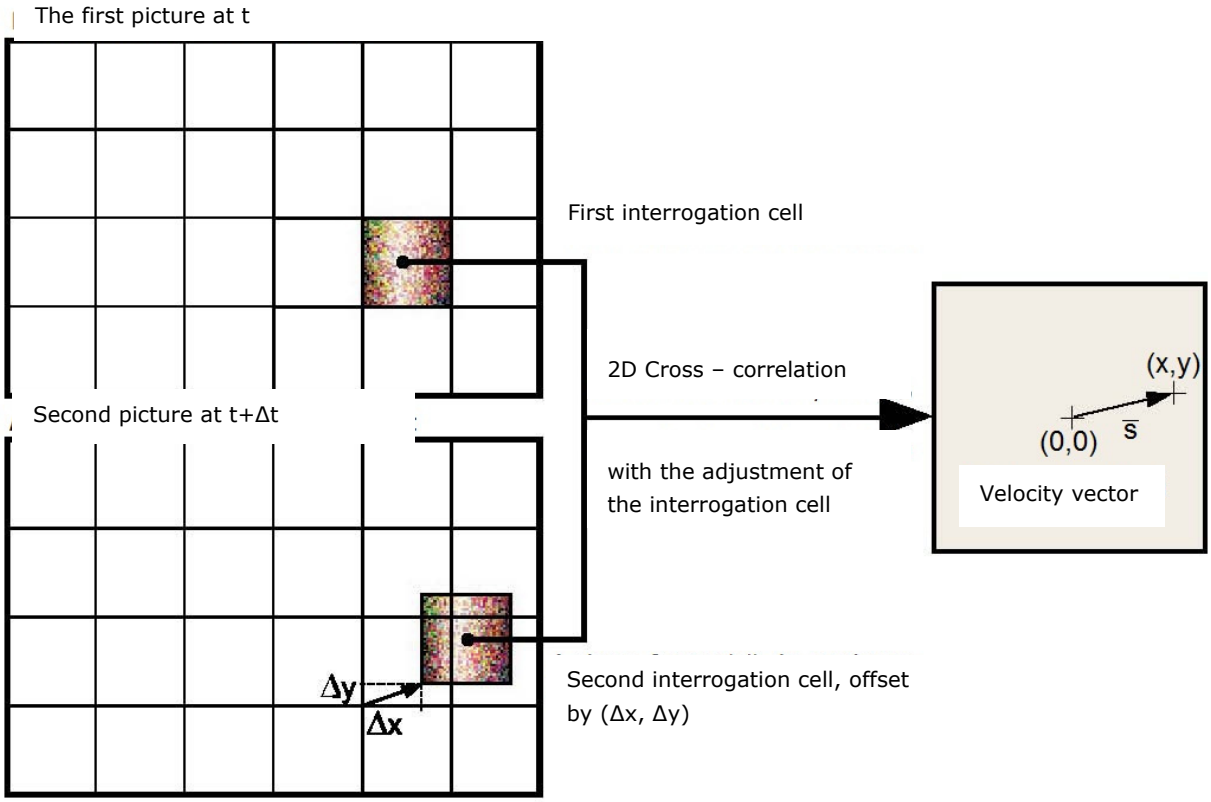

Figure 2-22: Schematic representation for obtaining speed vectors by cross-correlation of an evaluation frame in two successive images

This local displacement vector is determined through the global maximum of the cross correlation matrix for each interrogation cell from the possible velocity vectors. This supposes a homogeneous particle movement within the interrogation cell.

An eventual deformation rotation or deformation of the particles in not considered by the algorithm used in DAVIS, although recent research in this field have been conducted, as done by Krepki et al. (2000). As a statistical method to determine the displacement vector, the DAVIS software used for the PIV analysis uses the cross-correlation function.

For a known time step between images and a known scale, the algorithm is calibrated and it calculated the two components of a velocity vector from the test on the model. The cells are analysed one by one. Subsequently, all the

vectors are made of a 2D vector field with their origin in a unit raster with grid spacing equal with the interrogation cell size.

Through an "Adaptive Cell Shift" function of the PIV analysis software DAVIS, the interrogation cell of the second image is moved with a 2D pre-estimated distance in order to prevent the model from exceeding the cell's boundaries. Therefor the algorithm start calculation with larger interrogation cells, calculates the corresponding vectors and introduces the obtained vector field in the next calculation step. In the next step, the size of the interrogation cell is halved and the vectors calculated in the preceding step are used to more accurately approximate the preliminary displacement of the smaller cell. In this way, the displacement of the interrogation cell is iteratively improved, making thus possible a more stable and accurate calculation of the vectors in the following step. This adaptive function gives the opportunity to use smaller interrogation cells in the PIV analysis, obtaining an increased resolution and a more accurate vector field.

The calculated velocity vector fields were successfully checked not only for the static tests, but also for the dynamic ones, by comparing them with the displacement of the wall measured with the sensors. The consistency of the results obtained using both measuring methods was within a +/- 5% range, also including the errors of the inductive displacement sensors.

The 2D vector field obtained with the PIV algorithm can be post-processed to reduce measurement errors. The contrast of the coloured sand particles allowed their good recognition in the images of the contact surface with the side glass walls. The density and size of the black sand particles needs to meet a minimal condition for each interrogation cell, in order to perform the corresponding analysis.

The trial sand used here, approximately 1% dyed coarse particles offered a good contrast on the contact surface with the glass walls. The resolution of the cameras was optimally used, resulting in a black particle dimension within the image of 1-3 pixels (see Figure 2-21). To calculate the vector field with the PIV-DAVIS software, no post-processing that would produce uniform results was needed.

By representing the velocity vector fields obtained with the PIV software showed a sudden increase of the mobilized soil mass with the displacement of the wall.

2.4.3 PIV analysis results and possible interpretations

In order to evaluate the speed vectors, they have been converted to displacement vectors, by multiplying them with the Δt time step between consecutive images. In Figure 2-23, a complete mobilization of the passive prism can be observed for a static test.

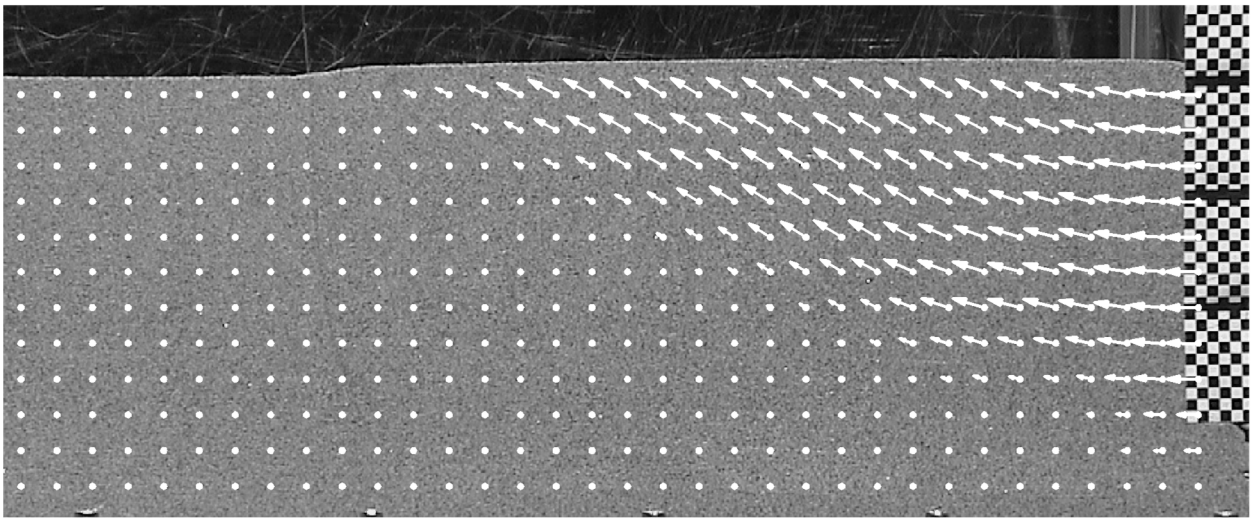

Figure 2-23: Displacement vectors mobilizing the passive prisms for the V31 static test; failure state

In Figure 2-24 a complete mobilization of the passive prism for a dynamic shock-type load test can be seen.

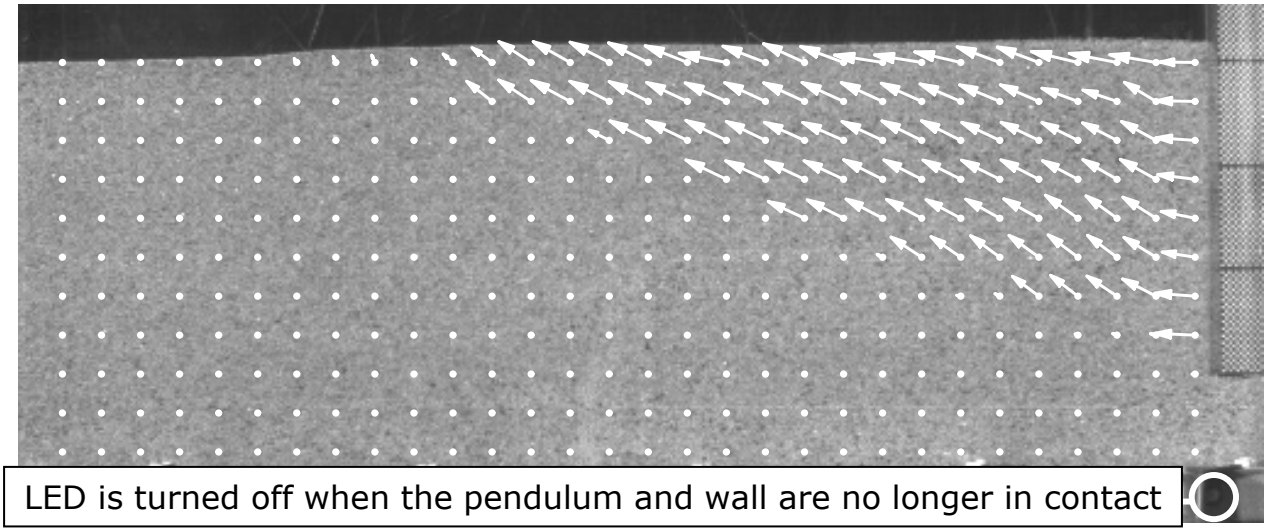

Figure 2-24: Displacement vectors mobilizing the passive prisms for the D44 dynamic shock-type load test; failure state

To allow a better outlining of the sand's deformations during its mobilization until failure, the gradient of the displacement vector field must be

calculate. By noting the displacement field with *X* and its norm $f = \|X\|$, the norm of the gradient becomes:

$$|\nabla f| = \sqrt{\left(\frac{\partial f}{\partial x}\right)^2 + \left(\frac{\partial f}{\partial y}\right)^2} \tag{2-13}$$

If it is meshed on two supporting points of the square grid with the coordinates of the origin of the vector field *X*,

$$M_m \times M_n = (m \cdot dx) \times (n \cdot dy) \tag{2-14}$$

with $dx=x_{i+1}-x_i$ and $dy=y_{i+1}-y_i$ the norm of the gradient field's mesh results as:

$$\|\nabla f_{i+1,j+1}\| = \sqrt{\left(\frac{f_{i+2,j+1} - 2f_{i+1,j+1} + f_{i,j+1}}{2dx}\right)^2 + \left(\frac{f_{i+1,j+2} - 2f_{i+1,j+1} + f_{i+1,j}}{2dy}\right)^2} \tag{2-15}$$

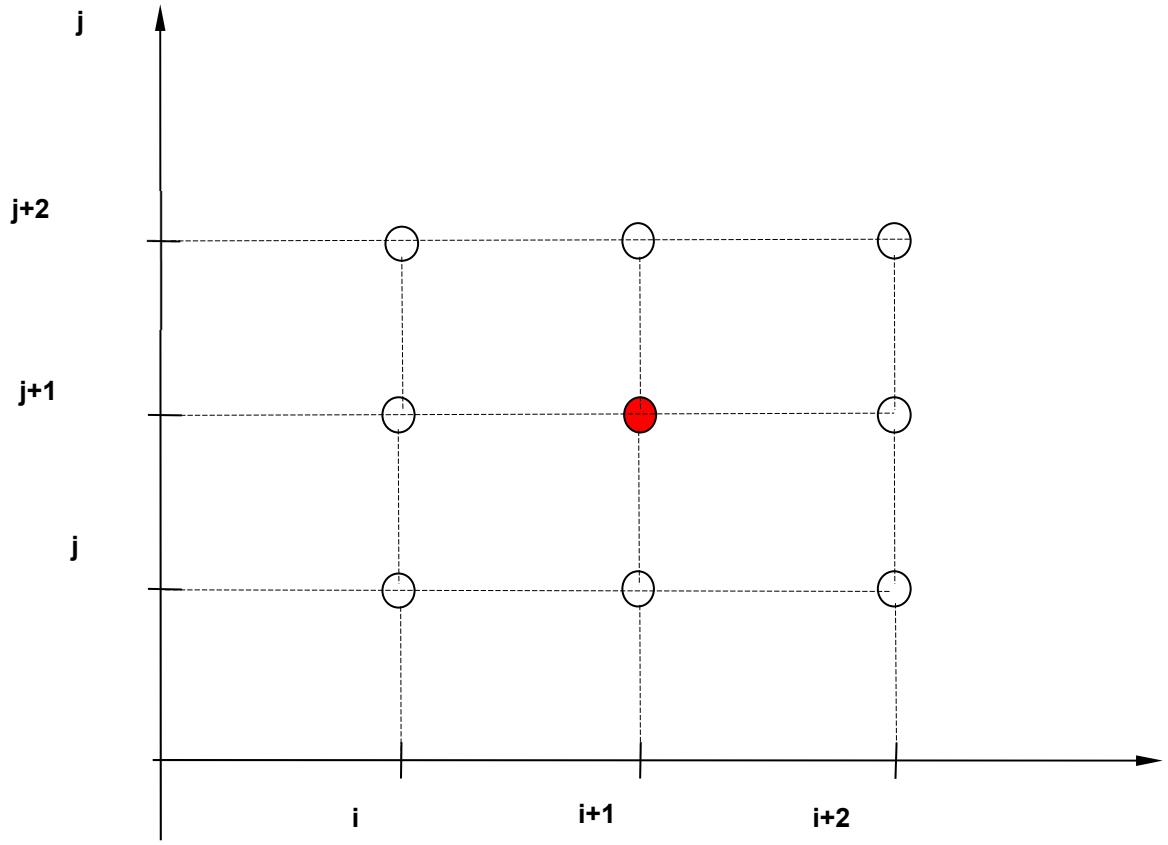

Figure 2-25: The supporting grid for the norm of the displacement gradient field's mesh

By calculating the norm of the displacement gradient presented in Figure 2-25 at failure, when the passive prism is mobilized, the failure surface is clearly highlighted, as is represented in Figure 2-26 for the static test.

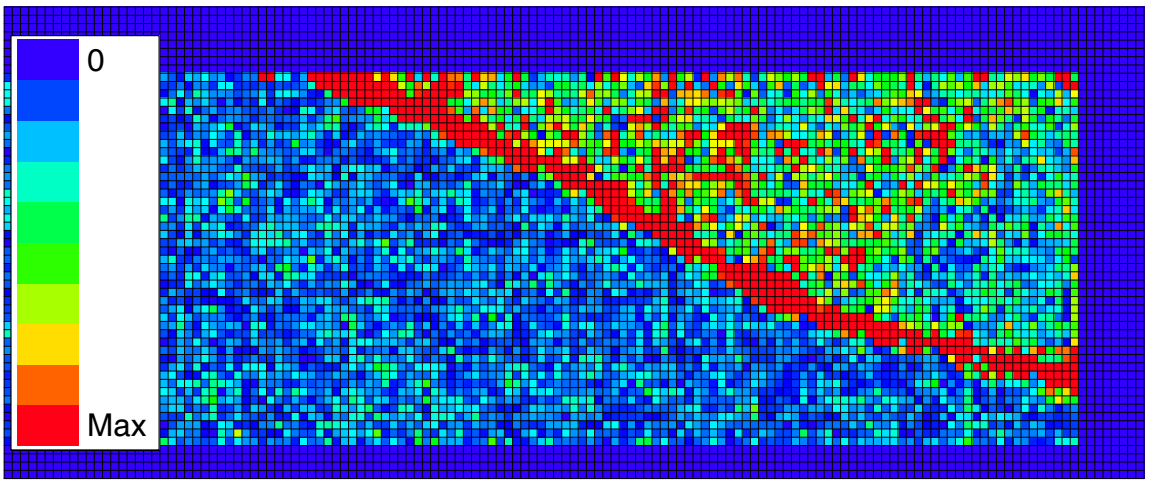

Figure 2-26: Norm of the displacement gradient when the passive prism is mobilized, for the static test V31

As mentioned for above for the static case, by calculating the norm of the displacement gradient presented in Figure 2-25 at failure, when the passive prism is mobilized, the failure surface is clearly highlighted, as is represented in Figure 2-27 for the dynamic test.

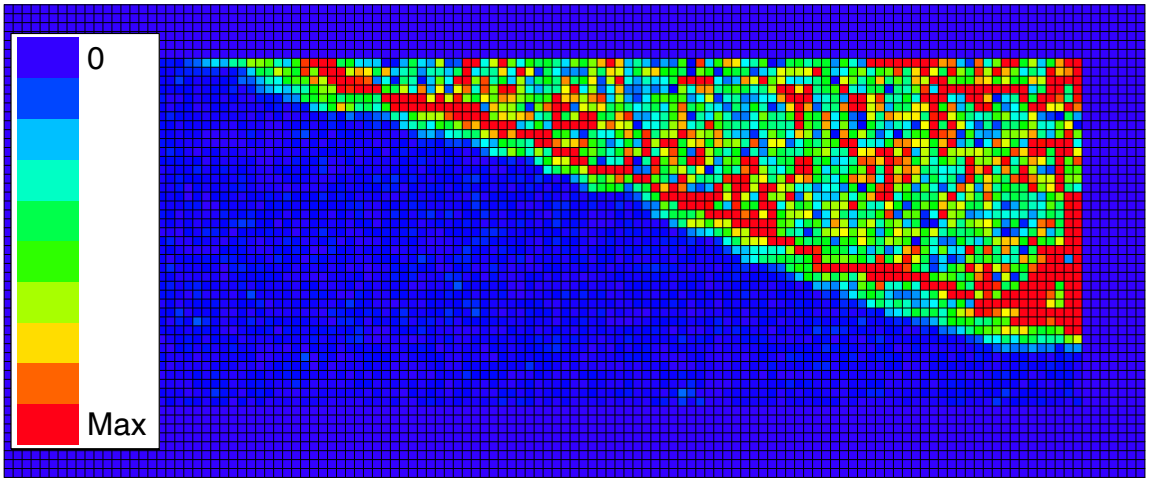

Figure 2-27: Norm of the displacement gradient when the passive prism is mobilized, for the dynamic test D44

By comparing Figure 2-26 and Figure 2-27, one can observe that the failure surface has the same linear shape and the same horizontal tilt, $\vartheta \cong 20°$, for both the static test and for the dynamic shock-type one, thus the results of

the PIV analysis give the possibility to directly compare the static and the dynamic shock-type tests. It also offers a good correlation between the results obtained on physical models and the calculation using the mathematical model developed by the author.

By calculating the local gradient using a similar method, but with four neighbouring supporting points resulted in diminished values and a blurry representation of the failure surface. Thus, this attempt was no longer pursued and the research was continued by determining the displacement gradient between four neighbouring vectors.

The norm of the gradient field is a visual and practical way of highlighting the areas where larger deformations of the sand occur and it is qualitatively represented for one static and one dynamic test in the following chapters.

2.5 Main experimental results

The built experimental stand allowed the study of static passive earth pressure, in order to establish a baseline for the passive earth pressure in dynamic conditions.

In this chapter the building process of the experimental stand, the analysis of the trial sand's parameters and the method of its laying in the physical model, as well as use for the first time worldwide of the video analysis method in the field of soil dynamics are described.

By comparing the experimental results obtained with the PIV optical analysis method, similar properties of the failure surface were observed, such as an almost planar shape having almost the same inclination, for both the static and dynamic shock-type load tests. This creates the possibility to directly compare the static and dynamic shock-type load tests and provides the basis to correlate the results obtained on the physical models with the practical calculation using the mathematical model developed by the author.

The next chapter will summarize the passive earth resistance in static conditions, and will present the evaluation and analysis of the test results performed by the author on 1g physical models. A mathematical model for the mobilization of the static and dynamic passive earth resistance will be developed. The suitability of the mathematical model to describe the phenomenon will be studied and checked based on the test results. Several parameters will be extracted from the results obtained on physical models, in

order to calibrate the mathematical one. Due the reduced scale of the model used in the laboratory, the influence of the boundary conditions and of the measurement errors can be considered proportionally higher, therefore the tests on reduced scale physical models must be regarded as pseudo-quantitative tests. A direct scaling of the results to real-scale problems will not be possible without further research, to validation and calibration tests either on real-scale models or on higher scale ones.

Chapter 3. Static passive earth pressure mobilization

3.1 General information

The static passive earth pressure was studied in this paper in order to establish a direct correlation with the dynamic passive earth pressure under shock-type loads.

In this chapter, the experimental tests and their results, performed on reduced scale 1g physical models are presented. Also, a mathematical model for the static passive earth pressure is developed. The suitability of the mathematical model which describes this issue is investigated using the tests performed on the physical model. Then, certain parameters are extracted from the test results in order to calibrate the mathematical model. Due to the reduced scale of the model, the tests performed on it must be considered pseudo-quantitative. A direct practical application of the physical model tests is not possible without other tests, like centrifuge, full-scale or considerably higher-scale models.

In order to concentrate the investigations on the main target, the research studies the case of plane vertical rigid wall, with a smooth surface and one degree of freedom, horizontal displacement. The trial sand is the one used for the models, dry and cohesionless, described in Chapter 2.

3.2 Theories of the static passive earth pressure

The passive earth pressure is usually used as a basic parameter in technical design to determine the supporting potential of the ground. In this case, the relationship between earth pressure and wall movement should be considered.

All the calculations of the earth pressure are approximations. This is especially valid for the passive pressure and for the passive resistance, obtained by integrating the pressure on the wall height, as well as for the distribution of the earth pressure.

The passive earth pressure or passive earth resistance, e_p is the maximum possible pressure, developed by the weight of the soil, additional loads or other loads on the wall when it is moving towards the soil body until the complete mobilization of the resistance. In the present paper, only the pressure developed by the soil weight is studied.

The passive earth pressure resultant, also named ground resistance and symbolized as E_p, begins to develop when the retaining structure moves towards the ground until its failure. Failure occurs when the allowable wall displacement v_p is obtained. The allowable wall displacement v_p is symbolized in this paper as in the SR EN 1997-1:2004 Romanian standard.

The mobilized passive earth resistance $E_p(v)$ corresponds with an intermediate wall displacement and it is lower than the passive limit state earth resistance but higher than the at-rest one.

The mobilization angle $\delta_p(v)$ of the static passive earth resistance, is the horizontal tilt of its resultant, for a given v displacement. For a wall moving horizontally towards the soil body, having a rough surface, the angle mobilized by the tilt of the static passive resistance is below zero and it is limited by the soil-wall interface friction angle $\delta \leq \delta_p(v) \leq 0$.

In order to completely describe the mobilized passive earth resistance, the following must be known:

- the at-rest earth pressure resistance;
- the passive limit state earth resistance;
- the needed limit displacements;
- passive earth resistance mobilization curve.

The classic models for calculating the passive earth resistance, like the methods of the well-known authors Coulomb – 1776, Rankine – 1857, Müller-Breslau – 1906 and others, only provide information on the passive limit state earth resistance. A review of these was made by Gudehus (2001).

In practice, the passive earth resistance is usually calculated with the Müller-Breslau (1947) method, which developed Coulomb's theory of the plane failure surface of a rough wall, for which tangential stresses on the wall's surface are allowed, thus the passive earth resistance resultant is tilted with the soil-wall interface friction angle $\delta \neq 0$ from the wall's normal. For $|\delta| > 0$ and by considering a plane state, this method results in over-estimating the passive earth pressure E_p, whose values deviate more and more from the measured values of the static passive resistance developed by the soil while the interface angle δ is increased. This error might be neglected for values of the soil-wall interface friction angle of up to $\delta = \frac{\varphi}{3}$, but for $\delta = \varphi$ it may exceed 30%.

It is thus usually recommended to determine the static passive earth resistance for rough walls by considering a circular or a segmented failure surface. The failure surface can be considered as a logarithmic spiral (OHDE), Sokolovski (1965), a circle (EHRENBERG) or a polyline (STRECK). The latter is not compatible from a kinematic point of view. The authors mentioned above proposed tables or diagrams to establish the static passive resistance coefficient K_p. None of the above-mentioned methods offer any information about the needed limit displacement or about the passive earth pressure mobilization function.

Numerous authors conducted research regarding the behaviour of plane retaining walls and the mobilization of the static passive earth resistance. Some of the most important publications, containing numerous recommendation on the passive earth pressure mobilization function, were analysed in order to establish their applicability for the purpose of this paper. The results obtained by a number of authors were summarized by Weissenbach (1975) and are presented in Table 3-1 of this paper. As done in previous papers, the mobilization of the static passive earth resistance is also described here as normalized values of v_p and v_g. The maximum displacement v_p appears when the total static passive earth resistance occurs or when the load would produce failure. The v_g displacement appears when half of static passive earth resistance occurs. The significant influence of the soil-wall friction is also presented in the table below, the interface friction angle defined as $\delta < 0$ means that the static passive earth resistance resultant is facing downwards.

Table 3-1. Reference values for wall displacement according to Weißenbach (1983)

Horizontal wall displacement	Loose soil		Dense soil	
	$\delta = 0$	$\delta < 0$	$\delta = 0$	$\delta < 0$
v_g/h [%]	—	2,5	—	1,5
v_p/h [%]	10	20	3,5	7

The SR EN 1997-1:2004 standard provides reference values for non-cohesive soils, as presented in Table 3-2 of this paper, which were based on measurements made by a series of authors on reduced-scale models. The

relationship between the earth pressure and the displacement of a vertical wall retaining a greenfield horizontal ground is synthesized in Figure 3-1 for loose and dense state soils. For medium dense soils, these values can be used for approximations by linear interpolation. The influence of the soil-wall interface friction angle on the displacements was not explicitly considered.

Table 3-2. Reference values for wall displacement according to SR EN 1997-1:2004

Horizontal wall displacement	Loose soil	Dense soil
v_p/h [%] for $50\%\ E_p$	0,9 – 1,5	0,5 – 1
v_p/h [%] for $100\%\ E_p$	5 – 10	3 – 6

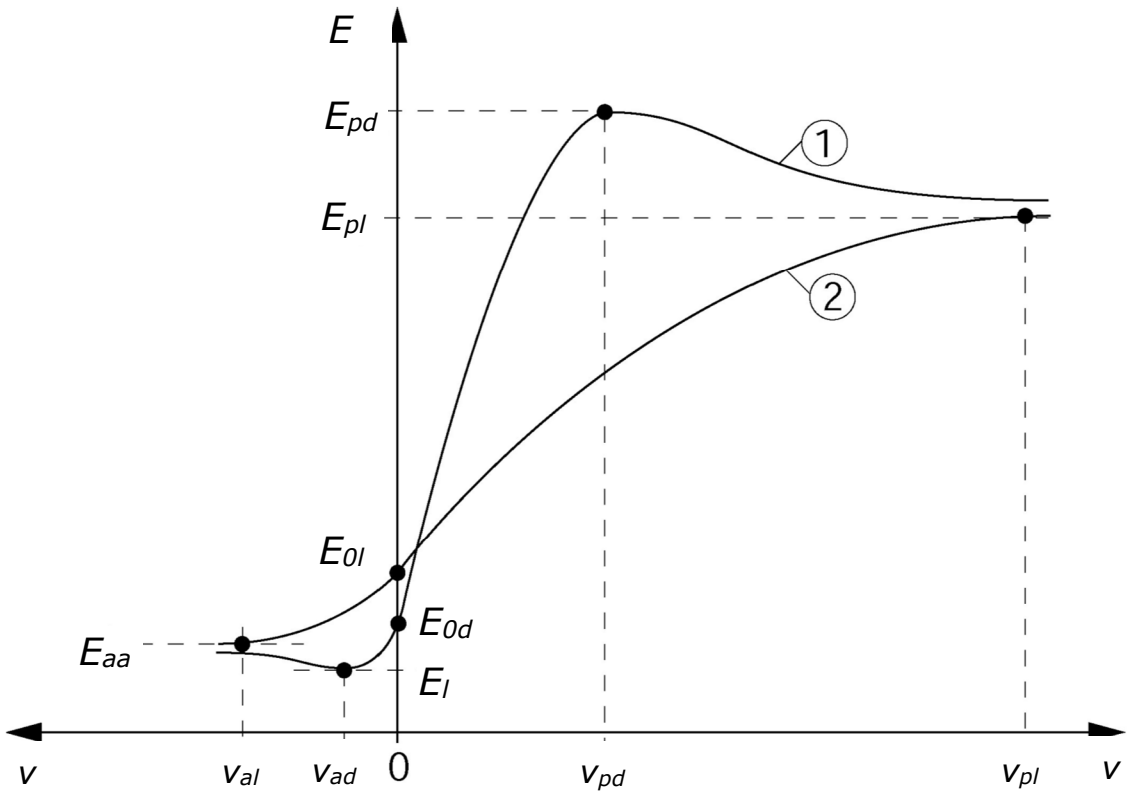

Figure 3-1: Static passive earth pressure mobilizations

1 – non-cohesive dense soils and 2 – loose soils

v – wall displacement

E – earth force

E_a – active earth force (failure for non-cohesive dense soils)

E_{aa} – active earth force for loose soils (residual value)

E_{0a} – at-rest earth force for loose soils

v_{aa} – displacement needed for developing an active earth resistance

E_{0d} – at-rest earth force (dense soils)

v_{pd} – displacement needed for developing a passive earth resistance for dense soils

v_{pa} – displacement needed for developing a passive earth resistance for loose soils

E_{pd} – static passive earth resistance for dense soils

E_{pa} – static passive earth resistance for loose soils (residual value)

Based on the experimental results of numerous authors, among which we mention Bartl (1995) and (1997), the new DIN 4085:2011 provides an exponential equation which describes the mobilization of the horizontal component of the passive earth pressure resistance, as follows:

$$E_{ph}(v) = \left(E_{ph} - E_0\right) \cdot \left[1 - \left(1 - \frac{v}{v_p}\right)^{1,45}\right]^{0,7} + E_0 \tag{3-1}$$

where:

v – wall displacement

E_0 – at-rest earth force

E_{ph} – horizontal component of the passive earth resistance

v_p – displacement needed for developing a passive earth resistance, defined in the same standard as a function of the density index D, based on empirical observations:

$$\frac{v_p}{h} = 0,12 - 0,08 \cdot D \tag{3-2}$$

The proposed relation applies for $D > 0,3$ and $\delta_p \leq \varphi/2$ (for δ_p with negative values). Given this domain, errors within ±20% are expected. Within this error domain, the values are increasing once the wall height increase. When δ_p has negative values, but its absolute one becomes $\delta_p \geq \varphi/2$, the values of the v_p/h may exceed the domain proposed in equation (3-2).

Therefore, in the standard mentioned above the wall displacement v was introduced, which was defined as s in the DIN standard, giving up the magnitude of displacement v_g under normal use. As reference values of the wall displacement for the ultimate limit state v_p, the same values given in DIN 4085-100 (see Table 3-2) are kept.

All these values of the magnitude of the wall displacement to mobilise the static passive earth resistance presented in literature Weissenbach (1985-Baugruben, part 2) (1975), and in the standards (DIN V 4085-100 (1996), EAU 2004 (2009), ÖNORM B 4434 (1993) etc.) are average empirical values, which have been obtained from test performed under various conditions. According to Gudehus (2001) equations to describe the relationship between earth pressure and wall displacement are missing. The need for a proven method to calculate the earth pressure as a function of wall displacement still remains. Knowing it is mandatory to calculate deformations and safety factors for given wall displacements.

In order to calculate the dynamic passive earth resistance using a mathematical model, not only knowing the mobilization function of the static passive earth resistance would be needed, but also development of the failure surface and of the mobilized soil mass with the wall displacement should be known.

As mentioned in Chapter 1, Holzlöhner (1994 and 1995) has used the static passive earth pressure mobilization hypothesis developed by Vogt (1984) and his own hypothesis for the mobilized soil mass, in order to develop his dynamic calculation model which describes the behaviour of retaining walls when collided by barges. The principles of this model are used for the proposed mathematical model. More information of the model are presented in 3.5.

3.3 The physical model

The purpose of testing physical models in static conditions was to determine the static passive earth resistance mobilization, as well as to observe deformations and the failure surfaces under the same experimental conditions in which the dynamic impact tests have been subsequently performed.

3.3.1 The settings of the physical model

The tests were carried out under a controlled displacement condition. Thus, the mobile wall was pushed by a gearbox electric engine of a direct shear test device, with constant speed towards the sand filled glazed channel.

Firstly, two preliminary tests were performed at different speeds, v_s = 0.01 mm/min and 1.2 mm/min respectively, to investigate a possible dependency of the results on the test speed. Since no relevant difference could be identified, the maximum speed v_g = 1.2 mm/min was chosen in order to reduce the test time. By using dry sand for all the tests, the mobilization of the static passive earth pressure in drained conditions was achieved. The value of the sand friction angle was determined using the same speed in the direct shear test device.

To obtain the maximum displacement of the wall ($v = 36mm = 15\%\, h$, for h = 24 cm), approximately 30 min were needed. Since the experimental model is fairly complex, and taking into account the time needed for laying the sand in the box, a maximum two tests could be conducted each week.

During the preliminary tests no obvious discrepancies at the mobilization of the passive earth pressure were identified when the soil-wall interface was changed. The smooth surface was obtained with a glossy polycarbonate sheet, while the rough one by sticking sandpaper with 100 grit size. According to this findings, all the subsequent tests were performed with the smooth wall surface.

Since the results were found to be independent from the displacement speed, all the tests were performed with the maximum speed v_g = 1.2 mm/min. All the tests were performed with a smooth surface of the mobile wall, for the following density indexes: D = 0.5, D = 0.7 and D = 0.9.

3.3.2 Recording and processing of the measured values

In addition to the preliminary tests, 33 other static tests were performed, with various sand density indexes, five wall heights (8, 12, 16, 24 and 32 cm) and two wall widths (16 and 32 cm). Table 3-3 summarizes the results of these tests.

Table 3-3. Static tests selected for analysis

Test	Series	Wall width b [cm]	Wall height h [cm]	Density index D	K_{ph} [-]	v_p/h [%]	Pressure distribution measurements	Photo recordings	Inclination of the failure surface ϑ [°]
V1	1	16	24	0,7	12,2	10,7	no	no	
V2		16	24	0,8	13,64	7,3	no	no	
V3		16	24	0,7	11,94	5,5	no	no	
V4		16	16	0,7	12,08	8,1	no	no	22,8
V5		16	24	0,9	15,24	3,9	no	no	21,8
V6		16	24	0,6	11,19	12,4	no	yes	
V7		16	24	0,8	13,64	8,4	no	yes	
V8		16	24	0,8	12,99	6,3	no	no	21,5
V9		16	24	0,8	12,48	6,3	no	no	21
V10		16	12	0,8	12,99	9	no	no	21,5
V11	2	32	24	0,7	11,68	11,9	no	no	20
V12		32	32	0,7	9,87	8	no	no	22
V13		32	16	0,6	9,95	12,9	no	no	21
V14	3	32	32	0,65	10,34	10,6	yes	no	
V15		32	32	0,6	9,98	11,3	yes	no	
V16		32	24	0,8	10,79	8,36	yes	no	
V17		32	16	0,8	11,99	7,5	yes	no	
V18		32	8	0,8	13,16	8,3	yes	no	
V19	4	16	32	0,9	15,27	5,2	yes	no	
V20		16	24	0,9	15,56	6,3	yes	no	
V21		16	8	0,9	16,13	5,9	yes	no	
V22		16	16	0,9	16,71	4,4	yes	no	
V23		16	8	0,9	16,13	5	yes	no	
V24	5	16	12	0,9	18,18	4	yes	yes	
V25		16	8	0,9	18,44	6,3	yes	no	19
V26		16	16	0,9	19,44	4,6	yes	no	
V27		16	24	0,9	12,8	7,7	yes	no	
V28		16	16	0,7	11,13	12,5	yes	no	
V29		32	8	0,7	10,69	10	yes	no	
V30	6	32	24	0,9	14,72	5,6	yes	yes	
V31		32	12	0,9	15,36	5,8	yes	yes	21,5
V32		32	24	0,7	10,73	9,6	yes	no	21,2
V33		32	24	0,5	8,16	14,5	yes	no	19,5

The following main parameters have been recorded during the entire test:

- The force applied by the electric engine with gearbox;
- Wall displacement using inductive displacement sensors;

- Contact pressure at the soil-wall interface using resistive pressure transducers.

The height of the measuring wall was divided in 8 cm segments, and in the central area of each segment one or two pressure sensors were installed. Figure 2-9 presents the typical position of the pressure sensors for the narrow width of the wall. To investigate the side friction influence on the distribution of the passive pressure on the wall width, for several tests an asymmetric position of the pressure sensors was set.

The tests were conducted with both wall widths, 16 and 32 cm. the difference between the values recorded by the sensors set at the same level and the ones set asymmetrically was within the tolerance range of the measurements, therefore the pressure distribution on the back of the wall was considered uniform.

The wall displacement was recorded for most of the tests with two displacement sensors set at the base and the upper edge of the wall (see point 6 in Figure 2-2). The value of the wall's rotation angle in vertical plane, determined by the ratio between the maximum displacement difference recorded by the two sensors Δv and the wall's height, fulfilled the condition $\tan\omega = \Delta v/h < 0{,}0025$ for most of the tests, suitable for a horizontal wall displacement according to DIN 4085 (1987).

After setting the experimental model (described in chapter 2.3), the tests on the physical model in static conditions have been conducted. The measurements were recorded with the devices described in chapter 2.2 and 2.4.

All the measured values have been viewed and recorded during the whole test using a data acquisition software with a frequency of 1 Hz for each channel. In this manner, the signals could be amplified and certain errors could be identified even while performing the tests. When each test was completed, the measured data was converted in ASCII format, stored and then processed with the MS Excel software.

The measured values have been converted to physical values using the calibration equation of each sensor. Then they have been processed and stored in the wanted manner, so they can be analysed and graphically represented.

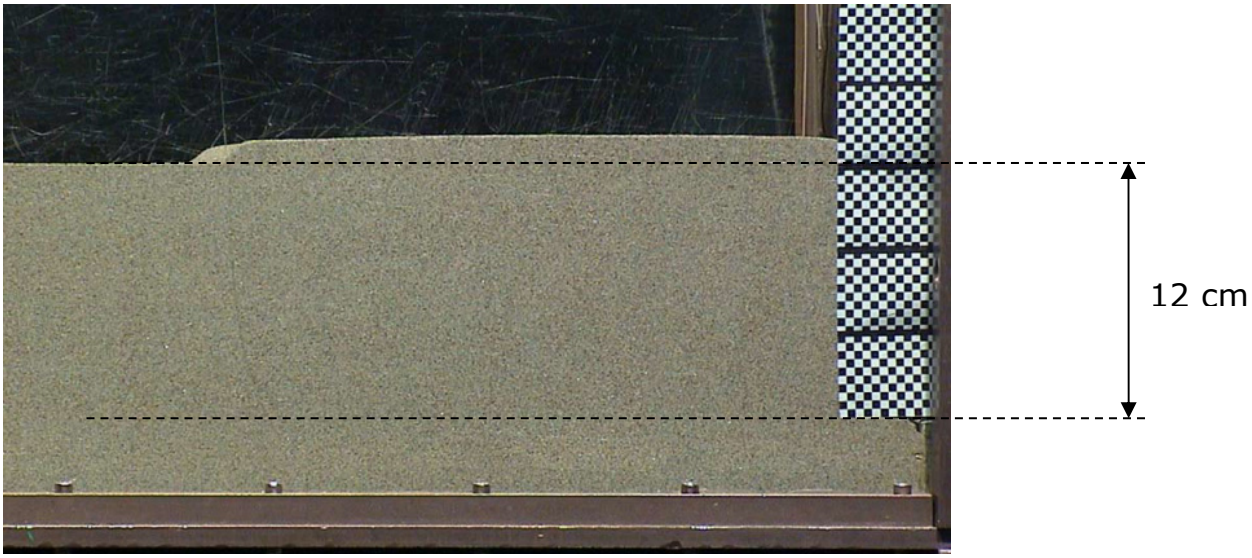

Figure 3-2: Static passive pressure mobilization of the sand for a fill height of 12 cm from the base of the wall, and with the coarse particles coloured with black

3.3.3 Conducting the static tests

Neither the hydraulic equipment used for the preliminary tests, nor the gearbox engine could offer a sufficiently stiff horizontal support, so the wall could withstand the at-rest earth pressure in the initial phase. The wall have been then horizontally supported on the circular bearing of the four sliding axes. In order to simplify the pressure appearing behind the wall while the sand was being laid in the glazed channel was no longer measured. Since the wall can be basically considered stiff and the four supporting connection are fixed, the initial stresses at the soil-wall interface is due to the at-rest earth pressure.

Starting from the original at-rest condition (zone 1 in Figure 3-7), the wall was pushed towards the soil body with a quasi-constant 1.2 mm/min velocity. The first tests were conducted until a maximum 36 mm was achieved.

It was found for the modelling conditions, that the evolution of the earth passive pressure has a post-failure (zone 3) behaviour after its complete mobilization (achieved at the end of zone 2 and the beginning of zone 3). This phenomenon was emphasized after the limit state displacement was exceeded for the D=0.9 density index (see Figure 3-7). The tests could be stopped immediately after the appearance of the post-failure behaviour, since the results were viewed in real-time.

A slight displacement difference between the sand near the glass walls and the one in the centre of the glazed channel was observed (see Figure 3-3),

due to the sand-glass wall interface. The small curvature of the completely mobilized sand at the side wall interface justifies the consideration of the plane stress state. In a simplifying manner, the displacement difference of the sand near the side walls and the one in the centre of the glazed channel had been neglected.

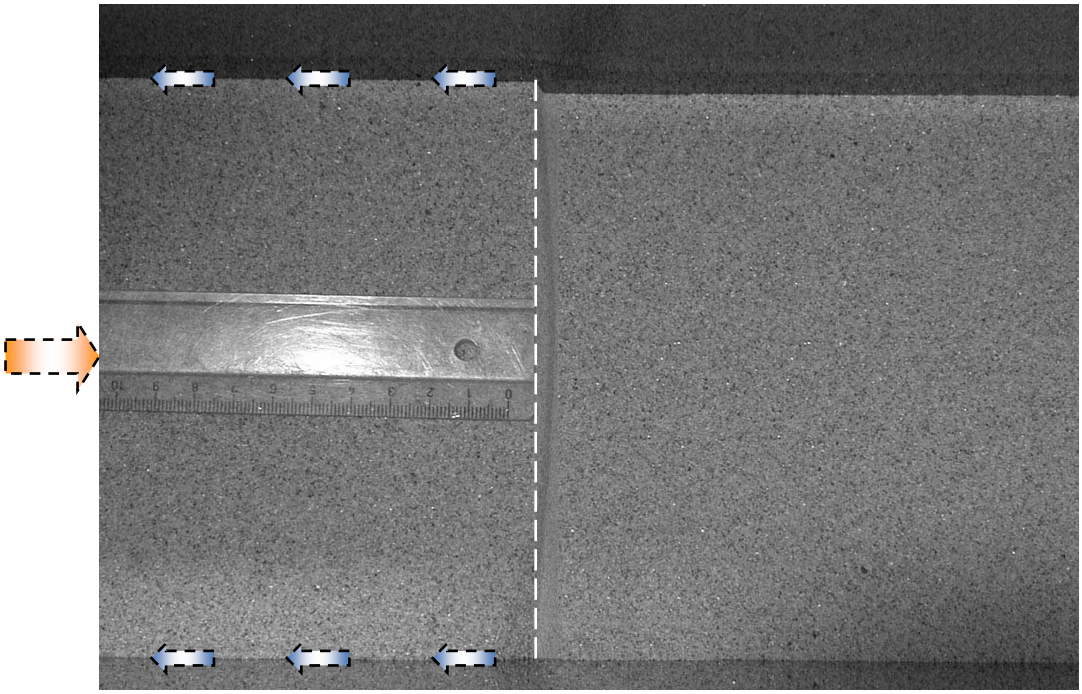

Figure 3-3: Top view of the sand prism after failure, for a static passive earth pressure mobilization test, for a narrow glazed channel, 16 cm wide

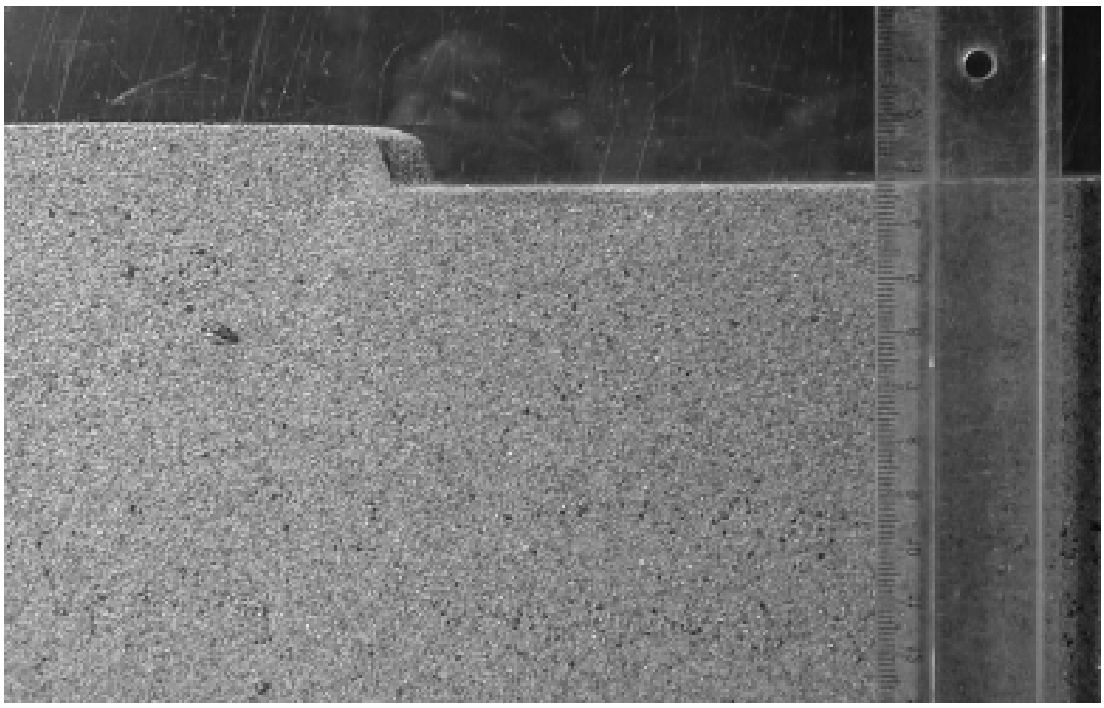

Figure 3-4: Side view of the sand prism after failure

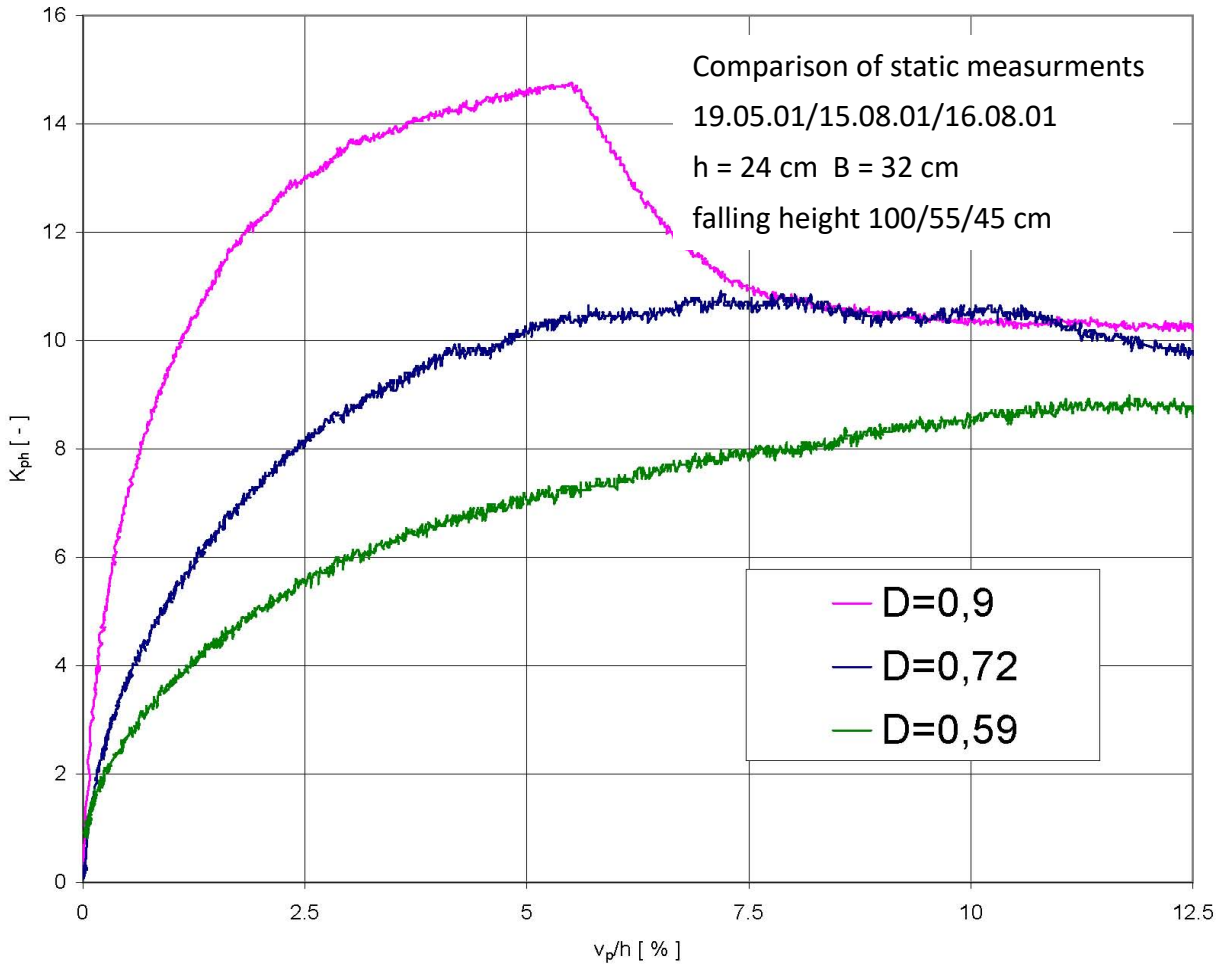

Figure 3-5: Passive earth resistance mobilization graphs measured for three representative density indexes

3.4 Evaluation of the static tests results

The main results of a static test on a model having a 24 cm height, a 32 cm width and a $D = 0.7$ soil density index are summarized in Figure 3-6.

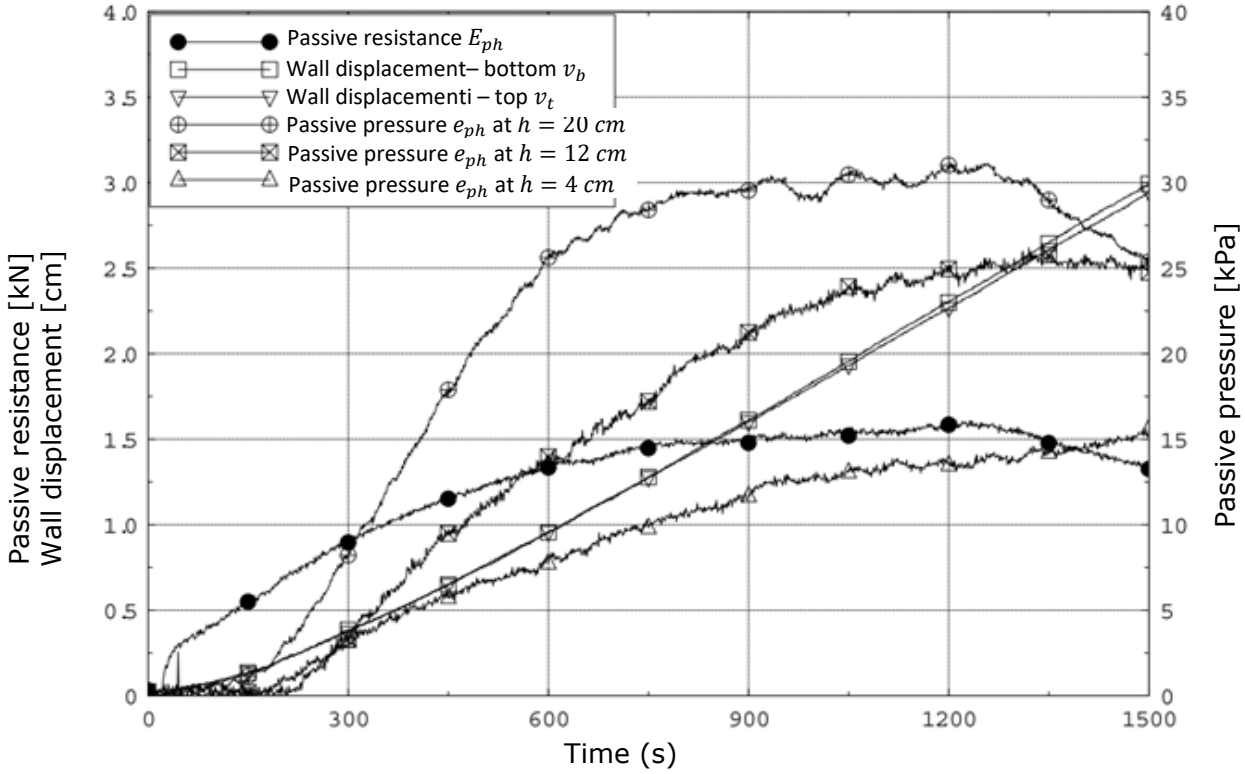

Figure 3-6: Measured values plotted on time for the V32 test

The amplification of the pressure transducers' output signal ought to make it uniform. The calibration of the pressure transducers for small confining pressures, up to 10 kPa, could only be done with significant errors in terms of repeatability of the results. Only a qualitative evaluation of the pressure distribution will be made in analysing subsequent results. This fact is not relevant in determining the passive earth pressure since the applied force was directly measured using a dynamometer installed between the pushing device and the wall, and it was not integrated from the values measured by local pressure transducers.

By removing the time variable from the graph in Figure 3-6, the remaining measured values are plotted on the ratio between the wall displacement and the height of the sand backfill, as shown in Figure 3-7. For a direct comparison of the measured values, they are presented dimensionless.

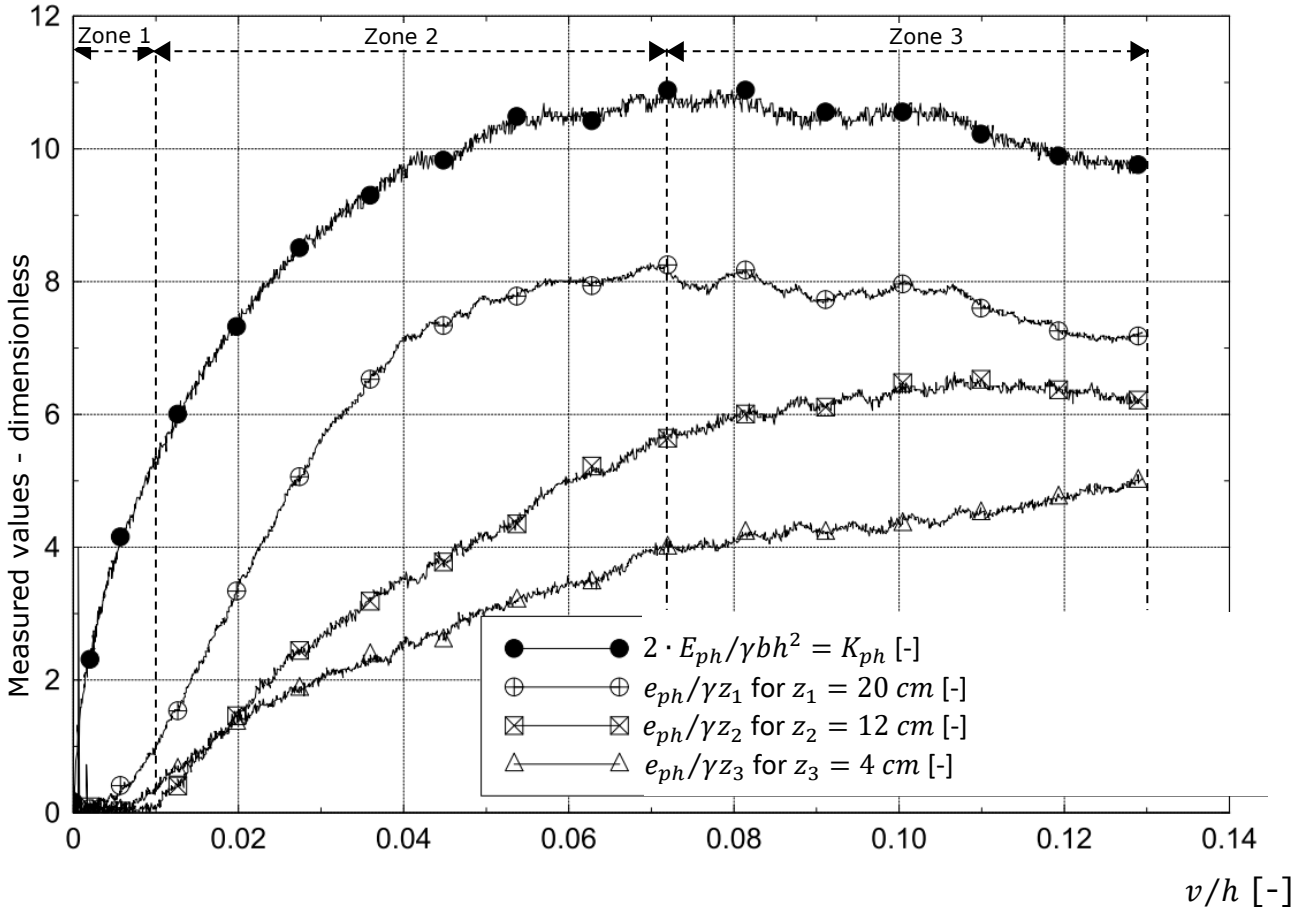

Figure 3-7: Dimensionless values obtained from the V32 test: normal pressure behind the wall normalized with the confining pressure of each sensor level, plotted against the relative displacement ($\boldsymbol{v/h}$, $\boldsymbol{h}$ = wall's nominal height)

As highlighted in Figure 3-7, the passive earth mobilization can be divided in three zones:

- Zone 1: "buffer zone", or small wall displacements zone. It is the transition zone from the at-rest earth pressure to the mobilization of its passive one, being subjected to certain local discrepancies mainly due to the lack of homogeneity at the interface, which appeared when the sand was pluviometrically laid;
- Zone 2: "mobilization zone", the passive earth pressure is mobilized until the maximum value is reached, represented by the passive resistance;
- Zone 3: "post-failure zone" the maximum passive resistance is exceeded, and the pressure behind the wall decreases for the dense sand; for the case of the loose one, this value remains quasi-constant.

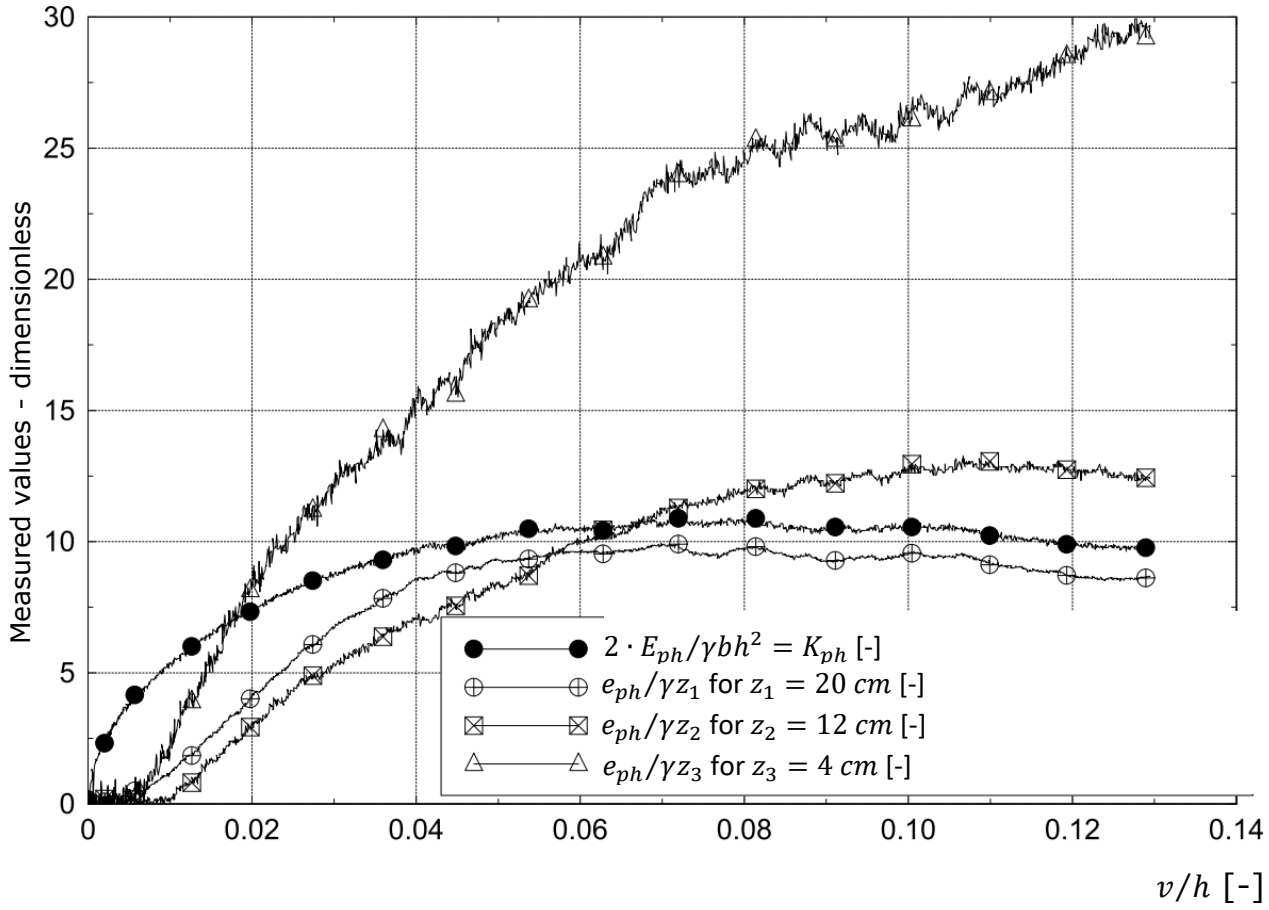

Figure 3-8: Dimensionless values of the V32 test: normal soil-mobile wall interface stresses normalized with the geological stress at the sensor level, plotted on the relative displacement ($\boldsymbol{v/h}$, $\boldsymbol{h}$ = nominal wall height)

By comparing the maximal values of the passive earth pressure mobilization, recorded for the three different depths (in Figure 3-8), higher values of the horizontal passive earth pressure coefficient $K_{ph} = \frac{e_{ph}}{\gamma \cdot z}$ are found at smaller measuring depths. This is due to the increase of the friction angle φ with the decrease of existing stresses (clenching of particles), as presented in Figure 2-13.

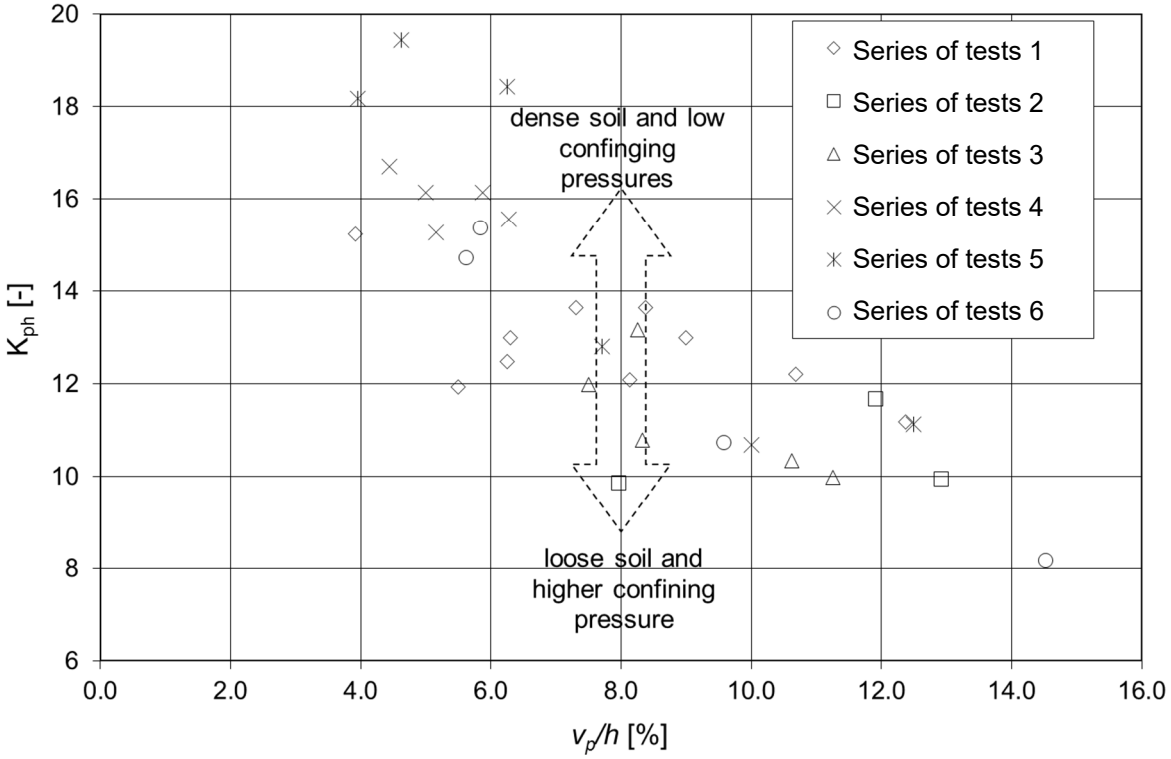

Figure 3-9: Passive earth resistance represented as the dimensionless value of the passive earth pressure coefficient plotted on the relative limit state wall displacement

As expected and as observed in Figure 3-9, the high values of the passive earth pressure coefficient characteristic to dense soils match the small values of limit state wall displacement, which correspond to the full mobilization of the passive resistance.

An additional influence to the one of the density index is the initial stress state, which depends on the height h of the soil behind the mobile wall.

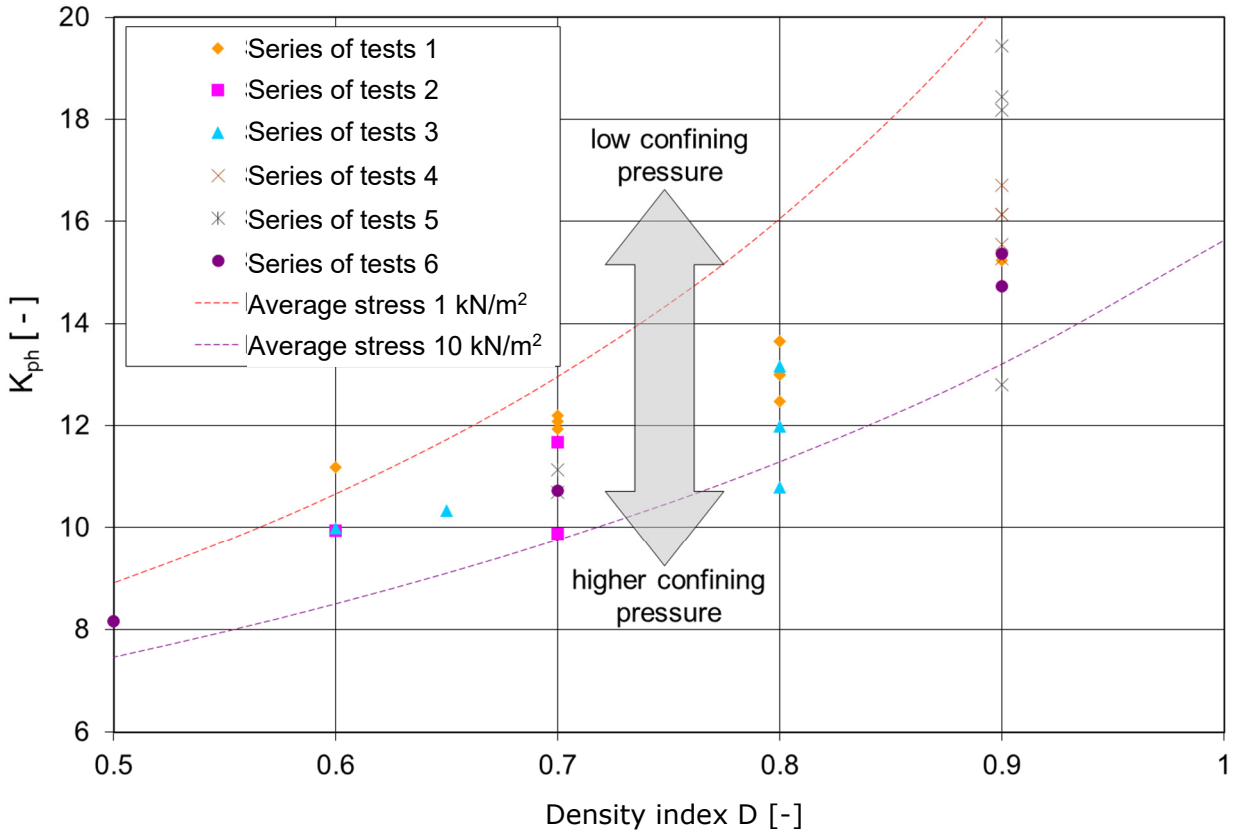

Figure 3-10: The passive earth pressure coefficient measured on physical models plotted on the density index versus the analytical values calculated according to the Müler-Breslau theory, obtained for a sand friction angle dependent on the confining pressure and the density index; the soil-wall interface friction angle was considered $\boldsymbol{\delta = 13°}$, and the one at the side walls $\boldsymbol{\delta_s = 8,5°}$

The graphical presentation in Figure 3-10 of the horizontal component of the passive earth pressure coefficient plotted on the density index, allows the acknowledgment that the measured values fall within the analytical range of values calculated according to:

$$K_{ph} = \left[\frac{\cos\varphi}{1 - \sqrt{\frac{\sin(\varphi - \delta)\sin\varphi}{\cos\delta}}} \right]^2 \tag{3-3}$$

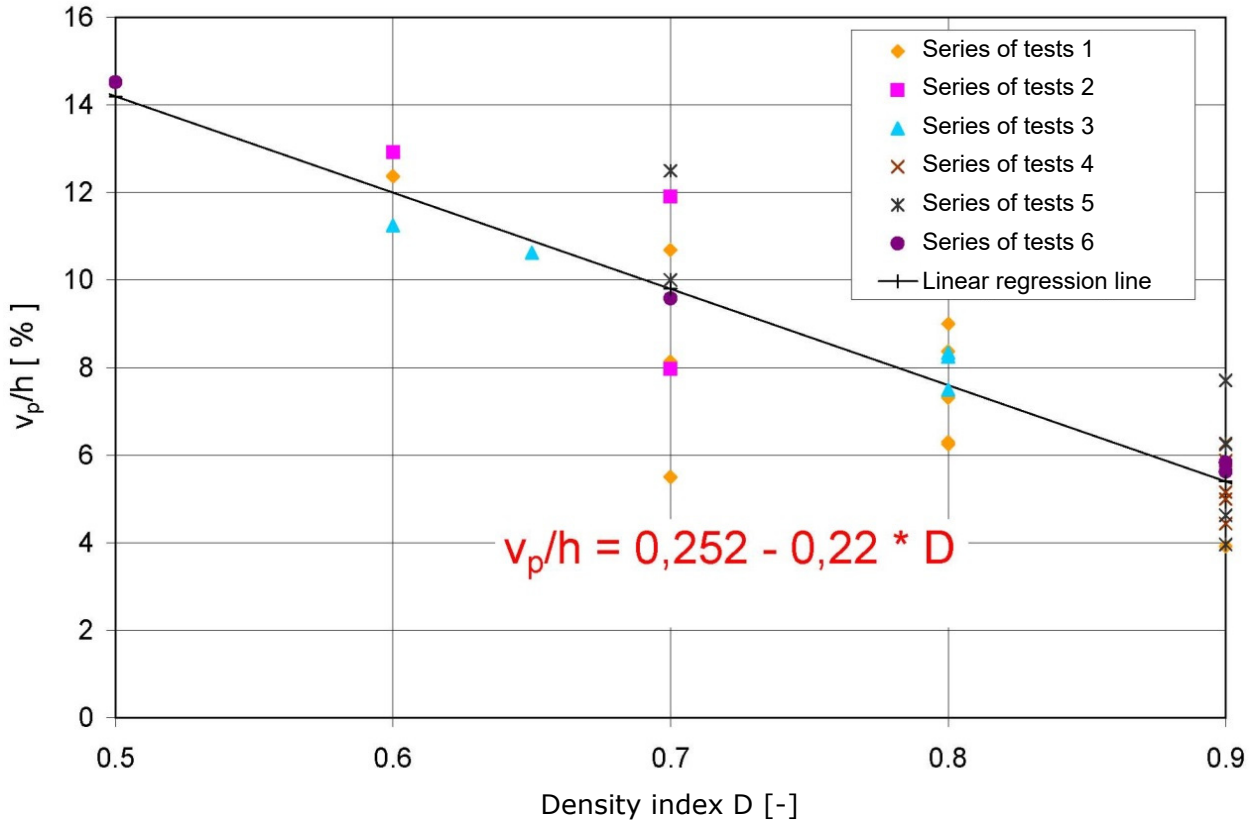

Figure 3-11: Dimensionless representation of the ultimate displacements for the passive earth resistance mobilization, normalized with the nominal height of the wall ($\boldsymbol{v_p/h}$), plotted on the initial density index; the function was obtained by linear regression

Based on the graphic recorded for each static passive earth pressure mobilization test plotted on the wall displacement, the pair of values for the maximum passive resistance and ultimate displacement was chosen, as it can be seen in Table 3-3.

The dimensionless presentation (Figure 3-11) of the relative limit state displacements (v_p/h) plotted on the density index, allows a linear correlation between the two for the performed tests:

$$\frac{v_p}{h} = 0{,}252 - 0{,}22 \cdot D \tag{3-4}$$

The similar linear relationship (3-2), based on reduced scale model tests performed by Vogt (1984) and taken from DIN 4085 (2011), will be used in Chapter 6 to apply the dynamic model to full-scale applications.

3.5 Static mathematical model

3.5.1 General description of the mathematical model

Since up until this research no coherent and verified theoretical model, to determine the passive earth resistance mobilization as a function of displacement, the evolution of the failure surface as a function of displacement and the mobilization of the involved soil mass altogether, is known, the author proposes a static model. Holzlöhner (1995) has used the empirical static passive earth pressure mobilization hypothesis developed by Vogt (1984) and his own parabolic hypothesis for the mobilized soil mass, in order to develop his dynamic calculation model which describes the behaviour of retaining walls when collided by barges. The basic principles of this model, consisting of the compressibility of the monolith and a progressive soil mass mobilization, are used for the proposed static mathematical model. However, the author proposes his own compressible monolith mass mobilization hypothesis, proportional to its displacement. Therefore, by applying conditions for static equilibrium during the mobilization of the passive resistance, as well boundary conditions, relevant functions for the static passive resistance mobilization and for the mass of the monolith are obtained.

The relatively small ratio between the sand-side walls friction and the earth passive resistance, estimated for the preliminary tests at $R_s/E_{ph} = (9 \div 12)\%$ (see equation (2-11)), allows the assumption of a plane strain state. To describe the passive earth resistance mobilization for plane, vertical, stiff and horizontally moving structures a series of idealizations, hypotheses and main approaches have been made below.

Considering the experienced gained from the own physical model tests, as well as the increased difficulty attributed to the consideration of a curved or irregular failure surface, the failure kinematic defined by Coulomb was chosen as a starting point for the mathematical model of the passive earth resistance mobilization.

In order to define the passive earth resistance mobilization $E_p(v)$ as a function of the horizontal wall displacement ($0 \le v \le v_p$), both the initial values ($v = 0$) and the final ones ($v = v_p$), as well as the variation curve between the two given points $0 < v < v_p$ must be known.

Firstly, the boundary conditions are defined. Initially the wall is subjected to the at-rest earth pressure:

$$E_p(v=0)=E_0=\frac{1}{2}\gamma h^2 K_0 \tag{3-5}$$

where:

γ is the specific weight of the soil;

h is the wall's height;

For simplifying, in Chapter 3, Chapter 4 and Chapter 5, the width b is considered equal with one unit, therefore it is not introduced in the presented equations.

K_0 is the at-rest pressure coefficient obtained with Jaky's relation:

$$K_0=1-\sin\varphi \tag{3-6}$$

where φ is the soil friction angle.

In the final stage ($v_x = v_p$, at failure), the full passive earth pressure is mobilized and the function becomes:

$$E_p(v_x=v_B)=E_p=\frac{1}{2}\gamma h^2 K_p \tag{3-7}$$

where the passive earth pressure coefficient is defined as:

$$K_p=\frac{1}{\cos\delta}\cdot\frac{\cos^2\varphi}{\left(1-\sqrt{\frac{\sin(\varphi-\delta)\sin\varphi}{\cos\delta}}\right)^2} \tag{3-8}$$

and the inclination of the failure surface, named hereafter failure plane, is according to Müller-Breslau (1947):

$$\vartheta=-\varphi+arc\cot\left[\tan(-\varphi)+\frac{1}{\cos(-\varphi)}\sqrt{\frac{\sin(\delta-\varphi)}{-\sin\varphi\cos\delta}}\right] \tag{3-9}$$

In the equations above, δ is the soil-wall interface friction angle, as can be seen in Figure 3-12.

According to SR EN 1997-1:2004, the wall displacement v, for each the entire passive earth resistance is mobilized, is defined as being the ultimate displacement v_p.

Vogt (1984) assumed for his passive pressure mobilization hypothesis, the proportionality between the ultimate displacement v_p, corresponding to a complete earth resistance, and the wall's height h. His tests resulted with values of the dimensionless ratio v_p/h ranging between 0.06 for a dense sand an 0.2 for a loose one. His tests concluded with equation (3-2), taken from DIN 4085:2011.

By applying a linear regression on the own test results (presented in Figure 3-11), for the sand used in the present research, the following linear relation between this ratio and the density index can be considered:

$$\frac{v_p}{h} = 0{,}252 - 0{,}22 \cdot D \tag{3-10}$$

The relation is in good correlation, for the entire considered range of density indexes, with the values measure by Vogt on reduced scale models. Differences between equation (3-2) and (3-4) are found, due to the reduced scale of the own physical models.

3.5.2 Mobilization of the compressible monolith

In the previous chapter the boundary conditions of the function expressing the mobilization of the passive earth resistance have been defined. For its complete description, its shape between the two boundaries must be defined. For this purpose, the mobilization of a monolith proposed by Coulomb is adopted. Consequently, the shape of the $E_p(v)$ function is obtained from the initial equilibrium of the soil body, for $0 \le v \le v_p$.

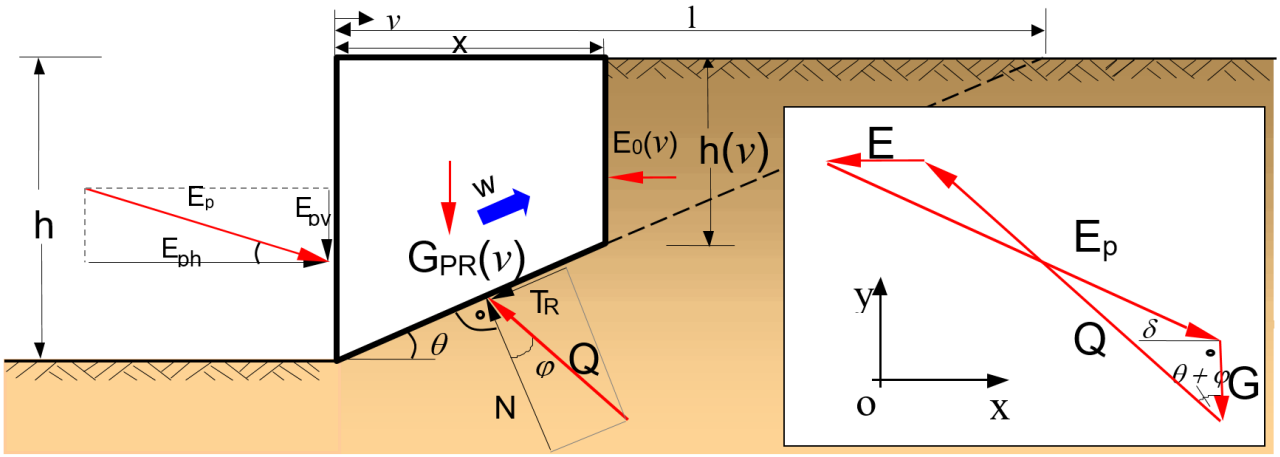

Figure 3-12: Force mobilization on the soil prism

As a deviation from Coulomb's theory, herein the assumption that the soil prism does not move as a joint block when the wall displacement starts, but rather its length depends on the wall displacement v is made. For this, a mobilized prism is considered, still at-rest, having a $G(v)$ weight, separated by the rest of the solid by a planar, vertical surface at a x distance from the wall. The wall displacement will be further referred to as v.

The boundary conditions can be written as:

$$x(v=0)=0 \Rightarrow G(v=0)=0 \tag{3-11}$$

$$x(v=v_p)=l \Rightarrow G(v=v_p)=\frac{1}{2}\gamma\frac{h^2}{\tan\vartheta} \tag{3-12}$$

From similar triangles, the mobilized area results as:

$$A(x)=\frac{1}{2}\frac{h^2}{\tan\vartheta}\left(2\frac{x}{l}-\left(\frac{x}{l}\right)^2\right) \tag{3-13}$$

and the corresponding weight:

$$G(x)=\gamma A(x) \tag{3-14}$$

The length x of the mobilized soil prism is dependent on the wall displacement v:

$$x=x(v) \tag{3-15}$$

where $0\le v\le v_p$ and $0\le x\le l$.

For $x(v)$ the use of the following proportion is proposed:

$$\left.\begin{array}{l} x \sim v^{\alpha} \Rightarrow x = c \cdot v^{\alpha} \\ l \sim v_p^{\alpha} \Rightarrow x = c \cdot v_p^{\alpha} \end{array}\right\} \Rightarrow \frac{x}{l} = \left(\frac{v}{v_p}\right)^{\alpha} \tag{3-16}$$

where $0{,}5 < \alpha \leq 1$. The choice of the exponent in the proportion was made based on own tests (chapter 3.5.4).

Considering the limit state conditions, the prism's mass $G_{PR}(v)$ results as a function of wall displacement v:

$$G_{PR}(v) = \begin{cases} \frac{1}{2}\gamma \frac{h^2}{\tan\vartheta}\left(2\left(\frac{v}{v_p}\right)^{\alpha} - \left(\frac{v}{v_p}\right)^{2\alpha}\right) & \text{for} \quad 0 \leq v < v_P \\ \frac{1}{2}\gamma \frac{h^2}{\tan\vartheta} & \text{for} \quad v \geq v_P \end{cases} \tag{3-17}$$

3.5.3 Equilibrium equations of the monolith

In addition to the above mentioned things, to determine the force equilibrium of the soil prism, the direction of the reaction force on the failure plane, as well as the direction of the passive resistance force of the mobilized soil prism are necessary.

For this purpose, by applying Coulomb's theory, it is ideally accepted that the angle between the reaction force Q and the normal to the failure surface, on its entire length, is equal with the soil friction angle.

Mao (1993) analysed the variation of the mobilized passive earth resistance inclination, as a function of wall displacement for different density indexes.

It is noted that for a relatively smooth wall surface, regardless the sand density index, at the total mobilization of the passive earth resistance, the soil-wall interface friction angle δ is completely mobilized.

Based on the same experimental results, it was observed that for a dense sand, the soil-wall interface friction angle is fully mobilized long before the earth's resistance is achieved.

Since the mobilization of the $\delta(v)$ angle has a significant influence on the mobilization of $E_p(v)$ for a range of small displacements and it does not

significantly influences it for a range of higher displacements, in a simplifying manner, a constant value of δ was considered for the entire mobilization area.

The interface between the already moving trapezoidal prism and the still at-rest part is subjected to the at-rest earth pressure E_0.

The height of the cross-section is:

$$h(v) = h \cdot \frac{l - x}{l} \tag{3-18}$$

By introducing equation (3-16) in equation (3-18), one obtains:

$$h(v) = h \cdot \left(1 - \left(\frac{v}{v_p} \right)^{\alpha} \right) \tag{3-19}$$

Considering the above mentioned equations, the at-rest pressure is obtained as a function of wall displacement, found at the other end of the compressible prism:

$$E_0(v) = \begin{cases} \frac{1}{2}\gamma h^2 \cdot \left(1 - \left(\frac{v}{v_p} \right)^{\alpha} \right)^2 K_0, & \text{for} \quad 0 \le v < v_P \\ 0, & \text{for} \quad v \ge v_P \end{cases} \tag{3-20}$$

In order to calculate the passive earth resistance $E_p(v)$ as a function of wall displacement, the trapezoidal prism is delimited by the vertical wall and the not-mobilized prism and the equilibrium equations of the applied forces is written in accordance with Figure 3-12:

The force equilibrium on the *x* and *y* axes, for a wall displacement $0 \le v < v_P$ leads to:

$$\begin{cases} \sum F_x = 0 \\ \sum F_y = 0 \end{cases} \Leftrightarrow \begin{cases} -Q(v)\sin(\vartheta + \phi) - E_0(v) + E_p(v)\cos\delta_p = 0 \\ Q(v)\cos(\vartheta + \phi) - G_{PR}(v) - E_p(v)\cos\delta_p = 0 \end{cases} \tag{3-21}$$

All the variables are a function of wall displacement v, besides φ, δ and the inclination of the failure plane ϑ.

By removing $Q(v)$ from the (3-21) system of equations, one obtains:

$$E_p(v) = \frac{G_{PR}(v)\tan(\vartheta+\phi) + E_0(v)}{\cos\delta_p - \sin\delta_p \tan(\vartheta+\phi)} \tag{3-22}$$

where the mobilized variables of the soil's weight $G_{PR}(v)$ and the at-rest pressure $E_0(v)$ are taken from equations (3-17) and (3-20).

When the ultimate displacement is reached, $v = v_p$, equation (3-22) can be reduced to equation (3-7) and it can be noted that the earth resistance according to Coulomb's theory is fully mobilized. For an additional wall displacement $v > v_p$, the earth resistance remains constant and equal to its maximum value E_p.

3.5.4 Validation of the static mathematical model

To verify the mathematical model described in the preceding chapter and to calibrate it, representative tests on the physical model were selected.

The main selection criteria of the tests consisted of minimal influence of the sand-side wall friction, as well as boundary conditions. Since the influence of the side friction on the results decreases when the wall's width is increased, to calibrate the mathematical model tests with a 32 cm wall width were selected.

Considering equation (2-5), which defines the variation of the sand friction angle as a function of density index and confining pressure, the calculation model is close to the real model, for higher confining pressures, in other words, for higher fill heights behind the wall. For these reasons, the tests with a 24 cm nominal wall height were selected for the analysis. For these tests, the ratio between the nominal height and the wall width, as well as the one with length of the glazed channel still remain in an acceptable domain.

Moreover, three representative density indexes have been chosen, *D* = 0,5, *D* = 0,7 and *D* = 0,9, in order to cover a wide range of soil density in natural state.

The criteria were fulfilled by the V30, V32 and V33 tests, which were selected to calibrate the mathematical model.

Table 3-4. The selected static tests

Parameter	Test	V30	V32	V33
	Test series	S6	S6	S6
	Density index *D*	0,9	0,7	0,5
	φ [°]	48,5	43,4	38,3
	δ [°]	20,25	17,75	15,25
Results of tests on the physical model	K_{ph} [-]	14,7	10,7	8,2
	$\frac{v_p}{h}$ [-]	0,055	0,098	0,145
Calculated values with the mathematical model	K_{ph} [-]	14,8	10,5	7,8
	$\frac{v}{h}$ [-]	0,055	0,100	0,145
	ϑ [°]	13,8	16,1	18,3
	Mass of the mobilized prism [kg]	199	164	138
	$\frac{R_s}{E_{ph}}$ [-]	0,0752	0,0937	0,114

By using different values of the α coefficient defined by equation (3-16), to calibrate the static model for V30, V32 and V33 tests, a good correlation was obtained for a 0.5 value of α.

In order to directly compare the static and dynamic models, uninfluenced by the friction force with the side walls of the glazed channel, the total passive earth resistance was considered.

Considering that the measured horizontal force from the performed tests is made of the horizontal component of the real passive resistance and the side friction, approximated using equation (2-10), is:

$$\overline{E_{ph}} = E_{ph} + R_s = \left(1 + 2K_0 \tan\delta_s\right) \cdot E_{ph} \tag{3-23}$$

By replacing E_{ph} from equation (3-7) in (3-23), the total horizontal component of the passive earth resistance is obtained for a given b wall width.

$$\overline{E_{ph}} = \frac{1}{2}\gamma \cdot h^{2} \cdot b \cdot \left(1 + 2K_0 \tan\delta_s\right) \cdot K_{ph} \tag{3-24}$$

therefore the passive earth pressure coefficient results:

$$\overline{K_{ph}} = \left(1 + 2K_0 \tan\delta_s\right) \cdot K_{ph} \tag{3-25}$$

For a plain strain state the real passive earth resistance coefficient (without the influence of the side friction) can be written as:

$$K_{ph} = \cos\delta \cdot K_p \tag{3-26}$$

where K_p is determined according to equation (3-8).

For comparison, Figure 3-13 presents the passive earth resistance mobilization curves, measured for the V30, V32 and V33 tests and the ones calculated with the proposed mathematical model. To ease the comparison, a weighted average of each 10 measured values. Each 100 measured values is symbolized by a point. The calculated curves are represented by a symbol for each 10th value.

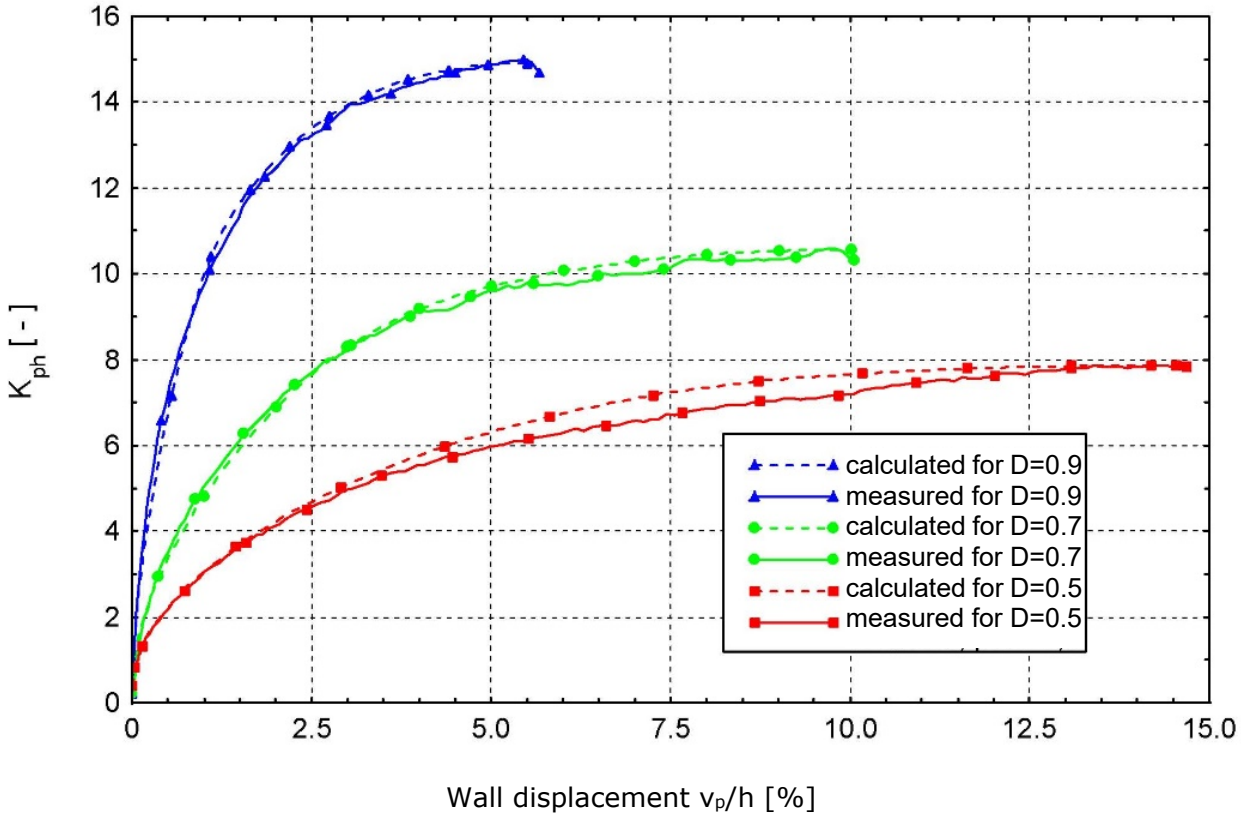

Figure 3-13: Comparison of the passive earth resistance mobilization curves (measurements of the V30, V32 and V33 tests versus the ones calculated with the mathematical model)

The overlap of the mathematical model results with the physical model measurements validates the own mathematical model, based on Coulomb's theory and completed with the compressible prism hypothesis, which mobilizes proportionally with the wall displacement. Moreover, it justifies the approximations made regarding the side interface friction, as well as not taking into account other error generating boundary conditions.

Thus, the static mathematical model, validated by the own tests, is extended in the next chapter to model the case of passive earth resistance mobilization under shock-type loads, by including the inertial forces. Moreover, the validation of the dynamic mathematical model based on own tests will be pursued.

Chapter 4. Dynamic passive earth pressure under shock-type loads

4.1 General information

The collision of motor vehicles with various obstacles can occur at numerous speeds and impact masses.

In an extreme case the collision of a ship with the quay walls can be considered, where the inertial forces have a secondary role and the overall behaviour is quasi-static. Unlike this case, if motor vehicles or rolling stock collide with earth retaining walls at high speeds, high accelerations occur. They cause significant inertial forces, influencing the dynamic equilibrium and the ground-structure interaction.

This chapter present the further development of the static mathematical model detailed in 3.5, with the addition of the inertial forces associated with the investigated dynamic phenomenon. The dynamic model is validated and calibrated based on the own tests performed on reduced scale models.

4.2 The tests results and their analysis

In addition to the preliminary tests, which had the main purpose to provide the basis for the development of the experimental stand, a total number of about 100 dynamic tests were performed on models with three density indexes and five sand backfill heights. Table 4-1 reviews the main parameters of several dynamic tests.

Table 4-1. Synoptic outline of the dynamic tests performed on physical models

No.	Name	Date	Wall width *b*	Wall height *h*	Density index *D*	Pendulum mass	Pendulum length	Initial pendulum deviation	Free-falling height	Impact force	Duration of the impact force	Impulse	Max. wall displacement	Pressure distribution measurements	Video recordings
			cm	cm	-	kg	m	cm	m	kN	s	kNs	cm		
D1	TS_DynBr_09_24	8-22-2001	32	24	0.9	12.75	0.8	horizontal	0.8	3.96	0.075	0.277	0.8	yes	
D2	TS_DynBr_07_24	8-20-2001	32	24	0.7	12.75	0.8	horizontal	0.8	3.33	0.078	0.27	1.8	yes	
D3	TS_DynBr_05_24	8-19-2001	32	24	0.5	12.75	0.8	horizontal	0.8	3.16	0.078	0.256	3.3	yes	
D4	TS_DynBr_6_8	4-5-2001	32	8	0.9	7.937	0.8	60°	0.4	0.76	0.08	0.096	1.6	yes	
D5	TS_DynBr_5_12	4-5-2001	32	12	0.9	7.937	0.8	horizontal	0.8	1.7	0.071	0.17	1	yes	
D6	TS_DynBr_4_16	4-2-2001	32	16	0.9	12.75	0.8	horizontal	0.8	3.9	0.076	0.273	1.46	yes	
D7	TS_DynBr_3_24	4-2-2001	32	24	0.9	12.75	0.8	vertical	1.5	9.79	0.06	0.35	1.44	yes	
D8	TS_DynBr_2_24	4-2-2001	32	24	0.9	12.75	0.8	vertical	1.5	9.79	0.06	0.35	1.34	yes	
D9	TS_DynBr_1_24	4-2-2001	32	24	0.9	12.75	0.8	horizontal	0.8	3.13	0.078	0.272	0.57	yes	
D21	DynamBreit_3	11-10-2000	32	32	0.9	12.75	0.8	vertical	1.5	20	0.062	0.7	0.5	yes	
D22	DynamBreit_2	11-10-2000	32	32	0.9	12.75	0.8	horizontal	0.8	7.68	0.075	0.562	0.27	yes	
D23	DynamBreit_1	11-10-2000	32	32	0.9	12.75	0.8	horizontal	0.8	6.61	0.077	0.55	0.3	no	
D44	**DynamV-05**	4-24-2000	16	12	0.9	5.9	1.13	vertical	2.2	1.01	0.038	0.018	0.945	no	yes

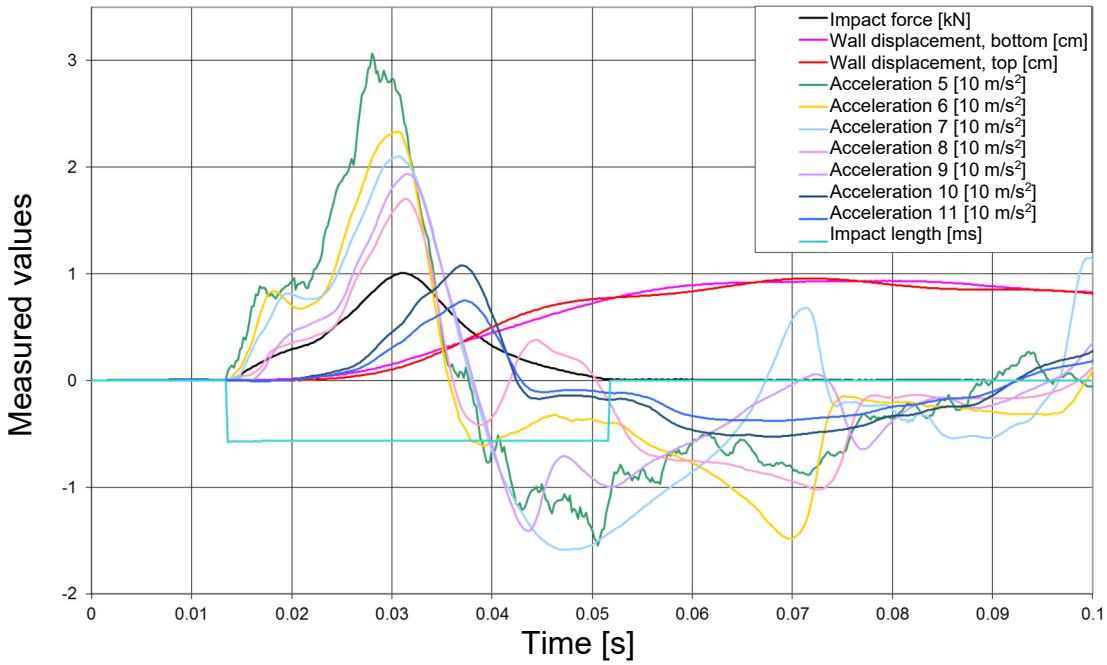

Figure 4-1: D44 – DynamV-05 test results

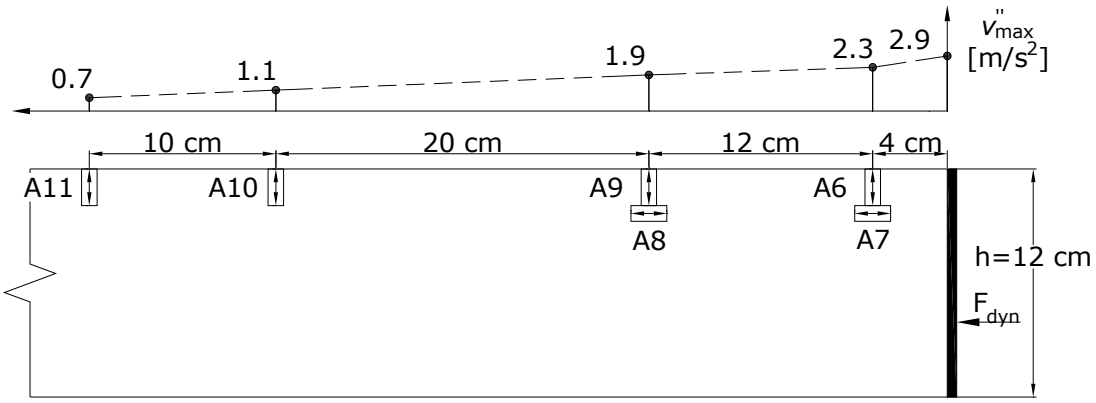

Figure 4-2: Vertical and horizontal accelerometer layout below the sand surface; the peak acceleration values recorded during the D44 – DynamV-05 test are presented above

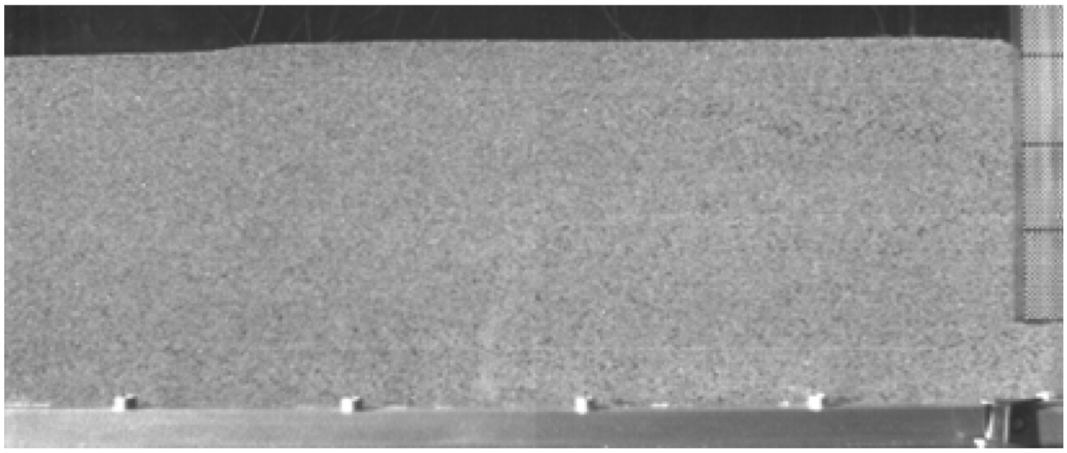

Figure 4-3: D44 tests at the maximum wall displacement

4.3 Prism mobilization analysis with the video method

In addition to direct measurements, several dynamic tests have been video recorded using the high-speed camera described in Chapter 2.

With the usual measurement methods, using displacement sensors and accelerometers, only local information, in specific measuring points, regarding the displacement and its derivatives can be obtained. It is seldom needed to know these measures within the entire studied field. By using the 2D-PIV method, velocity measurements in the whole visible plane becomes possible. Figure 2-17 presents the high-speed camera set in front of the sand-filled glazed channel.

This method allowed for the first time to observe the soil behaviour behind the wall subjected to a shock-type dynamic load and to compare it with the already known static case, investigated by the author using the same methods, as presented in Chapter 3.

Similar with the case of static tests of the physical model, described in Chapter 3, the tests were performed until the maximum wall displacement was obtained for this case too. Continuous video recordings were done during the test. At a high data transfer rate, characteristic of the 1000 frames/s recording frequency and a maximum resolution 512x512 pixels, the memory of the camera was able to store up to 0.5 seconds of recordings.

The video recording is triggered by the moving pendulum, through a laser beam, short before impact. The video sequences are converted and stored on the hard-disk as individual images. High speed recordings of the phenomenon, and decomposing the video in individual sequences, allowed a precise observation of the phenomenon. This was succeeded by the Particle-Image-Velocimetry (PIV) analysis of the images recorded during the tests.

In order to accurately synchronize the video record with the measuring devices, an electric conductor was mounted on the pendulum, connected to a contact sheet on the tip of the impact cap. It closes an electric circuit while in contact with the mobile wall and within a millisecond it turns on a LED signal. The signal was mounted in the right bottom corner of the glazed channel's frame, so it could be recorded by the camera (see Figure 4-5 to Figure 4-12). The electric circuit was connected in parallel with the measuring devices, therefore while the impact cap and the wall were in contact, they would record their specific measurements.

Based on the PIV analysis, obvious differences of the failure surface and its inclination from the horizontal axis could be observed for neither the static tests nor the dynamic ones, when a shock-type load was applied. This verifies the hypothesis stated in DIN 4085:2011-05: Subsoil - Calculation of earth-pressure, chapter 6.6.3 Soil pressure under dynamic excitation loads, that by approximation, the same inclination of the failure surface can be adopted in dynamic cases as the one determined for static conditions.

The optical analysis of a representative dynamic test is presented below. In the right bottom corner of the image, one can see the turned-on LED light while the pendulum and the wall are in contact with each other.

The first image shows the velocity vector field and the second one their local gradient, which was determined in order to emphasize the failure surface.

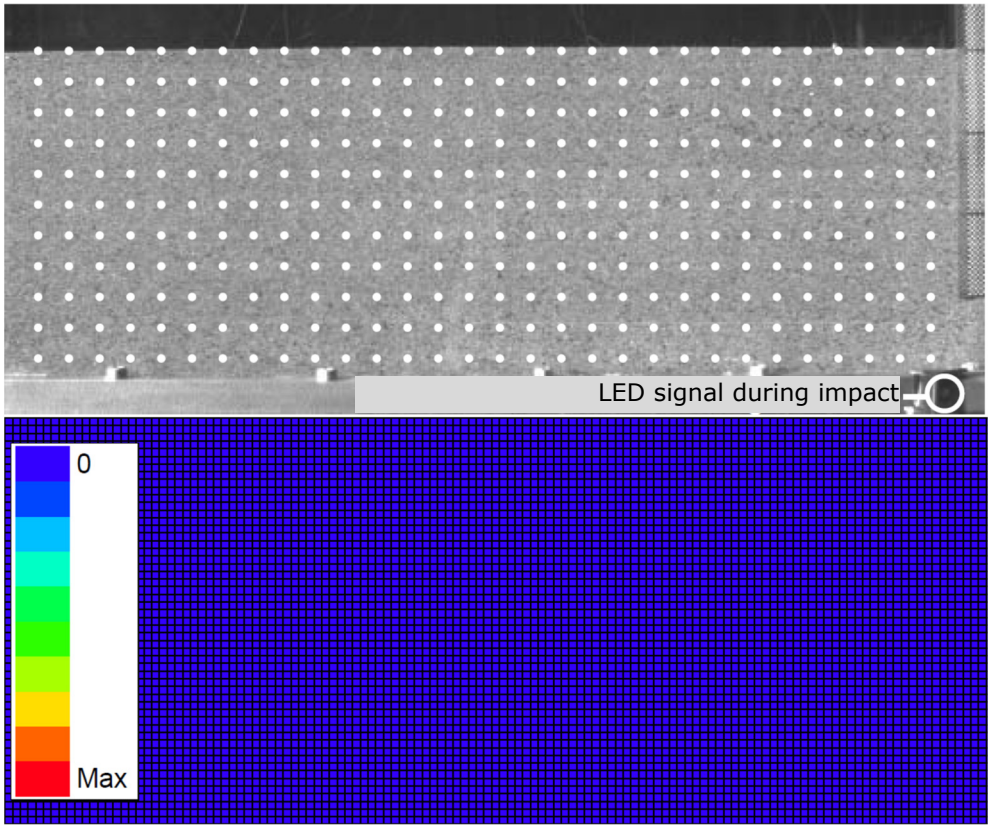

Figure 4-4: The D44 test, before contact of the pendulum with the mobile wall

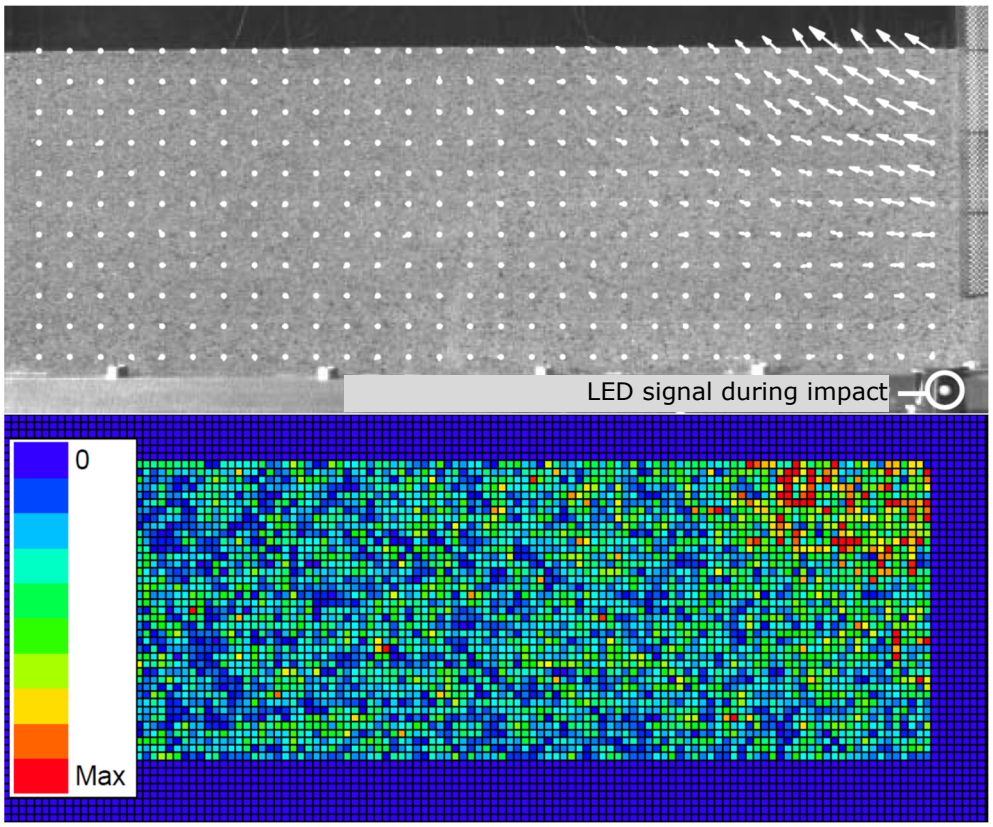

Figure 4-5: The D44 test, when the pendulum makes contact with the mobile wall, t=0

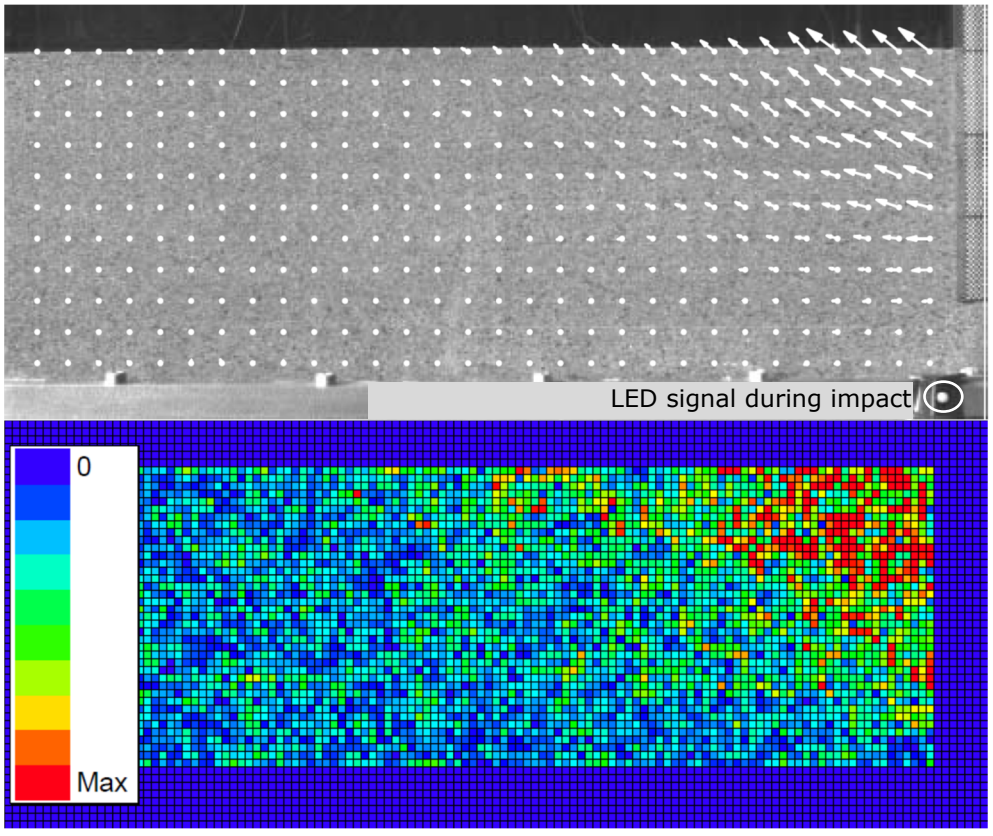

Figure 4-6: The D44 test at t=0,01 s

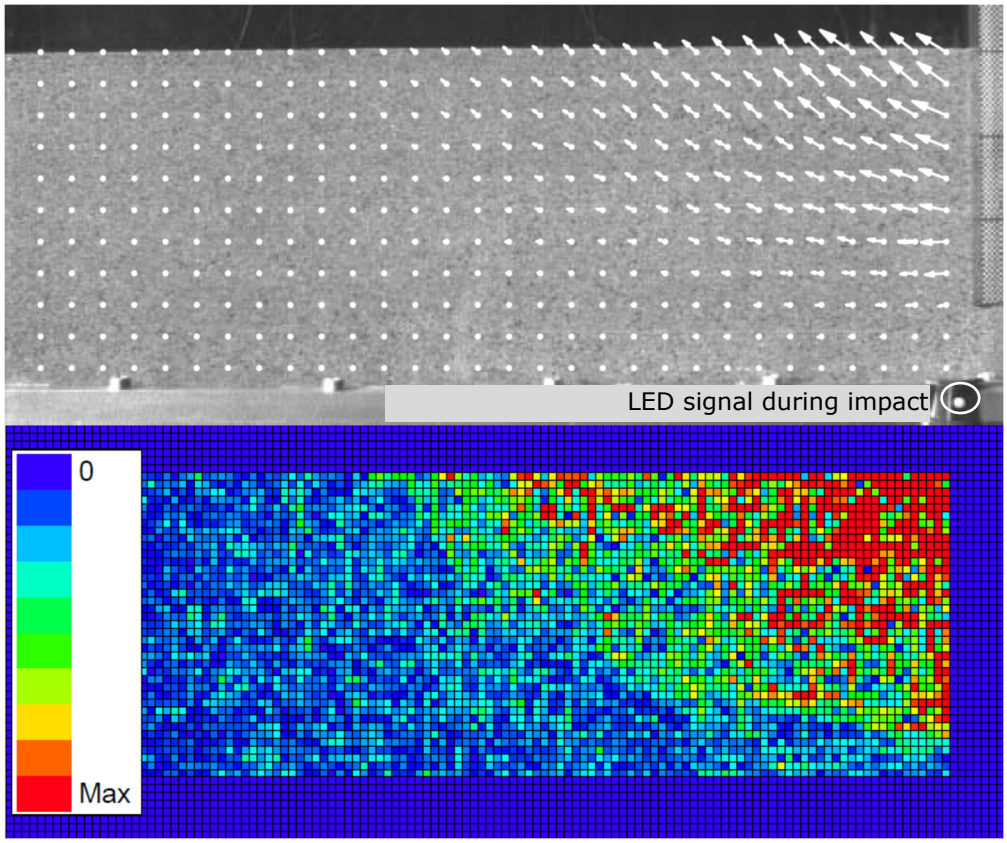

Figure 4-7: The D44 test at t=0,02 s

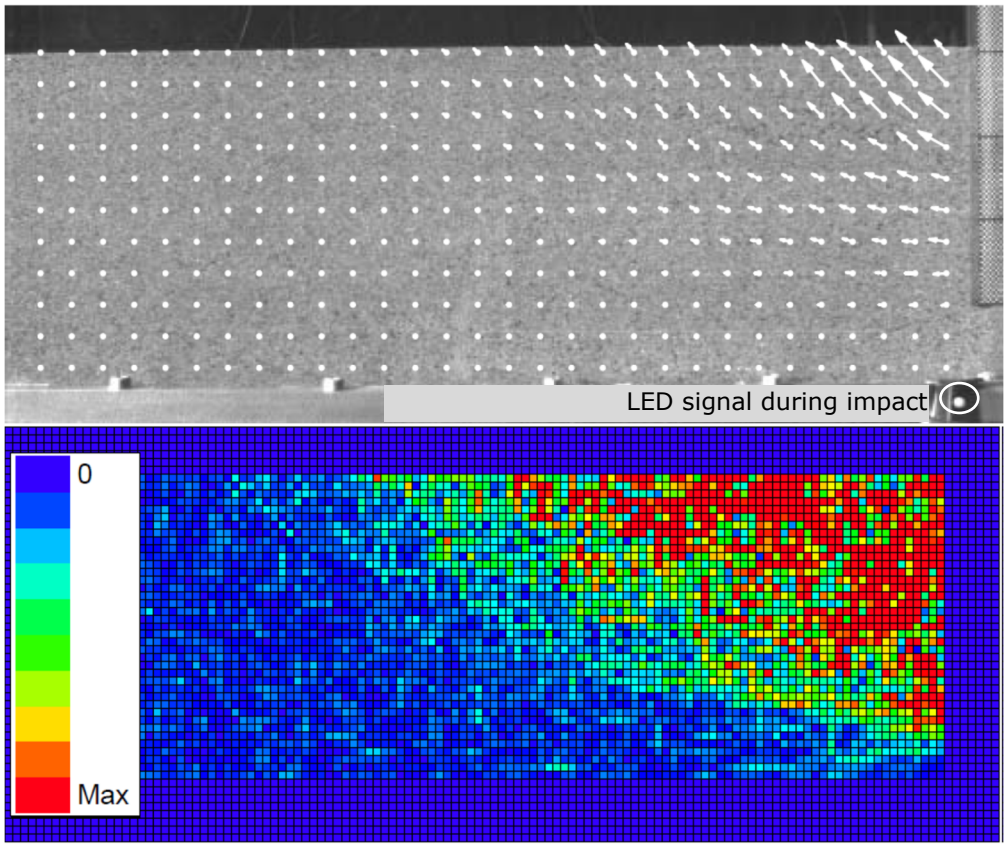

Figure 4-8: The D44 test at t=0,03 s

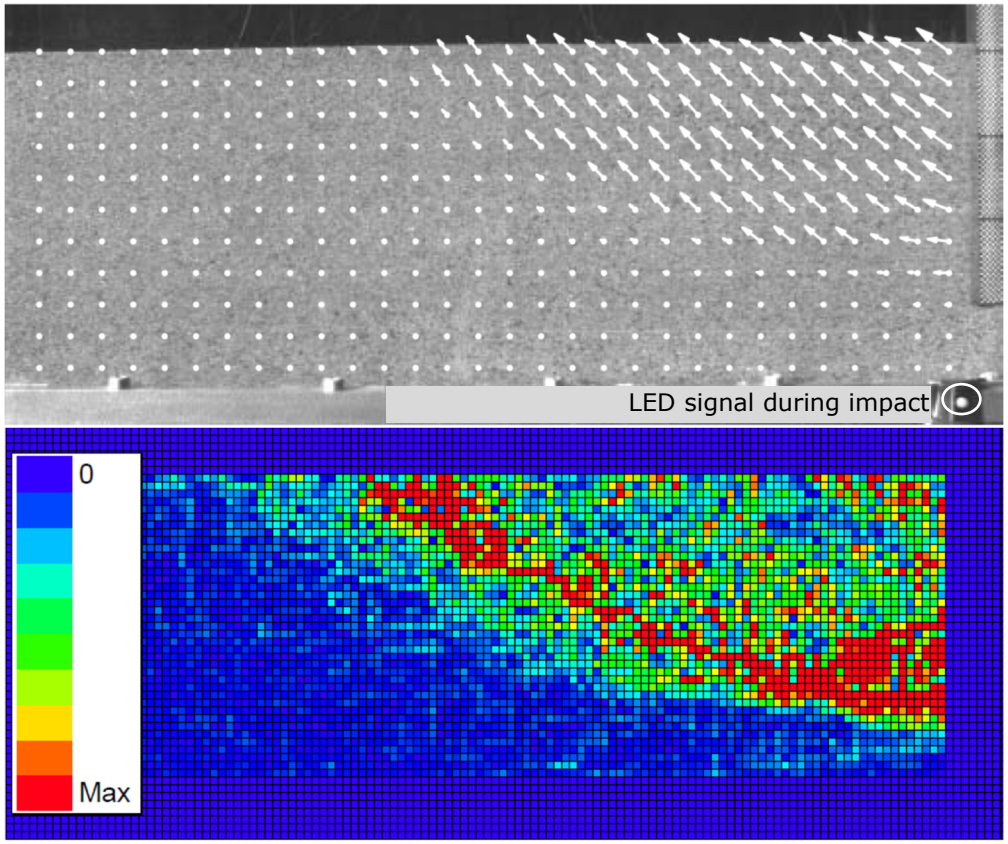

Figure 4-9: The D44 test at t=0,04 s

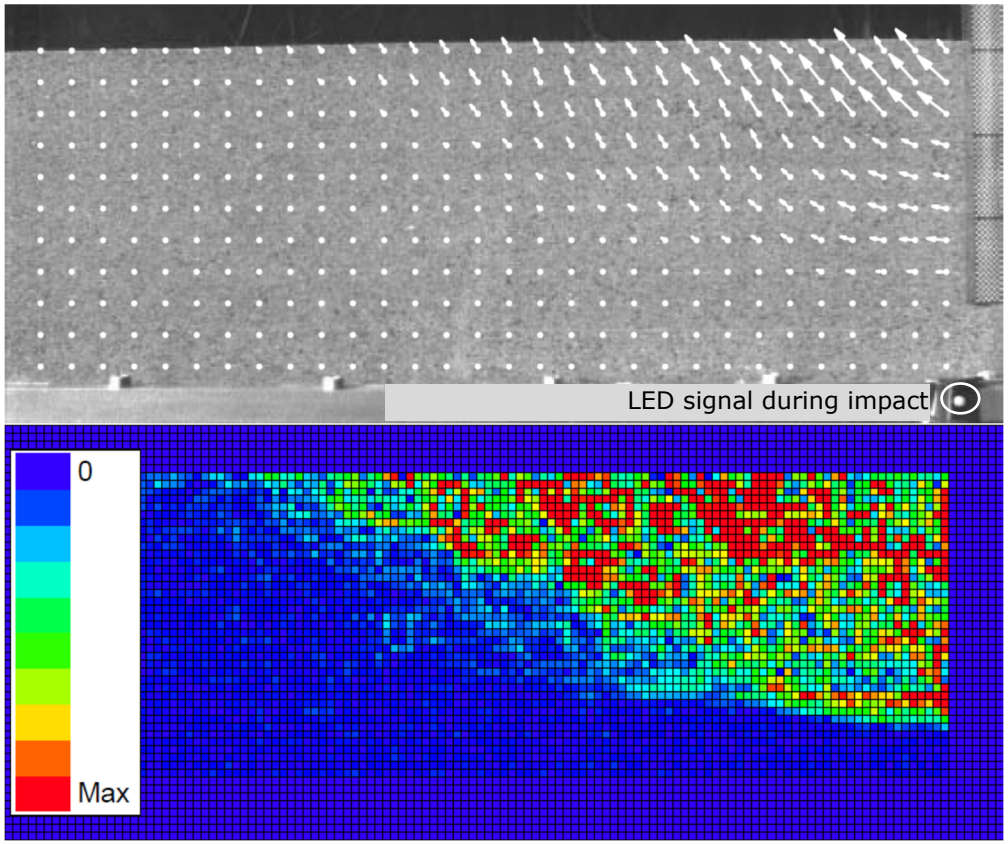

Figure 4-10: The D44 test at t=0,05 s

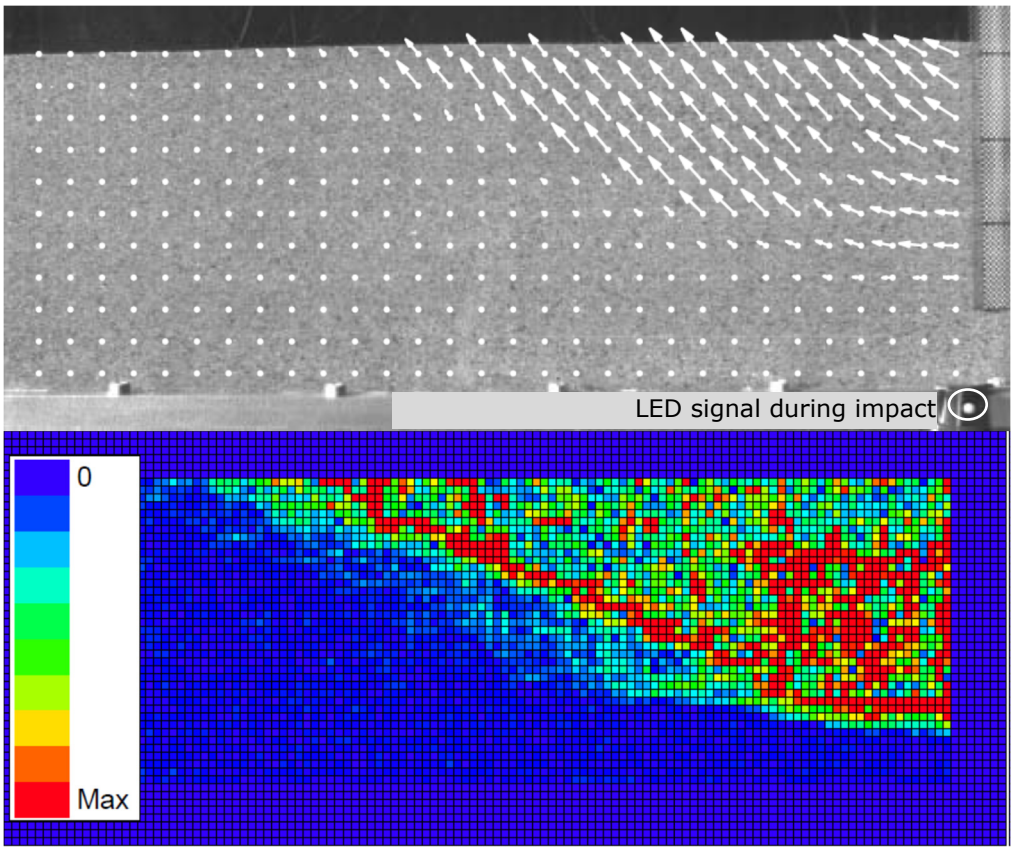

Figure 4-11: The D44 test at t=0,06 s

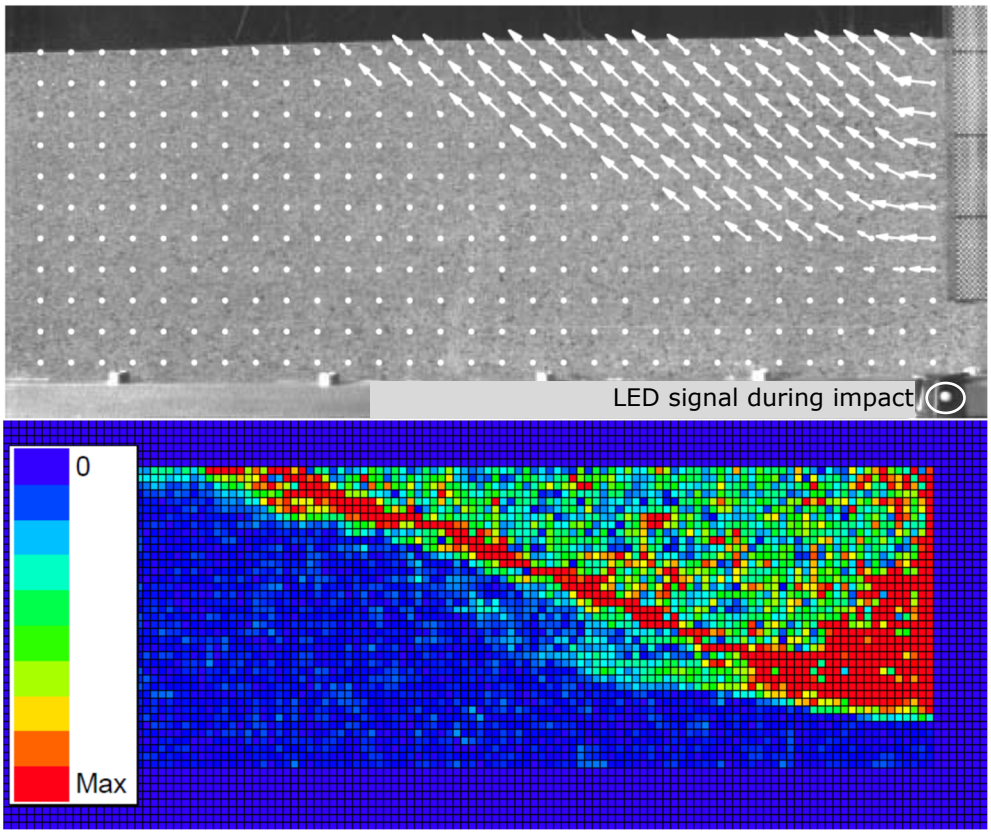

Figure 4-12: The D44 test at t=0,07 s

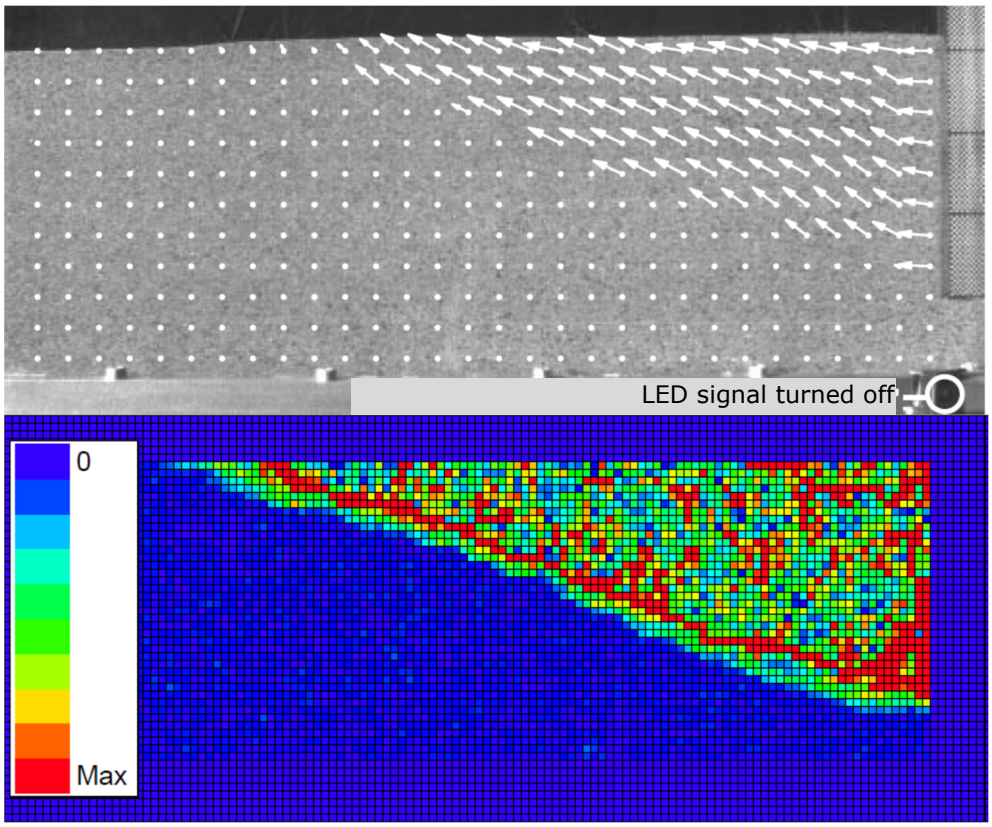

Figure 4-13: The D44 test at t=0,08 s, when the pendulum is no longer in contact with the mobile wall

The continuous displacement of the mobilized prism can be observed, even after the shock-type load is applied, which is due to the inertial forces.

The author has developed a computer program to determine the derivatives of the velocity vector field, obtained by PIV analysis, in order to obtain the representation of acceleration vector fields of the mobilized soil mass during displacement.

The obtained acceleration field was integrated for the entire surface of the glazed channel and the time dependent acceleration of the mobilized soil mass was obtained. By comparing the results for several models with the accelerometer measurements, a good overlap of the results was obtained. This confirms the applicability and potential of the method for soil dynamics research.

4.4 The dynamic mathematical model

In the following paragraphs the development of the static model, described in chapter 3.5, will be presented to calculate the dynamic passive earth pressure.

4.4.1 General overview of the model

The simplifying assumptions and idealization made for the static model (chapter 3.5) are acceptable in order to extend the mathematical model for passive resistance mobilization under shock-type dynamic loads.

Since the impact force is time dependent $F_{dyn}=F_{dyn}(t)$, it cannot be considered quasi-static, and studied model is no longer in static equilibrium, but in a dynamic one. Therefore, besides the forces considered in the static equilibrium condition (3-21), inertial forces also occur for this case. For this purpose, all the masses which will be accelerated by the impact force must be considered. The weight of the soil prism, which is mobilizes the passive earth resistance for the static case, results from equation (3-17) as:

$$G_{PR}=G_{PR}(v)=\begin{cases}\dfrac{1}{2}\gamma\dfrac{h^2}{\tan\vartheta}\cdot\left[2\cdot\left(\dfrac{v}{v_p}\right)^{\alpha}-\left(\dfrac{v}{v_p}\right)^{2\alpha}\right], & 0\le v<v_p\\ \dfrac{1}{2}\gamma\dfrac{h^2}{\tan\vartheta}, & v\ge v_p\end{cases} \tag{4-1}$$

Besides the weight of the soil prism G_{PR}, at the dynamic equilibrium the weight of the retaining wall G_w also intervenes, but it has a known value.

4.4.2 Dynamic equilibrium

The system subjected to a shock-type dynamic load consists of the retaining wall and the trapezoidal monolith (Figure 4-15). To calculate the dynamic passive earth resistance $E_{pdyn}=E_{pdyn}(v)$, the wall and the monolith of an $A(v)$ area are isolated and the forces acting on them are applied.

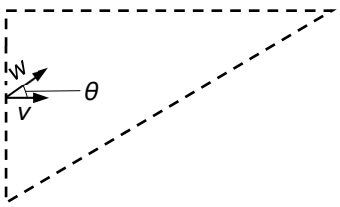

Figure 4-14: Wall and soil prism displacement

The symbols used in Figure 4-14 have the following meaning:

v – horizontal wall displacement;

w – soil prism displacement;

ϑ – inclination angle of the failure plane.

From Figure 4-14 the following relation results:

$$v = w\cos\vartheta \tag{4-2}$$

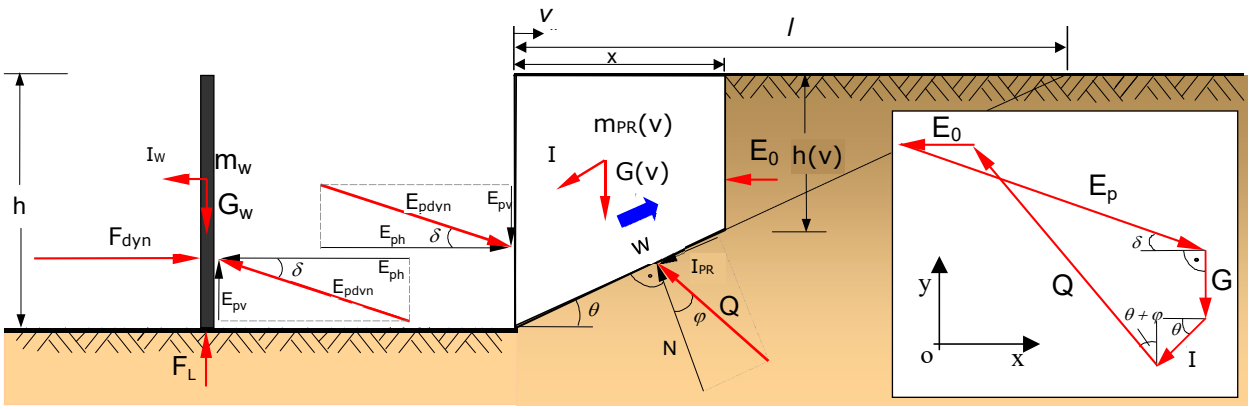

Figure 4-15: Mobilization of the forces in the soil prism

From the equilibrium of forces acting on the wall along the *x* and *y* axes, the following relation results:

$$\begin{cases} \sum F_x = 0 : -E_{pdyn}\cos\delta_p - I_W + F_{dyn} = 0 \\ \sum F_y = 0 : E_{pdyn}\sin\delta_p - F_L + G_W = 0 \end{cases} \tag{4-3}$$

and the equilibrium of forces acting on the soil monolith:

$$\begin{cases} \sum F_x = 0 : -I_{PR}\cos\vartheta - Q\sin(\vartheta+\phi) - E_0 + E_{pdyn}\cos\delta_p = 0 \\ \sum F_y = 0 : -I_{PR}\sin\vartheta - Q\cos(\vartheta+\phi) - G_{PR} - E_{pdyn}\sin\delta_p = 0 \end{cases} \tag{4-4}$$

where:

I_W - wall inertial force;

$F_{dyn}=F_{dyn}(t)$ - impact force;

F_L - vertical equilibrant force of the wall;

G_W - wall weight;

I_{PR} - monolith inertial force;

$Q = Q(v)$ - reaction force on the failure surface;

$E_0 = E_0(v)$ - at-rest earth pressure acting on the right side of the monolith;

$G_{PR} = G_{PR}(v)$ - soil weight;

δ_p - inclination of the passive resistance.

The wall displacement $v = v(t)$ and the monolith displacement on the inclined plane $w = w(t) = v(t)/\cos\vartheta$ are time dependent. All the physical quantities herein are either time (t) or wall displacement (v) dependents, besides the inclination of the failure surface (ϑ) and the friction angle (φ). To simplify notation, all the dependent quantities will be further written independently of their argument.

Since sliding device of the mobile wall, described in Chapter 2, did not permit to measure the force in the bearings F_L, the equilibrium of the forces acting along the vertical y axis (the second equation in (4-3)) will be eventually neglected. Therefore, the supporting force of the sliding bearings and the real inclination of the passive earth resistanceδ_p are not directly determined form the experiment. From the first equation of the same system, one can find that:

$$E_{pdyn} = \frac{F_{dyn} - I_W}{\cos\delta_p} \tag{4-5}$$

By eliminating the reaction force Q from the equation system (4-4) and by introducing the dynamic passive resistance E_{pdyn} from equation (4-5), the following relation results:

$$\begin{aligned} &- I_{PR}\cos\delta_p\left(\cos\vartheta + \sin\vartheta\tan\left(\vartheta+\phi\right)\right) - G_{PR}\cos\delta_p\tan\left(\vartheta+\phi\right) \\ &- E_0\cos\delta_p + \left(F_{dyn} - I_W\right)\left(\cos\delta_P - \sin\delta_P\tan\left(\vartheta+\phi\right)\right) = 0 \end{aligned} \tag{4-6}$$

The quantities G_{PR} and E_0 according to equation (3-17) and (3-20) respectively, are introduced in equation (4-6). The collision force $F_{dyn}=F_{dyn}(t)$ is known as an input data from the time variation of the impact force.

The inertial force of the wall I_W, the inertial force of the soil prism I_{PR} and the dynamic passive earth resistance E_{pdyn} reamain unknown. The force of inertia of the constant wall mass m_W, displaced by v, is:

$$I_W = I_W(v) = m_W \cdot \ddot{v} \tag{4-7}$$

The inertial force of monolith mass is equal with the impulse derivative, and can be written in two terms:

$$I_{PR} = I_{PR}(v) = \frac{d(m_{PR} \cdot \dot{w})}{dt} = \frac{dm_{PR}}{dt}\dot{w} + m_{PR}\frac{d\dot{w}}{dt} \tag{4-8}$$

The first term is the inertial force due to the variation of the monolith's mass, and the second one is the inertial force due to variation of the monolith's speed, or its acceleration.

The first term can be re-written with the derivative of the known mobilization function of the soil's mass, after the prism w displacement:

$$\frac{dm_{PR}}{dt}\dot{w} = \frac{dm_{PR}}{dw}\frac{dw}{dt}\dot{w} = \frac{dm_{PR}}{dw}\dot{w}^2 \tag{4-9}$$

The inertial force of the monolith can be found after equation (4-9) is introduced in equation (4-8), as follows:

$$I_{PR} = \frac{dm_{PR}}{dw}\dot{w}^2 + m_{PR}\ddot{w} \tag{4-10}$$

The monolith's mass is introduced in equation (4-10), based on equation (4-1), and by replacing v with $v = w\cos\vartheta$, the following equation results:

$$I_{PR} = \begin{cases} -m_{PR\max}\left\{\begin{aligned}&\frac{1}{w}\left[2\alpha\left(\left(\frac{w\cos\vartheta}{v_p}\right)^{\alpha} - \left(\frac{w\cos\vartheta}{v_p}\right)^{2\alpha}\right)\right]\dot{w}^2 + \\ &+\left(2\left(\frac{w\cos\vartheta}{v_p}\right)^{\alpha} - \left(\frac{w\cos\vartheta}{v_p}\right)^{2\alpha}\right)\ddot{w}\end{aligned}\right\}, & \text{for} \quad 0 \le w < v_p/\cos\vartheta \\ m_{PR\max}\ddot{w}, & \text{for} \quad w \ge v_p/\cos\vartheta \end{cases} \tag{4-11}$$

where

$$m_{PR\max} = \frac{1}{2}\gamma\frac{h^2}{g\tan\vartheta}$$

By introducing the displacement depend quantities in equation (4-6), the equation of motion of the monolith results as a nonlinear differential equation of w, which can be written for the $0 \le w < v_p/\cos\vartheta$ domain as follows:

$$\begin{aligned}
&\overbrace{-m_{PR\max}\left\{\underbrace{\frac{1}{w}\left[2\alpha\left(\left(\frac{w\cos\vartheta}{v_p}\right)^{\alpha}-\left(\frac{w\cos\vartheta}{v_p}\right)^{2\alpha}\right)\right]}_{I_{PR-m}}\dot{w}^2+\underbrace{\left(2\left(\frac{w\cos\vartheta}{v_p}\right)^{\alpha}-\left(\frac{w\cos\vartheta}{v_p}\right)^{2\alpha}\right)}_{I_{PR-a}}\ddot{w}\right\}\cdot\cos\delta_p\cdot\left(\cos\vartheta+\sin\vartheta\tan\left(\vartheta+\varphi\right)\right)}^{I_{PR}}\\
&\underbrace{-m_{PR\max}g\left(2\left(\frac{w\cos\vartheta}{v_p}\right)^{\alpha}-\left(\frac{w\cos\vartheta}{v_p}\right)^{2\alpha}\right)\cdot\cos\delta_p\cdot\tan\left(\vartheta+\varphi\right)}_{E_{pst}}\overbrace{-m_{PR\max}g\tan\vartheta\left(1-\left(\frac{w\cos\vartheta}{v_p}\right)^{\alpha}\right)^2K_0\cos\delta_p}^{E_0}+\\
&+\overbrace{\left(F_{dyn}-m_W\ddot{w}\cos\vartheta\right)\left(\cos\delta_p-\sin\delta_p\tan\left(\vartheta+\varphi\right)\right)}^{E_{pdyn}}=0
\end{aligned}\tag{4-12}$$

For $w\geq v_p\cos\vartheta$ equation (4-12) is simplified as:

$$\begin{aligned}
&-m_{PR\max}\ddot{w}\cos\delta_p\left(\cos\vartheta+\sin\vartheta\tan\left(\vartheta+\varphi\right)\right)-\\
&-m_{PR\max}g\cos\delta_p\tan\left(\vartheta+\varphi\right)+\\
&+\left(F_{dyn}-m_W\ddot{w}\cos\vartheta\right)\left(\cos\delta_P-\sin\delta_P\tan\left(\vartheta+\varphi\right)\right)=0
\end{aligned}\tag{4-13}$$

To highlight the forces that take part in the dynamic equilibrium of the system, equation (4-12) is re-written as:

$$\begin{aligned}
F_{dyn}=&\underbrace{m_W\ddot{w}\cos\vartheta}_{I_W}+\underbrace{\frac{\cos\delta_p\cdot\left(\cos\vartheta+\sin\vartheta\tan\left(\vartheta+\varphi\right)\right)}{\cos\delta_P-\sin\delta_P\tan\left(\vartheta+\varphi\right)}m_{PR\max}\frac{1}{w}\left[2\alpha\left(\left(\frac{w\cos\vartheta}{v_p}\right)^{\alpha}-\left(\frac{w\cos\vartheta}{v_p}\right)^{2\alpha}\right)\right]}_{I_{PR-m}}\dot{w}^2+\\
&+\underbrace{\frac{\cos\delta_p\cdot\left(\cos\vartheta+\sin\vartheta\tan\left(\vartheta+\varphi\right)\right)}{\cos\delta_P-\sin\delta_P\tan\left(\vartheta+\varphi\right)}m_{PR\max}\left(2\left(\frac{w\cos\vartheta}{v_p}\right)^{\alpha}-\left(\frac{w\cos\vartheta}{v_p}\right)^{2\alpha}\right)}_{I_{PR-a}}\ddot{w}+\\
&+\underbrace{\frac{\cos\delta_p\cdot\tan\left(\vartheta+\varphi\right)}{\cos\delta_P-\sin\delta_P\tan\left(\vartheta+\varphi\right)}m_{PR\max}g\left(2\left(\frac{w\cos\vartheta}{v_p}\right)^{\alpha}-\left(\frac{w\cos\vartheta}{v_p}\right)^{2\alpha}\right)}_{Q}+\\
&+\underbrace{m_{PR\max}g\frac{\cos\delta_p\tan\vartheta}{\cos\delta_P-\sin\delta_P\tan\left(\vartheta+\varphi\right)}\left(1-\left(\frac{w\cos\vartheta}{v_p}\right)^{\alpha}\right)^2K_0}_{E_0}
\end{aligned}\tag{4-14}$$

4.4.3 Numerical analysis and result comparison

The differential equation (4-12) can be written as follows:

$$A\ddot{w}+B\dot{w}^2+Cw+D=0\tag{4-15}$$

where $\{A,B,C\}=f(w,w^{\alpha})$ are nonlinear coefficients.

The differential equation (4-15) is an initial condition problem, with the following initial values:

$$\left.\begin{aligned} w &= 0 \\ \dot{w} &= 0 \\ \ddot{w} &= 0 \end{aligned}\right\} \quad \text{for} \quad t = 0, \tag{4-16}$$

which has no analytical solution. Based on Newmark's method, an attempt to develop an algorithm, based on the Newton-Raphson iterative procedure (see Chopra (2001)), in order to numerically solve the differential equation in (4-15). Due to non-linear coefficients, these attempts had no success.

From the above mentioned reasons, in order to solve the differential equation (4-15) with the initial values (4-16), the "NDSolve" numerical internal function of the numerical and symbolic mathematical software "Mathematica 7" was used. This function automatically adapts its numerical integration method for solving the differential equation.

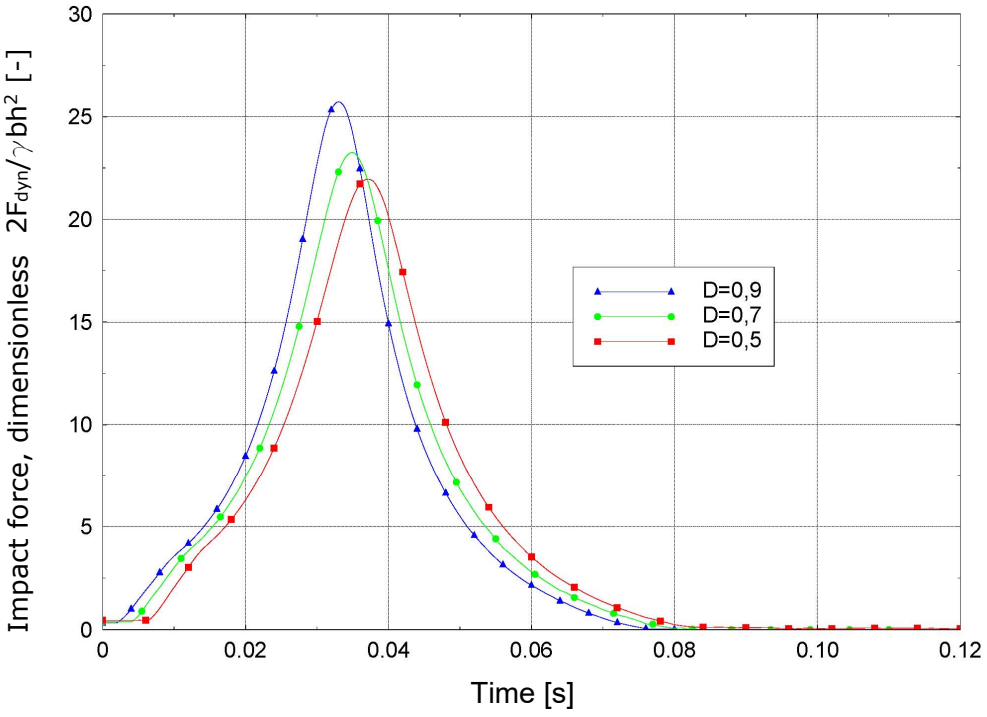

Figure 4-16: The impact force on the mobile wall, measured during dynamic tests for three density indexes and applied in the numerical analysis and in FEM models

The numerical calculation program, presented in Annex 1, has the main purpose of obtaining the maximum wall displacement as a result of the shock-type applied load, which is applied in short and defined time. Since the mathematical model is conceived to obtain the mobilized passive resistance, it stops shortly after the maximum wall displacement is obtained.

After the own tests on physical models, it was noticed that the displacement of the wall towards its initial position takes place after failure on a surface that has a similar shape with the one that would appear in the case of active earth pressure mobilization, for both the static and the dynamic cases. Consequently, the maximum wall displacement sufficiently describes the passive earth resistance under shock-type loads.

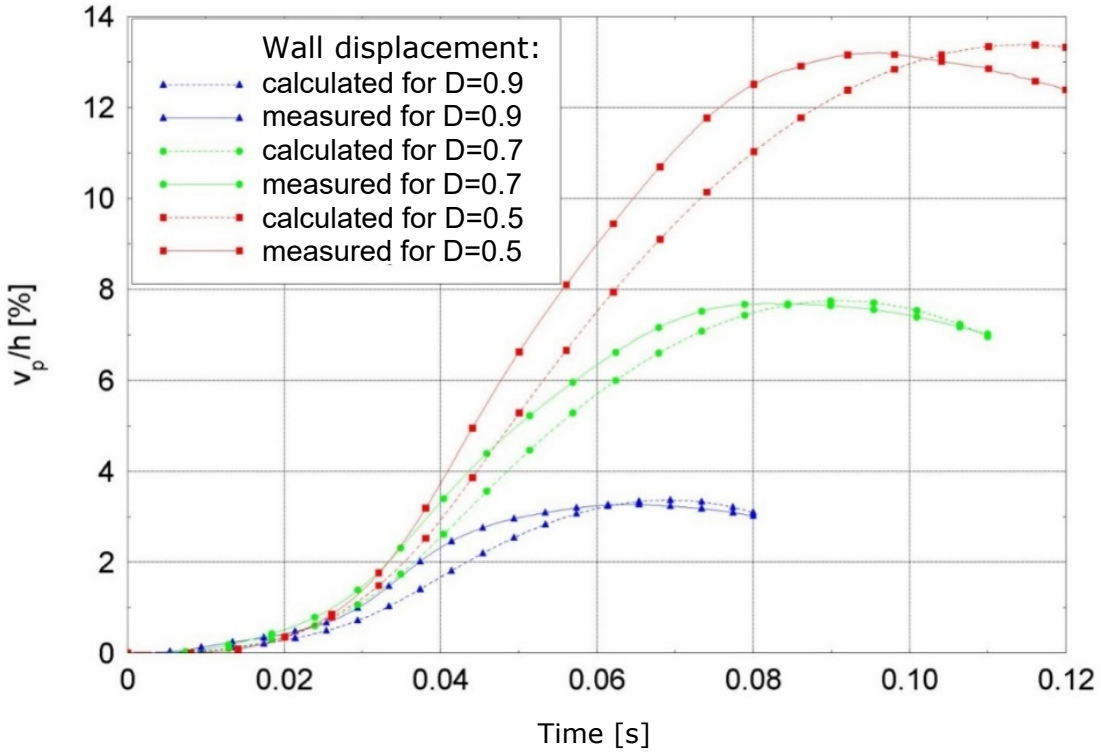

Figure 4-17: Comparison between the measured and calculated values for three density indexes: *D* = 0.9 – D1 test, *D* = 0.7 – D2 test and *D* = 0.5 – D3 test

Figure 4-16 presents the impact forces on the mobile wall, measured during dynamic tests for three density indexes, which are introduced as input parameters in the numerical program present in Annex 1. The value of the applied impulse $\int_0^{t_{max}} F\,dt$ varies due to the different stiffness of the system (different density indexes), in spite of having the same pendulum velocity and mass at impact.

The main results of the numerical program are presented in Figure 4-17 as mobile wall displacement graphs for the selected three tests: D1, D2 and D3, corresponding to three density indexes: *D* = 0.9, *D* = 0.7 and *D* = 0.5. A good correlation between the measured and calculated maximum displacements can be observed for all the three tests. Also, a good correlation between the occurring times of the maximum displacements can be seen.

This leads for the three cases, to the wall having different displacements during the collision and to the variation of the pendulum's impulse, which is equal with the one received by the system (see Table 4-1). In other words, the different stiffness of the soil forces the pendulum to bounce from the wall after collision, with different speeds, although its velocity before impact was equal for all three cases.

Figure 4-18 (a) presents the dynamic impact force applied on the mobile wall plotted on time for the D7 - TS_DynBr_3_24 test. In order to obtain a smooth increase of the applied force, that wouldn't generate disturbing vibrations in the physical model, a conical neoprene impact cap was build and stuck on the pendulum. Therefore, impulses that allowed to record and process the data in favourable conditions. In Figure 4-18 (b) one can see that the time when the maximum wall displacement is reached, is long after the maximum impact force appears, but it is close to the moment when the force stops loading the wall. A good correlation between measured and calculated maximum displacements can be observed. Also, a good correlation between the occurring times of the maximum displacements can be seen.

Figure 4-18 (c) presents the measure dynamic impact force applied on the wall, as input parameter for the mathematical model. As a result of mathematical modelling, time variations of the forces participating in dynamic equilibrium can be obtained, besides the wall displacement (presented in Figure 4-18 (b)). Therefore it can be observed that until moment 1 of the impact force the main reaction is the inertial force of the system, followed by the static passive earth resistance. The latter mobilizes much "slower", because a wall displacement equal with v_p is needed for a full mobilization of E_{ph}. The system's inertia I_{total} is equal with the sum of the wall's inertia I_W and soil prism's one I_{PR}. The second force can also be defined as the inertial force of the accelerated soil mass of the mobilized prism I_{PR-a}, to which the inertia due to mass variation I_{PR-m} is added. For this example, it can be observed that the system reacts to the impact force mainly by the inertial force due to the increase of the prism mass, which varies from zero to the fully mobilized prism mass, obtained at moment 2. Consequently, at the same moment, the I_{PR-m} term becomes null and the system continues to move due to the inertia of the mass of the mobilized prism I_{PR-a} and of the mobile wall I_W, but decelerated by the E_{ph} force, until moment 3, when the maximum displacement v_d is reached.

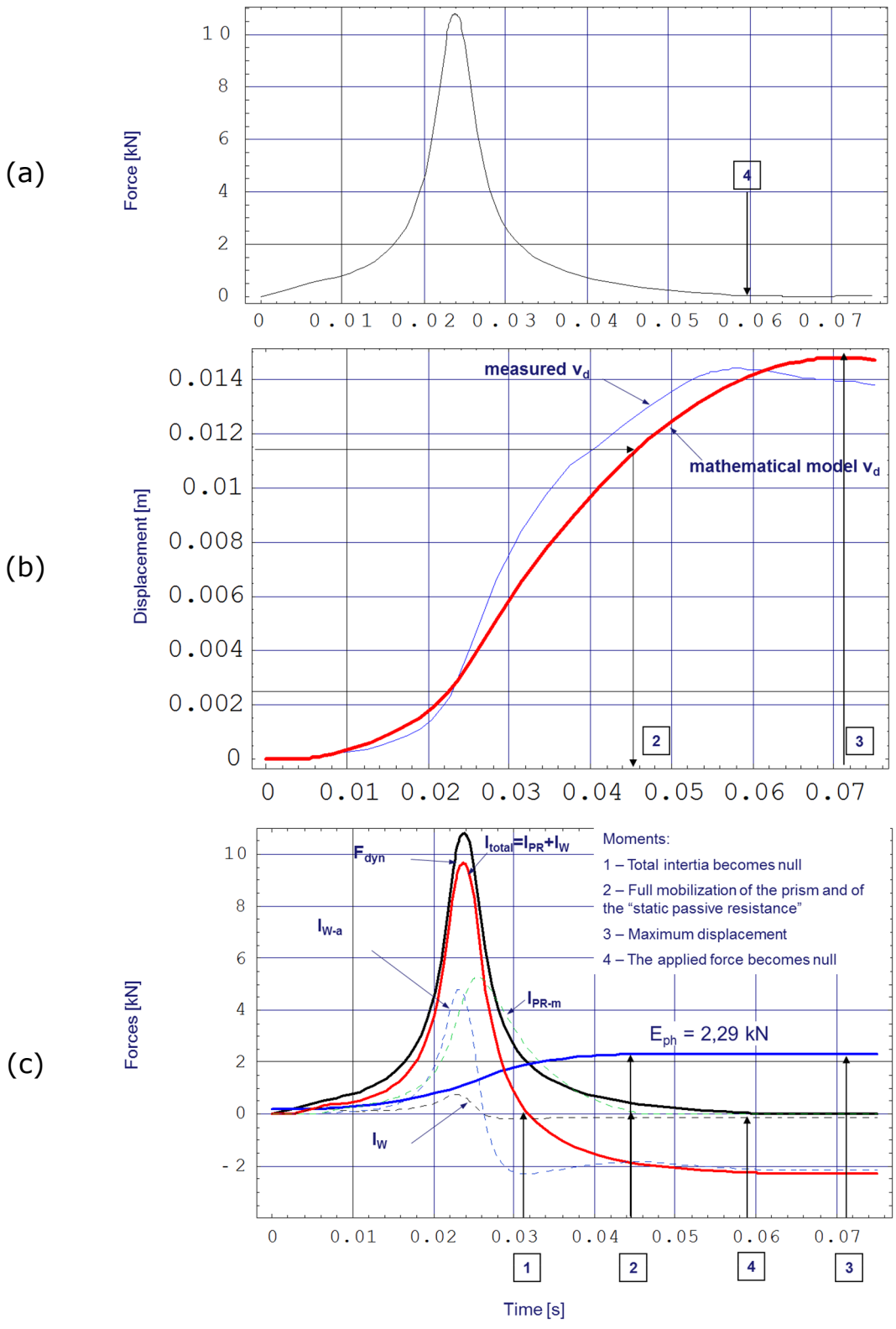

Figure 4-18: The D7 - TS_DynBr_3_24 dynamic test: (a) time variation of the dynamic impact force applied on the mobile wall; (b) the measured (with thin blue line) and calculated (with wide red line) wall displacement; (c) – the forces that participate in the dynamic equilibrium of the wall-soil prism system, as resulted from the mathematical model

Chapter 5. Comparative calculation by Finite Element Method

5.1 General information

In this chapter the finite element method FEM analysis of the physical models is presented. Also, the results obtained by numerical analysis are compared with the ones of the own experimental tests. The applicability of the method for the researched case is studied with geotechnical software based on the finite element method, which is widely use in practice. A nonlinear constitutive law, with stress dependent deformation moduli, was used to model the trial soil.

For the calculation the software package PLAXIS 7.2 Professional Version, developed by the Technical University in Delft to model practical geotechnical problems. The description of the software and the calculation algorithm can be found in the user's manual, Brinkgreve (1998). The use of this software for the studied case, as well as the specific parameters are described hereafter.

Post-calculation of the static tests by FEM was used to calibrate the model and to validate the geotechnical parameters characteristic to the low stress level in reduced scale 1g models. For the static case, the load was gradually applied on the mobile wall until failure occurs by the full mobilization of the passive earth resistance.

After the FEM model was calibrated for the static cases, post-calculation of the dynamic tests was done based on the same simplifying assumptions and boundary conditions. Different shock-type transient loads, recorded during the tests, were applied on the wall.

5.2 Description of the model and boundary conditions

The wall displacement towards the sand body in the physical model leads to predominant strains and stresses along the glazed channel. The channel can be basically considered as stiff, and the sand density index pluviometrically laid can be regarded as homogeneous in every horizontal cross-section of the glazed channel. Based on these facts and considering the relatively small ratio between the side friction and passive resistance (about 10%), a plane strain state was assumed. Therefore the tests were reproduced using a 2D FEM model.

In a simplifying manner, for modelling the tests using the finite element method, the side friction was compensated by increasing the mobile wall-sand interface angle δ.

The dimensions of the FEM 2D model are the ones of a longitudinal cross-section of the reduced scale physical model. The finite element meshed model is presented in Figure 5-1. Triangular elements having 15 nodes and 12 Gauß integration points were used to model the trial sand.

On the right boundary limit, at x = 84 cm and the lower one y = 0 cm, both the horizontal and vertical displacements are set as fixed. The upper boundary of the model, y = 29 cm, is represented by the free surface of the sand, and therefore no displacements are fixed. The left boundary, at x = 0, is composed from two parts. The upper one, for $0 \leq y \leq 5$ cm, being the fixed supporting element at the base of the mobile wall, is supported by a distributed load, represented by the at-rest pressure. This supporting method of the mobile wall is the only one that correctly models the physical support, allowing a horizontal sand displacement under the wall, towards the inner part of the glazed channel, while the wall is moving. The upper part, for $5 \leq y \leq 29$ cm, was modelled as a "L" shaped "BEAM" element, of infinite stiffness. Both sides of the modelled wall have the vertical displacement set as fixed. The supporting conditions of the wall were chosen to assure the same horizontal displacement as in the physical model. The mass of the beam element is the one of the mobile wall, together with the guiding device and stiffening attached beams, calculated for a theoretical wall with a 1 m width. To generate the beam element, its horizontal guiding part needed to also be in contact with the elements composing the trial sand. In order to do this, on the left side of wall, an artificial area was added, with the same properties as the sand, between $-10 \text{ cm} \leq x \leq 0$ and $0 \leq y \leq 29$ cm. This area will be deactivated before the initial stresses are calculated.

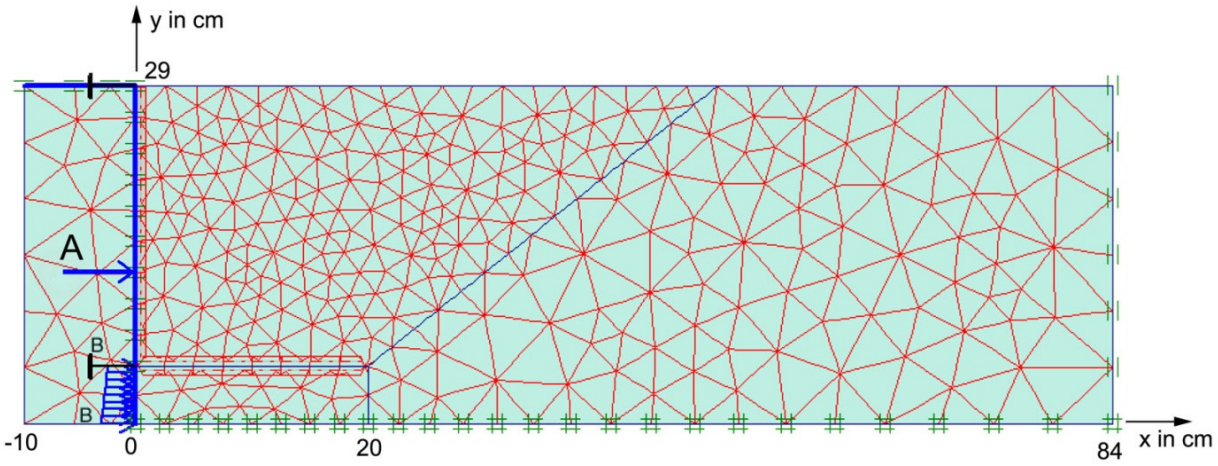

Figure 5-1: Meshed FEM model, with boundary conditions and the applied loads

When the wall displacement start to move towards the sand body, in front of it and at base level, a local shear occurs corresponding with the moment when the failure surface begins to develop. These local strain concentrations lead to inacceptable high deformation gradients of the node grid within the FEM model, right before the passive earth resistance is fully mobilized and the failure surface develops. Pairs of interface elements "Interface" were introduced at the mobile wall base to assure the deformation compatibility of the finite elements. They were horizontally placed on both sides in front of the wall base, on a 20 cm length, selected through trials.

Interface elements allow the paired nodes to slip between one another, in accordance with the shear parameters of the interface. They are proportional with those of the adjacent soil and they are usually affected by a parameter which reduces the shear strength in the interface plane. The $R_{inter} = \frac{tan\varphi_i}{tan\varphi_{soil}} \leq$ 1eter describes the ratio between the friction angle of the contact surface (interface) and the internal friction angle of the soil to whom it comes in contact with. For the present case, R_{inter} is unequivocally considered equal to 1, in order to reproduce the internal friction of the sand. By introducing the predefined fictive failure surface in front of the wall base, neither the mobilization phenomenon of the large deformation gradient domain, nor the failure surface are significantly affected (see Figure 5-2).

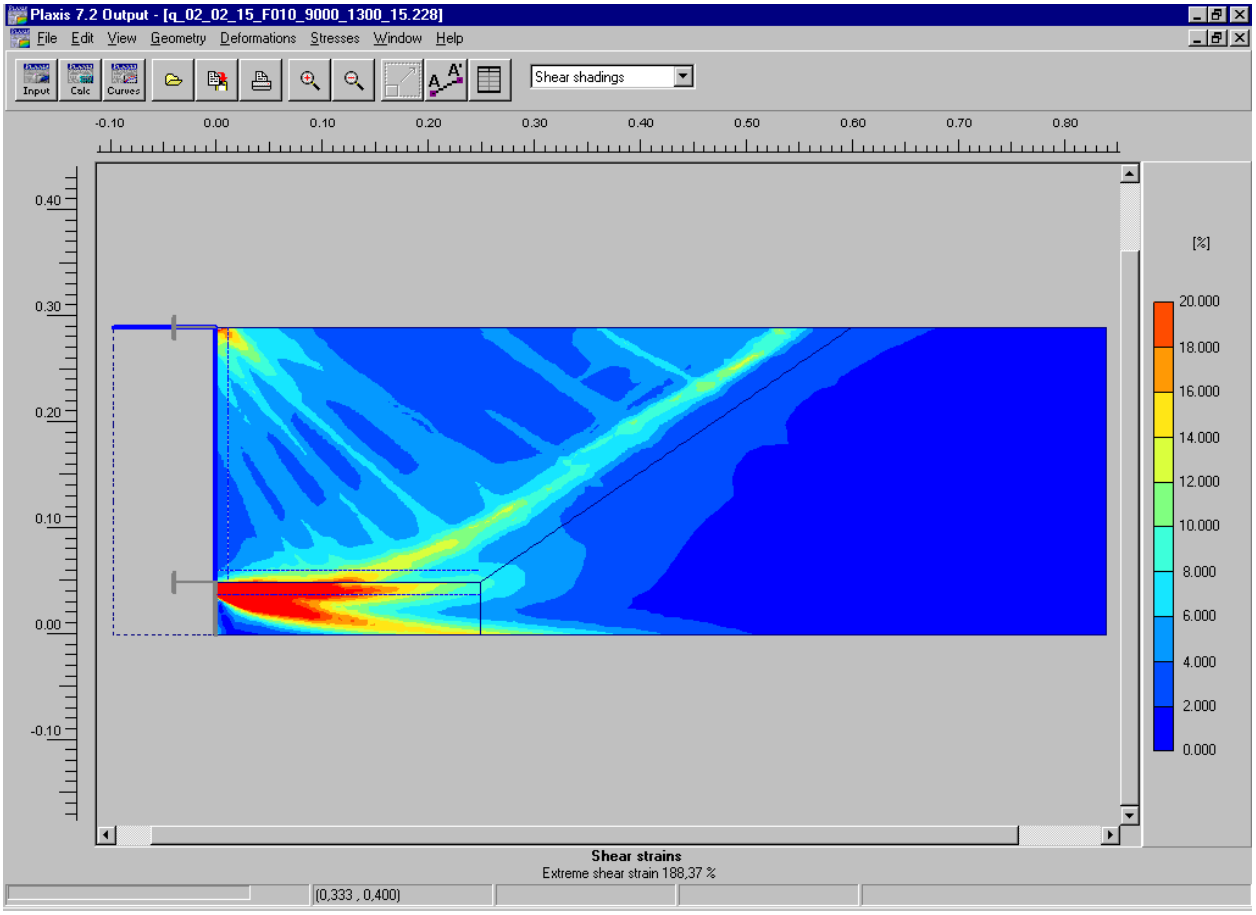

Figure 5-2: Shear deformations at failure in FEM analysis of a static test for a density index D=0.5

15-noded elements were used to model the sand for the FEM analyses and 10-noded elements which have five stress points between the pairs of nodes were used to model the interfaces (see Figure 5-3). Although the contact elements graphically represented with a finite thickness, for a finite element problem the coordinates of a pair of nodes are identical, thus the thickness of interface element being null.

The contact surface of the mobile wall with the sand inside the glazed channel is also modelled using interface elements. A different value $R_{inter} = \frac{\tan\delta}{\tan\varphi_{soil}} \leq 1$ was used to model them for each δ angle value of the different density indexes. The R_{inter} parameter was independently calculated for each sand density index, considering the actual values of the sand friction angle and soil-wall interface friction angle in the physical model. Finally, the values of the R_{inter} parameter were corrected as mentioned before, in order to compensate the side wall friction that occurs during the tests.

By introducing the interface elements described above in the FEM model, the soil elements were able to move vertically along the surface of the mobile wall in strain and stress condition similar with the ones in the physical model. They also allowed sliding at the base of the wall, corresponding with the shearing of the soil at the begging of the failure surface.

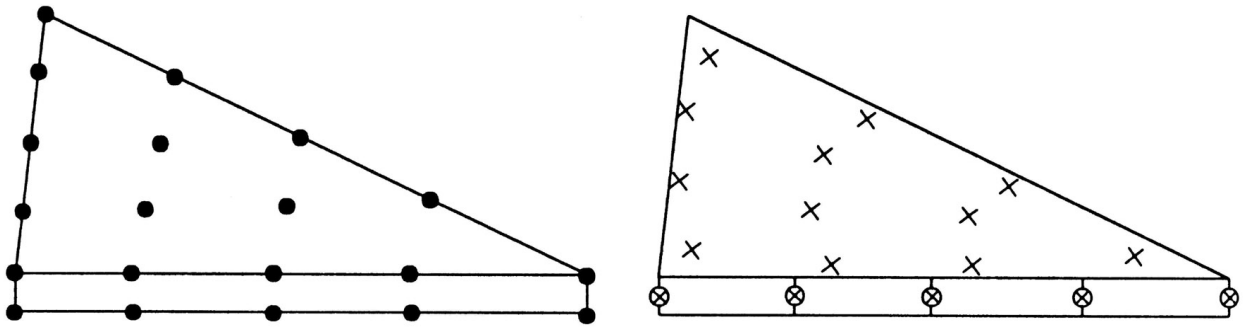

Figure 5-3: Nodes and integration points of the finite elements and of the interface elements used

A finer mesh was used for the areas were high plastic strains occur during the mobilization of the passive earth resistance. The automatic redistribution of the finite element network during the computing process in areas where high deformation gradients of the model's geometry occurred "updated mesh analysis", could not be used for modelling because it was not available for the dynamic calculation module of the Plaxis software. Using the same mesh size for the static and dynamic cases, a comparison of the results based on the same modelling conditions could be done.

Since during the mobilization of the passive earth resistance substantial changes in the stress state of the soil take place, the „Hardening-Soil" HS constitutive law was used to model the soil behaviour. It continuously adapts the soil deformation moduli to the local stress level. The HS constitutive model uses three deformation moduli, being able to make the difference between the modulus for deviatoric loads $\mathrm{E}_{50}^{\mathrm{ref}}$, the one for isotropic loads $\mathrm{E}_{\mathrm{oed}}^{\mathrm{ref}}$, and the one attributed to unloading $\mathrm{E}_{\mathrm{ur}}^{\mathrm{ref}}$. The deformation moduli used by the HS model are defined as a hyperbolic dependency on the stress level, and for a cohesionless soil $(\mathrm{c} = 0)$ and drained $(\sigma = \sigma')$ they are defined as:

$$E = E^{ref} \left(\frac{\sigma}{p^{ref}} \right)^{m} \tag{5-1}$$

In the equation above, $\mathrm{p}^{\mathrm{ref}}$ is the reference pressure for $\mathrm{E}^{\mathrm{ref}}$ and m is the exponent defining the hyperbolic strain-stress dependency.

Besides the three deformation moduli, the HS model needs another nine parameters: unit weight γ, Poisson's coefficient ν_{ur}, sand friction angle φ, cohesion c, dilatancy angle ψ, m exponent, reference pressure p^{ref}, at-rest pressure coefficient for normally consolidated soils K_0^{nc} and the failure ratio R_f. More information on the HS model and the needed input parameters for PLAXIS software are provided by Brinkgreve (1998).

For the present research, the passive resistance mobilization of a non-cohesive drained soil under both static and dynamic shock-type loads, the primary deviatoric load is predominant, so the φ, E_{50}^{ref}, γ and m exponent have the most influence.

5.3 FEM modelling of the static loads

FEM models of the static loads were used to calibrate both the model and the input parameters for the dynamic case. Based on these, the model conditions and the geotechnical parameters for the reduced confining pressures (specific to 1g scale models) were checked.

The static force was applied gradually at the base of the mobile wall, until the passive resistance was fully mobilized.

The average stress level in 1g reduced-scale models has a lower magnitude than in current practical geotechnical problems of engineering practice. The value of reference pressure for which parameters values recommended by PLAXIS manuals and technical literature is $p^{ref} = 100 \frac{kN}{m^2}$, compared with the low pressures developed with the own physical model of about $10 \frac{kN}{m^2}$.

For the used trial sand, named „Karlsruher Sand", different authors, as Bauer (1992 and 1995) and Herten (1999), published compressibility test results, obtain by oedometer and triaxial tests. The laboratory tests were conducted for a significantly higher stress level than the ones in the 1g reduced scale models. In most cases, the density indexes investigated by the authors mentioned above were reconstructed by vibrating the samples, whereas for the present tests the sand was laid pluviometrically. Vermeer and Schanz (1997), also studied the dependency of the deformation moduli on the confining pressure, for real pressure domains based on the tests performed by other authors.

The deformation moduli determined by Herten (1999) for $\mathrm{p}^{\mathrm{ref}} = 100\,\frac{\mathrm{kN}}{\mathrm{m}^2}$ were recalculated by the author for a reference confining pressure $\mathrm{p}^{\mathrm{ref}} = 10\,\frac{\mathrm{kN}}{\mathrm{m}^2}$, based on the (5-1) equation. The obtained values, listed in Table **5-1**, were used to model the static passive resistance mobilization in FEM models. The wall displacement values obtained for the full passive resistance mobilization were significantly below the measured ones, proving that the considered deformation moduli were too high.

The deformation moduli values were reduced by up to 50%, but maintaining their same ratio $E_{oed}^{ref}/E_{ref}^{50} = 1{,}5$ and $E_{ur}^{ref}/E_{oed}^{ref} = 3{,}3 \div 4{,}3$, thus obtaining a good overlap between the calculated and measured passive resistance mobilization curves. In a similar manner, the soil-wall interface friction angle was artificially increased, to compensate for the side friction in the glazed channel. By doing so, a good overlap between the measured and calculated passive resistance mobilization curve was obtained (Figure 5-4). The comparison was done for h=24 cm and b=32 cm and three density indexes of the trial sand. The density index $D = 0{,}9$ was obtained for a free-falling height of 100 cm, for $D = 0{,}7$ 55 cm and $D = 0{,}5$ for 45 cm.

The stiffness moduli and soil-wall interface friction angle, calibrated based on the static passive resistance mobilization obtained on physical models are presented in Table 5-1. They were also used to model the dynamic tests of passive resistance mobilization under shock-type loads. All the parameters used for the finite element models of the passive resistance mobilization tests are presented in Table 5-1 for the three reference density indexes of the trial sand.

Table 5-1. Model and geotechnical parameters used for the comparative analysis of the 1g reduced scale models

Parameters	**Density index**			**Measuring Unit**
	D = 0.5	*D* = 0.7	*D* = 0.9	
Specific weight γ	15.6	16.1	16.6	kN/m^3
Secant stiffness modulus E_{ref}^{50}	800	2000	6000	kN/m^2
Tangent stiffness modulus E_{oed}^{ref}	1200	3000	9000	kN/m^2
Unloading / reloading stiffness modulus E_{ur}^{ref}	3300	8000	20000	kN/m^2

Parameters	Density index			Measuring Unit
	D = 0.5	D = 0.7	D = 0.9	
Friction angle φ	40.5	43.8	47.5	°
Sand-wall interface friction angle δ	22	25	29.3	°
Cohesion c	0.01	0.01	0.01	kN/m^2
Dilatancy angle ψ	10.5	13.8	17.5	°
Poisson's ratio ν_{ur}	0.2	0.2	0.2	—
Exponent m	0.7	0.7	0.7	—
Reference confining pressure p^{ref}	10	10	10	kN/m^2
At-rest earth pressure coefficient K_0^{nc}	0.58	0.54	0.48	—
Failure ratio R_f	0.9	0.9	0.9	—

The dilatancy angle was determined as Brinkgreve (1998) recommends:

$$\psi = \varphi - 30^{\circ} \tag{5-2}$$

The values for the Poisson's ratio ν_{ur} and the failure ratio R_f recommended by Brinkgreve (1998) are considered acceptable.

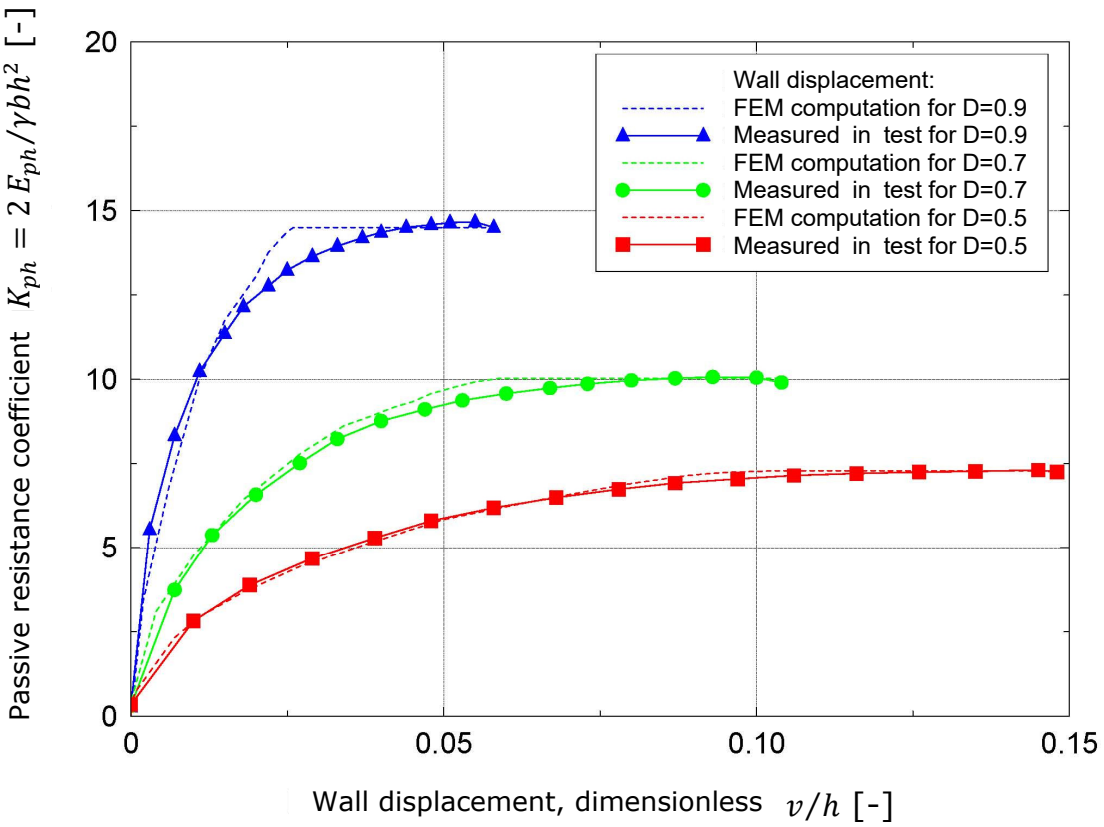

Figure 5-4: Comparison between the measured and FEM calculated static earth pressure mobilization for three density indexes

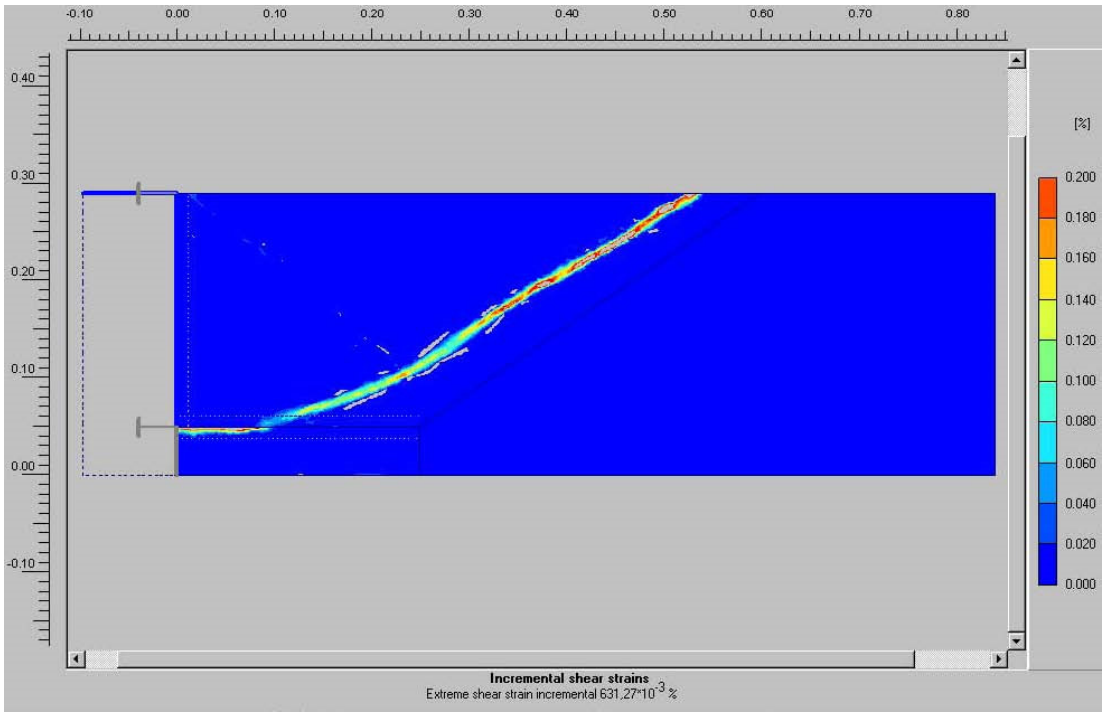

Figure 5-5: Incremental shear strain for full passive earth resistance mobilization for a static load in FEM models and a *D*=0,5 density index

5.4 FEM modelling of the dynamic loads

For the FEM models of the dynamic loads, the impact force on the mobile wall was applied, as it was measured during dynamic tests for each different density index (see Figure 4-16).

Therefore three representative test models were selected, numbered 1, 2 and 3 in the dynamic test list. The tests were conducted for a 32 cm width of the glazed channel and a 24 cm sand fill above the base of the wall. The impact force was applied with the pendulum, which had a total mass of 12.76 kg, including the handle and the impact cap. The same impact cap and free-falling height (80 cm) were used for the three tests and the pendulum was released from horizontal position.

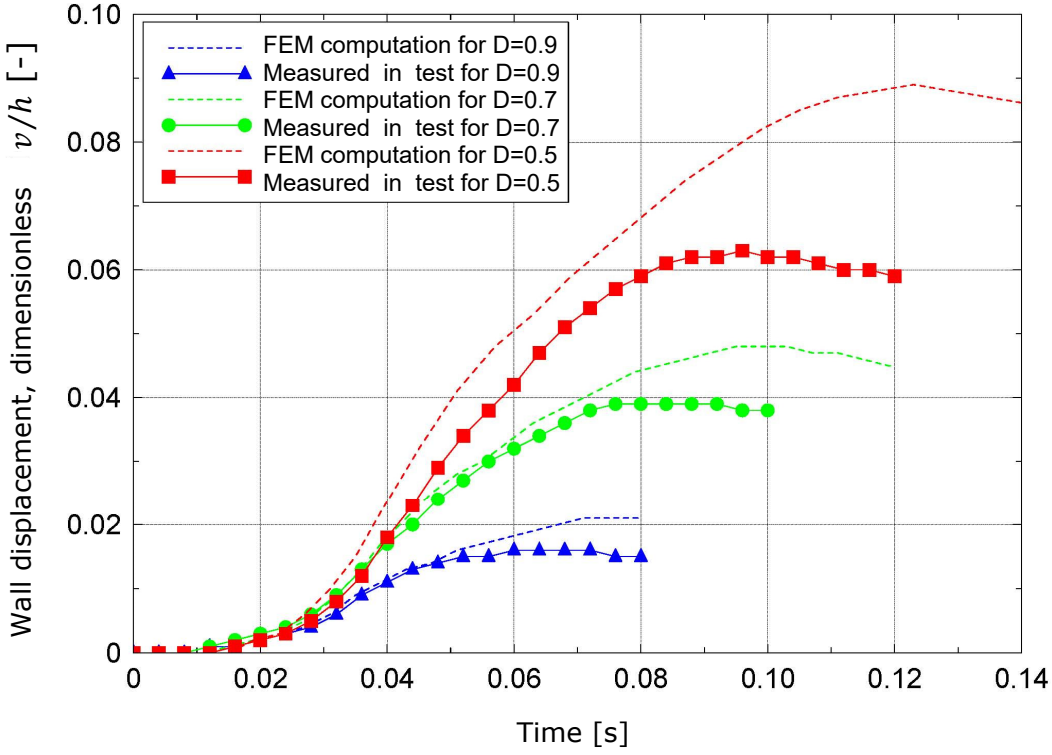

Figure 5-6: Comparison between the measured and FEM calculated wall displacement, for three density indexes

The calculated FEM wall displacements are constantly with 20% up to 40% higher than the measured ones for the three chosen density indexes, as can be observed in Figure 5-6. Also, the time when they occur exceeds the measured one.

5.5 Conclusions of the finite element method analysis

FEM models can also represent a practical method to resolve engineering problems in soil dynamics where plastic strains also occur, due to the increase in computing power and development of specialized software. Besides choosing appropriate constitutive laws and defining appropriate boundary conditions, the most important condition consists of introducing the input parameters, which must be correctly defined and validated by comparing the results with the ones obtained on physical models.

Assuming that for a dry sand, thus drained, the geotechnical parameters are considered independent from the shearing speed Wu (1992), Bauer (1992) and Zambelli (2006), the parameters validated on the static model were used for the dynamic one too. Therefore, FEM models of the static loads were used to calibrate both the model and its parameters for the dynamic case.

The displacement obtained by FEM modelling are constantly 20% to 40% above the ones measured directly on physical models, for the three chosen density indexes, using the boundary conditions valid for reduced scale physical models. FEM modelling of dynamic tests offered a safe approximation of the passive resistance mobilization under dynamic shock-type loads, in terms of displacement.

The analysis performed had the purpose to qualitatively validated the applicability of the finite element method to calculate the passive pressure under shock-type loads. The obtained results confirm the adequacy of the method.

The following research possibilities in using FEM to model the physical tests of passive earth resistance are revealed:

- the use of 3D FEM models to introduce adequate side friction between the trial sand and the glazed channel;
- consideration of damping and shear and compressibility parameters dependency on the load speed;
- consideration of validated boundary conditions for the application of a dynamic transient shock-type load;
- comparison of the obtained results using different constitutive laws;
- application of FEM models to calculate full-scale situations and comparison of the results with those obtained using the mathematical models developed in this paper.

Chapter 6. Application of the mathematical model to full-scale structures

6.1 Application of the static model

Starting from an elementary wall, with unit width and height, one obtains:

$$E_{ph} = K_{ph} \tag{6-1}$$

The specific weights of the soil are $\gamma_{max} = 20\ kN/m^3$ and $\gamma_{min} = 15\ kN/m^3$ and the shear strength parameters are $\varphi = 30°$, $\varphi = 35°$ and $\varphi = 40°$ for the three reference density indexes D = 0.5, D = 0.7 and D = 0.9. The sand-wall friction angle is $\delta = 2/3 \cdot \varphi$.

By comparing the graphs in Figure 6-1 a good correlation of the static passive earth resistance can be observed for all the three density indexes. This justifies the use of the mathematical model developed by the author for full-scale structures using the v_p/h ratio in accordance with the recommendations of the German standard DIN 4085:2011.

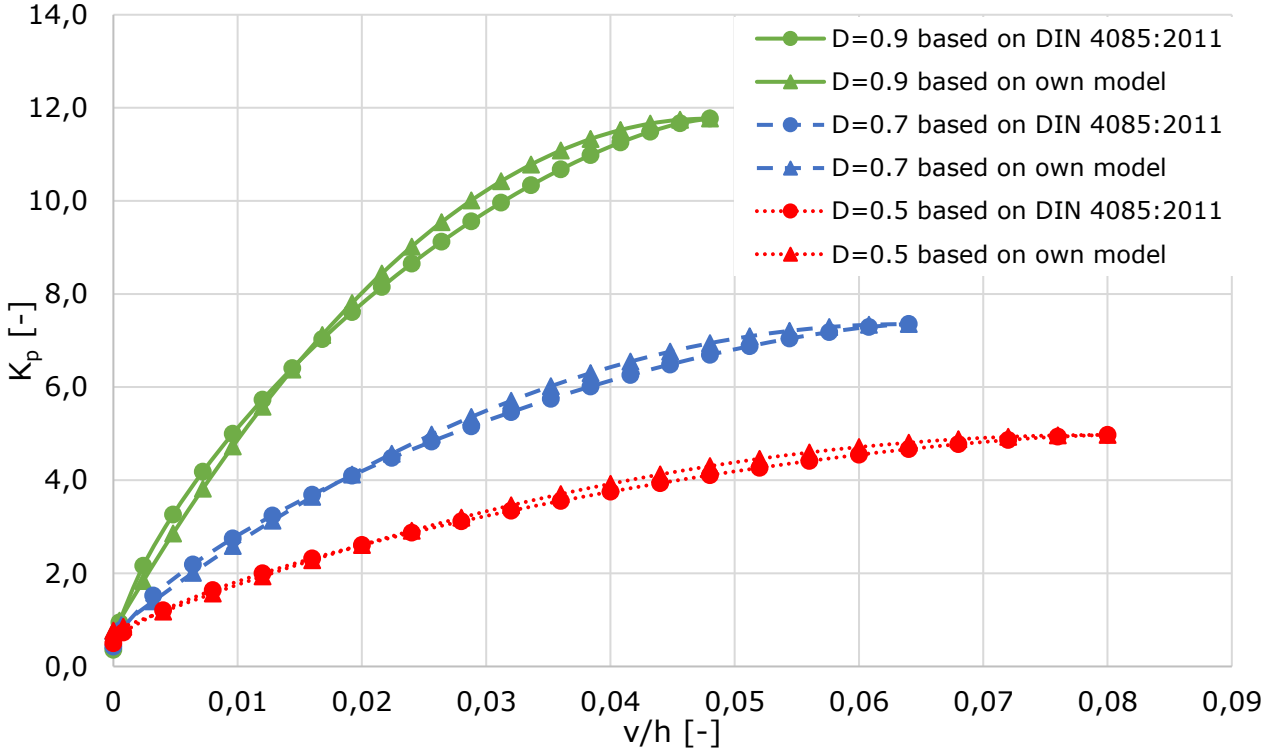

Figure 6-1: Comparison between the passive resistance mobilization for full-scale structures obtained with the own mathematical model and with DIN 4085:2011

6.2 Actions due to impact

The basic principles and combinations applied in design for the identified accidental actions are defined in SR EN 1990:2004 Basics of structural design. Partial safety factors applied for accidental design load cases are defined as 1.0 for all type loads (permanent, transitory and accidental).

The combination of accidental load cases involves either explicit accidental actions or may refer to an event after an accidental event. Usually, after an accidental event the structure will not have the necessary resistance in permanent or transient load cases and will need to be reinforced for a possible continued use. For temporary structures an ease of the requirements might be reasonable, for example by adopting a shorter recurrence period in a structural seismic analysis after an accidental event.

In SR EN 1991-1-7:2007, section 4 – Impact, the field of application of the accidental actions due to impact for different events is defined. The vehicles which may induce horizontal actions due to impact, relevant for the passive earth pressure mobilization on various structures, are:

- motor vehicles;
- fork lifts trucks;
- rolling stock;
- maritime and fluvial ships.

The accidental actions relevant for the present research will be presented below and the interaction with the structures according to the standard mentioned above. It states the strategies for the accidental load case based on the three classes of importance defined in SR EN 1990:2004:

- for the importance class CC1, which provides reduced effects of the failure, no special attention is necessary for the accidental load case provided that the regulations regarding resistance and stability, which are indicated in the Eurocodes (SR EN 1990:2004 to SR EN 1999:2007) are met;
- for the importance class CC2, which provides medium effects of the failure, depending on the specific circumstances of the structure, a simplified analysis may be adopted using equivalent static models or prescriptive design rules may be applied;
- for the importance class CC3, which provides major effects of the failure, a closer view on each load case is needed, to determine the safety level and the level of structural analysis required. This may need

a risk analysis and the use of more refined methods such a dynamic analysis, non – linear models and structure-action interaction.

The relevant loads due to impact that might be considered for the mobilization of the passive earth resistance, are for the retaining structures near a road or a railway. For bridges, impact loads and mitigation measures are considered based on the traffic type on the bridge and under it.

SR EN 1997-1:2004, Section 9 – Retaining structures, Chapter 9.3.1.7 states that for determining the design value of the collision forces, for example waves, ice or traffic, the energy absorbed by the impacting mass and by the supporting system, through dampers and/or guiding systems may be considered. The norm recommends that for lateral impacts on retaining walls, the increased stiffness exhibited by the retained ground should be considered, without mentioning any methods for determining it.

The standard DIN 1054 (2005) Ground – Verification of the safety of earthworks and foundations states that impact should be considered in designing foundations only if they are directly subjected to it. The standard also mentions that for horizontal forces due to impact on piles, the soil reaction magnitude can be above or below its static resistance during impact or pile movement. As an approximation, the new standard allows the use of the static subgrade reaction coefficient for dynamic actions, unlike the older standard DIN 4014 (1990) Bohrpfähle – Herstellung, Bemessung und Tragverhalten, which was more permissive and allowed the use of up to three times higher values in case of impact.

The force developed at the impacting object-structure interface depends on their interaction, is time dependent and is named dynamic force (see Figure 6-2). The main variables of the impact are the impact velocity of the impacting object and the mass distribution, deformation characteristics of both the impacting object and the structure.

For structural design purposes the actions due to impact may be determined by a dynamic analysis or it may be represented by an equivalent static force giving the equivalent action effects in the structure, named structure’s reaction. This simplified model may be used for the verification of static equilibrium, for strength verifications or for determining the impacted structure deformations.

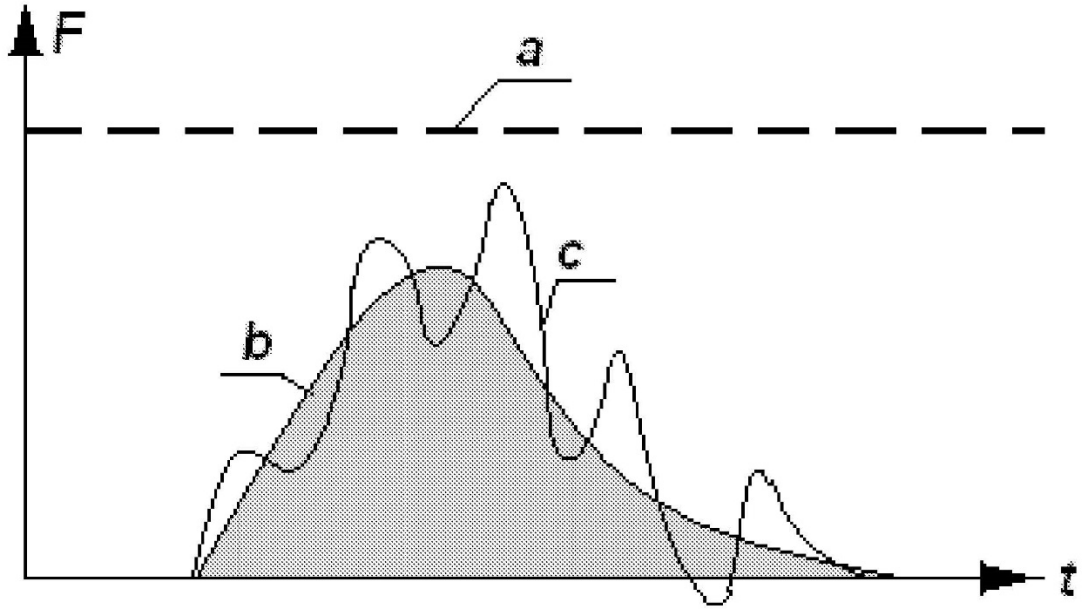

Figure 6-2: Schematic representation of the dynamic impact force (b), static equivalent force (a) and structure's dynamic response (c), (figure taken from SR EN 1991-1-7:2007)

For structures which are designed to absorb impact energy by elastic-plastic deformations of members, a soft impact results and the equivalent static loads may be determined by considering both plastic strength and deformation capacity of such elements.

By considering that the energy is entirely absorbed by the impacting object, safe impact forces result. For this ideal case, named hard impact, the dynamic or equivalent static forces may be determined from chapters 4.3 to 4.7 of the previously mentioned standard. A selective presentation of the actions due to impact of vehicles with structures able to mobilize the passive earth pressure under shock-type loads is done.

6.3 Basis of impact dynamic analysis

Collision mechanics is a complex interaction phenomenon between a moving body and a stationary structure. The kinetic energy of the impacting object is transformed by collision in elastic-plastic deformation energy or local failure in both the object and impacted structure. The other types of energy developed during collision are neglected in a simplifying manner. Small changes of position and impact angle may lead to substantial changes of the impact effect. These traits will not be described in this paper, and in a simplifying

manner the analysis will focus on the basic case, when the impacted object collides with the structure at a 90-degree angle.

In order to determine the interaction force, which is developed at the impacting object-structure interface, they need to be treated as an integrated system.

Starting from the simplifying hypothesis that the structure is rigid and immobile and the impacting object can be modelled as an elastic pendulum with one degree of freedom (see Figure 6-3 (a)), the maximum interaction force can be obtained:

$$F = v_r\sqrt{k \cdot m} \tag{6-2}$$

where,

v_r – object velocity at impact;

k – equivalent elastic stiffness of the object;

m – mass of the colliding object.

This result is obtained from the transformation equation of the impacting object kinetic energy $m \cdot {v_r}^2/2$ in work of displacing force F, which travels the distance u until maximum compression of the spring after which it does the same work to accelerate the mass to the same speed v_r but opposite direction:

$$F \cdot u/2 = F^2/2\,k \tag{6-3}$$

Therefore, the total duration of the impact force can be obtained:

$$t = \pi\sqrt{m/k} \tag{6-4}$$

Figure 6-3 (b) presents the characteristics of an ideal elastic-plastic pendulum, which has an elastic behaviour until the maximum deformation is reached, then the force instantly drops to zero, according to an ideal plastic behaviour. Applying the same reasoning as the one mentioned above, the same maximum value of the impact force is obtained as for the ideal elastic pendulum, but the duration of the impact force halves, as well as the impulse transmitted to the structure.

An alternative model of the impacting object is as an equivalent rod of uniform cross-section (see Figure 6-3 (c)). Considering the mass density of the

rod ρ, the modulus of elasticity E, the cross-sectional area A and the length L, the interaction force can be written as:

$$F = Z \cdot v_r \tag{6-5}$$

where,

$Z = EA/c$ – mechanical impedance of the rod;

$c = \sqrt{E/\rho}$ – compression wave velocity in the rod.

Substituting Z and c we obtain:

$$F = v_r \cdot A\sqrt{E \cdot \rho} \tag{6-6}$$

Considering $k = EA/l$ and $m = \rho AL$ equation (6-2) is obtained again. Therefore, one can notice that the maximum obtained force is the same for the elastic pendulum with one degree of freedom, as well as for the elastic rod. The difference consists of the time variation of the force. The results of the three models are presented in Figure 6-3.

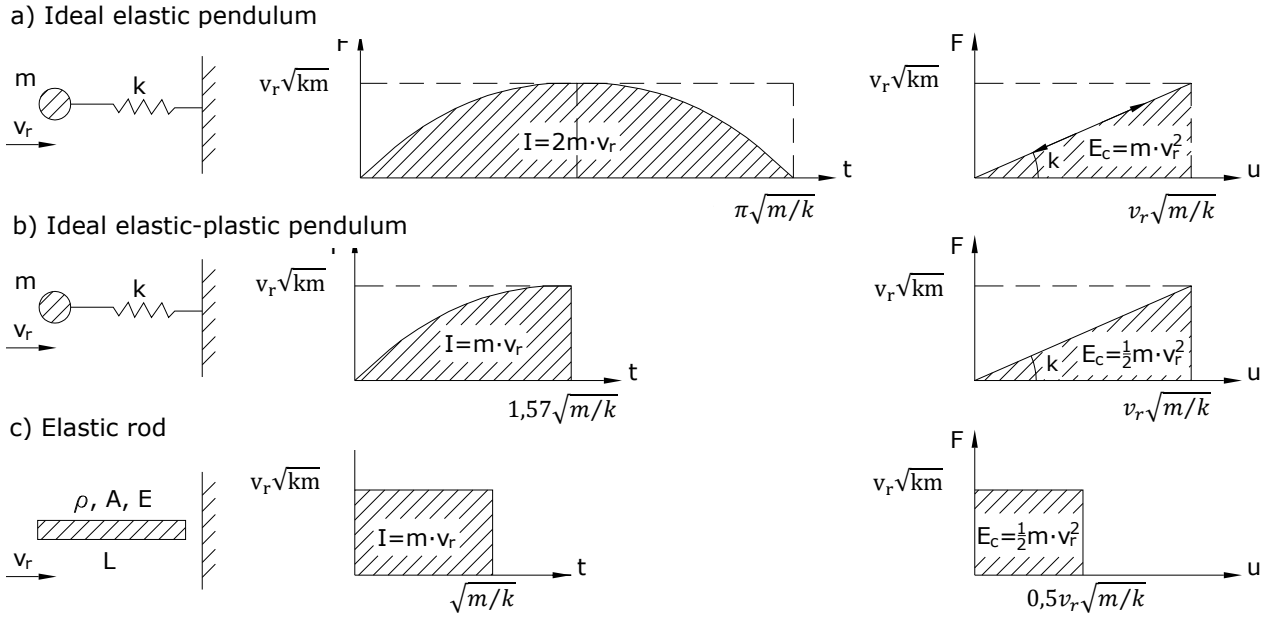

Figure 6-3: Ideal elastic pendulum (a), ideal elastic-plastic pendulum (b) and elastic rod of uniform cross-section (c)

In reality the impacting object does not have a perfectly elastic behaviour. The value of the impact force dependent on the deformation can be assimilated by a linear ascending function (see Figure 6-4), with a limit value.

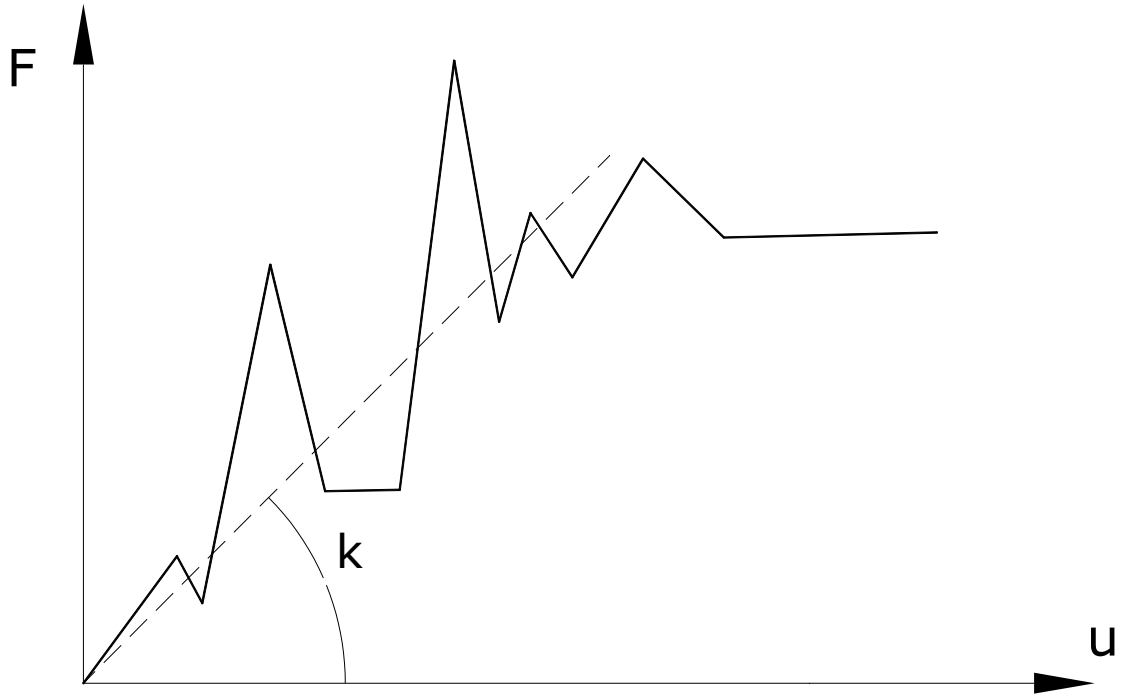

Figure 6-4: Force-displacement diagram of a colliding object

Therefore, by using equation (6-2) useful approximations can be obtained. It must be noted that the impact force decreases after it reaches its maximum, in a much steeper manner than it increases. This has an important effect on the evolution of the force in time. Considering a 100% plastic deformation, an infinite stiffness of the decreasing impact force is obtained. For the pendulum model, it means that for a maximum force, the spring's stiffness becomes infinite, and the interaction force instantly drops to zero. Therefore, the total duration of the impact force can be obtained:

$$t = \frac{\pi}{2}\sqrt{m/k} = 1{,}57\sqrt{m/k} \tag{6-7}$$

For the rod model, the impact force reaches its maximum when the compression wave gets at the opposite end of the rod. An infinite velocity corresponds to the reflected wave. Therefore, the total duration of the impact force can be obtained:

$$t = L/c = L\sqrt{\rho/E} = \sqrt{m/k} \tag{6-8}$$

In both cases the impulse-momentum theorem for the impacting object is verified:

$$\int F dt = m \cdot v_r \tag{6-9}$$

Equation (6-2) gives the maximum force value on the outer surface of the structure. Inside the structure these forces may rise dynamic effects. An upper limit value is obtained if the load is conceived as a step function. In that case the dynamic amplification factor is maximal and equal with 2.0. If the pulse nature of the load is considered, reduced amplification factors can be obtained, which are dependent on the duration of the pulse. For this case, Vrouwenvelder (2005) proposes dynamic amplification factors ranging from 1.0 up to 1.4. SR EN 1991-1-7:2007 extends the range for the dynamic amplification factors φ_{dyn} from below 1.0 up to 1.8 depending on the dynamic characteristics of the structure and the object. The same standard recommends to use a direct dynamic analysis to determine the dynamic amplification factor, using the loads specified in Annex C, resumed in Table 6-1.

Table 6-1. Design values for mass, velocity and collision force F_0 of vehicles (taken from Table C.2 Annex C, SR EN 1991-1-7:2007)

Type of road	Mass m [kg]	Velocity v_0 [km/h]	Deceleration A [m/s^2]	Collision force ($v_r = v_0$) F_0 [kN]
Motorway	30.000	90	3	2.400
Urban area	30.000	50	3	1.300
Courtyards				
-cars only	1.500	20	3	120
-all vehicles	30.000	15	3	500
Parking garages				
-cars only	1.500	10	3	60

It is important to mention that the limit value of the dynamic amplification stated above is only valid for an impact force that does not exceed the linear elastic behaviour of the structure. The behaviour of the retaining structures subjected to impact loads is mainly governed by the mobilization of the passive earth resistance in the retained soil body. Therefore, and by analogy with the static passive earth resistance, the behaviour of the retaining structures subjected to dynamic shock-type loads is expected to be highly non-linear.

In this chapter the structure was considered infinitely rigid up until this paragraph. This assumption leads to safe approximations of the impact force. Another safe value can be obtained by assuming that the entire kinetic energy is absorbed by the structure.

If the structure has an ideal elastic behaviour, the interaction force has the following form:

$$\frac{1}{2}mv_r{}^2 = \frac{1}{2}\frac{F^2}{k} \tag{6-10}$$

where k is the stiffness of the structure.

In case of rigid-plastic response of the structure, the maximum displacement can be obtained from:

$$\frac{1}{2}mv_r{}^2 = F_{cs}u_f \tag{6-11}$$

where

F_{cs} – plastic strength of the structure;

u_f – plastic deformation of the structure after failure.

In the limit case of ideal plastic behaviour, failure occurs if u_f exceeds the deformation capacity of the structure. Both equations ((6-10) and (6-11)) have the disadvantage that the impact force depends on the structure's properties. For this reason, they will not be used in this paper.

Vrouwenvelder (2005) and ENV 1991-1-7 (2005) verify and confirm the applicability of equation (6-2), as well as the equivalent stiffness of motor vehicles, defined in SR EN 1991-1-7:2007 as a constant value $k = 300\ kN/m$, based on the tests performed by Popp (1961), Chiapella and Costello (1981), and also based on the unpublished and later initiated tests of the British High Way Agency. It can be noticed that surprisingly, the equivalent stiffness has the same value for both cars and trucks.

The collision of a motor vehicle with a retaining wall is considered to be like the behaviour of an elastic pendulum until the maximum deformation is obtained, then the behaviour is plastic. The spring stiffness for the elastic state, corresponding to the increase in deformation, is $k = 300\ kN/m$, and for the plastic state it becomes $k \to \infty$.

The natural period of the elastic pendulum is:

$$T = 2\pi\sqrt{m/k} \tag{6-12}$$

6.4 Limit state displacements in both static and dynamic cases

Since a comparison between the dynamic and static analyses is intended, the following measures and limit states are defined:

- **"static displacement v_s"** is the structure's displacement calculated by static analysis. In this case the magnitude of the collision force is applied as a static force which horizontally pushes the retaining wall;
- the structure is **"static stable"** when its displacement is $v_s \leq v_{p,75} \cong 50\%\, v_p$. According to equation (3-22), the passive earth resistance is 75% mobilized for $v_{p,75} \cong 50\%\, v_p$. $E_p(v_{p,75}) = 0{,}75 \cdot E_p = E_{ph,75}$ can be written;
- the structure is **"static unstable"** for displacements $v_s > v_{p,75} \cong 50\%\, v_p$;
- the structure is **"dynamic stable"** when its maximum displacement v_d, obtained with a dynamic analysis, is lower than an admissible value. The admissible displacement can be individually established for each design situation depending on the consequences. A higher displacement can be admitted for collision in contrast with the static case for two reasons: the dynamic force stops after the maximum structure displacement occurred and collision is an accidental action after which some damages can be considered; for directly comparing the dynamic and static stability, the same admissible condition $v_{p,75} \cong 50\%\, v_p$ was chosen for the dynamic case. Consequently, a structure is **"dynamic stable"** if it meets the condition $v_d \leq v_{p,75} \cong 50\%\, v_p$;
- the structure is **"dynamic unstable"** when its maximum displacement v_d exceeds the admissible value. This is equivalent with stating that for $v_d > v_{p,75}$ the structure is dynamic unstable.

The weight of the passive soil prism, which is mobilized for the displacement $v_{p,75} \cong 50\%\, v_p$ results using the equation (4-1) and is written as G_{75}.

In analogy to the natural period of the elastic pendulum, $T = 2\pi\sqrt{m/k}$, the natural period of the above defined dynamic system may be written $T_{75} = 2\pi\sqrt{m_{75}/k_{75}} = 2\pi\sqrt{G_{75} \cdot v_{p,75}/g \cdot E_{ph,75}}$.

6.5 Collision of a motor vehicle with a retaining wall

The input values for an impact vehicle are taken from Table 6-1 as follows:

- Vehicle mass $m = 30.000\ kg$
- Vehicle velocity at impact $v_r = 90\,\frac{km}{h}$

The retaining wall is considered to have the following characteristics:

- Height $h = 3\,m$
- Width $b = 3{,}2\,m$
- Thickness $d = 0{,}5\,m$
- Specific weight $\gamma = 25\frac{kN}{m^3}$
- Soil-wall interface friction angle $\delta = {}^{2}/_{3}\,\varphi$

A plane strain state and a non-cohesive soil backfill behind the wall with a horizontal level are considered:

- Specific weight $\gamma = 20\frac{kN}{m^3}$
- Internal friction angle $\varphi = 30°$
- Density index $D = 1$
- Displacement to reach the passive resistance ${}^{v_p}/_{h} = 0{,}12 - 0{,}08D = 0{,}04$

By introducing the above values in equation (6-2) $F = v_r\sqrt{k \cdot m}$ is found to be $F = 2{,}4\,MN$, which coincides with the one in Table 6-1.

By introducing the above values in equation (6-7) $t = \frac{\pi}{2}\sqrt{m/k}$ becomes $t = 0{,}497\,s$.

Table 6-2. Progression of the impact force, for the case of an ideal elastic-plastic collision of a vehicle with a stiff structure

t [s]	*0*	*0,0497*	*0,0994*	*0,1491*	*0,1988*	*0,2485*	*0,2982*	*0,3479*	*0,3976*	*0,4473*	*0,497*
F_{dyn} [kN]	*0*	*375*	*742*	*1090*	*1411*	*1697*	*1942*	*2138*	*2283*	*2370*	*2400*

The above defined dynamic force will be referred to as "normal impact" from now on.

By introducing the above values in equation (6-7) $t = \frac{\pi}{2}\sqrt{m/k}$ becomes $t = 0{,}497\,s$.

6.5.1 Determining the maximum displacement after impact

By applying the maximum value of the impact force as a static equivalent one, $F_s = 2{,}4\,MN$, one obtains $v_s > v_p \geq v_{p,75} = 0{,}055\,m$. This means that the wall is "static unstable".

By applying the "normal impact", presented in Table 6-2 and represented in Figure 6-4, on the above-defined retaining wall, the wall displacement-time curve is obtained, which is represented in Figure 6-6. It presents the maximum displacement $v_d = 0{,}273\,m > v_{p,75} = 0{,}055\,m$, occurring after $t = 0{,}619\,s$ from starting the impact. It can be observed that the maximum displacement occurs

long after the maximum force at $t = 0{,}497$ s. This is due to inertial forces which delay the acceleration of the wall-soil mass system.

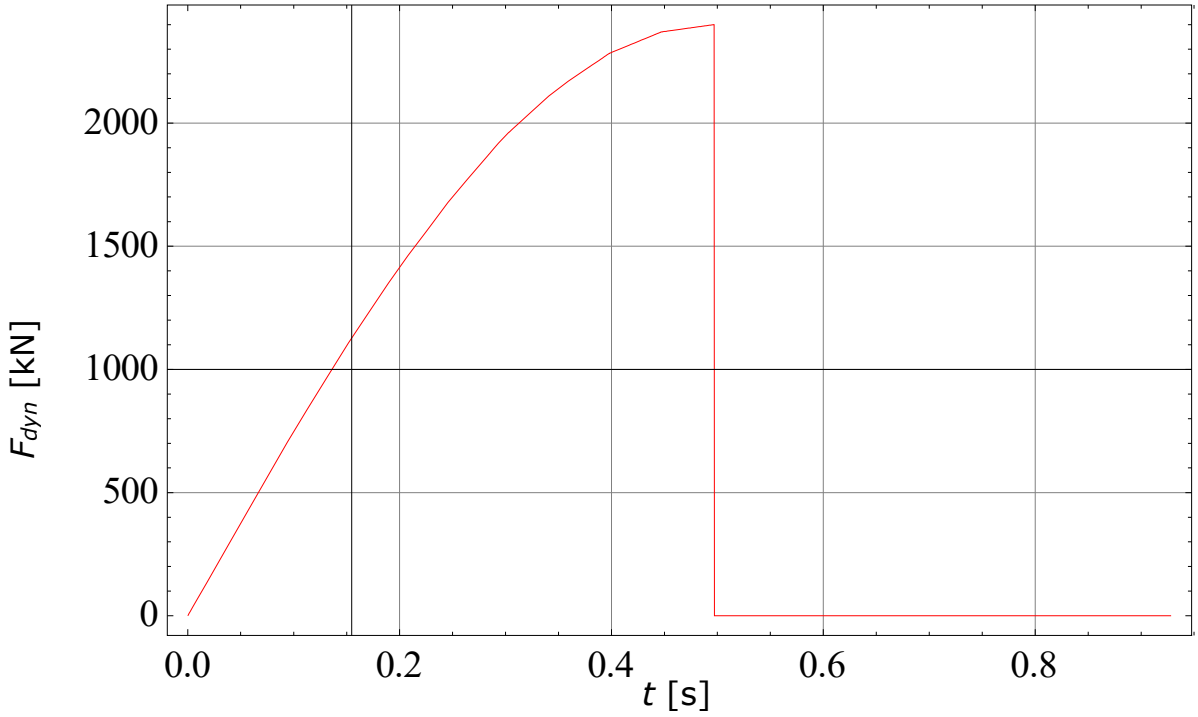

Figure 6-5: Dynamic shock-type force – "normal impact" – applied by a motor vehicle with a 30 t mass and a 90 km/h velocity on a rigid retaining structure

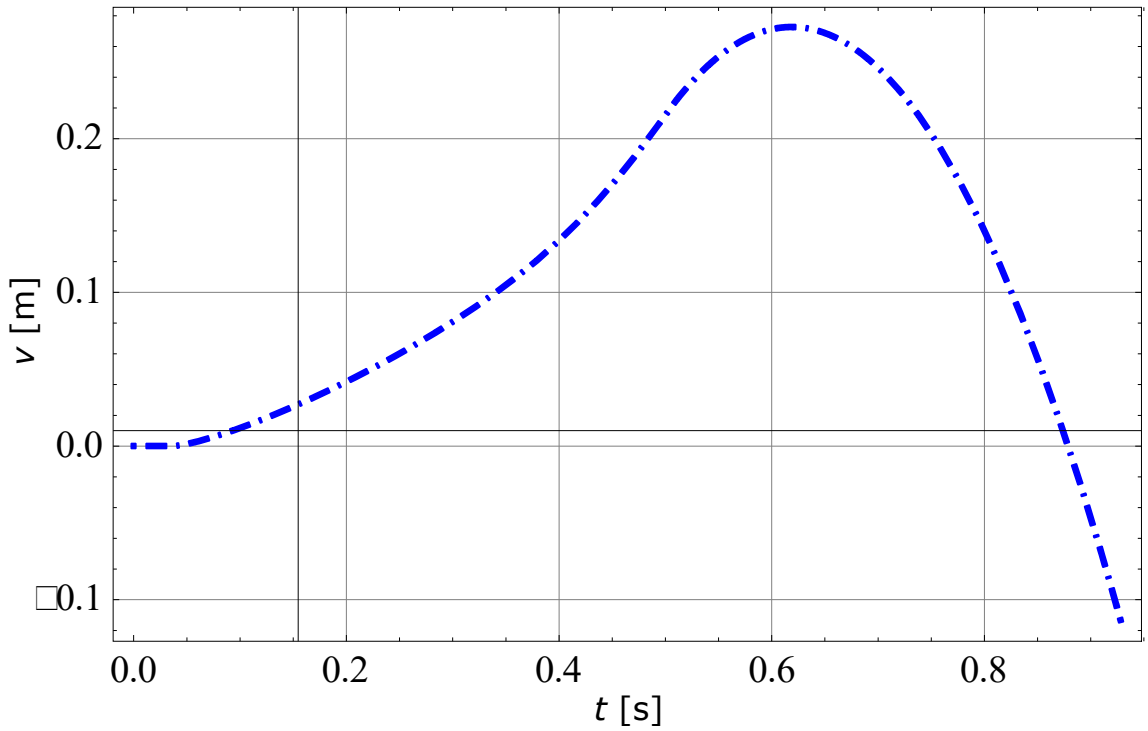

Figure 6-6: Wall displacement plotted on time, resulting from an ideal elastic-plastic collision of a motor vehicle. The wall is "static unstable" with $\boldsymbol{h = 3\,m}$.

The displacement of the "static unstable" wall stops due to friction on the failure surface, which decelerates the monolith. According to Chapter 4, the calculation of the wall displacement stops shortly after the maximum displacement is obtained, when the wall's velocity becomes null. The maximum wall displacement v_d is defined as a characteristic of the shock-type dynamic action. In the following parameter study the influence of various parameters on the maximum wall displacement will be analysed in different series.

6.5.2 Influence of wall height on maximum displacement

The wall height h will be varied from $1\,m$ up to $6\,m$ to investigate the "static stable" and the "static unstable" systems. This variation is named series 1.

Firstly, a static analysis is done as defined above. By applying the maximum impact force $F_s = 2.4\,MN$ as a static equivalent one, v_s values are obtained and presented in Table 6-3.

Table 6-3. Results of the static analysis applying the $F_s = 2.4\,MN$ force for different wall heights

h [m]	1	2	**3**	4	5	6	7
v_s *[m]*	>0,04	>0,08	**>0,12**	>0,16	0,050	0,033	0,020
v_p *[m]*	0,04	0,08	**0,12**	0,16	0,20	0,24	0,28
$v_{p,75}$ *[m]*	0,018	0,037	**0,055**	0,073	0,092	0,110	0,128
$v_s/v_{p,75}$ *[-]*	>2,18	>2,16	**>2,18**	>2,19	0,54	0,30	0,16
Static system	*unstable*				*stable*		

The ratio between the maximum static displacement v_s and the one corresponding to a 75% mobilization of the passive earth pressure $v_{p,75}$ defines the static stability of the system. Therefore, the system is static stable for ratio values below 1 and consequently it is static unstable for values above 1. It can be noted that the system is static unstable for wall heights lower than $h = 4\,m$ and for heights above $5\,m$ it becomes static stable and the displacements have a significant decrease once the wall height is increased (see Figure 6-7).

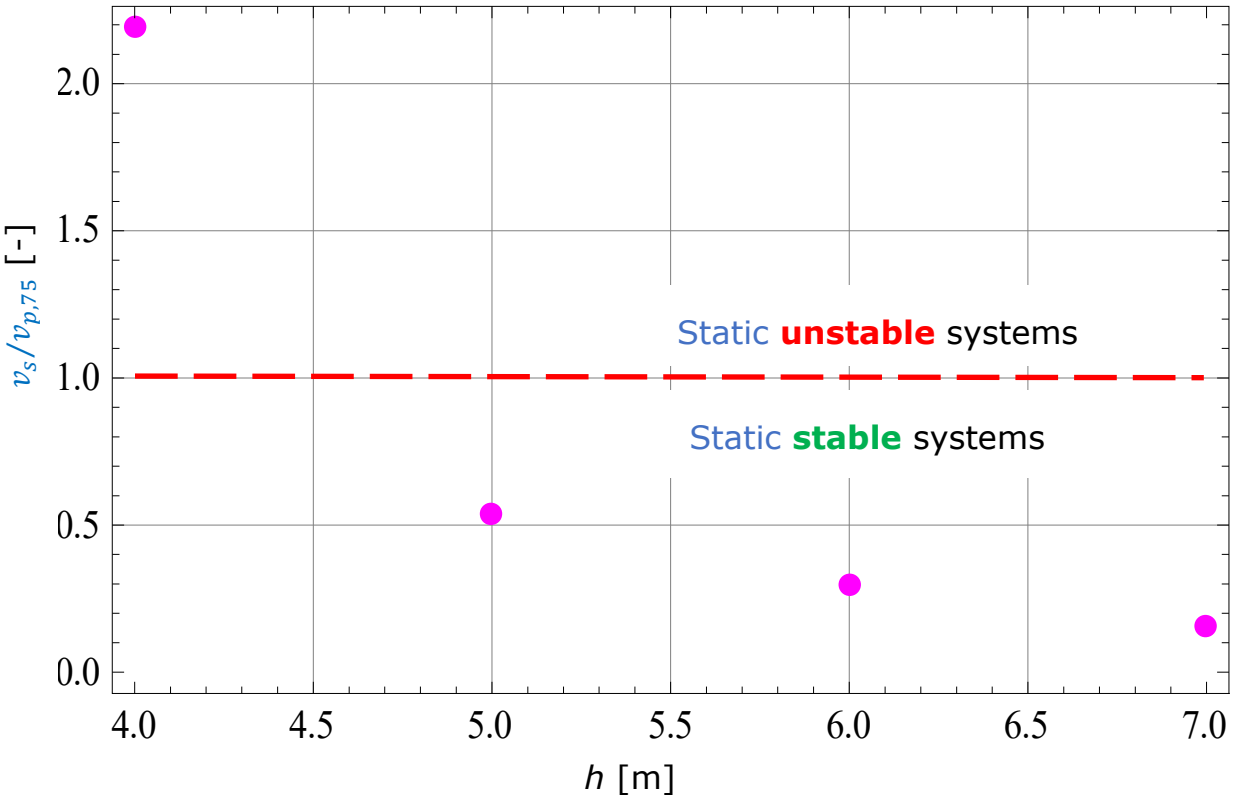

Figure 6-7: The ratio between the static wall displacement and the one corresponding to $\mathbf{75\%}$ of $\boldsymbol{E_p}$, after applying the static equivalent force of the dynamic $\boldsymbol{F_{dyn} = 2.4\ MN}$ one, for different wall heights

Figure 6-8 shows the maximum dynamic displacement obtained with the calculation program presented in Annex 2 for several different wall heights.

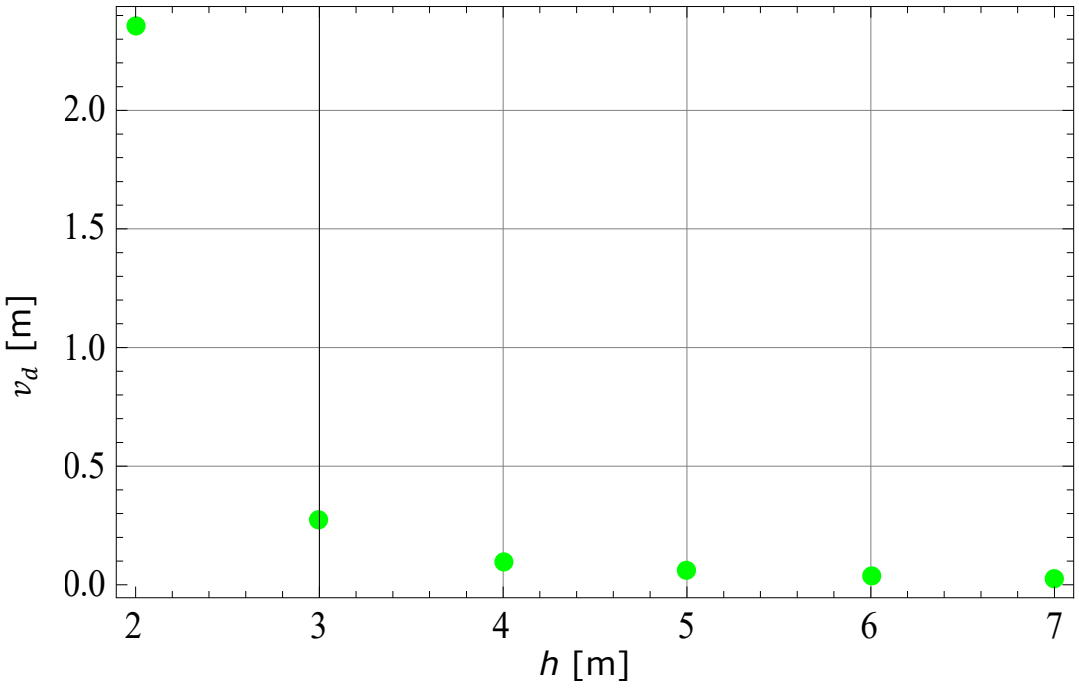

Figure 6-8: Maximum wall displacement due to collision plotted on the wall height

Figure 6-9 shows ratio between the maximum dynamic wall displacement and the one corresponding to 75% of E_p, obtained with the calculation program after applying the dynamic $F_{dyn} = 2.4\,MN$ force for different wall heights. Both from Figure 6-9, and from Table 6-10, high dynamic displacements of the static unstable systems (with wall heights $h \leq 4\,m$) can be observed, which are way above the displacement corresponding to 75% of the static passive resistance. For the static unstable systems, the $\frac{v_d}{v_{p,75}}$ ratio is also found to be above 1 and it significantly increases once the wall height is decreased. For the cases presented in Table 6-4, the applied static force is not exceeding the maximum static passive resistance and the model allowed the calculation of the static displacement, it is noted that its value can be both higher and lower in comparison with the dynamic one. For the systems whose static passive resistance is exceeded by the amplitude of the dynamic force $F_{dyn} > E_{ph}$, static failure is reached, the static displacement v_s exceeds the maximum value $v_s > v_p$, and it cannot be calculated any longer with the developed mathematical model.

Considering the admissible dynamic displacement value $v_{p,75}$, the walls with $h \leq 4\,m$ heights are dynamic unstable, as resulted from series 1 of the parametric study, presented in Table 6-4. The wall's stability in the dynamic case cannot be predicted by the static analysis, as emphasized by series 1.

Table 6-4. Results of the dynamic analysis compared to the static one, applying the $F_{dyn} = 2.4\,MN$ force for different wall heights, corresponding to series 1

h [m]	1	2	3	**4**	5	6	7
v_s [m]	>0,04	>0,08	>0,12	**>0,16**	0,050	0,033	0,020
v_p [m]	0,04	0,08	0,12	**0,16**	0,20	0,24	0,28
$v_{p,75}$ [m]	0,018	0,037	0,055	**0,073**	0,092	0,110	0,128
$v_s/v_{p,75}$ [-]	>2,18	>2,16	>2,18	**>2,19**	0,54	0,30	0,16
Static system	*unstable*				*stable*		
m_w [t]	0,75	1,51	2,26	**3,01**	3,77	4,52	5,27
E_{ph} [kN]	183	734	1652	**2937**	4590	6609	8995
$E_{ph,75}$ [kN]	138	550	1239	**2203**	3442	4957	6747
$F_{dyn}/E_{ph,75}$ [-]	17,4	4,36	1,94	**1,09**	0,697	0,484	0,356
G_{75} [kN]	71,7	287	645	**1147**	1792	2580	3512
T_{75} [s]	0,201	0,284	0,345	**0,397**	0,442	0,484	0,522
t_d/T_{75} [-]	0,433	0,306	0,252	**0,219**	0,197	0,180	0,167
k_{75} [MN/m]	7,1	14,3	21,4	**28,5**	35,7	42,8	49,9
v_d [m]	53	2,36	0,273	**0,097**	0,058	0,037	0,023
$v_d/v_{p,75}$ [-]	2944	63,8	4,96	**1,33**	0,63	0,34	0,18

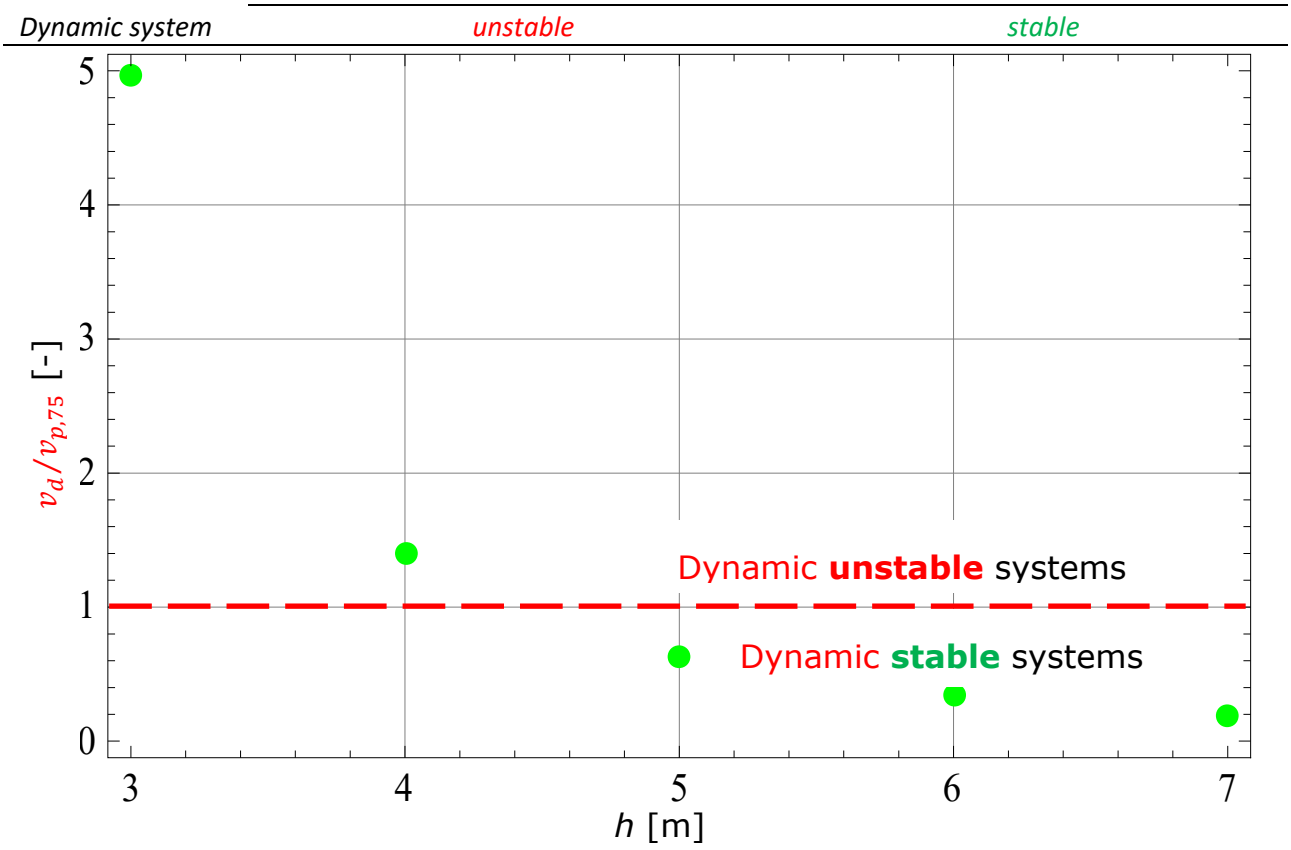

Figure 6-9: The ratio between the dynamic wall displacement and the one corresponding to $\mathbf{75\%}$ of $\boldsymbol{E_p}$, after applying the dynamic force $\boldsymbol{F_{dyn} = 2.4\ MN}$, for different wall heights – series 1

6.5.3 The influence of the impulse form on the maximum displacement

The normal impact, defined in Table 6-2 can by modified by two factors: the amplitude of the dynamic force is multiplied with the F_f factor and the duration of the impulse is multiplied with the t_f factor. In the following paragraphs the form of the impulse is varied, while its value remains constant, in compliance with the condition $F_f \cdot t_f = 1$. This variation is named series 2. The wall height is chosen to be $h = 4\ m$. The results of the static and dynamic calculations obtained using the own programs (see Annex 2) are presented in Table 6-5 and in Figure 6-10.

Table 6-5. Results of the static and dynamic analyses for the ideal elastic-plastic collision of a vehicle with a retaining wall, obtained by scaling the amplitude of the force and impact duration, so the value of the impulse remains constant – series 2

h [m]						**4**			
F_f *[-]*	10	5	3	2	1,5	**1**	0,75	0,5	0,2
t_f *[-]*	0,1	0,2	0,333	0,5	0,667	**1**	1,333	2	5
F_{dyn} *[kN]*	24000	12000	7200	4800	3600	**2400**	1800	1200	480
t_{dyn} *[s]*	0,050	0,099	0,166	0,249	0,331	**0,497**	0,663	0,994	2,485
I [kNs]						**759**			
v_s *[m]*	>0,16	>0,16	>0,16	>0,16	>0,16	**>0,16**	0,0522	0,0268	0,0016
v_p *[m]*						**0,16**			
$v_{p,75}$ *[m]*						**0,073**			
$v_s/v_{p,75}$ *[-]*	>2,19	>2,19	>2,19	>2,19	>2,19	**>2,19**	0,72	0,37	0,02
Static system				*unstable*				*stable*	
m_w *[t]*						**3,01**			
E_{ph} *[kN]*						**2937**			
$E_{ph,75}$ *[kN]*						**2203**			
$F_{dyn}/E_{ph,75}$ *[-]*	10,89	5,45	3,27	2,18	1,63	**1,09**	0,82	0,54	0,22
G_{75} *[kN]*						**1147**			
T_{75} *[s]*						**0,397**			
k_{75} *[MN/m]*						**28,5**			
$t_{d\,max}$ *[s]*	0,330	0,301	0,343	0,368	0,408	**0,520**	0,665	0,994	2,485
t_{dyn}/T_{75} *[-]*	0,125	0,250	0,417	0,626	0,835	**1,252**	1,669	2,504	6,259
v_d *[m]*	0,359	0,290	0,260	0,202	0,160	**0,097**	0,058	0,027	0,0016
$v_d/v_{p,75}$ *[-]*	4,92	3,97	3,56	2,77	2,19	**1,33**	0,79	0,37	0,022
Dynamic system				*unstable*				*stable*	

The column for "normal impact" for a height of the wall $h = 4\,m$ in Table 6-4 is found in Table 6-5 as central reference. It can be found that the amplitude of the force has a decisive role on the static displacement and more reduced one on the dynamic one. If the amplitude of the dynamic force exceeds $E_{ph,75}$, equivalent with static unstable systems, the value of the dynamic displacement approaches the admissible displacement $v_{p,75}$, so the systems also become dynamic unstable. The dynamic displacement in the unstable domain does not increase proportionally with the applied force, but subproportional. It can be affirmed that the impulse value $I = 759\,kNs$ is enough at the limit state to take the system out of dynamic equilibrium.

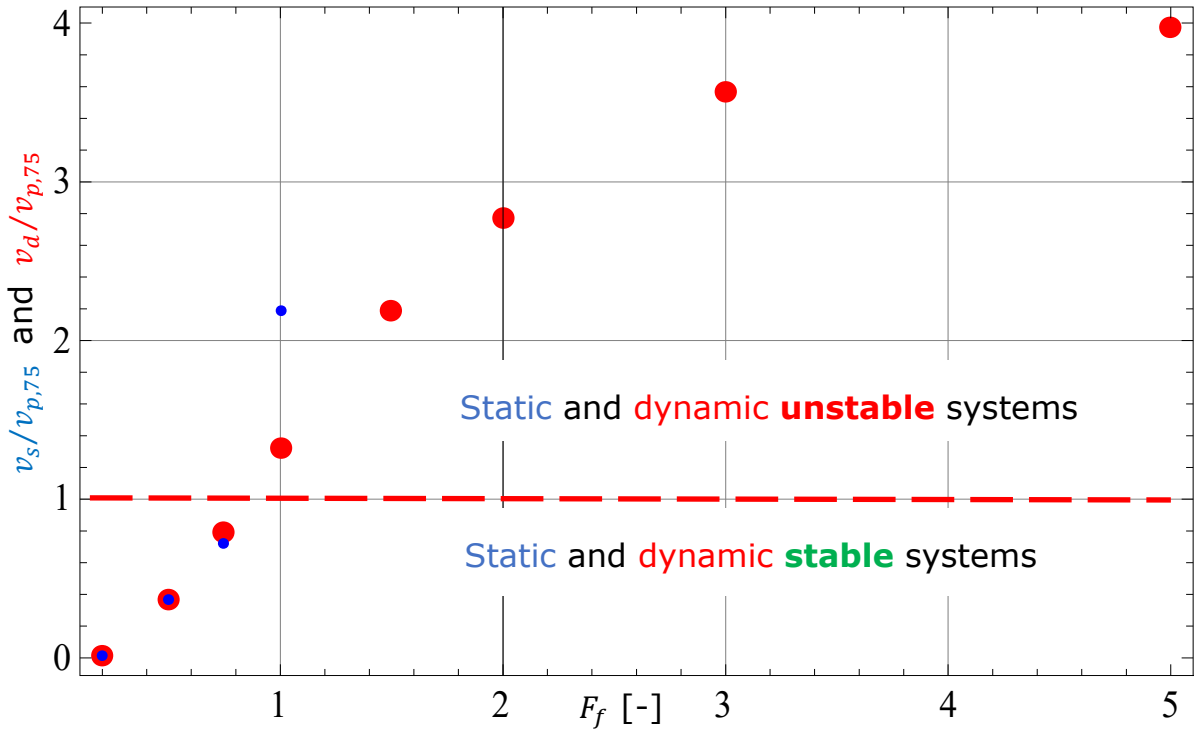

Figure 6-10: Collision of a vehicle with a retaining wall. The static and dynamic displacements are presented dimensionless as a function of amplitude of the dynamic force, represented by the $\boldsymbol{F_f}$ factor, maintaining a constant impulse value

An almost linear dependency between the variation factor F_f of the dynamic force amplitude and the ratios $\frac{v_s}{v_{p,75}}$ and $\frac{v_d}{v_{p,75}}$ can be observed for the stable systems domain. The static displacement v_s can be calculated using the mathematical model only until the static passive resistance is fully mobilized, corresponding with the ultimate displacement v_p. Over the ultimate displacement, the static system is no longer in equilibrium, as failure occurs and the displacement is no longer calculable. For these reasons, the static displacement for the static unstable systems can be calculated if $v_s \leq v_p$. By chance, for these analysed series, the cases for which the system is static stable, are the same for which it is dynamic stable.

It must be highlighted that the dynamic stability limit is chosen by the author as $v_{p,75}$ and designing engineers can also chose other values, depending on the response of the system and consequences of the maximum reached displacement and of the remanent one.

6.5.4 The influence of the impulse value on maximum displacement

The impulse value for "normal impact", defined in Table 6-2, will be modified for the following analyses in two distinct series named 3 and 4.

For series 3 the amplitude of the dynamic force will be varied by multiplying it with the F_f factor, but maintaining a constant duration of the impulse.

Table 6-6. Results of the static and dynamic analyses for the collision of a vehicle with a retaining wall, obtained by scaling the amplitude of the force with the F_f factor, but the duration of the impulse remains constant – series 3

	h [m]						**4**				
Input impulse data	*F_f [-]*	10	7,5	5	3	2	**1**	0,667	0,5	0,333	0,2
	t_f [-]						**1**				
	F_{dyn} [kN]	24000	18000	12000	7200	4800	**2400**	1599,84	1200	800	480
	t_{dyn} [s]						**0,497**				
	I [kNs]	7594	5695	3797	2278	1519	**759**	506	380	253	152
Static analysis	*v_s [m]*	>0,16	>0,16	>0,16	>0,16	>0,16	**>0,16**	0,0432	0,0268	0,0122	0,0016
	v_p [m]						**0,16**				
	$v_{p,75}$ [m]						**0,073**				
	$v_s/v_{p,75}$ [-]						**>2,19**	0,5918	0,3671	0,1671	0,0219
	Static system			*unstable*					*stable*		
Dynamic analysis	*m_w [t]*						**3,01**				
	E_{ph} [kN]						**2937**				
	$E_{ph,75}$ [kN]						**2203**				
	$F_{dyn}/E_{ph,75}$ [-]	10,89	8,17	5,45	3,27	2,18	**1,09**	0,73	0,54	0,36	0,22
	G_{75} [kN]						**1147**				
	T_{75} [s]						**0,397**				
	k_{75} [MN/m]						**28,5**				
	t_{dyn}/T_{75} [-]						**1,252**				
	v_d [m]	22,2	11,49	4,475	1,252	0,429	**0,097**	0,0494	0,0296	0,0128	0,0016
	$v_d/v_{p,75}$ [-]	304	157,40	61,30	17,15	5,88	**1,33**	0,677	0,405	0,175	0,022
	Dynamic system			*unstable*					*stable*		

The results of the static and dynamic analyses obtained for series 3 using the own calculation programs (see Annex 2) are presented in Table 6-6 and in Figure 6-11.

For series 4 the duration of the impulse will be varied by multiplying it with the t_f factor and maintaining a constant amplitude of the dynamic force.

Table 6-7. Results of the static and dynamic analyses for the collision of a vehicle with a retaining wall, obtained by scaling the duration of the impulse with the t_f factor, but the amplitude of the dynamic force remains constant – series 4

	h [m]						**4**				
Input impulse data	*F_f [-]*						**1**				
	t_f [-]	10	7,5	5	3	2	**1**	0,667	0,5	0,333	0,2
	F_{dyn} [kN]						**2400**				
	t_{dyn} [s]	4,970	3,728	2,485	1,491	0,994	**0,497**	0,331	0,249	0,166	0,099
	I [kNs]	7594	5695	3797	2278	1519	**759**	506	380	253	152
	v_s [m]						**0,086**				
	v_p [m]						**0,16**				
Static analysis	*v_s [m]*						**0,073**				
	$v_s/v_{p,75}$ [-]						**1,18**				
	Static system						***unstable***				
	m_w [t]						**3,01**				
	E_{ph} [kN]						**2937**				
Dynamic analysis	*$E_{ph,75}$ [kN]*						**2203**				
	$F_{dyn}/E_{ph,75}$ [-]						**1,09**				
	G_{75} [kN]						**1147**				
	T_{75} [s]						**0,397**				
	k_{75} [MN/m]						**28,5**				
	t_d/T_{75} [-]	12,52	9,389	6,259	3,756	2,504	**1,252**	0,835	0,626	0,417	0,250
	v_d [m]	0,086	0,086	0,104	0,09	0,094	**0,097**	0,083	0,071	0,053	0,035
	$v_d/v_{p,75}$ [-]	1,178	1,178	1,425	1,233	1,288	**1,33**	1,137	0,973	0,726	0,479
	Dynamic system				*unstable*					*stable*	

The results of the static and dynamic analyses obtained for series 4 using the own calculation programs (see Annex 2) are presented in Table 6-7 and in Figure 6-11.

Comparing the results of the series 3 and 4 on the left side of the reference column it can be seen that for the same impulse value, the force amplitude affects the maximum dynamic wall displacement much stronger than the duration of the impact force. Moreover, one can notice that the duration of the impulse will not significantly amplify the maximum wall displacement above the corresponding static one. This can be explained by the fact that in case of series 4 the system is only slightly static unstable, the $\frac{v_s}{v_{p,75}}$ ratio being little above one, while the $\frac{v_s}{v_p}$ ratio is below.

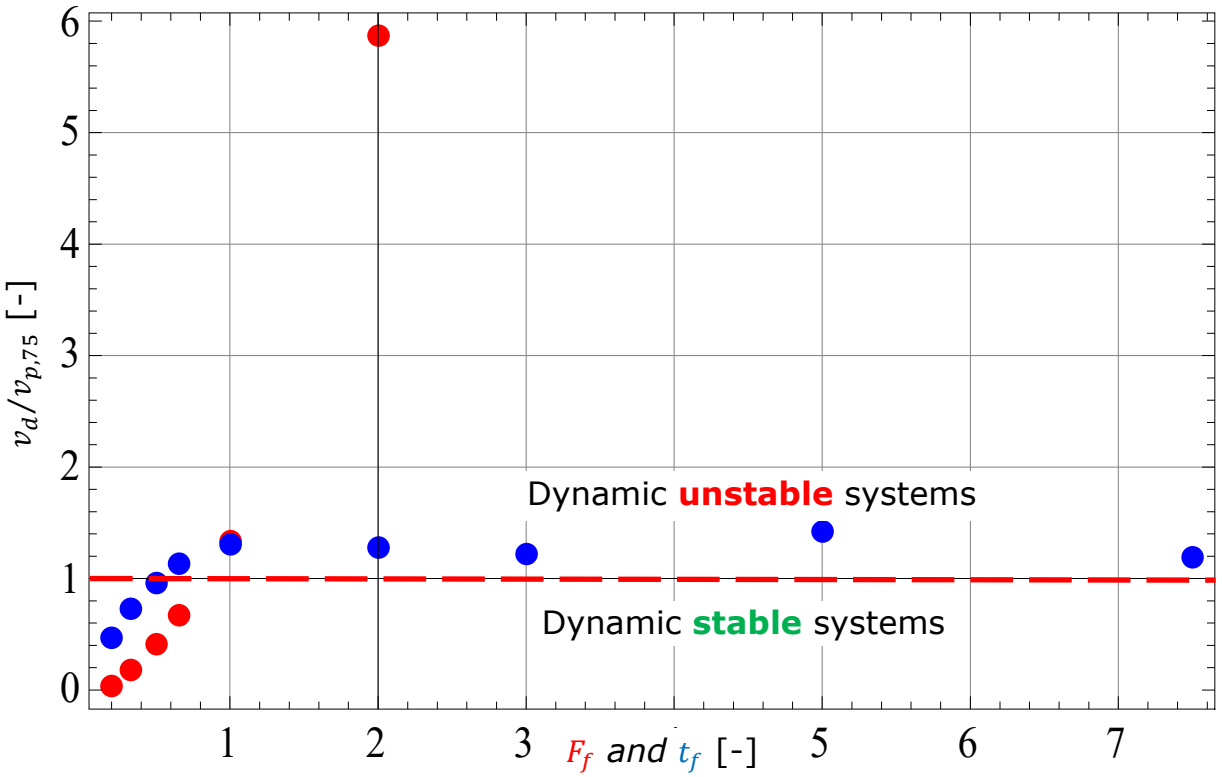

Figure 6-11: Collision of a vehicle with a retaining wall. Series 3 is presented with red, corresponding to the scaling of the force amplitude with the F_f factor and series 4 is presented with blue, corresponding to the scaling of the force duration with the t_f factor

6.6 Elastic ship response that collides with a retaining wall on inland waterways

According to SR EN 1991-1-7:2007 the dynamic impact force should be modelled as a half-sine wave pulse if the dynamic impact force is $F_{dyn} \leq 5\,MN$.

When the value of the design impact force is known, from table C.3 of the same standard, and the associated impact duration must be determined, the m^* mass is obtained from the relation:

$$m^* = \left({}^{F_{dyn}}/_{v_n}\right)^2 * \left({}^{1}/_{c}\right) \tag{6-12}$$

where

v_n is the velocity of the colliding ship normal to the impact surface, which is equal with the sailing speed v_r. The recommended design velocities are $v_{rd} = 3\frac{m}{s}$ increased by water velocity and $v_{rd} = 1{,}5\frac{m}{s}$ in harbours;

$c = 60\frac{MN}{m}$ is the elastic stiffness of the ship on internal waterways.

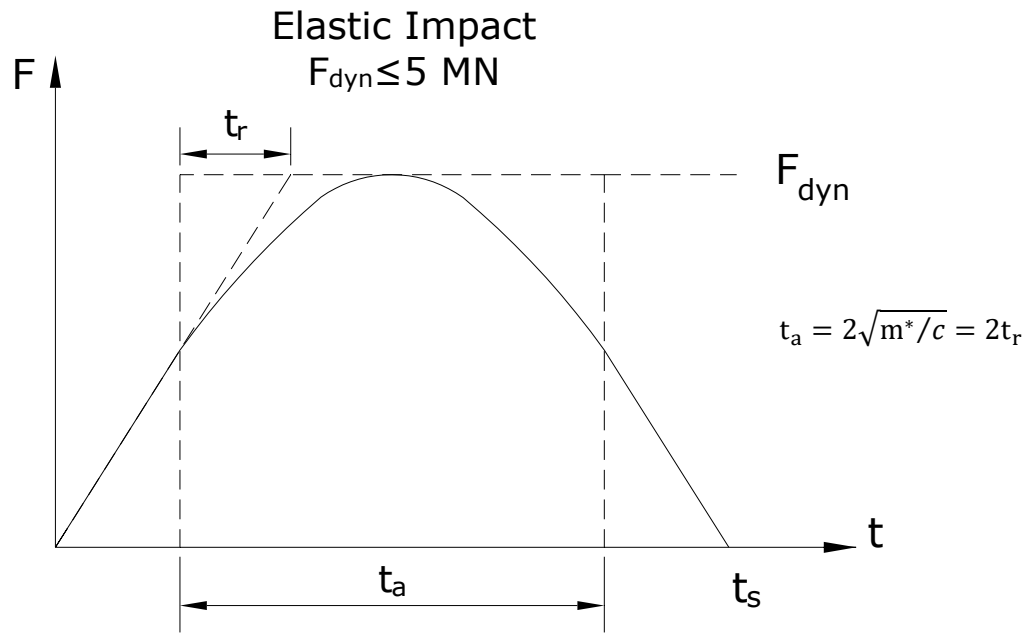

Figure 6-12: Load-time function for ship collision, respectively for elastic ship response (Figure C.3, taken from Annex C of SR EN 1991-1-7:2007)

6.6.1 Input and reference data

Considering a class "Europe" ship, taken from table C.3 of SR EN 1991-1-7:2007, which has a mass between 1000 and 1500 tonnes, the dynamic impact force $F_{dyn} = 5\ MN$ and $v_{rd} = 3\frac{m}{s}$ one obtains:

$$m^* = \left(\frac{F_{dyn}}{v_n}\right)^2 \cdot \left(\frac{1}{c}\right) = \left(\frac{5 \cdot 10^6}{3}\right)^2 \cdot \left(\frac{1}{60 \cdot 10^6}\right) = 46{,}3\ tons \tag{6-13}$$

$$t_s = \pi\sqrt{\frac{m^*}{c}} = \pi\sqrt{\frac{46{,}3 \cdot 10^3}{60 \cdot 10^6}} = 0{,}087\ s \tag{6-14}$$

The values in Table 6-8 are obtained by discretization of the impact force.

Table 6-8. Variation of the impact force for a ship colliding with a rigid structure, elastic ship response

t [s]	0	0,0087	0,0174	0,0261	0,0348	0,0435	0,0522	0,0609	0,0696	0,0783	0,087
F_{dyn} [kN]	0	1545	2939	4045	4755	5000	4755	4045	2939	1545	0

The parameters of a plausible retaining structure are chosen as follows:

- Width of the retaining wall $b = 9{,}5\ m$
- Height of the retaining wall $h = 3\ m$
- Thickness of the sheet pile wall $d = 0{,}03\ m$

- Mass of the sheet pile wall $m = 6{,}7\ tons$
- Specific weight of the soil $\gamma = 20\ kN$
- Internal friction angle of the soil $\varphi = 30°$
- Soil-wall interface friction angle $\delta = 15°$
- Density index of the soil $D = 1$
- Displacement to mobilize limit passive pressure ${}^{v_p}/_{h} = 0{,}12 - 0{,}08D = 0{,}04$

The equivalent width of the retaining structure is chosen as equal with the ship's width, of approximately $9{,}5\ m$, neglecting in a conservative manner, any additional soil elements that would be involved during the collision. The width of the ship is taken from „Resolution No. 92/2 on New Classification of Inland Waterways".

6.6.2 Calculation of the maximum displacement after impact

By applying the maximum impact force $F_s = 5\ MN$ as a static one, $v_s > v_p \geq v_{p,75} = 0{,}055\ m$ is obtained. This means that the wall is "static unstable".

By applying the "normal impact", defined in Table 6-8 and represented in Figure 6-13, on the above-defined retaining wall, the wall displacement-time curve is obtained, which is represented in Figure 6-14. It presents the maximum displacement $v_d = 0{,}054\ m < v_{p,75} = 0{,}055\ m$, occurring after $t = 0{,}133\ s$ after the start of the impact. One may observe that the maximum dynamic displacement occurs long time after the time when the force has its peak at $t = 0{,}0435$ s. This is due to inertial forces which delay the acceleration of the wall-soil mass system.

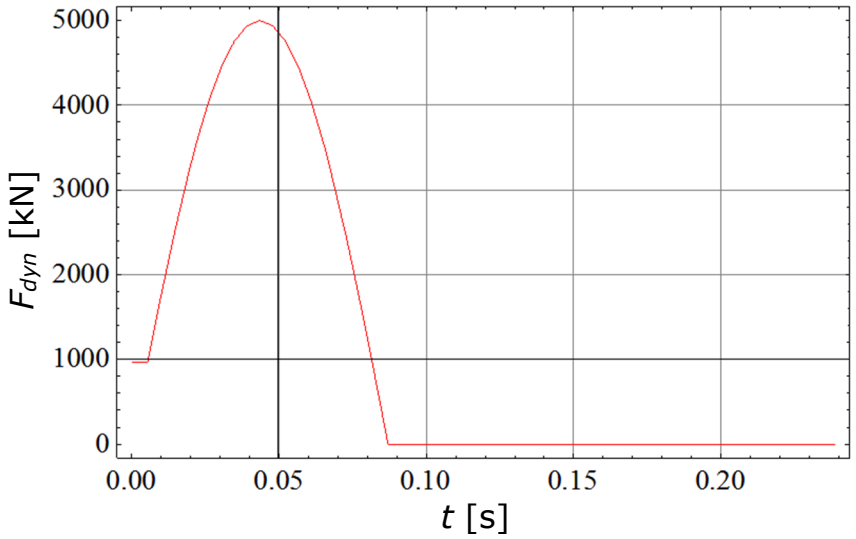

Figure 6-13: Dynamic shock-type force – "normal impact" – applied by a class "Europe" ship on a rigid retaining structure

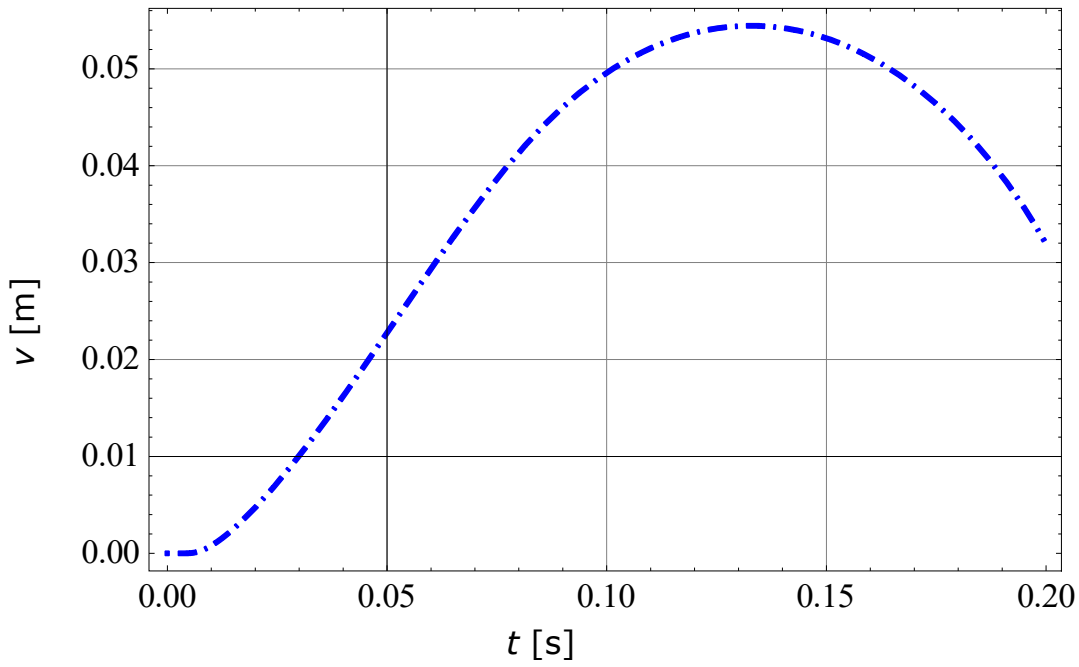

Figure 6-14: Wall displacement plotted on time, resulting from the collision of a class "Europe" ship with an elastic response. The wall is "static unstable" with $\boldsymbol{h = 3\ m}$

The displacement of the "static unstable" wall stops due to friction on the failure surface, which decelerates the monolith. The maximum wall displacement v_d is defined as a characteristic of the shock-type dynamic action. In the following parametric study, the influence of various parameters on the maximum wall displacement will be analysed in different series.

6.6.3 Influence of wall height on maximum displacement

The wall height h will be varied from $1\ m$ up to $6\ m$ to investigate the "static stable" and the "static unstable" systems. This variation is named series 1.

Firstly, a static analysis is done as defined above. By applying the maximum impact force $F_s = 5\ MN$ as a static equivalent one, v_s values are obtained and presented in Table 6-9.

Table 6-9. Results of the static analysis applying the $F_s = 5\ MN$ force for different wall heights

h [m]	1	2	2.5	**3**	4	5	6
v_s [m]	>0,12	>0,12	>0,12	**>0,12**	0.062	0.037	0.022
v_p [m]	0.04	0.08	0.1	**0.12**	0.16	0.2	0.24
$v_{p,75}$ [m]	0.018	0.036	0.045	**0.055**	0.073	0.091	0.109
$v_s/v_{p,75}$ [-]	>6,7	>3,3	>2,67	**>2,18**	0.85	0.41	0.20
Static system	*unstable*				*stable*		

The ratio between the maximum static displacement v_s and the one corresponding to a 75% mobilization of the passive earth pressure $v_{p,75}$ defines the stability of the system. Therefore, the system is static stable for ratio values below one and consequently it is static unstable for values above one. It can be noted that the system is static unstable for a wall height $h = 3\,m$ and for heights above $4\,m$ it becomes static stable and the displacements have a significant decrease once the wall height is increased (see Figure 6-15).

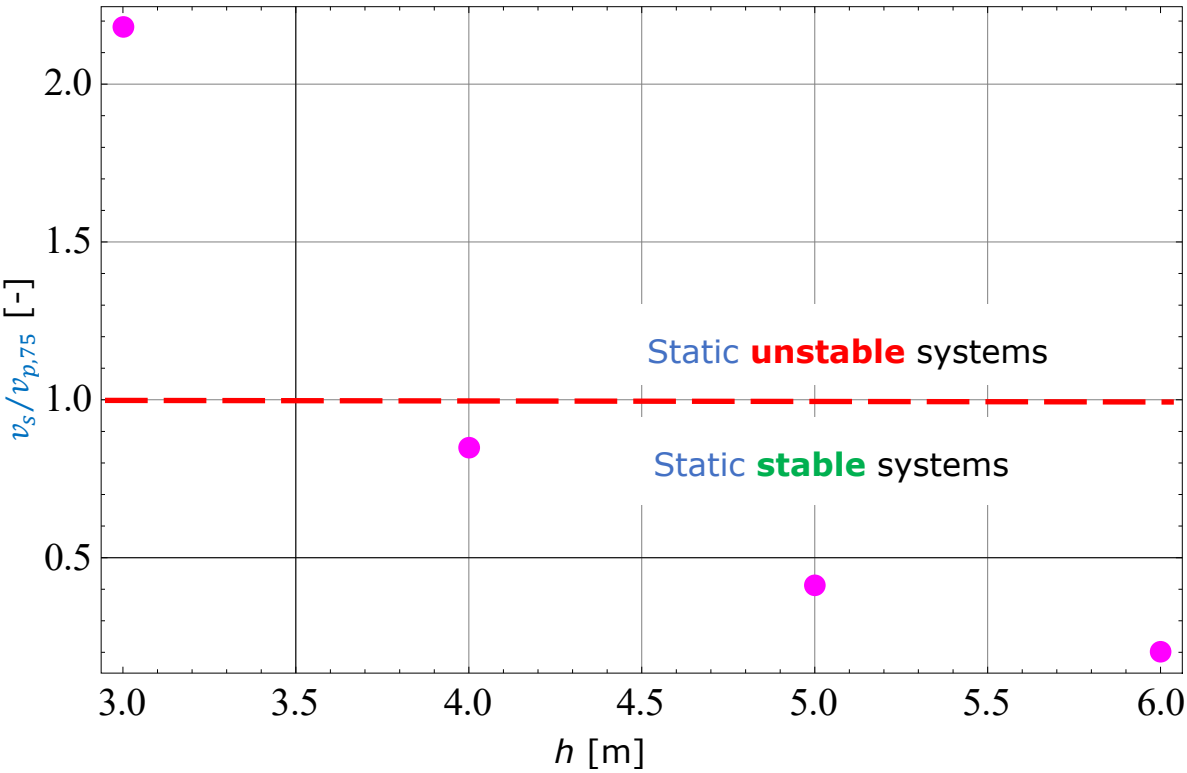

Figure 6-15: The ratio between the static wall displacement and the one corresponding to $\mathbf{75\%}$ of $\boldsymbol{E_p}$, after applying the static equivalent force of the dynamic one $\boldsymbol{F_{dyn} = 5\,MN}$, for different wall heights

Figure 6-16 shows the maximum dynamic displacement obtained with the calculation program presented in Annex 2 for several different wall heights.

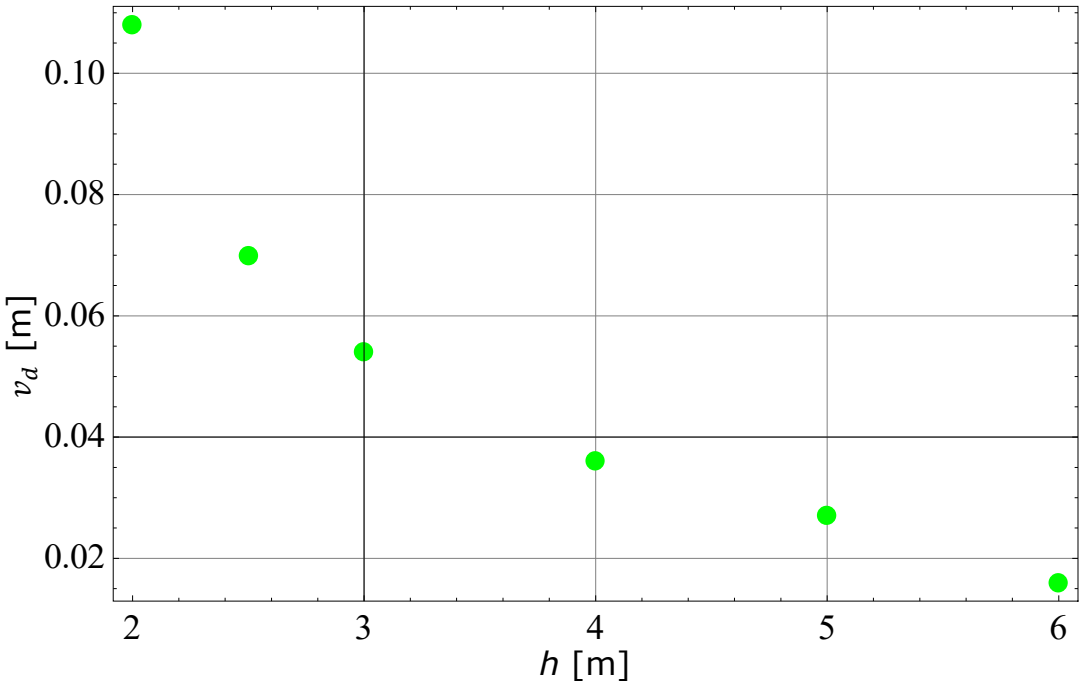

Figure 6-16: Maximum wall displacement due to collision plotted on the wall height

Figure 6-17 shows ratio between the maximum dynamic wall displacement and the one corresponding to 75% of E_p, obtained with the calculation program after applying the dynamic $F_{dyn} = 5\ MN$ force for different wall heights. Both from Figure 6-17, and from Table 6-10, high dynamic displacements of the static unstable systems (with wall heights $h \leq 3\ m$) can be observed, which are way above the displacement corresponding to 75% of the static passive resistance. For the static unstable systems, the $\frac{v_d}{v_{p,75}}$ ratio is also found to be above one and it significantly increases once the wall height is decreased. For the cases presented in Table 6-10, the applied static force is not exceeding the maximum static passive resistance and the model allowed the calculation of the static displacement, it is noted that its value can be both higher and lower in comparison with the dynamic one. For the systems whose static passive resistance is exceeded by the amplitude of the dynamic force $F_{dyn} > E_{ph}$, static failure is reached, the static displacement v_s exceeds the maximum value $v_s > v_p$, and it cannot be calculated any longer with the developed mathematical model.

Table 6-10. Results of the dynamic analysis applying the $F_{dyn} = 5\ MN$ force for different wall heights, corresponding to series 1 and compared with the static analysis

h [m]	1	2	2.5	**3**	4	5	6
v_s *[m]*	>0,12	>0,12	>0,12	**>0,12**	0.062	0.037	0.022
v_p *[m]*	0.04	0.08	0.1	**0.12**	0.16	0.2	0.24
$v_{p,75}$ *[m]*	0.018	0.036	0.045	**0.055**	0.073	0.091	0.109
$v_s/v_{p,75}$ *[-]*	>6,7	>3,3	>2,67	**>2,18**	0.85	0.41	0.20
Static system	*unstable*				*stable*		
m_w *[t]*	2.2	4.5	5.6	**6.71**	8.9	11.2	13.4
E_{ph} *[kN]*	456	1826	2854	**4110**	7306	11416	16440
$E_{ph,75}$ *[kN]*	342	1370	2140	**3082**	5480	8562	12330
$F_{dyn}/E_{ph,75}$ *[-]*	14.6	3.65	2.3	**1.62**	0.912	0.584	0.406
G_{75} *[kN]*	185	743	1161	**1672**	2973	4646	6690
T_{75} *[s]*	0.212	0.291	0.323	**0.353**	0.406	0.452	0.494
t_d/T_{75} *[-]*	0.410	0.300	0.269	**0.246**	0.214	0.192	0.176
k_{75} *[MN/m]*	17.6	35.1	43.9	**52.7**	70.2	87.8	105
v_d *[m]*	1.35	0.108	0.070	**0.054**	0.036	0.027	0.016
$v_d/v_{p,75}$ *[-]*	75	3	1.56	**0.99**	0.493	0.297	0.147
Dynamic system		*unstable*				*stable*	

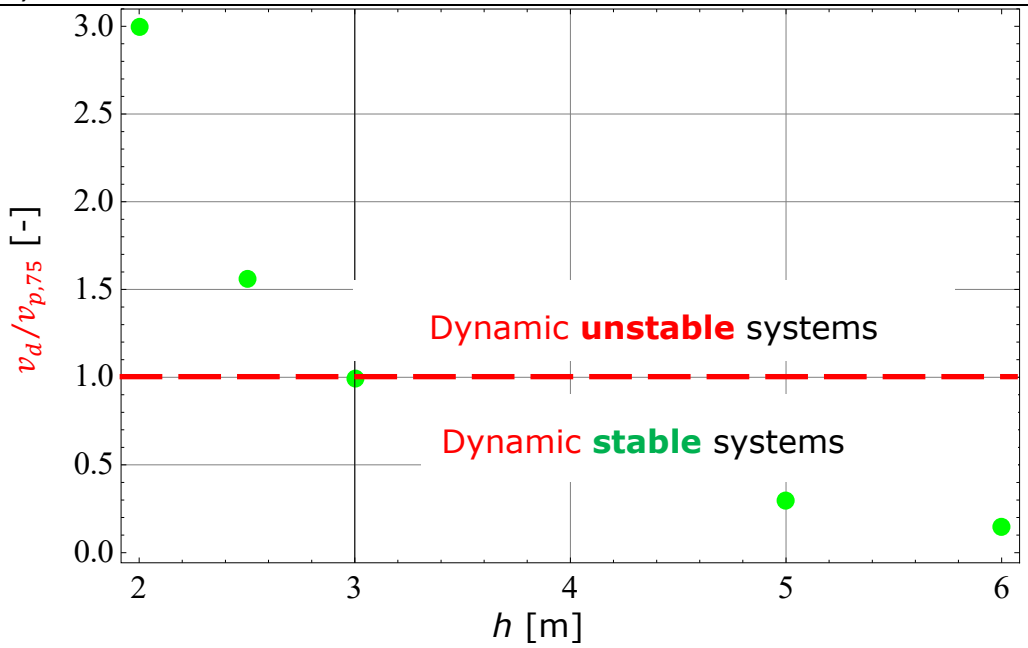

Figure 6-17: The ratio between the dynamic wall displacement and the one corresponding to 75% of E_p, after applying the dynamic $F_{dyn} = 5\ MN$ force, for different wall heights – series 1

Considering the admissible dynamic displacement value $v_{p,75}$, the walls with $h \leq 2{,}5\ m$ heights are dynamic unstable, as resulted from series 1 of the parametric study, presented in Table 6-10. The wall's stability in the dynamic case cannot be predicted by the static analysis, as emphasized by series 1.

6.6.4 The influence of the impulse form on the maximum displacement

The normal impact, defined in Table 6-8 can by modified by two factors: the amplitude of the dynamic force is multiplied with the F_f factor and the duration of the impulse is multiplied with the t_f factor. In the following paragraphs the form of the impulse is varied, while its value remains constant, in compliance with the condition $F_f \cdot t_f = 1$. This variation is named series 2. The wall height is chosen to be $h = 3\ m$. The results of the static and dynamic calculations obtained using the own programs (see Annex 2) are presented in Table 6-11 and in Figure 6-18.

The column for "normal impact" for a height of the wall $h = 3\ m$ in Table 6-10 is found in Table 6-11 as central reference. It can be found that the amplitude of the force has a decisive role on the static displacement and more reduced one on the dynamic one.

Table 6-11. Results of the static and dynamic analyses for the collision of a ship, having an elastic response, with a retaining wall, obtained by scaling the amplitude of the force and impact duration, so the value of the impulse remains constant – series 2

h [m]						**3**			
F_f [-]	10	5	3	2	1,5	**1**	0,75	0,5	0,2
t_f [-]	0,1	0,2	0,333	0,5	0,667	**1**	1,333	2	5
F_{dyn} [kN]	50000	25000	15000	10000	7500	**5000**	3750	2500	1000
t_{dyn} [s]	0,009	0,017	0,029	0,044	0,058	**0,087**	0,116	0,174	0,435
I [kNs]						**277**			
v_s [m]	>0,12	>0,12	>0,12	>0,12	>0,12	**>0,12**	0,0814	0,0383	0,0065
v_p [m]						**0,12**			
$v_{p,75}$ [m]						**0,055**			
$v_s/v_{p,75}$ [-]	>2,18	>2,18	>2,18	>2,18	>2,18	**>2,18**	1,48	0,70	0,12
Static system				***unstable***				*stable*	
m_w [t]						**6,71**			
E_{ph} [kN]						**4110**			
$E_{ph,75}$ [kN]						**3082**			
$F_{dyn}/E_{ph,75}$ [-]	16,22	8,11	4,87	3,24	2,43	**1,62**	1,22	0,81	0,32

G_{75} [kN]						**1672**			
T_{75} [s]						**0,353**			
k_{75} [MN/m]						**52,7**			
$t_{d\,max}$ [s]	0,1	0,104	0,109	0,115	0,121	**0,087**	0,145	0,173	0,2415
t_{dyn}/T_{75} [-]	0,025	0,049	0,082	0,123	0,164	**0,246**	0,329	0,493	1,232
v_d [m]	0,0646	0,0637	0,062	0,061	0,059	**0,054**	0,053	0,040	0,009
$v_d/v_{p,75}$ [-]	1,17	1,16	1,13	1,10	1,07	**0,99**	0,97	0,73	0,16
Dynamic system			***unstable***					***stable***	

If the amplitude of the dynamic force exceeds $E_{ph,75}$, equivalent with static unstable systems, the value of the dynamic displacement approaches the admissible displacement $v_{p,75}$, so the systems also become dynamic unstable. The dynamic displacement in the unstable domain does not increase proportionally with the applied force, but subproportional. It can be affirmed that the impulse value $I = 277\ kNs$ is enough at the limit state to take the system out of dynamic equilibrium.

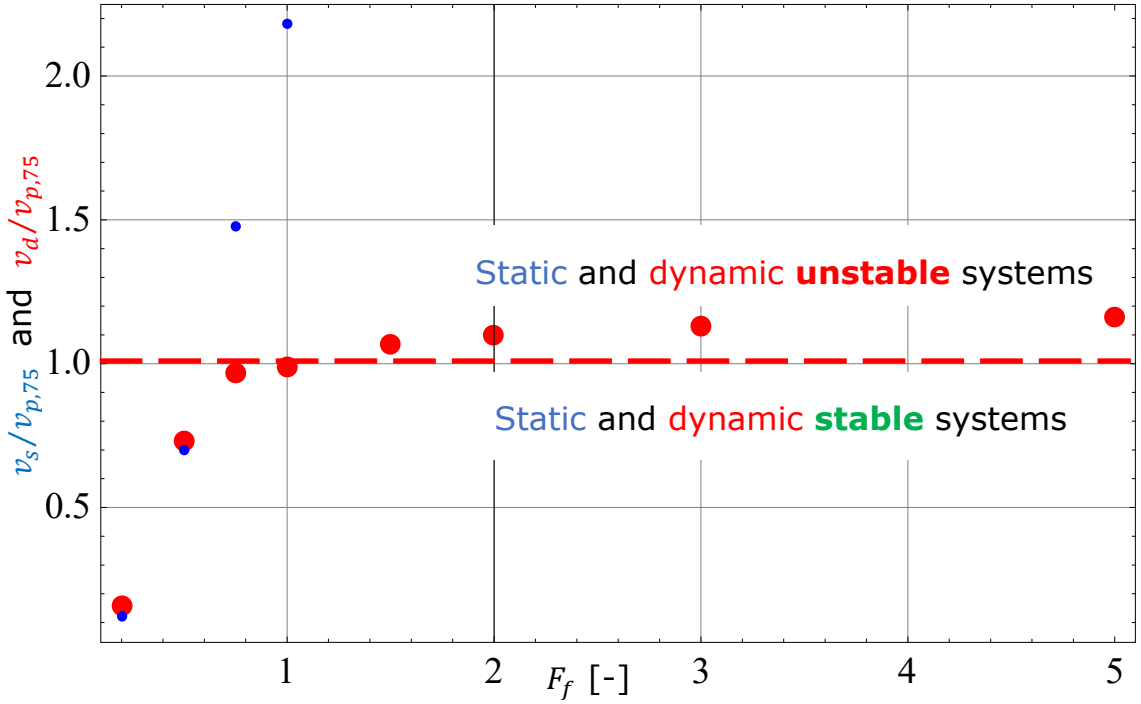

Figure 6-18: Collision of an internal ship with a retaining wall. The static and dynamic dimensionless displacements are presented as a function of amplitude of the dynamic force, represented by the F_f factor, maintaining a constant impulse value – series 2

An almost linear dependency between the variation factor F_f of the dynamic force amplitude and the ratios $\frac{v_s}{v_{p,75}}$ and $\frac{v_d}{v_{p,75}}$ can be observed for the stable systems domain. The static displacement v_s can be calculated using the mathematical model only until the static passive resistance is fully mobilized,

corresponding with the ultimate displacement v_p. Over the ultimate displacement, the static system is no longer in equilibrium, as failure occurs and the displacement is no longer calculable. For these reasons, the static displacement for the static unstable systems can be calculated only until $v_s \leq v_p$. By chance, for the analysed series 2, for the two analysed cases corresponding to the reference column and the next one to the right the systems are static unstable but still dynamic stable.

It must be remembered, as mentioned in chapter 6.5.3, that the dynamic stability limit chosen by the author $v_{p,75}$ can be changed by the designing engineers for specific cases.

6.6.5 The influence of the impulse value on maximum displacement

The impulse value for "normal impact", defined in Table 6-8, will be modified for the following analyses in two distinct series named 3 and 4.

For series 3 the amplitude of the dynamic force will be varied by multiplying it with the F_f factor, but maintaining a constant duration of the impulse.

Table 6-12. Results of the static and dynamic analyses for the collision of an internal ship with a retaining wall, obtained by scaling the amplitude of the force with the F_f factor, but the duration of the impulse remains constant – series 3

h [m]						**3**				
F_f [-]	10	7.5	5	3	2	**1**	0.667	0.5	0.333	0.2
t_f [-]						**1**				
F_{dyn} [kN]	50000	37500	25000	15000	10000	**5000**	3333	2500	1667	1000
t_{dyn} [s]						**0.087**				
I [kNs]	2769	2077	1385	831	554	**277**	185	138	92	55
v_s [m]	>0,12	>0,12	>0,12	>0,12	>0,12	**>0,12**	0.0307	0.0188	0.0082	0.0003
v_p [m]						**0.12**				
$v_{p,75}$ [m]						**0.055**				
$v_s/v_{p,75}$ [-]	>2,18	>2,18	>2,18	>2,18	>2,18	**>2,18**	0.56	0.34	0.15	0.01
Static system				***unstable***					***stable***	
m_w [t]						**6.71**				
E_{ph} [kN]						**4110**				
$E_{ph,75}$ [kN]						**3082**				
$F_{dyn}/E_{ph,75}$ [-]	16.22	12.17	8.11	4.87	3.24	**1.62**	1.08	0.81	0.54	0.32
G_{75} [kN]						**1672**				

T_{75} [s]						**0.353**				
k_{75} [MN/m]						**52.7**				
t_d/T_{75} [-]						**0.246**				
v_d [m]	1.785	1.001	0.464	0.193	0.111	**0.054**	0.036	0.028	0.016	0.0070
$v_d/v_{p,75}$ [-]	32.45	18.20	8.44	3.51	2.02	**0.99**	0.656	0.509	0.291	0.127
Dynamic system			***unstable***					***stable***		

For series 4 the duration of the impulse will be varied by multiplying it with the t_f factor and maintaining a constant amplitude of the dynamic force.

Table 6-13. Results of the static and dynamic analyses for the collision of an internal ship with a retaining wall, obtained by scaling the duration of the impulse with the t_f factor, but the amplitude of the dynamic force remains constant – series 4

h [m]						**3**				
F_f [-]						**1**				
t_f [-]	10	7.5	5	3	2	**1**	0.667	0.5	0.333	0.2
F_{dyn} [kN]						**5000**				
t_{dyn} [s]	0.870	0.653	0.435	0.261	0.174	**0.087**	0.058	0.044	0.029	0.017
I [kNs]	2769	2077	1385	831	554	**277**	185	138	92	55
v_s [m]	>0.12	>0.12	>0.12	>0.12	>0.12	**>0.12**	>0.12	>0.12	>0.12	>0.12
v_p [m]						**0.12**				
$v_{p,75}$ [m]						**0.055**				
$v_s/v_{p,75}$ [-]						**>2.18**				
Static system						***unstable***				
m_w [t]						**6.7**				
E_{ph} [kN]						**4110**				
$E_{ph,75}$ [kN]						**3082**				
$F_{dyn}/E_{ph,75}$ [-]						**1.62**				
G_{75} [kN]						**1672**				
T_{75} [s]						**0.353**				
k_{75} [MN/m]						**52.7**				
t_d/T_{75} [-]	2.465	1.848	1.232	0.739	0.493	**0.246**	0.164	0.123	0.082	0.049
v_d [m]	0.371	0.282	0.194	0.125	0.091	**0.054**	0.040	0.032	0.023	0.015
$v_d/v_{p,75}$ [-]	6.75	5.13	3.53	2.27	1.65	**0.99**	0.73	0.58	0.42	0.27
Dynamic system			***unstable***					***stable***		

The results of the static and dynamic analyses obtained with the own calculation programs (see Annex 2) are presented in Table 6-12, Table 6-13 and in Figure 6-19.

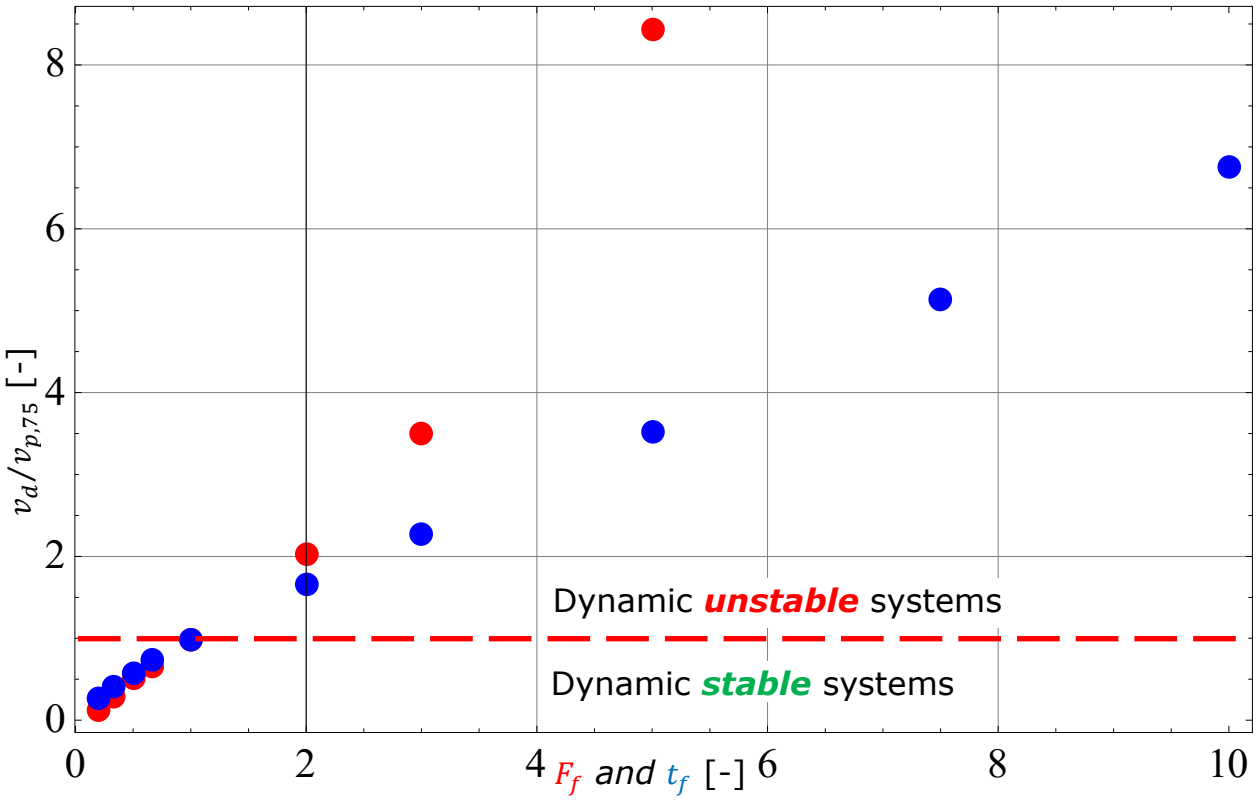

Figure 6-19: Collision of an internal ship with a retaining wall. Series 3 is presented with red, corresponding to the scaling of the force amplitude with the F_f factor and series 4 is presented with blue, corresponding to the scaling of the force duration with the t_f factor

For the same impulse value, the force amplitude has a more pronounced effect on the maximum wall displacement than the duration of the force.

Comparing the results of the series 3 and 4 both in Figure 6-19 as well as in the Table 6-12 and Table 6-13 on the left side of the reference column it can be seen that for the same impulse value, the force amplitude affects the maximum dynamic wall displacement much stronger than the duration of the impact force. Moreover, different to the results of the vehicle collision in chapter 6.5.4, one can notice that the duration of the impulse will also amplify the maximum wall displacement above the corresponding static one. This can be explained by the fact that in case of series 4 the system is highly static unstable, the $\frac{v_s}{v_{p,75}}$ ratio being above two, while the $\frac{v_s}{v_p}$ ratio is above one.

6.7 Plastic ship response that collides with a retaining wall on inland waterways

6.7.1 Input and reference data

If the dynamic impact force is $F_{dyn} > 5\,MN$, it must be modelled as a trapezoidal pulse in accordance with SR EN 1991-1-7:2007, corresponding to a plastic ship response.

By considering the largest ship, class VII (a tow and 9 barges), from table C.3 of SR EN 1991-1-7:2007, having the mass $m^* = 20.000\,tonnes$ and $v_{rd} = v_n = 3\frac{m}{s}$, one obtains:

$$E_{def} = 0{,}5m^*\,{v_{rd}}^2 = 0{,}5 \cdot 20 \cdot 10^6 \cdot 9\,\frac{kg \cdot m^2}{s^2} = 90\,MNm \tag{6-15}$$

$$F_{dyn,pl} = 5\sqrt{1 + 0{,}128E_{def}} = 5\sqrt{1 + 0{,}128 \cdot 90} = 17{,}7\,MN \tag{6-16}$$

From table C.3 of SR EN 1991-1-7:2007 the frontal impact force is taken as $F_{dx} = 20\,MN$. In accordance with Figure 6-20, taken from the same standard, one obtains:

$$F_D = \left(F_0 + F_{dyn}\right)/2 = (5 + 20)/2 = 12{,}5\,MN \tag{6-17}$$

$$t_p = m^* v_{rd}/F_D = (20 \cdot 3)/20 = 3\,s \tag{6-18}$$

$$t_r = x_e/v_{rd} = 0{,}1/3 = 0{,}033\,s \tag{6-19}$$

$$t_e = \frac{\pi}{2}\sqrt{\frac{m^*}{c}} = \frac{\pi}{2}\sqrt{\frac{20}{60}} = 0{,}906\,s \tag{6-20}$$

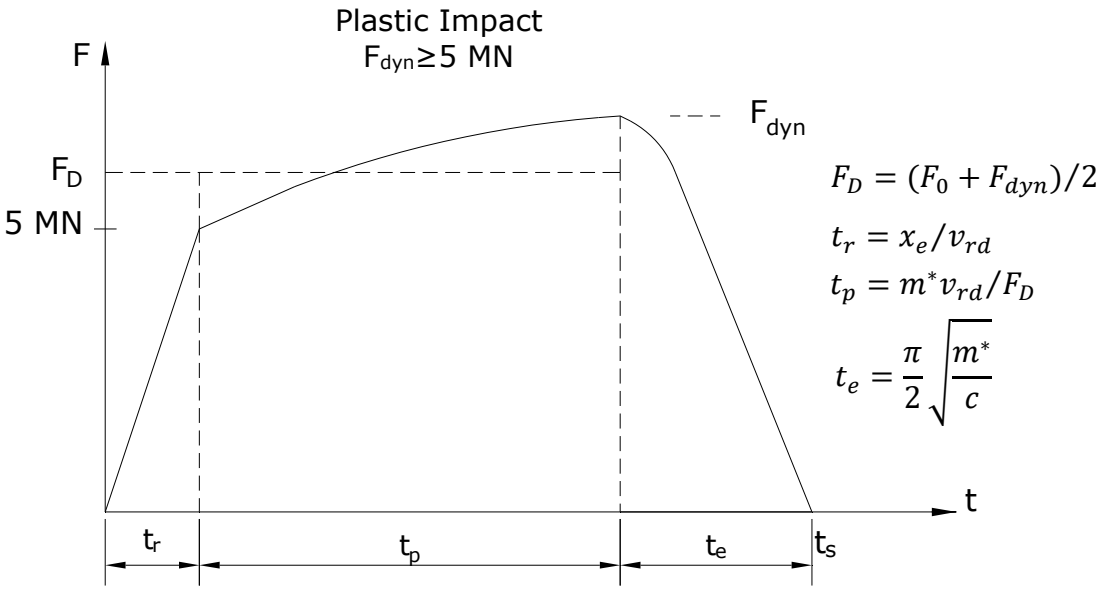

Figure 6-20: Load-time function for ship collision, respectively for plastic ship response (Figure C.3, taken from Annex C of SR EN 1991-1-7:2007)

The values in Table 6-14 are obtained by discretization of the dynamic impact force in 10 intervals.

Table 6-14. Variation of the impact force for a ship colliding with a rigid structure, plastic ship response

t [s]	0	0,033	1	2	2,8	2,95	3,033	3,078	3,125	3,486	3,939
F_{dyn} [kN]	0	5000	11500	16800	19600	19940	20000	19650	18800	10500	0

The variation of the above defined dynamic force will be referred to as "normal impact".

The parameters of a plausible retaining structure are chosen as follows:

- Width of the retaining wall $b = 33\ m$
- Height of the retaining wall $h = 3\ m$
- Thickness of the sheet pile wall $d = 0{,}03\ m$
- Mass of the sheet pile wall $m = 23{,}3\ tonnes$
- Specific weight of the soil $\gamma = 20\ kN$
- Internal friction angle of the soil $\varphi = 30°$
- Soil-wall interface friction angle $\delta = 15°$
- Density index of the soil $D = 1$
- Displacement to mobilize limit passive pressure ${}^{v_p}/_{h} = 0{,}12 - 0{,}08D = 0{,}04$

The equivalent width of the retaining structures is chosen as for the elastic impact case, equal with the ship's width, of approximately $33\ m$, neglecting in a

conservative manner, any additional soil elements that would be involved during the collision. The width of the ship is taken from „Resolution No. 92/2 on New Classification of Inland Waterways".

6.7.2 Calculation of the maximum wall displacement after impact

By applying the static equivalent of the maximum impact force $F_s = 20\ MN$, $v_s \gg v_p \geq v_{p,75} = 0{,}055\ m$ is obtained. This means that the wall is "static unstable".

By applying the "normal impact" from Figure 6-21 on the above defined retaining structure the wall displacement-time function is obtained (Figure 6-22). It presents the maximum displacement $v_d = 4{,}7\ m \gg v_{p,75} = 0{,}055\ m$, occurring at the time $t = 4{,}07\ s$ after starting the collision. One may observe that the maximum dynamic displacement occurs after the moment when the force has its peak at $t = 3{,}033\ s$. This is due to inertial forces which delay the acceleration of the wall-soil mass system.

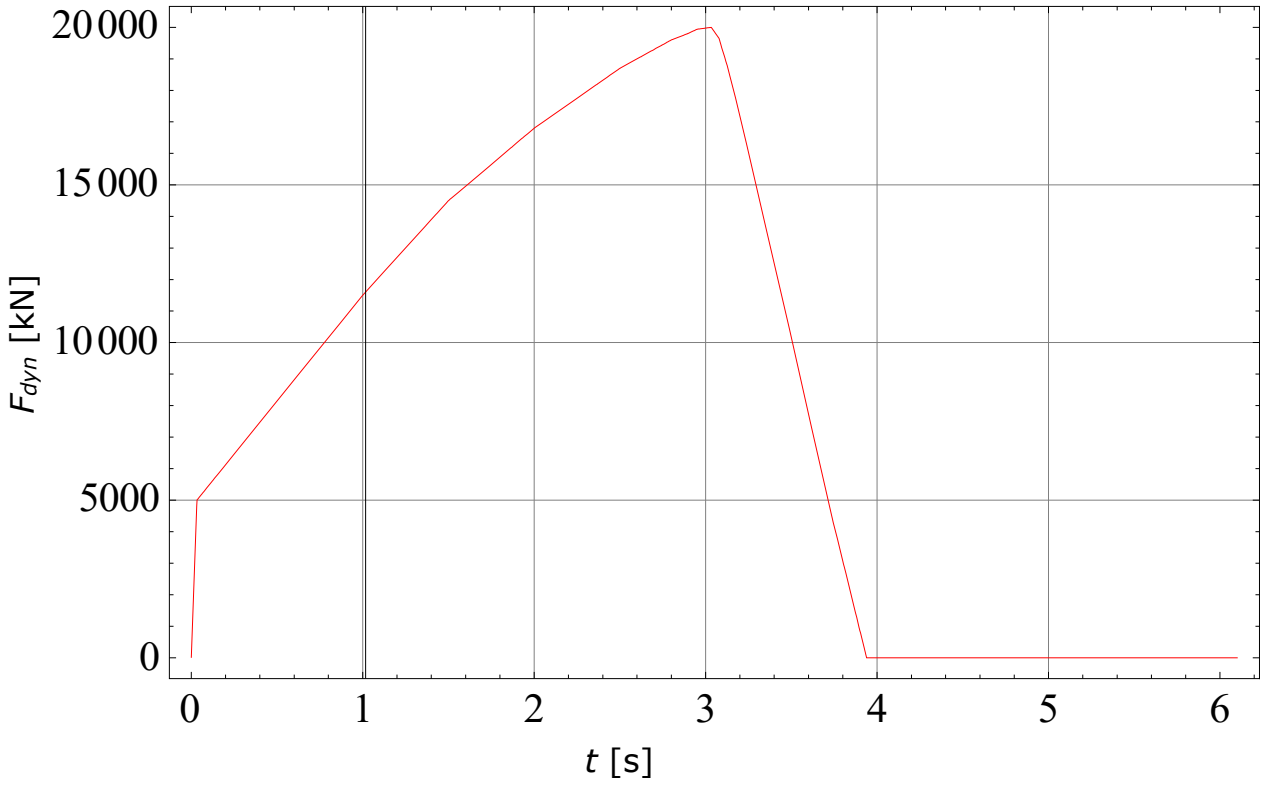

Figure 6-21: The dynamic shock-type force applied by the largest class VII ship on a rigid retaining structure

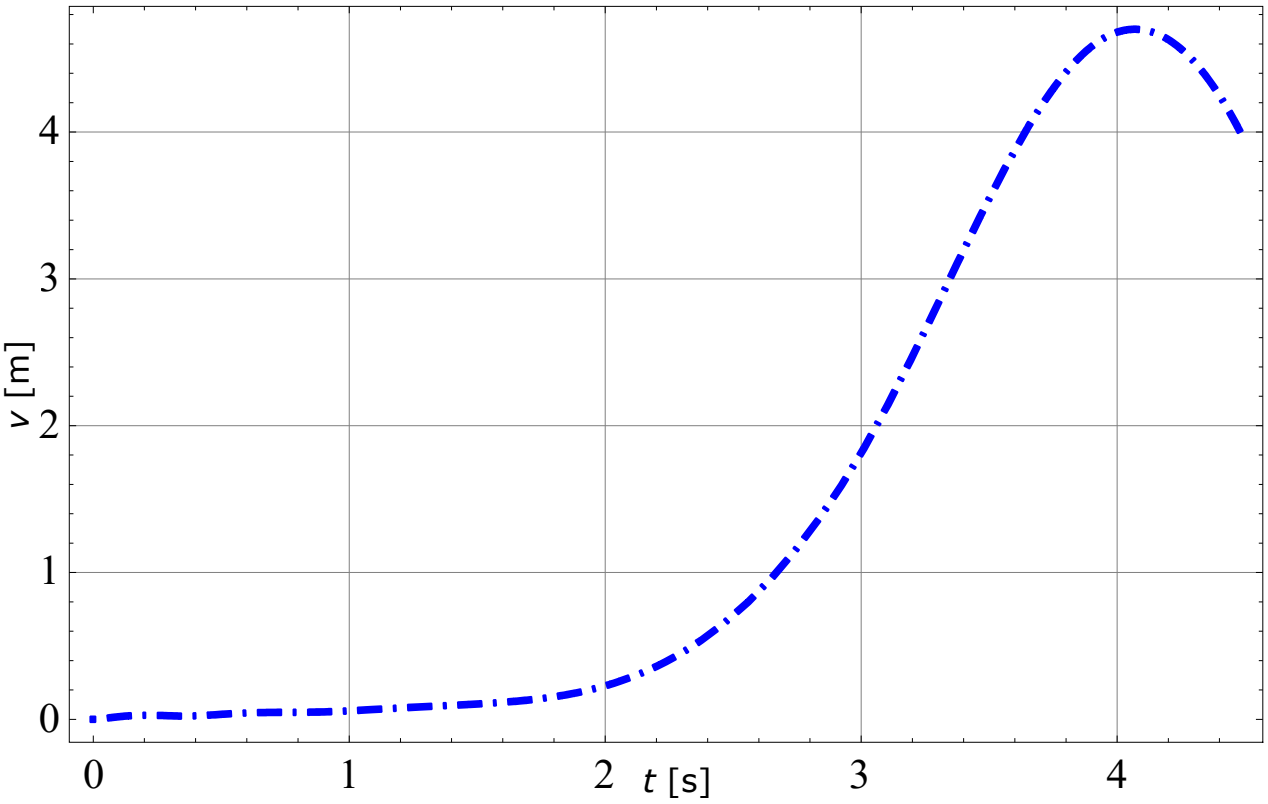

Figure 6-22: The wall displacement plotted on time, resulted from the collision of a class VII ship. The "static unstable" wall with $\boldsymbol{h = 3\ m}$

The detailed results of the calculation are provided in Annex 3. The program can run for any dynamic impact force variation and for different geometries and masses of the impacted wall. The geotechnical parameters can also be varied and the side friction of the mobilized soil prism with the rest of the ground can be introduced.

6.8 Problem framing and estimated approach

Biggs (1964) calculated the response of an ideal elastic-plastic pendulum subjected to impact. Figure 6-23 firstly presents the form of the considered impulse and the force-displacement diagram, which is linearly elastic until the y_{el} displacement is reached and ideally plastic above this value. On the horizontal axis the duration of the applied impulse t_d is represented, normalized by the T period of the system, when it oscillates in the elastic domain.

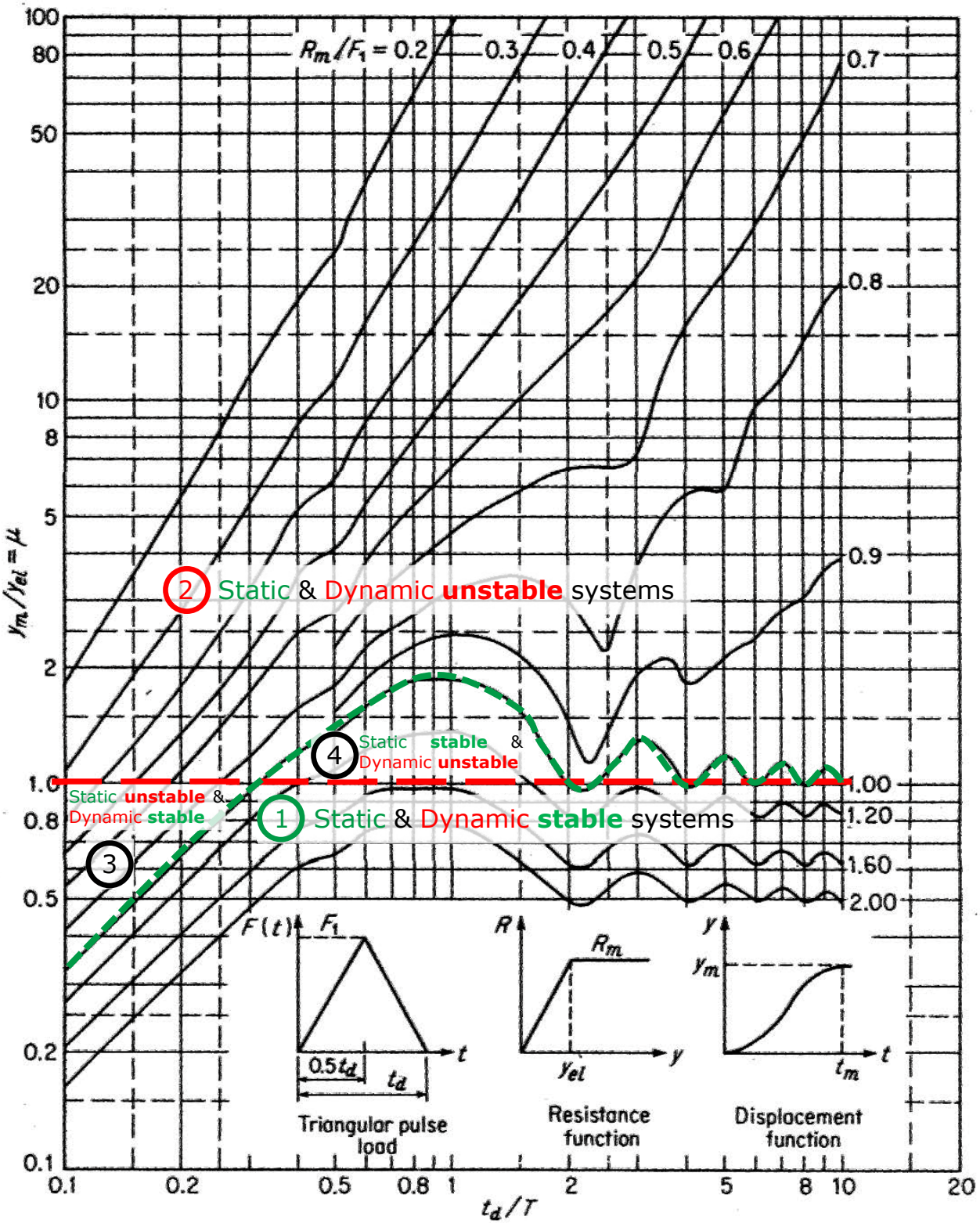

Figure 6-23: Maximum displacement of an ideal elastic-plastic pendulum, after Biggs (1964)

On the vertical axis, the maximum displacement y_m is represented, normalized by the maximum amplitude of the system's displacement y_{el}, when it oscillates in the elastic domain.

The main parameter of graphs is R_m/F_1, being the ratio between the maximum static resistance and the maximum amplitude of the dynamic impact force. If $R_m/F_1 \geq 1$ the system is static stable, corresponding to the domains 1 and 4.

The oscillations of the ideal elastic plastic system when a triangular pulse load is applied, are more emphasized close to the limit domain of the static stability, corresponding to $R_m/F_1 \approx 1$. For the static unstable systems, the amplitude of the response in terms of maximum displacements increases logarithmic with the normalized impulse duration t_d/T, as well as with the normalized dynamic force amplitude.

In analogy to the definitions of the static and dynamic stable and unstable systems presented in chapter 6.4, four stability domains distinguish in Figure 6-24. If $y_m/y_{el} \geq 1$ the system is dynamic unstable, corresponding to the domains 2 and 4.

As presented in the previous chapters, the form of the real impulse in case of collision defers from the triangular one. The passive resistance and soil mass mobilization function are as well highly non-linear, making the use of the graphs presented in Figure 6-23 unsafe to determine the maximum dynamic displacement of the system.

By analogy with the graph in Figure 6-23, the ratio R_m/F_1 is replaced with $F_{dyn}/E_{p,75}$ and y_m/y_{el} with $v_d/v_{p,75}$.

A corresponding mobilized mass m_{75} to $v_{p,75}$ can be obtained from equation (3-17) for the 75% mobilized passive earth pressure. In the case of elastic impulse, the fundamental vibration period of the elastic-plastic pendulum is obtained:

$$T_{75} = 2\pi \sqrt{\frac{m_{75} \cdot v_{p,75}}{E_{p,75}}}. \qquad (6\text{-}21)$$

By analogy with the graph in Figure 6-23, the ratio t_d/T is replaced with t_d/T_{75}.

Using for the sake of convenience all input and reference data given in Chapter 6.6.1, for the ideal elastic impact of a class "Europe" ship with the given rigid structure, computations were performed with the calculation program presented in Annex 2. By multiplying separately both the amplitude and the

duration of the half-sine wave pulse with factors ranging from 0.1 to 10 a parametric study for 180 different loadings was performed.

The results of the computations are given normalized in the Table 6-14 and represented in the Figure 6-24, in analogy with the response of the ideal elastic-plastic pendulum to a triangular pulse as represented in Figure 6-23.

Table 6-15. Maximum dynamic normalized displacement of a rigid retaining wall subject to an ideal elastic impact by scaling independently both the amplitude and the duration of the half-sine wave pulse

$F_{dyn}/E_{p,75}$	5	3,33	2,5	2	1,67	1,43	1,25	1,11	1	0,833	0,625	0,5
t_d/T_{75}	$v_d/v_{p,75}$											
0,1	1,32	0,92	0,71	0,58	0,49	0,42	0,37	0,33	0,30	0,24	0,17	0,13
0,2	2,61	1,64	1,24	1,00	0,84	0,72	0,64	0,56	0,51	0,42	0,30	0,22
0,5	10,2	4,70	2,89	2,10	1,68	1,40	1,20	1,05	0,93	0,75	0,51	0,37
0,75	20,9	8,69	4,80	3,14	2,31	1,84	1,54	1,31	1,14	0,89	0,59	0,41
1	35,3	13,9	7,19	4,36	2,97	2,22	1,78	1,48	1,27	0,96	0,61	0,42
1,5	75,3	28,1	13,3	7,27	4,37	2,87	2,09	1,65	1,36	0,99	0,60	0,39
2	130	47,0	21,3	10,8	5,84	3,38	2,22	1,68	1,35	0,95	0,56	0,36
3	284	99,0	45,0	20,0	8,98	4,09	2,21	1,57	1,24	0,86	0,50	0,33
4	497	170	70,1	30,4	12,5	4,50	2,08	1,46	1,15	0,80	0,48	0,32
5	769	206	100	43,8	16,6	5,08	1,98	1,39	1,10	0,77	0,47	0,31
6	1099	328	147	59,7	21,4	5,61	1,90	1,34	1,07	0,76	0,46	0,31
7	1488	446	195	78,3	27,0	6,20	1,84	1,31	1,05	0,75	0,46	0,31
8	1935	524	252	99,6	33,4	6,84	1,80	1,29	1,03	0,75	0,46	0,31
9	2441	763	315	124	43,0	7,50	1,76	1,27	1,03	0,74	0,46	0,31
10	3005	989	400	150	55,0	8,35	1,74	1,26	1,02	0,74	0,46	0,31

Using the definitions of the static and dynamic stable and unstable systems, as presented in chapter 6.4, four stability domains distinguish in Figure 6-24 as follows:

1. The domain of Static & Dynamic **stable** systems corresponding to the area which fullfills simultaneously the conditions $F_{dyn}/E_{p,75} < 1$ and $v_d/v_{p,75}$ <1;

2. The domain of Static & Dynamic **unstable** systems corresponding to the area which fullfills simultaneously the conditions $F_{dyn}/E_{p,75} > 1$ and $v_d/v_{p,75}$ >1; ;

3. The domain of Static **unstable** & Dynamic **stable** systems corresponding to the area which fullfills simultaneously the conditions $F_{dyn}/E_{p,75} > 1$ and $v_d/v_{p,75}$ <1;

4. The domain of Static **stable** & Dynamic **unstable** systems corresponding to the area which fullfills simultaneously the conditions $F_{dyn}/E_{p,75} < 1$ and $v_d/v_{p,75}$ >1.

Similarly to the results represented in Figure 6-23, the diagrams in Figure 6-24 show that for the static unstable systems, the amplitude of the response in terms of maximum displacements $v_d/v_{p,75}$ increases logarithmic with the normalized impulse duration t_d/T_{75}, as well as with the normalized dynamic force amplitude $F_{dyn}/E_{p,75}$. For static stable systems the maximum displacements $v_d/v_{p,75}$ increase also logarithmic with the normalized impulse duration t_d/T_{75} until the ratio reaches the value 1, as well as with the normalized dynamic force amplitude $F_{dyn}/E_{p,75}$, but is limited by value 2. For half-sine wave pulses longer than the fundamental vibration period of the elastic-plastic pendulum T_{75} the maximum displacements $v_d/v_{p,75}$ decrease smooth. For the ratio t_d/T_{75} increasing to 10, the maximum displacements $v_d/v_{p,75}$ decreases towards values less equal one.

Knowing the dynamic force amplitude of an elastic impact force F_{dyn} as well as the duration of the half-sine wave pulse of the force t_d, and calculating $E_{p,75}$ as defined in chapter 6.4 and T_{75} by the equation (6-21), result both t_d/T_{75} and $F_{dyn}/E_{p,75}$. Thus, it appears that the chart represented in Figure 6-24 may be used to estimate the dynamic displacement of a rigid wall against passive earth resistance subject to an ideal elastic impact by reading the $v_d/v_{p,75}$ value when both t_d/T_{75} and $F_{dyn}/E_{p,75}$ are calculated as described above.

Figure 6-24 presents the results of the four series investigated in chapter 6.6 together with the diagrams from Figure 6-24. The diagrams corresponding to the four series cut across the reference case corresponding to the central column in the Tables 6-9 to 6-13. This reference case is static unstable for $F_{dyn}/E_{p,75} = 1.62$ and very narrow at the limit dynamic stable for $v_d/v_{p,75} = 0.99$.

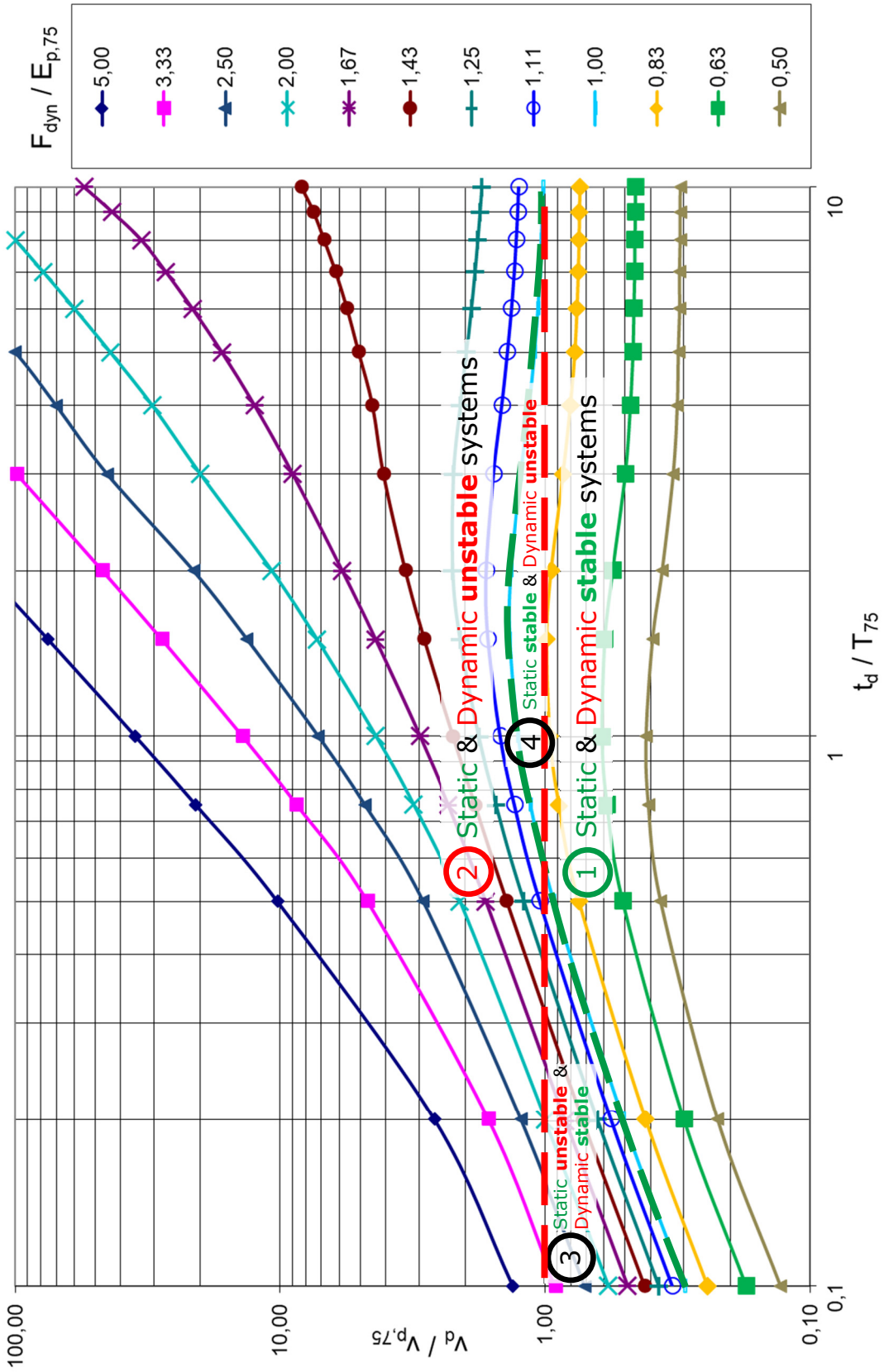

Figure 6-24: Dimensionless representation of the maximum dynamic displacement plotted on the impact duration for different amplitudes of the dynamic force of an ideal elastic impact, as given in the Table 6-14

Series 1 corresponds to the variation of the wall height of the structure impacted by a half-sine pulse load having a constant maximal amplitude. The diagram of series 1 indicates that starting from the reference case and reducing the wall height the passive resistance decreases, corresponding to an increase of the static instability and the system dynamic instability increases logarithmic. By increasing the wall height, the system becomes static stable and more dynamic stable by decreasing logarithmically the ratio $v_d/v_{p,75}$. The diagram of series 1 shows also a slight variation of the normal period of the dynamic system. By increasing the wall's height, h, the normal period of the system T_{75} increases and the ratio t_d/T_{75} decreases. It has to be reminded that series 1 emphasizes that the wall's stability in the dynamic case cannot be predicted by the static analysis.

Series 2 corresponds to the variation of the amplitude of the dynamic force F_{dyn}, represented by the F_f factor, maintaining a constant impulse value.

Series 3 is presented with red, corresponding to the scaling of the force amplitude with the F_f factor and series 4 is presented with blue, corresponding to the scaling of the force duration with the t_f factor.

For the same impulse value, the force amplitude has a more pronounced effect on the maximum wall displacement than the duration of the force. Comparing the results of the series 3 and 4 both in Figure 6-19 as well as in the Table 6-12 and Table 6-13 on the left side of the reference column it can be seen that for the same impulse value, the force amplitude affects the maximum dynamic displacement much stronger than the duration of the impact force. Moreover, different to the results of the vehicle collision in chapter 6.5.4, one can notice that the duration of the impulse will also amplify the maximum dynamic displacement above the corresponding static one. This can be explained by the fact that in case of series 4 the system is highly static unstable, the $\frac{v_s}{v_{p,75}}$ ratio being above two, while the $\frac{v_s}{v_p}$ ratio is above one.

A good overlap of the results, as well as the usefulness of the graph representation for a preliminary analysis of practical situations are found.

For example using the values of the second column in Table 6-10, $t_d/T_{75} = 0{,}3$, $F_{dyn}/E_{p,75} = 3{,}65$ and $v_d/v_{p,75}$ =3, it results that the red marked dot, corresponding to the series 1 represented in Figure 6-24, interpolates graphically well between the diagrams for $F_{dyn}/E_{p,75} = 3{,}33$ and $5{,}00$.

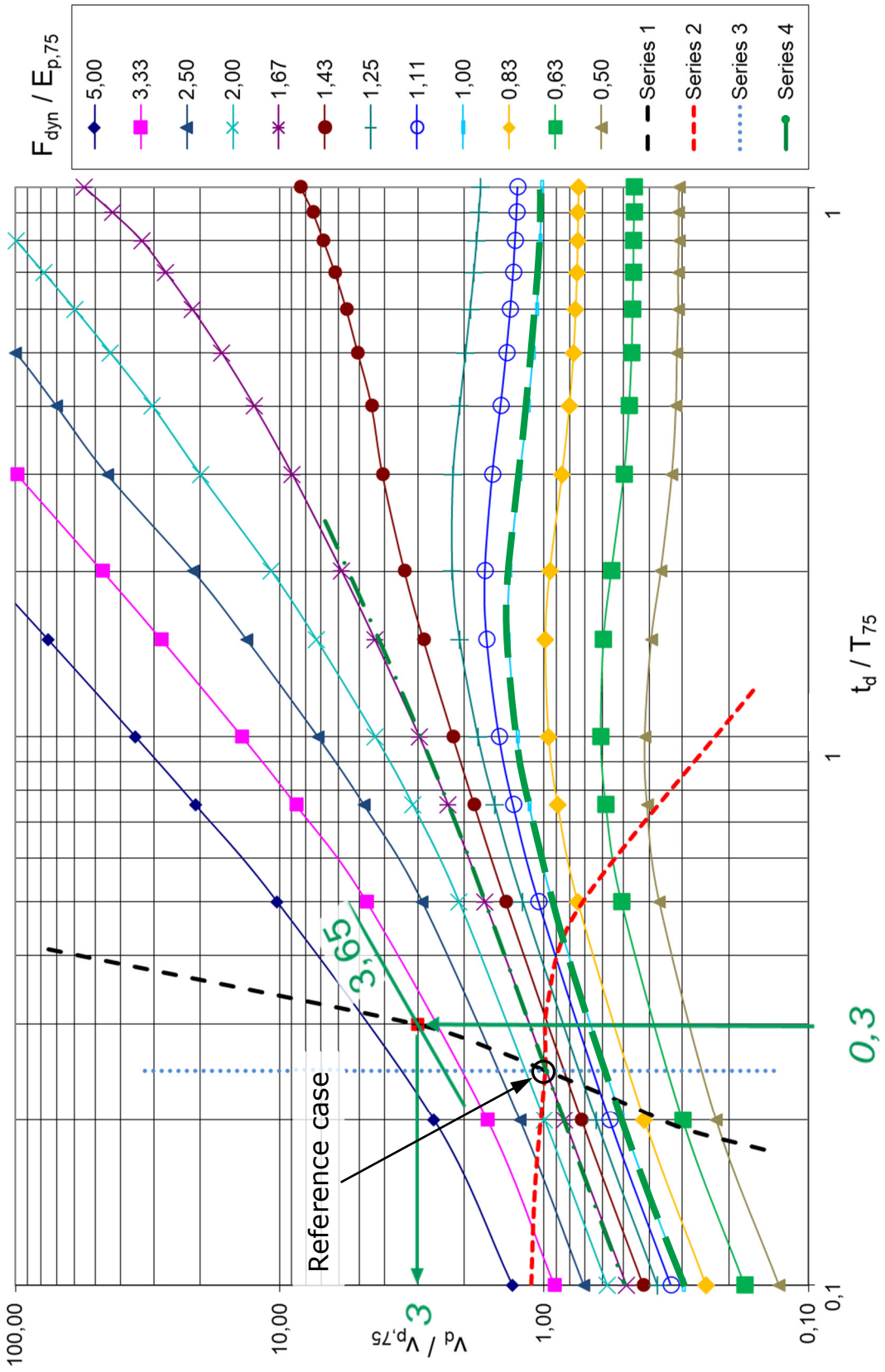

Figure 6-25: Dimensionless representation of the maximum dynamic displacement for the four series presented in Chapter 6.6 plotted together with the diagrams from Figure 6-24

Chapter 7. Conclusions and further development

7.1 Conclusions of own research

Knowing the passive earth resistance under shock-type loads is extremely important to assure that the ultimate and serviceability limit states are not exceeded in the case of accidental actions due to collision of vehicles with structures.

Previous papers that provide a calculation model validated by tests are not known. Thus, the paper approaches a fundamental subject of the nonlinear soil dynamics field and it concentrates on investigating the passive earth resistance under shock-type loads in ideal conditions. These are the parallel plane and horizontal movement of the wall, as well as the plane strain state. The soil is non-cohesive and dry.

The return of the structure to the initial position after the maximum impact displacement is reached depends on more factors and boundary conditions, than those involved until that moment and therefore becomes uncertain. The author considered essential to determine the maximum displacement of the structure induced by the dynamic load for the case of passive earth resistance under shock-type loads.

The research started with the static passive earth resistance mobilization in order to develop and validate a mathematical model, which was later extended for the dynamic case, by adding the inertial forces. The model was transposed in a calculation program and was validated on physical models.

Holzlöhner (1995) based his dynamic calculation model to describe the behaviour of a retaining structure collided by a barge on Vogt's (1984) empirical hypothesis of passive earth resistance mobilization under static loads, and his own hypothesis for the mobilization of the soil's mass. The basic assumptions of this model, consisting of the compressibility of the monolith and a progressive soil mass mobilization, are used for the model developed within this research. The author proposes his own passive earth resistance mobilization hypothesis which depends on the mobilized mass of the monolith and its displacement. Therefore, by applying static equilibrium conditions during the mobilization of the passive resistance, as well boundary conditions, relevant functions for the static passive resistance mobilization and for the mass of the monolith were obtained.

Firstly, the author studied the static passive earth resistance mobilization phenomenon based on reduced-scale physical models. For this purpose he developed an experimental stand devoted to this fundamental research subject. The main component of the experimental stand is the glazed channel which has a mobile wall with one degree of freedom – horizontal displacement. The author compared the kinematics of the passive earth resistance mobilization in static and dynamic conditions by using the optical analysis method of the physical model tests, proving the applicability of Coulomb's theory for the dynamic shock-type load case. Based on the author's knowledge, this research analysis method was premiered in soil dynamics.

The mathematical model of passive earth resistance mobilization under a horizontal, monotonous and constant velocity movement was validated and calibrated based on passive resistance and pressure distribution measurements, as a function of wall displacement, obtained by physical model tests.

The low geological stress level in the physical model is due to reduced-scale models in 1 g gravitational acceleration conditions. A direct transposal of the results measured on physical models to real-scale, by dimensional analysis, was not aimed because of the dependence of the internal friction angle upon the stress level. Instead, the validation of the mathematical models was pursued, which can be used for any scale. By taking the static parameter v_p/h out of the EN 1997:1 standard, or more detailed in the DIN 4085:2011 one, the model proposed by the author can be scaled for real size situations, thereby it can be used in design and analysis practice for accidental impact actions due to vehicles colliding with structures.

The applicability of the model can be extended to any type of vertical plane structures, which are in contact with the retained soil, and for which a horizontal displacement is expected, and which can be assimilated by a plane strain state. Although in many cases the problem is not a plane one, this approach is the most conservative, since it leads to a safe design displacement value. This is due to the imaginary isolation of a portion or vertical strip of the impact wall corresponding to a least the width of the colliding object. Following the test results on own physical models, it was observed that the wall returns to the initial position following a similar failure surface as the one of the active earth pressure mobilization for both the static case, as well as for the dynamic one. Therefore, the adjacent areas of the impacted structure and the neighbouring soil masses are no longer involved through friction and own inertia in the impact,

and in the imaginary model thus created a similar stress state with the physical model is obtained, but for which the sand-side wall friction is not considered. This plane stress state, with the neglected soil prism-side wall friction, is the most conservative approach that any problem can be reduced to. An intermediate hypothesis, also on the conservative side, can be the inclusion of the soil-side wall friction in the calculation model, by conservatively admitting that the sides are subjected to friction forces obtained by integrating the at-rest pressure on the surface and multiplying it with the tangent of the soil's internal friction angle. All of the above mentioned approaches include the simplification assumption that the entire energy transmitted to the structure after impact is consumed during the movement of the wall in the direction of the passive resistance mobilization, by the work produced by the friction forces on the inclined plane and the variation of the potential energy of the soil prism's mass, which is moving upwards on the inclined plane. In fact, a certain part of the received energy during impact is transformed inside the deformable prism in work produced by internal friction forces, and another part is transmitted as waves and absorbed by the soil body. For the cases where the approaches above are too conservative, based on a structural volume analysis, extending the isolated equivalent strip's width can be considered to assimilate the plane strain state in each section with a value that should be calculated based on strength and stiffness of the impacted structure.

As an alternative, the physical tests were also analysed by finite element method, using the PLAXIS 2D software package. The results obtained for the dynamic case offer a safe approximation and they are presented within this paper. The FEM model was calibrated using the static physical model tests. The analysis performed for this research had the purpose to qualitatively validate the application of FEM to calculate the passive pressure under shock-type loads. The obtained results confirm the adequacy of the method. The use of FEM is recommended to calculate the passive resistance under shock-type loads only if they are verified with real-scale models, centrifuge tests or by using theoretical models as the one proposed in this paper.

Finally, several selected practical examples of applying the mathematical model developed by the author are presented in chapters 6.5, 6.6 and 6.7. The examples consist of passive earth pressure calculations, in case several common transportation vehicles collide with retaining walls.

Furthermore, a simplified preliminary analysis is recommended as exemplified in chapter 6.8, in order to identify the design cases in which the dynamic response may lead to the system's loss of stability.

7.2 Significance of the research

The investigation of the passive resistance mobilization phenomenon under shock-type loads is a fundamental research subject in the field of nonlinear soil dynamics. It offered the author the possibility to be the first to approach several basic subjects, as well to find ways to resolve them. The main contributions of the research are:

1. Making a bibliographical research on the passive resistance mobilization under shock-type loads;
2. Making an experimental stand to investigate the passive pressure mobilization under both static and dynamic shock-type loads, assuring the same boundary conditions in both cases;
3. Experimental results on passive pressure mobilization under static loads;
4. Experimental results on passive pressure mobilization under shock-type loads;
5. Using optical analysis with a high-speed camera to investigate the mobilization phenomenon of the passive resistance in the soil prism during dynamic shock-type tests;
6. Making an algorithm and a calculation program to derivate the velocity vector field of the mobilized soil prism, in order to highlight the maximum gradient of the failure surface;
7. Making an algorithm and a calculation program to integrate over surface the acceleration vector field of the mobilized soil prism, in order to validate the method by comparison with the accelerometer measurements;
8. Making a mathematical model based on an own static passive resistance mobilization hypothesis as a function of the mobilized mass of the compressible monolith and its displacement;
9. Calibrating the mathematical model based on the static and dynamic physical model tests results;
10. Implementing the mathematical model in programs to calculate passive pressure under both static and dynamic shock-type loads, developed in the "Mathematica 7" numeric and symbolic mathematics software;
11. Making a comparative calculation using the finite element method to model the static and dynamic shock-type loads;

12. Applying the mathematical model for full-scale structures subjected to dynamic actions due to collision of different vehicle types;
13. Proposing a preliminary analysis method for practical situations by using the maximum dynamic displacement graph plotted on impact duration, for different amplitudes of the dynamic force;
14. Publishing the preliminary results of the experimental research in the book "Passiver Erddruck auf Stützkonstruktionen bei stoßartiger Belastung", which served as a basis for the provision introduced in the DIN 1054:2005 German standard, stating that the soil reactions due to impact can be lower or higher than the static case.

7.3 Further research and development opportunities

From the main paths and possibilities for the development of the research conducted by the author, the following one are the most promising in the future:

1. Making thorough numerical analyses, through finite element method, finite difference method or discrete element method, on planar and spatial models and comparing them with the results of the physical and mathematical models produced by the author;
2. Making a representative centrifuge test series, considering a large variation range of amplitudes and impulse durations and starting from the modelling of the most probable situations, like the impact of vehicles, trains or ships on internal waterways with bridge columns;
3. Considering the rotational motion around the upper and lower margins of the plane structure's face on which the passive pressure is mobilized under shock-type loads;
4. Considering embedded structures like diaphragm walls or high diameter bored piles supported by different types of elements;
5. Consideration of a cohesive soil provided that dynamic parameters adequate to the strain state, the degree of saturation and the effective stress state are used and that excessive pore water pressure develops. It is recommended to extend the proposed mathematical model by adding cohesion forces on the inclined plane and adhesion forces on the vertical wall side, if geotechnical parameters characteristic to the phenomenon's "dynamic" can be defined based on the results of specific tests and they can be assumed constant or offer a cautious estimation during the dynamic displacement. Caution is advised at considering the geotechnical parameters in this case.

The author considers that from all the research possibilities listed above, further research of the phenomenon by FEM modelling is the most feasible in the near future, apart from the particular case of special funding through a research program. Therefore, in an initial stage the results of the models

developed by the author can be used to compare the FEM results, followed by the mutual validation through tests at real stress levels.

In figure 7-1 is represented a synoptic outline of the research made, starting with the static physical model as basis for the validation of the mathematical model which was extended for the dynamic case of the impact loading based on the results of the dynamic physical model. As a main result of the research, for practical cases the design engineer may use the values of the ultimate static passive displacement and resistance given by any standard, literature reference or model as input in the mathematical model developed by the author in order to calculate the horizontal parallel displacement of a planar full-scale structure subjected to any shock-type load. For a simplified preliminary approach, the use of the charts represented in the figures 6-24 and 6-25 is recommended. For more complex cases or need for accurate results in special cases, further research is required as outlined in the proposed development possibilities.

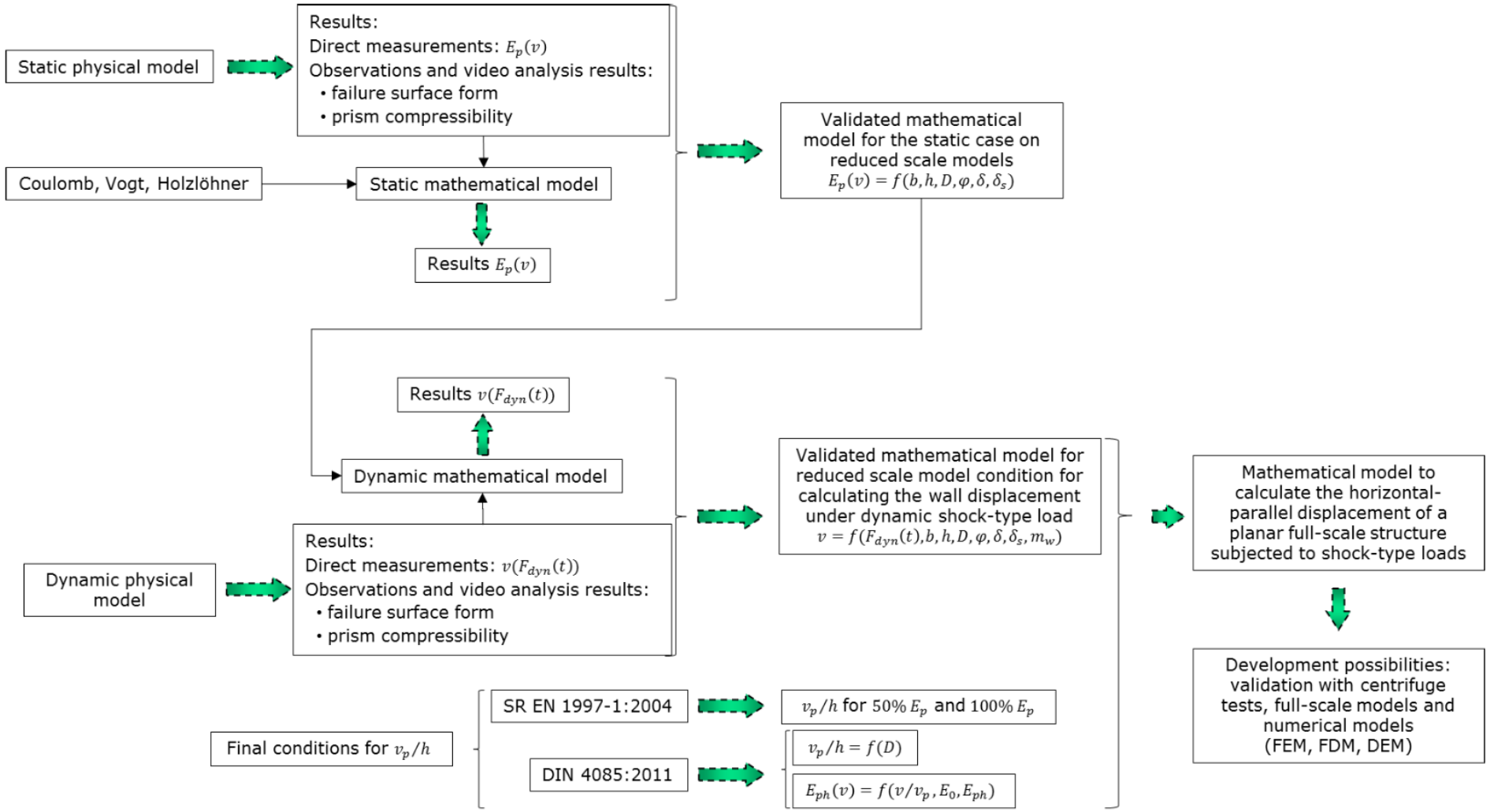

Figure 7-1: Synoptic outline of the research made, the results obtained and the development possibilities

Annex 1 Numerical calculation program which uses the mathematical model to model the static and dynamic tests

```
Clear[ϕ, θ, ka0, kap, kk, h, a, ac, o, b, c, w, m, e, p, T, t, ta, tkraft,
  kraft, kt, pinterp, imp, tversch, versch, vt, vinterp, ddp] Clear[imp];
 SetDirectory["D:\\DISS6"]; imp = "TS_DynamBreit-09_24_bearbeitet.txt";
ta = Import[imp, "Table"]; tkraft = ta[[All, 1]];
 kraft = 1 ta[[All, 2]]; imax = Length[kraft];
tmax = 0.1`; tversch = ta[[All, 1]]; versch = ta[[All, 3]]

vt = Table[{tversch[[i]], versch[[i]]}, {i, 1, imax - 1}]
 vtinterp = Interpolation[vt];
h = 0.24`; b = 0.32`; g = 9.81`; LD = 0.9`; Print["D = ", LD]; ρmax = 1.72`;
 ρmin = 1.47`; ρ := ρmin + LD (ρmax - ρmin); Print["ρ = ", ρ];
W[t_] := Evaluate[vtinterp[t]]; Z[t_] := Evaluate[t];
 imax = 25; dt = tmax/imax; fxvekt = {}; fyvekt = {};
 Do[fxvekt = Append[fxvekt, W[j dt]]; fyvekt = Append[fyvekt, Z[j dt]], {j, 0, imax}];
 WEG = ListPlot[Transpose[{Flatten[fyvekt], Flatten[fxvekt]}], Joined → False]
 (*Export["VERSCH_09_GEMESSEN fuer PLAXIS_DYNAMISCH.txt",
   Transpose[{Flatten[fyvekt],Flatten[fxvekt]}],"Table"];*) imax = Length[kraft];
PVI09 = Plot[vtinterp[t], {t, 0, tmax}, Frame → True, GridLines → Automatic,
  AxesLabel → {"Zeit in s", "Wandverschiebung in cm"}, AxesOrigin → {0.02`, 0.002`},
  PlotStyle → {{Thickness[0.004`], RGBColor[0, 0, 1]}},
  PlotRange → All, BaseStyle → {FontSize → 16}]
Kraftmax = Max[kraft]; Print["Kraftmax =", Kraftmax];
 kt = Table[{tkraft[[i]], kraft[[i]]}, {i, 1, imax}];
 (*ListPlot[kt,PlotRange→All];*) pinterp = Interpolation[kt];
W[t_] := Evaluate[100 pinterp[t]/32]; Z[t_] := Evaluate[t];
 imax = 100; dt = tmax/imax; fvvekt = {}; fwvekt = {};
 Do[fvvekt = Append[fvvekt, W[j dt]]; fwvekt = Append[fwvekt, Z[j dt]], {j, 0, imax}];
 STOSS = ListPlot[Transpose[{Flatten[fwvekt], Flatten[fvvekt]}], Joined → False]
 (*Export["STOSS_09_GEMESSEN fuer PLAXIS_DYNAMISCH.txt",
   Transpose[{Flatten[fwvekt],Flatten[fvvekt]}],"Table"];*) imax = Length[kraft];
PPI09 = Plot[pinterp[t], {t, 0, tmax}, Frame → True, GridLines → Automatic,
    AxesLabel → {"Zeit in s", "Stoßkraft in kN"}, AxesOrigin → {0.02`, 1},
    PlotStyle → {Thickness[0.005`], RGBColor[0, 0, 0], PointSize[0.015`]},
    PlotRange → All, BaseStyle → {FontSize → 16}]
  verschi = Table[{tversch[[i]], 1/5 (versch[[i - 2]] + versch[[i - 1]] +
          versch[[i]] + versch[[i + 1]] + versch[[i + 2]])}, {i, 3, imax - 3}];
  aaa = verschi[[All, 1]]; bbb = verschi[[All, 2]]; Clear[ddp, ddpint]; aaa[[0]] = 0;
  ddp = Table[{aaa[[i]], (bbb[[i + 2]] - 2 bbb[[i]] + bbb[[i - 2]])/(2 (aaa[[i]] - aaa[[i - 1]]))^2}, {i, 5, imax - 5}];
```

```
ddpint = Interpolation[ddp]
PDDVI09 = Plot[0.01` ddpint[t], {t, 0.01`, tmax - 0.01`},
  PlotStyle → {{Thickness[0.0005`], RGBColor[1, 0, 1]}}, PlotRange → All,
  AxesOrigin → {0.`, 0.`}, GridLines → Automatic, BaseStyle → {FontSize → 16}]
g = 9.81`; LD = 0.9`; Print["D = ", LD]; ρmax = 1.72`; ρmin = 1.47`;
ρ := ρmin + LD (ρmax - ρmin); Print["ρ = ", ρ]; φ :=
1/180 (25.5` + 25.5` LD) π; Print["φ = ", φ 180/π, "°"];
δ := 13 π/180; Print["δ = ", δ 180/π, "°"];
α = 2; Print["α = ", α]; h = 0.24`; a :=
 0.0275` - 0.113` (LD - 0.9`);
Print["2a h = ", 2 a h] b = 0.32`; mw = 0.01275` b/0.32`;
 Print["mw = ", mw];
 θ := ArcCot[Csc[φ] Sec[δ + φ] √(Cos[δ] Sin[φ] Sin[δ + φ]) + Tan[δ + φ]];
 θ = N[θ]; Print["θ = ", θ 180/π, "°"]; MBoden = ρ h^2 b/(2 Tan[θ]);
 Print["MBoden = ", MBoden, " to"]; Mmax = mw + ρ h^2 b/(2 Tan[θ]);
 Print["Mmax = ", Mmax, " to"]; L = h/Tan[θ];
 Print["L = ", L]; k0 = N[1 - Sin[φ]]; Print["k0 = ", k0];
 δs = 8.5` π/180; Print["δs = ", δs 180/π, "°"];
 RsBeiwert = 2 k0 Tan[δs]; Print["RsBeiwert = ", RsBeiwert];
k0h = k0; Print["k0h = ", k0h]; E0 = 1/2 (ρ g h^2 b) k0;
 Print["\!\(\*\nStyleBox[\nSubscriptBox[\nStyleBox[\"E\",\nFontSize->12],
    \"0\"],\nFontSize->11]\)= ", E0]; E0h = 1/2 (ρ g h^2 b) k0h;
 Print["\!\(\*\nStyleBox[\nSubscriptBox[\nStyleBox[\"E\",\nFontSize->12],
    \"0\"],\nFontSize->11]\) = ", E0h];
 kp[θ] := Tan[φ + θ]/(Tan[θ] (Cos[δ] - Sin[δ] Tan[φ + θ])); kp[θ] = N[kp[θ]];
 Print["kp[θ] = ", kp[θ]];
Ep = 1/2 (ρ g h^2 b) kp[θ]; Eph = Ep Cos[δ]; Print["Eph[θ] = ", Eph]; kph = kp[θ] Cos[δ];
 kapformula[i_] = kph; Print["kph[θ] = ", kph]; Mmax = mw + ρ h^2 b/(2 Tan[θ]);
 Print["Mmax = ", Mmax, " to"]; m[t_] := Which[w[t] ≤ 0, 0, 0 < w[t] < 2 a h/Cos[θ],
```

$$(\text{Mmax}-\text{mw})\left(2\left(\frac{\text{w[t]}\,\text{Cos}[\theta]}{2\,\text{a}\,\text{h}}\right)^{1/\alpha}-\left(\frac{\text{w[t]}\,\text{Cos}[\theta]}{2\,\text{a}\,\text{h}}\right)^{2/\alpha}\right),\ \text{w[t]}\geq\frac{2\,\text{a}\,\text{h}}{\text{Cos}[\theta]},\ \text{Mmax}-\text{mw}\Big];$$

$$(*\text{tm[t\_]:=Which}\Big[\text{w[t]}\leq 0,0,0<\text{w[t]}<\frac{2\,\text{a}\,\text{h}}{\text{Cos}[\theta]},\frac{2^{1-\frac{1}{\alpha}}\,\text{Cos}[\theta]\,\left(\frac{\text{Cos}[\theta]\,\text{w[t]}}{\text{a}\,\text{h}}\right)^{-1+\frac{1}{\alpha}}}{\text{a}\,\text{h}\,\alpha}-\frac{2^{1-\frac{2}{\alpha}}\,\text{Cos}[\theta]\,\left(\frac{\text{Cos}[\theta]\,\text{w[t]}}{\text{a}\,\text{h}}\right)^{-1+\frac{2}{\alpha}}}{\text{a}\,\text{h}\,\alpha},$$

$$\text{w[t]}\geq\frac{2\,\text{a}\,\text{h}}{\text{Cos}[\theta]},0\Big];*)$$

$$\text{tm[t\_]}:=\partial_{\text{w[t]}}\text{m[t]};\ \text{eee[t\_]}:=\text{Which}\Big[\text{w[t]}\leq 0,\ \frac{1}{2}\left(\rho\,\text{g}\,\text{h}^2\,\text{b}\right)\text{k0h},\ 0<\text{w[t]}<\frac{2\,\text{a}\,\text{h}}{\text{Cos}[\theta]},$$

$$\frac{1}{2}\left(\rho\,\text{g}\,\text{h}^2\,\text{b}\right)\left(1-\left(\frac{\text{w[t]}\,\text{Cos}[\theta]}{2\,\text{a}\,\text{h}}\right)^{1/\alpha}\right)^2\text{k0h},\ \text{w[t]}\geq\frac{2\,\text{a}\,\text{h}}{\text{Cos}[\theta]},\ 0\Big];$$

$$\text{d}=3.9`;\ \beta[\text{w}]:=\text{Which}\Big[\text{w[t]}\leq 0,\ 0,\ 0<\text{w[t]}<\frac{2\,\text{a}\,\text{h}}{\text{d}\,\text{Cos}[\theta]},$$

$$\delta\left(2\left(\frac{\text{d}\,\text{w[t]}\,\text{Cos}[\theta]}{2\,\text{a}\,\text{h}}\right)^{1/\alpha}-\left(\frac{\text{d}\,\text{w[t]}\,\text{Cos}[\theta]}{2\,\text{a}\,\text{h}}\right)^{2/\alpha}\right),\ \text{w[t]}\geq\frac{2\,\text{a}\,\text{h}}{\text{d}\,\text{Cos}[\theta]},\ \delta\Big];$$

$$\text{p[t\_]}:=\text{If}\Big[\text{pinterp[t]}\leq(1+\text{RsBeiwert})$$

$$\Bigg(\Bigg(\text{Cos}\Big[\delta\left(2\left(\frac{\text{d}\,\text{w[t]}\,\text{Cos}[\theta]}{2\,\text{a}\,\text{h}}\right)^{1/\alpha}-\left(\frac{\text{d}\,\text{w[t]}\,\text{Cos}[\theta]}{2\,\text{a}\,\text{h}}\right)^{2/\alpha}\right)\Big](\text{Mmax}-\text{mw})$$

$$\left(2\left(\frac{\text{w[t]}\,\text{Cos}[\theta]}{2\,\text{a}\,\text{h}}\right)^{1/\alpha}-\left(\frac{\text{w[t]}\,\text{Cos}[\theta]}{2\,\text{a}\,\text{h}}\right)^{2/\alpha}\right)\text{g}\,\text{Tan}[\theta+\varphi]\Bigg)\Big/$$

$$\Bigg(\text{Cos}\Big[\delta\left(2\left(\frac{\text{d}\,\text{w[t]}\,\text{Cos}[\theta]}{2\,\text{a}\,\text{h}}\right)^{1/\alpha}-\left(\frac{\text{d}\,\text{w[t]}\,\text{Cos}[\theta]}{2\,\text{a}\,\text{h}}\right)^{2/\alpha}\right)\Big]-$$

$$\text{Sin}\Big[\delta\left(2\left(\frac{\text{d}\,\text{w[t]}\,\text{Cos}[\theta]}{2\,\text{a}\,\text{h}}\right)^{1/\alpha}-\left(\frac{\text{d}\,\text{w[t]}\,\text{Cos}[\theta]}{2\,\text{a}\,\text{h}}\right)^{2/\alpha}\right)\Big]\,\text{Tan}[\theta+\varphi]\Bigg)+$$

$$\Bigg(\left(\rho\,\text{g}\,\text{h}^2\,\text{b}\right)\left(1-\left(\frac{\text{w[t]}\,\text{Cos}[\theta]}{2\,\text{a}\,\text{h}}\right)^{1/\alpha}\right)^2\text{k0h}$$

$$\text{Cos}\Big[\delta\left(2\left(\frac{\text{d}\,\text{w[t]}\,\text{Cos}[\theta]}{2\,\text{a}\,\text{h}}\right)^{1/\alpha}-\left(\frac{\text{d}\,\text{w[t]}\,\text{Cos}[\theta]}{2\,\text{a}\,\text{h}}\right)^{2/\alpha}\right)\Big]\Bigg)\Big/$$

$$\Bigg(2\left(\text{Cos}\Big[\delta\left(2\left(\frac{\text{d}\,\text{w[t]}\,\text{Cos}[\theta]}{2\,\text{a}\,\text{h}}\right)^{1/\alpha}-\left(\frac{\text{d}\,\text{w[t]}\,\text{Cos}[\theta]}{2\,\text{a}\,\text{h}}\right)^{2/\alpha}\right)\Big]-$$

$$\text{Sin}\Big[\delta\left(2\left(\frac{\text{d}\,\text{w[t]}\,\text{Cos}[\theta]}{2\,\text{a}\,\text{h}}\right)^{1/\alpha}-\left(\frac{\text{d}\,\text{w[t]}\,\text{Cos}[\theta]}{2\,\text{a}\,\text{h}}\right)^{2/\alpha}\right)\Big]\,\text{Tan}[\theta+\varphi]\Bigg)\Bigg)\Bigg)\ \&\&$$

$$\text{t}<\frac{\text{tmax}}{5},\ (1+\text{RsBeiwert})\Bigg(\Bigg(\text{Cos}\Big[\delta\left(2\left(\frac{\text{d}\,\text{w[t]}\,\text{Cos}[\theta]}{2\,\text{a}\,\text{h}}\right)^{1/\alpha}-\left(\frac{\text{d}\,\text{w[t]}\,\text{Cos}[\theta]}{2\,\text{a}\,\text{h}}\right)^{2/\alpha}\right)\Big]$$

$$(\text{Mmax}-\text{mw})\left(2\left(\frac{\text{w[t]}\,\text{Cos}[\theta]}{2\,\text{a}\,\text{h}}\right)^{1/\alpha}-\left(\frac{\text{w[t]}\,\text{Cos}[\theta]}{2\,\text{a}\,\text{h}}\right)^{2/\alpha}\right)\text{g}\,\text{Tan}[\theta+\varphi]\Bigg)\Big/$$

$$\left(\text{Cos}\left[\delta\left(2\left(\frac{\text{d w[t] Cos}[\theta]}{2\,\text{a h}}\right)^{1/\alpha}-\left(\frac{\text{d w[t] Cos}[\theta]}{2\,\text{a h}}\right)^{2/\alpha}\right)\right]-\right.$$

$$\left.\text{Sin}\left[\delta\left(2\left(\frac{\text{d w[t] Cos}[\theta]}{2\,\text{a h}}\right)^{1/\alpha}-\left(\frac{\text{d w[t] Cos}[\theta]}{2\,\text{a h}}\right)^{2/\alpha}\right)\right]\text{Tan}[\theta+\varphi]\right)+$$

$$\left(\left(\rho\,\text{g h}^2\,\text{b}\right)\left(1-\left(\frac{\text{w[t] Cos}[\theta]}{2\,\text{a h}}\right)^{1/\alpha}\right)^2\text{k0h}\right.$$

$$\left.\text{Cos}\left[\delta\left(2\left(\frac{\text{d w[t] Cos}[\theta]}{2\,\text{a h}}\right)^{1/\alpha}-\left(\frac{\text{d w[t] Cos}[\theta]}{2\,\text{a h}}\right)^{2/\alpha}\right)\right]\right)\Big/$$

$$\left(2\left(\text{Cos}\left[\delta\left(2\left(\frac{\text{d w[t] Cos}[\theta]}{2\,\text{a h}}\right)^{1/\alpha}-\left(\frac{\text{d w[t] Cos}[\theta]}{2\,\text{a h}}\right)^{2/\alpha}\right)\right]-\text{Sin}\right.\right.$$

$$\left.\left.\left[\delta\left(2\left(\frac{\text{d w[t] Cos}[\theta]}{2\,\text{a h}}\right)^{1/\alpha}-\left(\frac{\text{d w[t] Cos}[\theta]}{2\,\text{a h}}\right)^{2/\alpha}\right)\right]\text{Tan}[\theta+\varphi]\right)\right)\Big],\ \text{pinterp[t]}\Big];$$

```
(*p[t_]:=If[pinterp[t]≤( Cos[δ] (Mmax-mw) Cos[θ] (w[t]/(a*h)-Cos[θ] (w[t]/(2*a*h))^2)
        g Tan[θ+φ]/ (Cos[δ]-Sin[δ] Tan[θ+φ])+
      (1/2 (ρ g h^2 b)*(1-Cos[θ] w[t]/(2a h))^2 k0h Cos[δ])/ (Cos[δ]-Sin[δ] Tan[θ+φ]))&&
   t<tmax/10, Cos[δ] (Mmax-mw) Cos[θ] (w[t]/(a*h)-Cos[θ] (w[t]/(2*a*h))^2) g Tan[θ+φ]/
    (Cos[δ]-Sin[δ] Tan[θ+φ])+
    (1/2 (ρ g h^2 b)*(1-Cos[θ] w[t]/(2a h))^2 k0h Cos[δ])/
    (Cos[δ]-Sin[δ] Tan[θ+φ]),pinterp[t]];*)
```

$$\text{T = NDSolve}\left[\left\{\text{mw w''[t] Cos}[\theta]+(1+\text{RsBeiwert})\right.\right.$$

$$\left(\frac{\text{Cos}[\beta[w]]\,\text{m[t] g Tan}[\theta+\varphi]}{\text{Cos}[\beta[w]]-\text{Sin}[\beta[w]]\,\text{Tan}[\theta+\varphi]}+\frac{\text{eee[t] Cos}[\beta[w]]}{\text{Cos}[\beta[w]]-\text{Sin}[\beta[w]]\,\text{Tan}[\theta+\varphi]}\right)+$$

$$\frac{\text{Cos}[\beta[w]]\,\text{m[t] w''[t] (Cos}[\theta]+\text{Sin}[\theta]\,\text{Tan}[\theta+\varphi])}{\text{Cos}[\beta[w]]-\text{Sin}[\beta[w]]\,\text{Tan}[\theta+\varphi]}+$$

$$\frac{\text{Cos}[\beta[w]]\,\text{tm[t] w'[t]}^2\,(\text{Cos}[\theta]+\text{Sin}[\theta]\,\text{Tan}[\theta+\varphi])}{\text{Cos}[\beta[w]]-\text{Sin}[\beta[w]]\,\text{Tan}[\theta+\varphi]}-\text{p[t]}==0,$$

$$\left.\left.\text{w[0]}==0,\ \text{w'[0]}==0\right\},\ \text{w},\ \{\text{t},\ 0,\ \text{tmax}\}\right];\ \text{Print["Gata ec."];}$$

```
W[t_] := Evaluate[Cos[θ] w[t] /. T];

wSol[z_] := w[x] /. T /. x → z;

i = 0; iMax = 0;
wMax = First[wSol[0]];

thr = -10^10;
```

```
i = 0;
While[First[wSol[i]] ≥ thr && i ≤ 5, i += 0.01`;
  If[wMax < First[wSol[i]], wMax = First[wSol[i]]; tMaxW = i;];
  If[First[wSol[i]] > 0 && i ≥ Tstoß/2, thr = 0;];];
Print["wMax = ", wMax];

P09 = Plot[Evaluate[p[t] /. T], {t, 0, tmax}, Frame → True, GridLines → Automatic,
    AxesLabel → {"Zeit in s", "Stoßkraft in kN"}, AxesOrigin → {0.002`, 0.002`},
    PlotStyle → {{Thickness[0.0001`], RGBColor[1, 0, 0]}},
    BaseStyle → {FontSize → 16}, PlotRange → All] PW09 =
  Plot[Evaluate[100 Cos[θ] w[t] /. T], {t, 0, tmax}, Frame → True,
    GridLines → Automatic, AxesLabel → {"Zeit in s", "Wandverschiebung in cm"},
    AxesOrigin → {0.002`, 0.002`}, PlotStyle → {{Thickness[0.005`],
      RGBColor[0, 0, 1], Dashing[{0.002`, 0.01`, 0.02`, 0.01`}]}},
    BaseStyle → {FontSize → 16}, PlotRange → All] Show[PVI09, PW09] PEE09 =
   Plot[Evaluate[β[w] /. T], {t, 0, tmax}, Frame → True, GridLines → Automatic,
    AxesLabel → {"Zeit in s", "BETA in RAD"}, AxesOrigin → {0.01`, 0.2`},
    PlotStyle → {{Thickness[0.005`], RGBColor[1, 0, 0]}},
    BaseStyle → {FontSize → 16}, PlotRange → All]
PEE09 = Plot[Evaluate[(1 + RsBeiwert) (eee[t] Cos[β[w]])/(Cos[β[w]] - Sin[β[w]] Tan[θ + φ]) /. T],
  {t, 0, tmax}, Frame → True, GridLines → Automatic,
  AxesLabel → {"Zeit in s", "Erdruhedruck in kN"}, AxesOrigin → {0.01`, 0.2`},
  PlotStyle → {{Thickness[0.005`], RGBColor[1, 0, 0]}},
  BaseStyle → {FontSize → 16}, PlotRange → All]
PE09 = Plot[Evaluate[(1 + RsBeiwert)
      (Cos[β[w]] m[t] g Tan[θ + φ])/(Cos[β[w]] - Sin[β[w]] Tan[θ + φ]) + (eee[t] Cos[β[w]])/(Cos[β[w]] - Sin[β[w]] Tan[θ + φ]) /. T],
    {t, 0, tmax}, Frame → True, GridLines → Automatic, AxesLabel →
     {"Zeit in s", "Erdwiderstand in kN"}, AxesOrigin → {0.01`, 0.2`},
    PlotStyle → {{Thickness[0.005`], RGBColor[0, 0, 1]}},
    BaseStyle → {FontSize → 16}, PlotRange → All] PDDW09 =
  Plot[Evaluate[w''[t] /. T], {t, 0, tmax}, Frame → True,
    GridLines → Automatic, AxesLabel → {"Zeit in s",
      "Beschleunigung in m/\!\(\*SuperscriptBox[\(s\), \(2\)]\)"},
    AxesOrigin → {0.02`, 0}, PlotStyle → {{Thickness[0.0005`],
      RGBColor[1, 0, 0]}}, BaseStyle → {FontSize → 16},
    PlotRange → {-25, 40}] Show[PDDW09, PDDVI09] PM09 =
   Plot[Evaluate[m[t] /. T], {t, 0, tmax}, Frame → True, GridLines → Automatic,
    PlotRange → All, AxesLabel → {"Zeit in s", "Masse in t"}, AxesOrigin →
     {0.02`, 0}, PlotStyle → {{Thickness[0.0005`], RGBColor[1, 0, 0]}},
    BaseStyle → {FontSize → 16}] PMTX09 = Plot[Evaluate[
```

$$mw\,w''[t]\,\text{Cos}[\theta] + \frac{\text{Cos}[\beta[w]]\,m[t]\,w''[t]\,(\text{Cos}[\theta] + \text{Sin}[\theta]\,\text{Tan}[\theta+\varphi])}{\text{Cos}[\beta[w]] - \text{Sin}[\beta[w]]\,\text{Tan}[\theta+\varphi]} + \frac{\text{Cos}[\beta[w]]\,tm[t]\,w'[t]^2\,(\text{Cos}[\theta] + \text{Sin}[\theta]\,\text{Tan}[\theta+\varphi])}{\text{Cos}[\beta[w]] - \text{Sin}[\beta[w]]\,\text{Tan}[\theta+\varphi]} /. T\Big],$$

```
{t, 0, tmax}, Frame → True, GridLines → Automatic, AxesLabel →
 {"Zeit in s", "Gesamte Trägheit in kN"}, AxesOrigin → {0.02`, 0},
PlotStyle → {{Thickness[0.007`], RGBColor[1, 0, 0]}},
BaseStyle → {FontSize → 16}, PlotRange → {-2.5`, 3}] PMWX09 =
Plot[Evaluate[mw w''[t] Cos[θ] /. T], {t, 0, tmax}, Frame → True,
 GridLines → Automatic, AxesLabel → {"Zeit in s",
   "Trägheit WAND in kN"}, AxesOrigin → {0.02`, 0}, PlotStyle →
  {{AbsoluteDashing[{5, 5}], Thickness[0.0015`], RGBColor[0, 0, 0]}},
 BaseStyle → {FontSize → 16}, PlotRange → {-0.2`, 0.4`}] PMDBX09 =
Plot[Evaluate[Cos[β[w]] m[t] w''[t] (Cos[θ] + Sin[θ] Tan[θ + φ]) /
    (Cos[β[w]] - Sin[β[w]] Tan[θ + φ]) /. T],
 {t, 0, tmax}, Frame → True, GridLines → Automatic,
 AxesLabel → {"Zeit in s", "Trägheit BODENMASSE in kN"},
 AxesOrigin → {0.02`, 0}, PlotStyle → {{AbsoluteDashing[
     {5, 5}], Thickness[0.0015`], RGBColor[0, 0.2`, 0.8`]}},
 BaseStyle → {FontSize → 16}, PlotRange → {-2, 2}] PMDMX09 =
Plot[Evaluate[Cos[β[w]] tm[t] w'[t]^2 (Cos[θ] + Sin[θ] Tan[θ + φ]) /
    (Cos[β[w]] - Sin[β[w]] Tan[θ + φ]) /. T],
 {t, 0, tmax}, Frame → True, GridLines → Automatic, PlotRange → All,
 AxesLabel → {"Zeit in s", "Trägheit VERÄNDERUNG DER MASSE in kN"},
 AxesOrigin → {0.02`, 0}, PlotStyle → {{AbsoluteDashing[
     {5, 5}], Thickness[0.0015`], RGBColor[0, 0.8`, 0.2`]}},
 BaseStyle → {FontSize → 16}] Show[PMTX09, PMWX09, PMDBX09,
 PMDMX09, PlotRange → {-2, 3}] Show[PPI09, PE09, PMTX09, PMWX09, PMDBX09,
 PMDMX09, PlotRange → {-2, 4}] W[t_] := Evaluate[Cos[θ] w[t] /. T];
Z[t_] := Evaluate[t /. T]; STOSSKRAFT[t_] := Evaluate[p[t] /. T];
imax = 25; dt = tmax/imax; fxvekt = {}; fyvekt = {}; fzvekt = {};
Do[fxvekt = Append[fxvekt, W[i dt]] TextCell[""]; fyvekt = Append[fyvekt,
   Z[i dt]]; fzvekt = Append[fzvekt, STOSSKRAFT[i dt]], {i, 0, imax}];
LPDyn1 = ListPlot[Transpose[{Flatten[fyvekt], Flatten[fxvekt]}],
  Joined →
   False]
LPDyn2 = ListPlot[Transpose[
 {Flatten[
   fyvekt], Flatten[
   fzvekt]}],
Joined → False](*Export[
"VERSCH_09_DYNAMISCH.txt",
Transpose[
```

```
    {Flatten[
      fyvekt],Flatten[
      fxvekt]}],"Table"];*)
  Export["STOSS_09_DYNAMISCH.txt", Transpose[{Flatten[fyvekt], Flatten[fzvekt]}],
    "Table"];
```

D = 0.9

ρ = 1.695

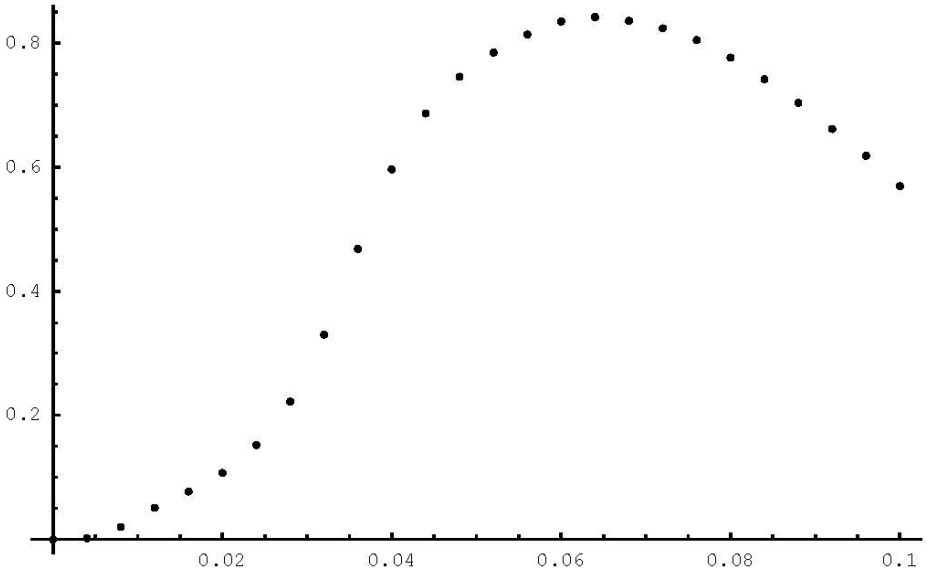

Wandverschiebung in cm

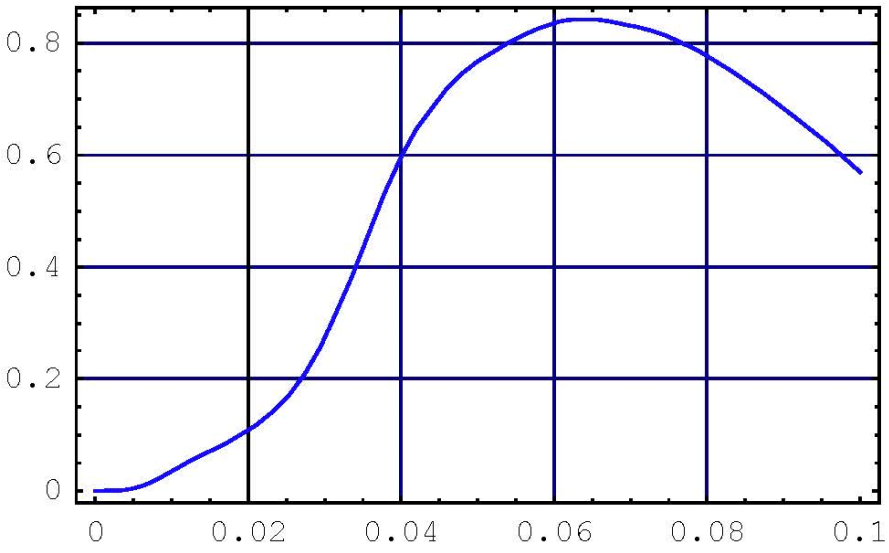

Kraftmax =3.942

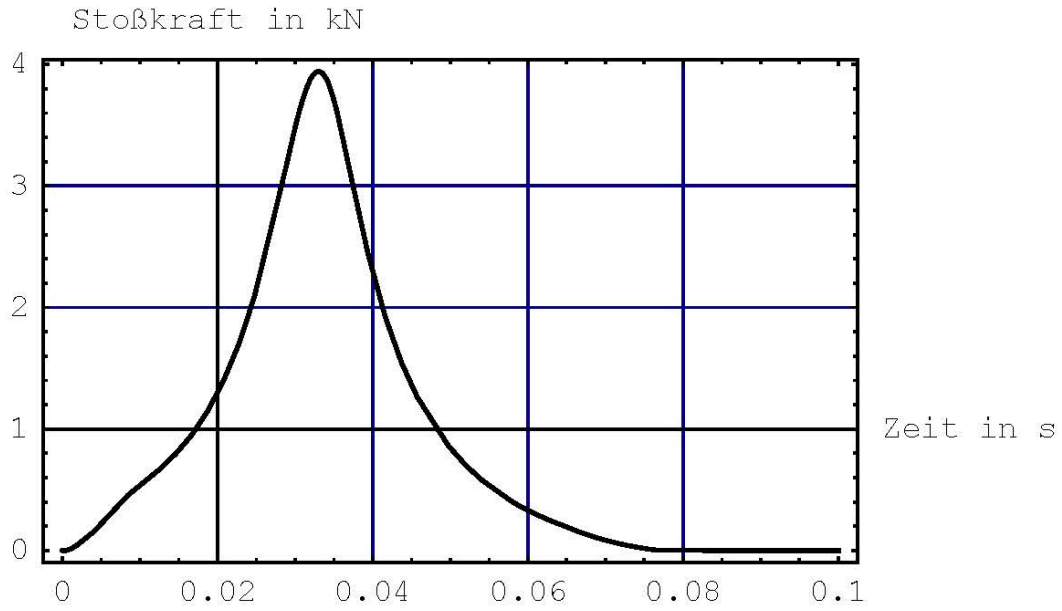

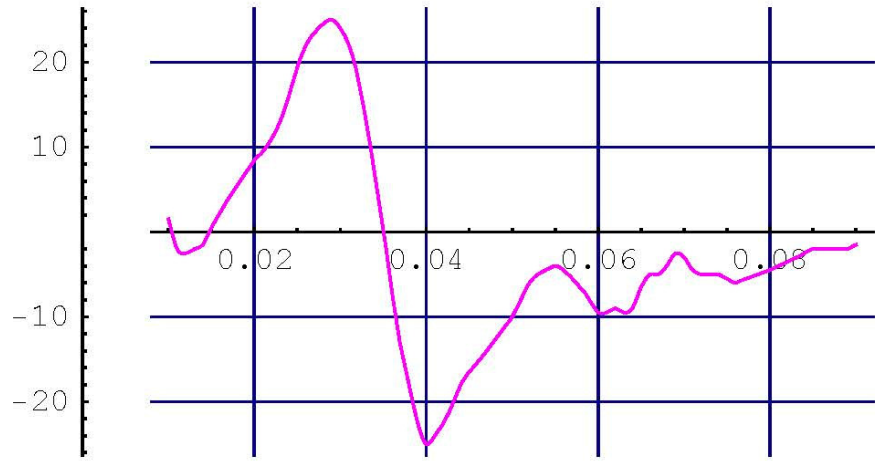

D = 0.9

ρ = 1.695

φ = 48.45°

δ = 13°

α = 2

2a h = 0.0132

mw = 0.01275

θ = 13.786°

MBoden = 0.063665 to

Mmax = 0.076415 to

L = 0.978137

k0 = 0.251623

δs = 8.5°

RsBeiwert = 0.0752106

k0h = 0.251623

E_0= 0.0385595

E_0 = 0.0385595

kp[θ] = 14.1516

Eph[θ] = 2.11305

kph[θ] = 13.7889

Mmax = 0.076415 to

Gata ec.

wMax = 0.00853313

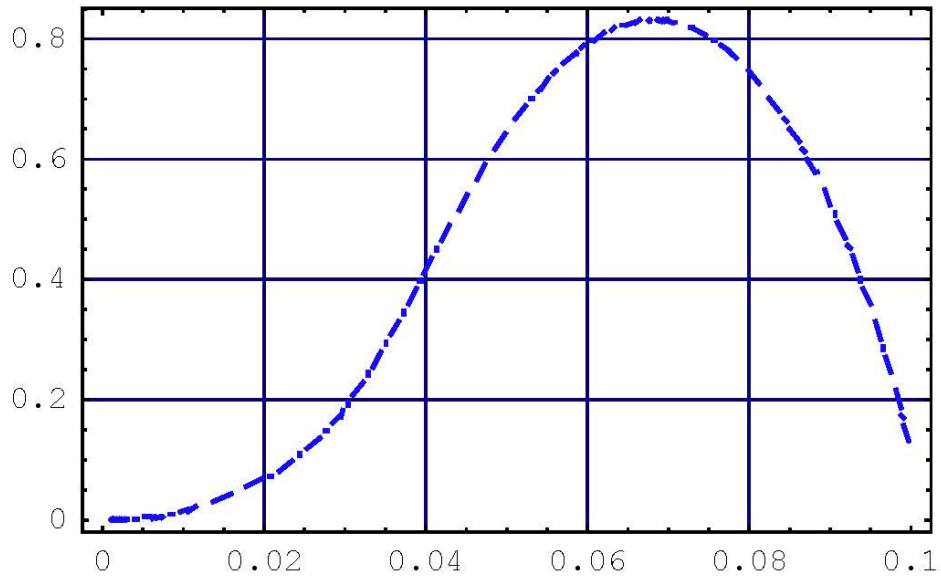

Wandverschiebung in cm

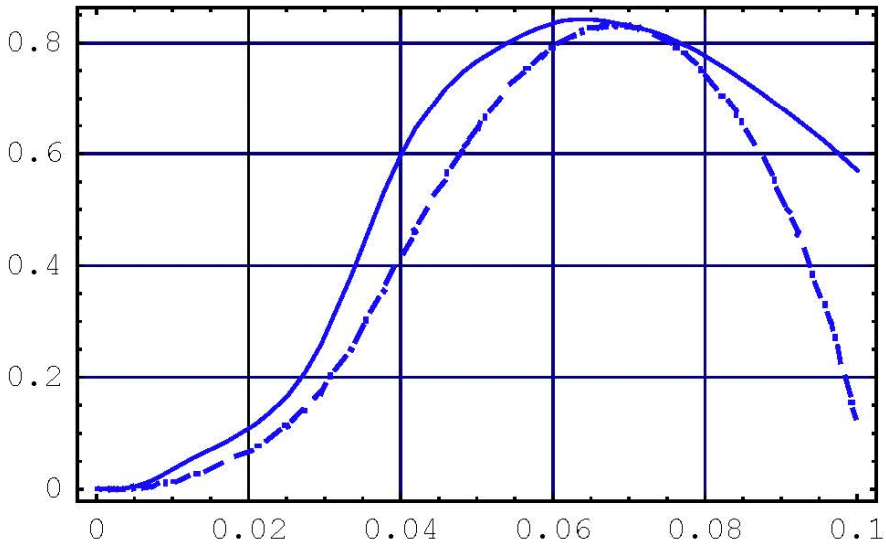

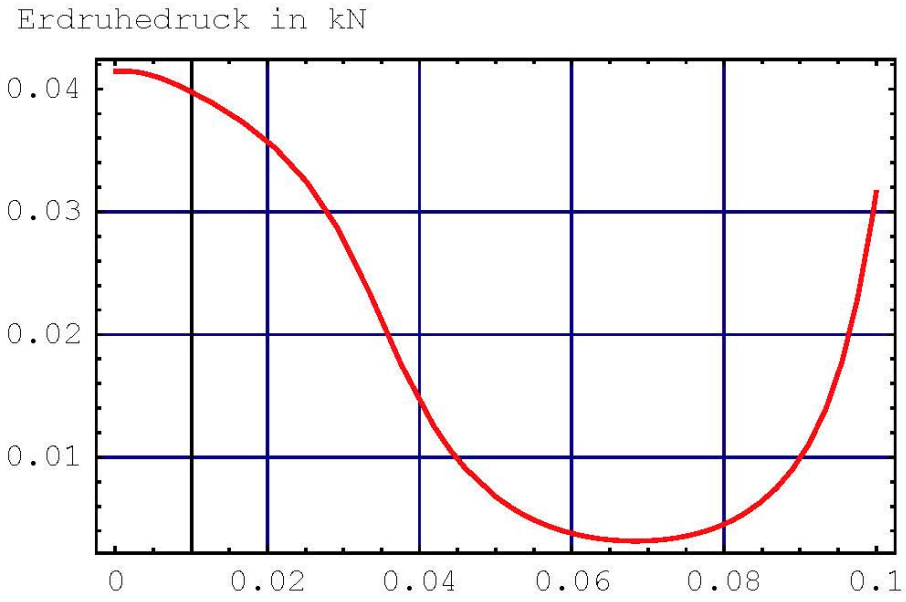
Erdruhedruck in kN
0.04
0.03
0.02
0.01
0
0.02
0.04
0.06
0.08
0.1

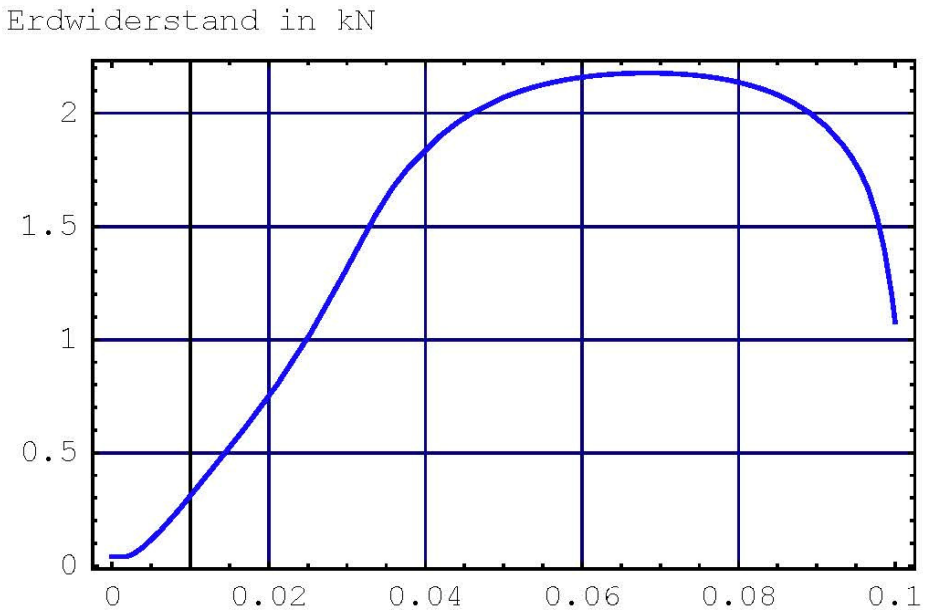
Erdwiderstand in kN
2
1.5
1
0.5
0
0
0.02
0.04
0.06
0.08
0.1

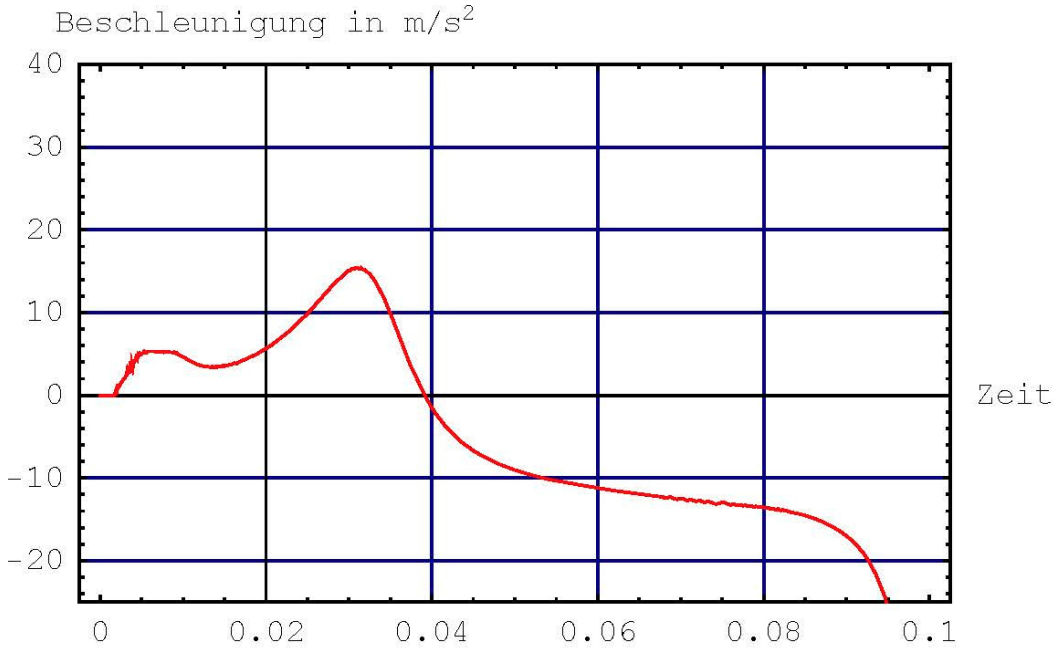
Beschleunigung in m/s²
40
30
20
10
0
-10
-20
0
0.02
0.04
0.06
0.08
0.1
Zeit

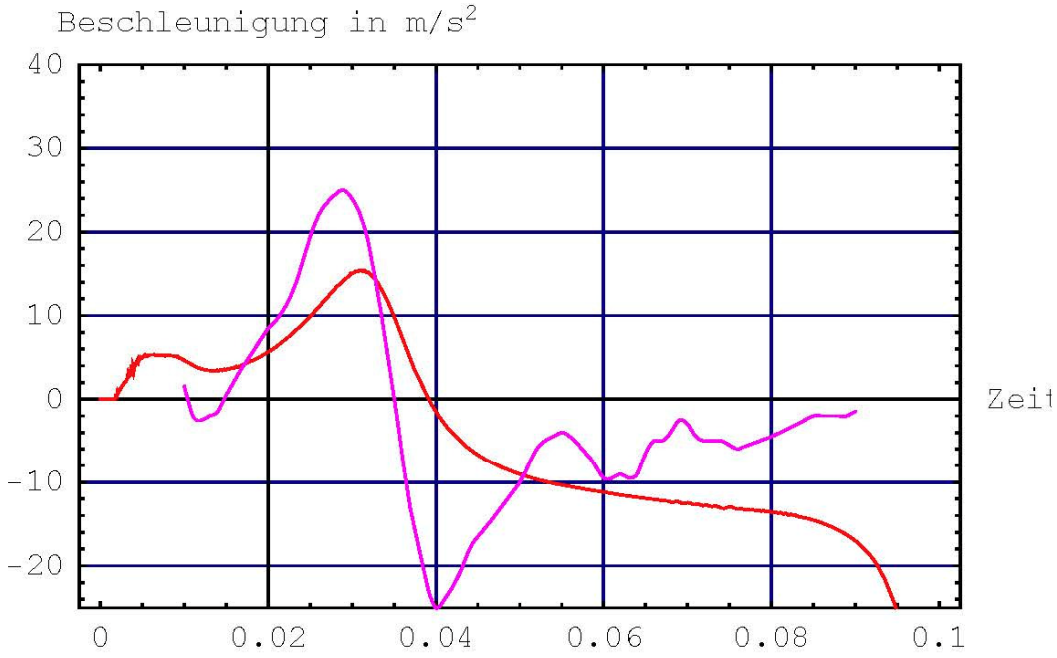
Beschleunigung in m/s²
40
30
20
10
0
-10
-20
0
0.02
0.04
0.06
0.08
0.1
Zeit

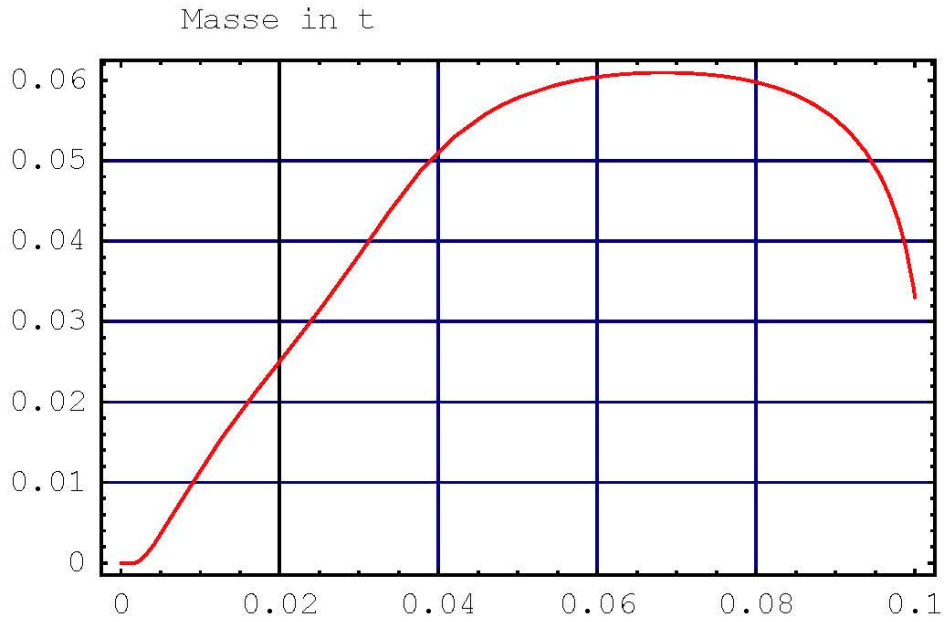
Masse in t
0.06
0.05
0.04
0.03
0.02
0.01
0
0
0.02
0.04
0.06
0.08
0.1

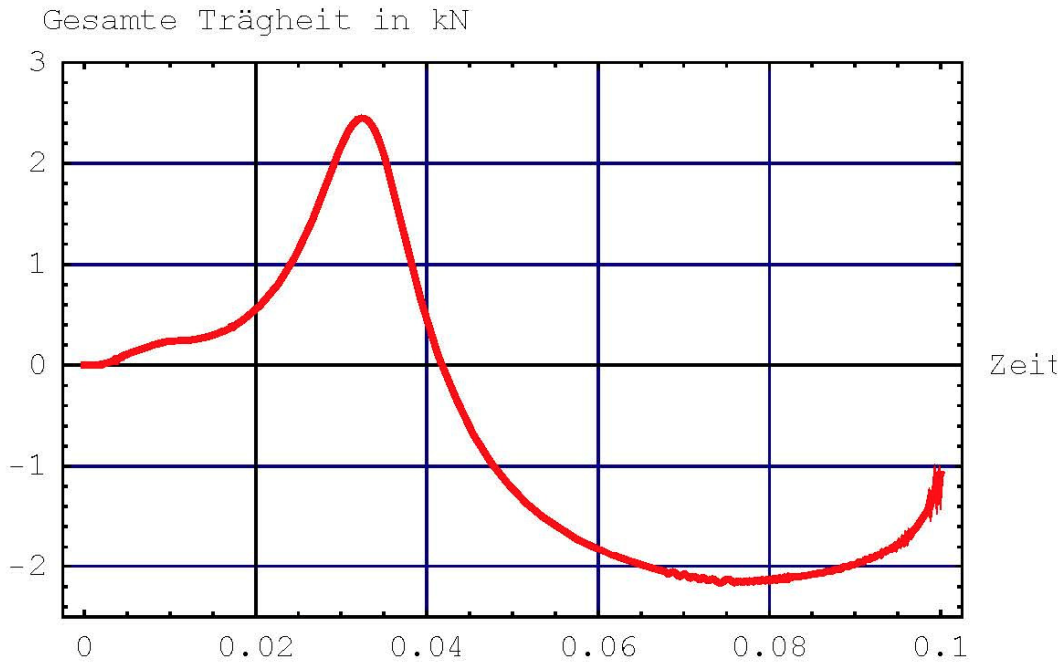
Gesamte Trägheit in kN
3
2
1
0
-1
-2
0
0.02
0.04
0.06
0.08
0.1
Zeit

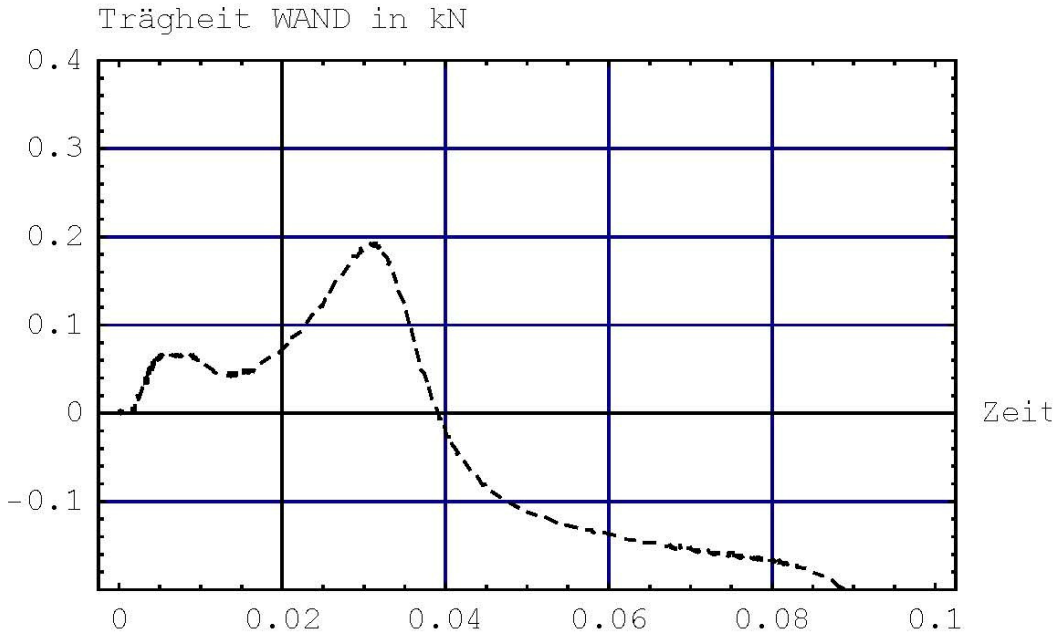
Trägheit WAND in kN
0.4
0.3
0.2
0.1
0
-0.1
0
0.02
0.04
0.06
0.08
0.1
Zeit

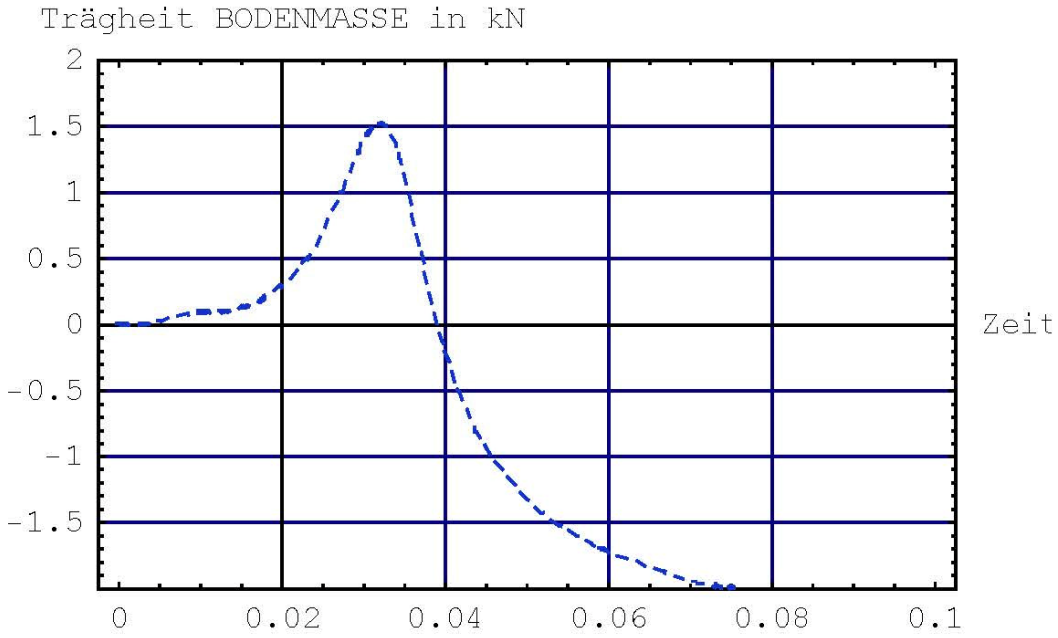
Trägheit BODENMASSE in kN
2
1.5
1
0.5
0
-0.5
-1
-1.5
0
0.02
0.04
0.06
0.08
0.1
Zeit

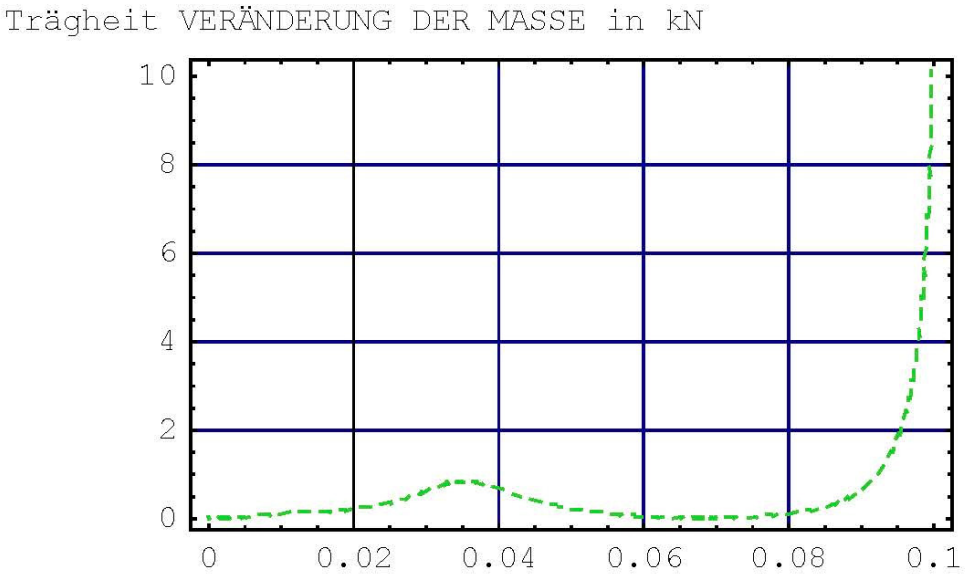
Trägheit VERÄNDERUNG DER MASSE in kN
10
8
6
4
2
0
0
0.02
0.04
0.06
0.08
0.1

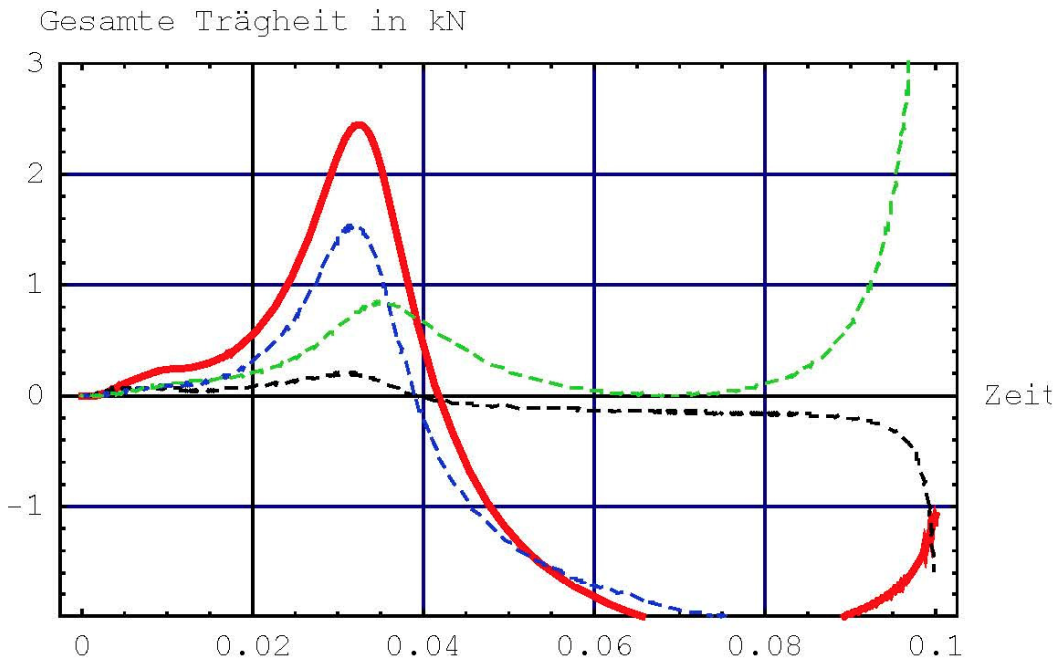
Gesamte Trägheit in kN
3
2
1
0
-1
Zeit
0
0.02
0.04
0.06
0.08
0.1

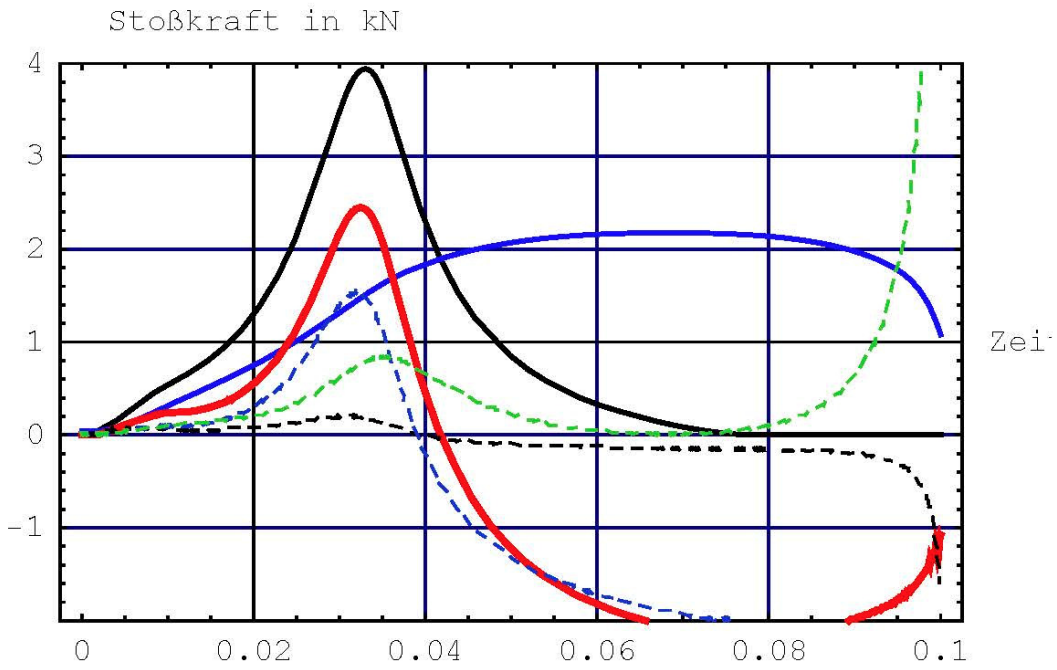
Stoßkraft in kN
4
3
2
1
0
-1
0
0.02
0.04
0.06
0.08
0.1
Zei

Annex 2 Numerical calculation program which uses the mathematical model for modelling the passive resistance mobilization for full-scale applications – elastic collision

```
Clear[ϕ, θ, ka0, kap, kk, h, a, ac, o, b, c, w, m, e, p, T, t, ta,
  tkraft, kraft, kt, pinterp, imp, tversch, versch, vt, vinterp, ddp];
Clear[imp, TsVect, FsVect];

Fstoß = Eph75;
Tstoß = T75;

TsVect = {1};        (* Valori Tstoß *)
FsVect = {1};        (* Valori Fstoß *)

TsMax = Length[TsVect];
FsMax = Length[FsVect];

Clear[WArray, TArray];                    (* Pentru rezultate *)
WArray = Table[0, {i, 1, TsMax}, {j, 1, FsMax}];
TArray = Table[0, {i, 1, TsMax}, {j, 1, FsMax}];
(*************************************************************************************\
 ******)
g = 10;

b = 9.5;  Print["b = ", b, " m"];
h = 3;    Print["h = ", h, " m"];
α = 1;    Print["α = ", α];

ρ := 2;  Print["ρ = ", ρ, " tone/mc"];
φ := 30 * π/180;  Print["φ = ", φ * 180/π, "°"];
δ := 15 * π/180;  Print["δ = ", δ * 180/π, "°"];
θ := ArcCot[Csc[φ] Sec[δ + φ] √(Cos[δ] Sin[φ] Sin[δ + φ]) + Tan[δ + φ]];
Print["θ = ", N[θ * 180/π], "°"];
a := 0.02;  Print["v_p = ", 2 a h, " m"];

mw = 7.85 * 0.03 * h * b;  Print["mw = ", mw, " tone"];
MBmax = 1/(2 Tan[θ]) ρ h^2 b;  Print["MBmax = ", N[MBmax], " tone"];
(*-------------------------------------------------------------------------*)
ka0 = N[1 - Sin[φ]];                    Print["ka0=", ka0];
ee0 = 1/2 (ρ g h^2 b) ka0;              Print["E0= ", ee0, " kN"];
```

```
E0[w_] := MBmax g Tan[θ] (1 - (w Cos[θ] / (2 a h))^(1/α))^2 ka0;

Ge[w_] := g MBmax (2 (w Cos[θ] / (2 a h))^(1/α) - (w Cos[θ] / (2 a h))^(2/α));

Gemax = MBmax g;      Print["Gemax = ", Gemax, " kN"];

Eph[w_] := Cos[δ] / (Cos[δ] - Sin[δ] Tan[φ + θ]) * (Ge[w] Tan[φ + θ] + E0[w]);

Ephmax = Cos[δ] / (Cos[δ] - Sin[δ] Tan[φ + θ]) * MBmax g Tan[φ + θ];
Print["Ephmax = ", N[Ephmax], " kN"];

SolW = NSolve[Eph[w] == 0.75 Ephmax, w]

Eph75 = 0.75 Ephmax; Print["Eph75 = ", Eph75, " kN"];

w75 = Min[N[Part[SolW, 1, 1, 2]], N[Part[SolW, 2, 1, 2]]];
Print["w75 = ", w75, " m"];
v75 = w75 * Cos[θ];
Print["v75 = ", v75, " m"];

m75 = N[Ge[v75] / g + mw]; Print["m75 = ", m75, " t"];

T75 = 2 π Sqrt[m75 v75 / (0.75 * Ephmax)]; Print["T75 = ", T75, " s"];
Print["Tstoß = ", Tstoß];
Print["Fstoß = ", Fstoß];
k75 = Eph75 / v75; Print["k75 = ", k75, " kN/m"];

(*---------- Incepe bucla dupa toate valorile ----------------*)
For[iTS = 1, iTS ≤ TsMax, iTS++,
  For[iFS = 1, iFS ≤ FsMax, iFS++,

Tstoßj = Tstoß * TsVect[[iTS]]; Print["Tstoßj =", Tstoßj];
    Fstoßj = Fstoß * FsVect[[iFS]];
    Tintegration = Tstoßj * 10; (*---- valoarea "10" este aleatoare iar Tintegration
      este limita pana unde se cauta solutia ecuatiei diferentiale----------*)
```

```
Print["Calcul ", iFS + (iTS - 1) * FsMax, " din ", TsMax * FsMax,
 "  ***   Tstoßj * ", TsVect[[iTS]], ",  Fstoßj * ", FsVect[[iFS]]];

(*------- p1 este forta in functie de t in forma "pura" --------*)
p1[t_] := Which[t ≤ 0, 0, 0 < t < Tstoßj, Sin[t π / Tstoßj] Fstoßj, t ≥ Tstoßj, 0];
Print["Fstoßj =", Fstoßj];

(*---- Find max p1[t] -> pMax ---si tMax pentru varful impulsului*)
i = 0; iMax = Tstoßj;
tMax = 0; pMax = p1[0];
For[i = 0 , i ≤ iMax , i += 0.001 * Tstoßj;
 If [pMax < p1[i],
  pMax = p1[i] ; tMax = i;
 ];
];

Print["pMax = ", pMax];
Print["tMax = ", tMax];
(*---- valoarea "0.001" este aleatoare -
 este rezolutia de cautare a maximului lui p1[t],
pMax si tMax sunt coordonatele maximului lui p1[t] iar iMax = Tstoßj este
   limita pana unde merge i iar 0.0001*Tstoßj este pasul lui i -----------*)

(*---- End Find max ( iMax si Tmax pt p1[t] ------------*)

p[t_] := If[t >= 0 && t < Tstoßj && p1[t] < ee0 * Cos[δ] / (Cos[δ] - Sin[δ] Tan[θ + φ]),
   ee0 * Cos[δ] / (Cos[δ] - Sin[δ] Tan[θ + φ]), p1[t]];
(*------- p[t] este forta care tine sa nu cada peretele cand forta de
 impact nu invinge presiunea pamnatului in stare de repaus --------*)

Tstoßj = Tstoß * TsVect[[iTS]];
Fstoßj = Fstoß * FsVect[[iFS]];

SolS = NSolve[Eph[s] == 0.75 Fstoßj, s];
ws = Min[N[Part[SolS, 1, 1, 2]], N[Part[SolS, 2, 1, 2]]];
Print["ws = ", ws, " m"];
Print["vs = ", ws * Cos[θ], " m"];

If[ws * Cos[θ] < v75, Print["static stabil"], Print["static INSTABIL!!!"]];
```

```
(*  "w[x]/.T"inseamna ca lui w[x] ii aplic regula "T" sau alfel spus
 il inlocuiesc pe  w[x] in "T" si apoi x devine z, adica am T(w[z]) *)
(*  astfel am obtinut functia aproape adevarata,
nu mai este numai o regula de inlocuire *)

(*---- Find max al solutiei and plot until max + eps ------------*)

i = 0; iMax = 0;
wMax = First[W[0]];

(*"First" alege valoarea primului element dintr-
 o lista de elemente - in cazul nostru solutia ecuatiei dif. *)

thr = -10^5;
(* definesc pragul pentru care consider ca w <
 0 pentru a nu se bloca calculul la primii pasi, inainte sa inceapa*)

(* conditia cu i ≤ "ceva" din While are rostul de a opri cautarea in cazul in care
  functia e monoton crescatoare (pana peste "5"), deci nu mai revine prin "0"*)
i = 0.01;
tMax = 0;
Tcautarevmax = 0.11 Tintegration;
While[First[W[i]] ≥ thr && i ≤ Tcautarevmax,
 i += 0.001;
 (*Print["i=",i,"    First[W[i]]=",First[W[i]]];*)
 If[wMax < First[W[i]],
   wMax = First[W[i]] ; tMax = i;
  ]
  If[First[W[i]] > 0,
   thr = 0;
  ];
];

Print["tMax =", tMax, "       si Tcautarevmax =", Tcautarevmax];
(*---- "First" alege prima solotie din multimea de solutii,
in cazul nostru pt o ec dif Cauchy exista numai o singura solutie -----------*)
(*---- valoarea "Tcautarevmax" este aleatoare si este limita superioara
  unde se opreste cautarea maximului pe graficul w[t]-----------*)
(*---- valoarea "0.001" este o rezolutie aleatoare pt
  cautarea maximului-----------*)
(*---- daca solutia a trecut de zero atunci limita inferioara
  pentru oprire "thr" devine 0 -----------*)

If[i >= Tcautarevmax, Print["w nu are solutie unica pana in ", Tcautarevmax]];
```

```
Print["Tstoß = ", Tstoßj]; Print["Fstoß = ", Fstoßj];

(*------- p[t] este forta in functie de t in forma "scalata cu F_f" --------*)

m[t_] := Which[w[t] <= 0, 0, 0 < w[t] < 2 a h / Cos[θ],
  MBmax * (2 (w[t] Cos[θ] / (2 a h))^(1/α) - (w[t] Cos[θ] / (2 a h))^(2/α)), w[t] >= 2 a h / Cos[θ], MBmax];
(*------- m[t] este masa in functia proprie --------*)
eee[t_] := Which[w[t] <= 0, MBmax g Tan[θ] ka0, 0 < w[t] < 2 a h / Cos[θ],
  MBmax g Tan[θ] ka0 * (1 - (w[t] Cos[θ] / (2 a h))^(1/α))^2, w[t] >= 2 a h / Cos[θ], 0];

k[t_] := Which[w[t] <= 0, 0, 0 < w[t] <= v75, k75, v75 < w[t], k75 * v75 / w[t]];
(* functia de elasticitate *)

tm[t_] := D[m[t], w[t]]; (* derivata masei in functie de w *)

w0 = 0;

Print["Incep ec."];
T = NDSolve[{mw (w''[t]) Cos[θ] + (m[t] g Tan[θ + φ] * Cos[δ] / (Cos[δ] - Sin[δ] Tan[θ + φ]) +
      eee[t] Cos[δ] / (Cos[δ] - Sin[δ] Tan[θ + φ])) + (m[t] (w''[t]) + tm[t] (w'[t])^2)
    (Cos[θ] + Sin[θ] Tan[θ + φ]) Cos[δ] / (Cos[δ] - Sin[δ] Tan[θ + φ]) - p[t] == 0,
  w[0] == 0, w'[0] == 0}, w, {t, 0, Tintegration}];
Print["Gata ec."];

(* "T-ul" din solutie nu este o functie ci o regula de inlocuire*)
Print["Tstoßj =", Tstoßj];
Print["tMax =", tMax];
Print["Tintegration =", Tintegration];

W[t_] := Evaluate[w[t] /. T];
(* (Cos[θ] w[t])/.T inseamna ca inlocuiesc
  w[t] cu solutia ecuatiei T si apoi il inmultesc cu Cos[θ] *)
(*wSol[z_] := w[x]/.T/.x→z;*)
```

```
        (* introducere date in matrice *)
        WArray[[iTS, iFS]] = Cos[θ] wMax / v75; Print["wMax = ", wMax, "vMax = ",
         Cos[θ] wMax, "    v75 = ", v75, "   si   vMax/v75 = ", Cos[θ] wMax / v75];
        TArray[[iTS, iFS]] = tMax / T75; Print["tMax=", tMax,
         "    T75=", T75, "   si   tMax/T75 = ", tMax / T75];

        (* End introducere date in matrice de export*)

       ];
      ];

    (* Afisare*)
    Clear[AllArray, CombinedArray];
    CombinedArray = Table[0, {i, 1, TsMax}, {j, 1, 2 * FsMax}];
    AllArray = Table[0, {i, 1, TsMax + 1}, {j, 1, 2 * FsMax + 1}];
    (* Combining the arrays in AllArray care se obtine din CombinedArray +
      coordonatecap tabel)*)

    For[iTS = 1, iTS ≤ TsMax, iTS++,
      For[iFS = 1, iFS ≤ FsMax, iFS++,
        CombinedArray[[iTS, 2 * iFS - 1]] = TArray[[iTS, iFS]] ;
        CombinedArray[[iTS, 2 * iFS ]] = WArray[[iTS, iFS]] ;
       ];
     ];
    (* deasupra s-a obtinut CombinedArray*)

    (*Prepareing for export*)

    (* mai jos se adauga coordonatele pe coloana 1 si linia 1 *)
    For[iTS = 1, iTS ≤ TsMax, iTS++,
      AllArray[[iTS + 1, 1]] = TsVect[[iTS]];
     ];
    For[iFS = 1, iFS ≤ FsMax, iFS++,
      AllArray[[1, 2 * iFS ]] = FsVect[[iFS]];
      AllArray[[1, 2 * iFS  + 1]] = FsVect[[iFS]];
     ];

    For[iTS = 1, iTS ≤ TsMax, iTS++,
      For[iFS = 1, iFS ≤ 2 * FsMax, iFS++,
        AllArray[[iTS + 1, iFS + 1]] = CombinedArray[[iTS, iFS]] ;
       ];
     ];
    MatrixForm[AllArray]
```

b = 9.5 m

h = 3 m

α = 1

ρ = 2 tone/mc

φ = 30°

δ = 15°

θ = 20.6538°

v_p = 0.12 m

mw = 6.71175 tone

MBmax = 226.822 tone

ka0=0.5

E0= 427.5 kN

Gemax = 2268.22 kN

Ephmax = 4109.93 kN

Out[213]= {{w → 0.0585076}, {w → 0.197977}}

Eph_{75} = 3082.44 kN

Out[215]= 0.0585076

w_{75} = 0.0585076 m

v_{75} = 0.0547472 m

m_{75} = 159.037 t

T_{75} = 0.333935 s

Tstoß = 0.333935

Fstoß = 3082.44

k_{75} = 56303.2 kN/m

Tstoßj =0.333935

Calcul 1 din 1 *** Tstoßj * 1, Fstoßj * 1

Fstoßj =3082.44

pMax = 3082.44

tMax = 0.166968

w_s = 0.0359919 m

v_s = 0.0336787 m

static stabil

Tstoß = 0.333935

Fstoß = 3082.44

Incep ec.

Gata ec.

Tstoßj =0.333935

tMax =0.166968

Tintegration =3.33935

tMax =0.293 si Tcautarevmax =0.367329

w nu are solutie unica pana in 0.367329

wMax = 0.0740333vMax = 0.069275 v75 = 0.0547472 si vMax/v75 = 1.26536

tMax=0.293 T75=0.333935 si tMax/T75 = 0.877416

Out[232]//MatrixForm=

$$\begin{pmatrix} 0 & 1 & 1 \\ 1 & 0.877416 & 1.26536 \end{pmatrix}$$

In[257]:=
```
Plot[Evaluate[p1[t] /. T], {t, 0, Tcautarevmax}, Frame -> True,
 GridLines -> Automatic, AxesLabel -> {"t [s]", "F_dyn [kN]"},
 AxesOrigin -> {tMax 0.25, 1000}, PlotStyle -> {{Thickness[0.0001], RGBColor[1, 0, 0]}},
 BaseStyle -> {FontSize -> 12}, PlotRange -> All]

Plot[Evaluate[Cos[θ] w[t] /. T], {t, 0., Tcautarevmax}, Frame -> True,
 GridLines -> Automatic, AxesLabel -> {"t [s]", "v [m]"}, AxesOrigin -> {tMax 0.25, 0.01},
 PlotStyle -> {{Thickness[0.005], RGBColor[0, 0, 1], Dashing[{0.002, 0.01, 0.02, 0.01}]}},
 BaseStyle -> {FontSize -> 12}, PlotRange -> All]

Plot[Evaluate[mw * w''[t] Cos[θ] /. T],
 {t, Tcautarevmax}, Frame -> True, GridLines -> Automatic,
 AxesLabel -> {"t [s]", "T1-inertia peretelui"}, AxesOrigin -> {tMax 0.25, 0.01},
 PlotStyle -> {{Thickness[0.005`], RGBColor[0, 0, 1], Dashing[{0.002, 0.01, 0.02, 0.01}]}},
 BaseStyle -> {FontSize -> 12}, PlotRange -> All]

Plot[Evaluate[m[t] g Tan[θ + φ] * Cos[δ] / (Cos[δ] - Sin[δ] Tan[θ + φ]) /. T],
 {t, 0., Tcautarevmax}, Frame -> True, GridLines -> Automatic,
 AxesLabel -> {"t [s]", "T2-frecarea prismului"}, AxesOrigin -> {tMax 0.25, 200},
 PlotStyle -> {{Thickness[0.005], RGBColor[0, 0, 1], Dashing[{0.002, 0.01, 0.02, 0.01}]}},
 BaseStyle -> {FontSize -> 12}, PlotRange -> All]

Plot[Evaluate[eee[t] Cos[δ] / (Cos[δ] - Sin[δ] Tan[θ + φ]) /. T],
 {t, 0., Tcautarevmax}, Frame -> True, GridLines -> Automatic,
 AxesLabel -> {"t [s]", "T3-presiunea in stare de repaus"}, AxesOrigin -> {tMax 0.25, 100},
 PlotStyle -> {{Thickness[0.005], RGBColor[0, 0, 1], Dashing[{0.002, 0.01, 0.02, 0.01}]}},
 BaseStyle -> {FontSize -> 12}, PlotRange -> All]

Plot[Evaluate[(m[t] (w''[t]) + tm[t] (w'[t])^2)
     (Cos[θ] + Sin[θ] Tan[θ + φ]) Cos[δ] / (Cos[δ] - Sin[δ] Tan[θ + φ]) /. T],
 {t, 0., Tcautarevmax}, Frame -> True, GridLines -> Automatic,
 AxesLabel -> {"t [s]", "T4-inertia prismului"}, AxesOrigin -> {tMax 0.25, 0.01},
 PlotStyle -> {{Thickness[0.005], RGBColor[0, 0, 1], Dashing[{0.002, 0.01, 0.02, 0.01}]}},
 BaseStyle -> {FontSize -> 12}, PlotRange -> All]

Plot[Evaluate[(m[t] (w''[t])) (Cos[θ] + Sin[θ] Tan[θ + φ]) Cos[δ] / (Cos[δ] - Sin[δ] Tan[θ + φ]) /. T],
 {t, 0., Tcautarevmax}, Frame -> True, GridLines -> Automatic,
```

```
  AxesLabel -> {"t [s]", "T4/1-inertia prismului din acceleratie"},
  AxesOrigin -> {tMax 0.25, -2000},
  PlotStyle -> {{Thickness[0.005], RGBColor[0, 0, 1], Dashing[{0.002, 0.01, 0.02, 0.01}]}},
  BaseStyle -> {FontSize -> 12}, PlotRange -> All]

Plot[
  Evaluate[(tm[t] * (w'[t])^2) (Cos[θ] + Sin[θ] Tan[θ + φ]) Cos[δ] / (Cos[δ] - Sin[δ] Tan[θ + φ]) /. T],
  {t, 0., Tcautarevmax}, Frame -> True, GridLines -> Automatic,
  AxesLabel -> {"t [s]", "T4/2-inertia prismului din variatia masei"},
  AxesOrigin -> {tMax 0.25, 1000},
  PlotStyle -> {{Thickness[0.005], RGBColor[0, 0, 1], Dashing[{0.002, 0.01, 0.02, 0.01}]}},
  BaseStyle -> {FontSize -> 12}, PlotRange -> All]
```

Out[257]=

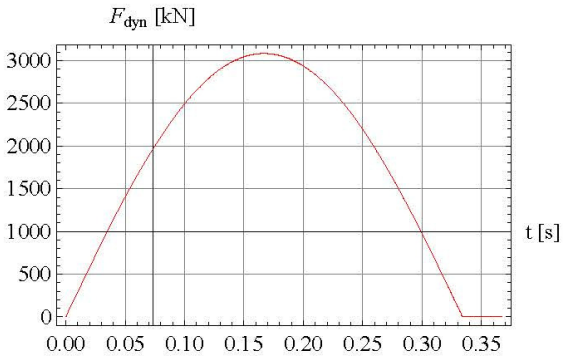

Out[258]=

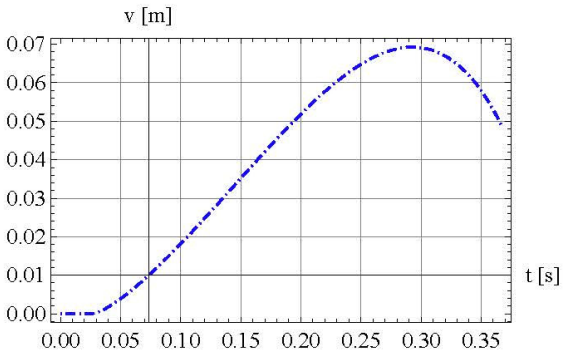

Out[260]=

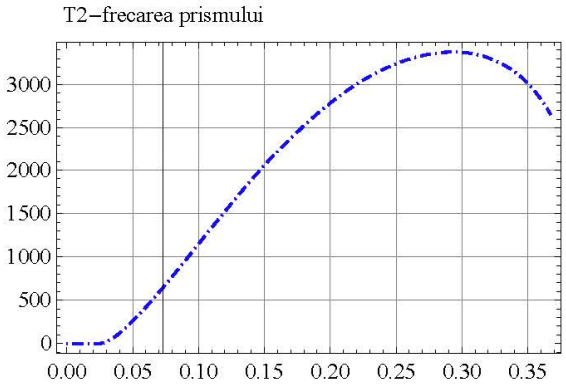

T3−presiunea in stare de repaus

Out[261]=

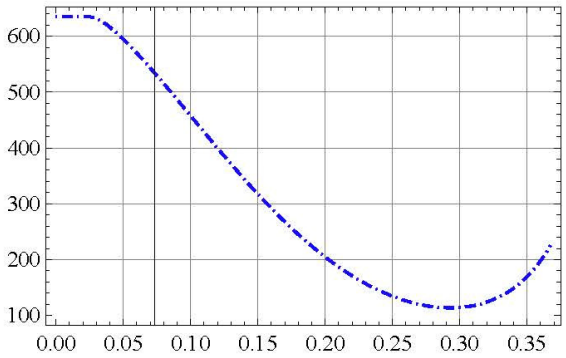

T4−inertia prismului

Out[262]=

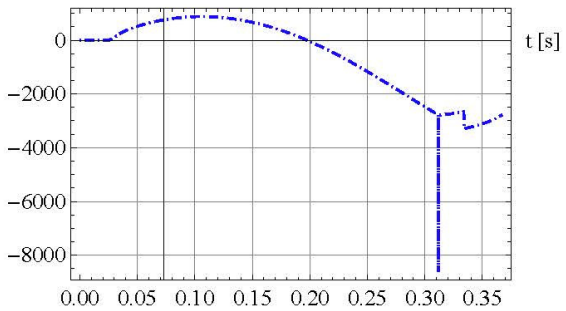

T4/1−inertia prismului din acceleratie

Out[263]=

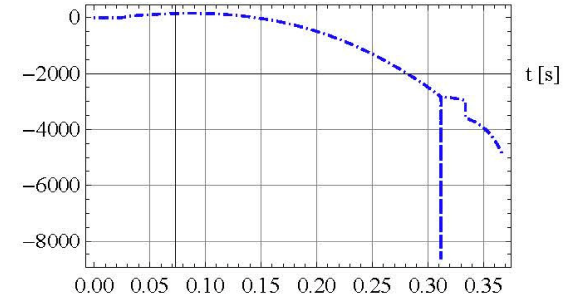

T4/2−inertia prismului din variatia masei

Out[264]=

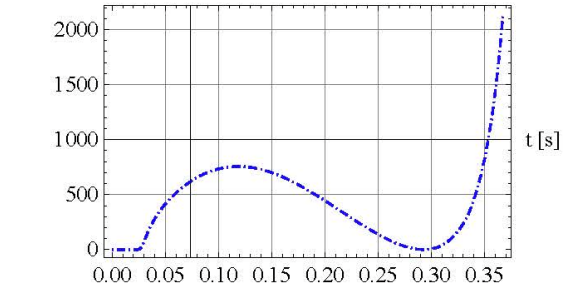


```
Export["\\\\Ppgsv\manager\DISS\2016\export_sin-75-20161109-4.xls", AllArray, "TSV"];
```

Annex 3 Numerical calculation program which uses the mathematical model for modelling the passive resistance mobilization for full-scale applications – ideal elastic-plastic collision

```
(* Modelul Matematic aplicat in cazul impactului plastic al unei nave generand F_dyn>
 5MN, b = latimea navei de 33 m*)

Clear[ϕ, θ, ka0, kap, kk, h, a, ac, o, b, c, w, w75, m, e,
 p, T, t, ta, tkraft, tmax, tmaxW, kraft, kt, pinterp, imp, tversch,
 versch, vt, vinterp, ddp, imax, w, TsMax, FsMax]; Clear[imp];
SetDirectory["\\\\ppgsv\\manager\\DISS\\2016"];
imp = "impact-plastic.TXT";

ta = Import[imp, "Table"];
tkraft = ta[[All, 1]];
Tstoß = Max[tkraft];
Print["Tstoß = ", Tstoß];
kraft = ta[[All, 2]];
Fstoß = Max[kraft];
Print["Fstoß = ", Fstoß];

imax = Length[kraft];
kt = Table[{tkraft[[i]], kraft[[i]]}, {i, 1, imax}];

TsVect = {1};                          (* definim o lista cu Valori Tstoß *)
FsVect = {1};                          (* Valori Fstoß *)

TsMax = Length[TsVect] ;
FsMax = Length[FsVect];

Clear[WArray, TArray];                 (* Pentru rezultate *)
WArray = Table[0, {i, 1, TsMax}, {j, 1, FsMax}]; (* definim o matrice plina cu 0 *)
TArray = Table[0, {i, 1, TsMax}, {j, 1, FsMax}];

Print["TsMax = ", TsMax];
Print["FsMax = ", FsMax];

(* Urmeaza definirea parametrilor STATICI a caracteristicilor geotehnice  si
 a Functiilor de Mobilizare ***********************************************)
g = 10;

b = 33;
h = 3;
α = 1;  Print["α = ", α];

(*ρmax=1.72;
ρmin=1.47;
ρ:=ρmin+LD(ρmax-ρmin);  Print["ρ = ",ρ];
φ:=(25.5+25.5*LD)*π/180;  Print["φ = ",φ*180/π,"°"];(*30+16.5*LD*)
δ:=13*π/180;  Print["δ = ",δ*180/π,"°"];(*8+10.5*LD si la variantele
```

```
  precedente se utiliza Beta ca o variatie a lui Delta de w!*)*)

ρ := 2;  Print["ρ = ", ρ];
φ := 30 * π/180;  Print["φ = ", φ * 180/π, "°"];(*30+16.5*LD*)
δ := 15 * π/180;  Print["δ = ", δ * 180/π, "°"];
θ := ArcCot[Csc[φ] Sec[δ + φ] √(Cos[δ] Sin[φ] Sin[δ + φ]) + Tan[δ + φ]];
Print["θ = ", N[θ * 180/π], "°"];

a := 0.02;
Print["2ah = ", 2 a h];

mw = 7.85 * 0.03 * h * b;
Print["mw = ", mw];
MBmax = 1/(2 Tan[θ]) ρ h^2 b;                    Print["MBmax = ", N[MBmax]];
(*-------------------------------------------------------------------------------*)
ka0 = N[1 - Sin[φ]];                  Print["ka0=", ka0];
ee0 = 1/2 (ρ g h^2 b) ka0;            Print["E_0= ", ee0, " kN"];
δs := 0 * π/180;                      Print["δs = ", δs * 180/π, "°"];
RsBeiwert = 2 ka0 Tan[δs];            Print["RsBeiwert = ", RsBeiwert];

E0[w_] := MBmax g Tan[θ] (1 - (w Cos[θ]/(2 a h))^(1/α))^2 ka0;
Ge[w_] := g MBmax (2 (w Cos[θ]/(2 a h))^(1/α) - (w Cos[θ]/(2 a h))^(2/α));
(* E0[w_]:=
 Which[w<=0,MBmax g Tan[θ] ka0,0<w<2 a h/Cos[θ],MBmax g Tan[θ] (1-(w Cos[θ]/2a h)^(1/α))^2 ka0,w>=2 a h/Cos[θ],0];
m[w_]:=Which[w<=0,0,0<w<2 a h/Cos[θ],MBmax (2(w Cos[θ]/2a h)^(1/α)-(w Cos[θ]/2a h)^(2/α)),w>=2 a h/Cos[θ],MBmax];  *)

Gemax = MBmax g;                      Print["Gemax = ", N[Gemax]];

Eph[w_] := Cos[δ]/(Cos[δ] - Sin[δ] Tan[φ + θ]) * (Ge[w] Tan[φ + θ] + E0[w]);
```

```
Ephmax = Cos[δ] / (Cos[δ] - Sin[δ] Tan[φ + θ]) * MBmax g Tan[φ + θ]; Print["Ephmax = ", N[Ephmax], "kN"];

SolW = NSolve[Eph[w] == 0.75 Ephmax, w]

Eph75 = 0.75 Ephmax; Print["Eph75 = ", Eph75, " kN"];

w75 = Min[N[Part[SolW, 1, 1, 2]], N[Part[SolW, 2, 1, 2]]]
Print["w75 = ", w75, " m"];
Print["v75 = ", w75 * Cos[θ], " m"];

SolS = NSolve[Eph[w] == Fstoßj, w]
ws = Min[N[Part[SolS, 1, 1, 2]], N[Part[SolS, 2, 1, 2]]]
Print["ws = ", ws, " m"];
Print["vs = ", ws * Cos[θ], " m"];

If[ws * Cos[θ] < w75 * Cos[θ], Print["static stabil"], Print["static INSTABIL!!!"]];

G75 = N[Ge[w75 / Cos[θ]]]; Print["G75 = ", G75, " kN"];

N[G75 / (g MBmax)]

m75 = N[Ge[w75] / g + mw]; Print["m75 = ", m75, " t"];

T75 = 2 π Sqrt[m75 w75 / (0.75 Ephmax)]; Print["T75 = ", T75, " s"];

(*conform ec 24 de la pag 22 din Holzloehner *)
Print["Tstoß = ", Tstoß];
Print["Fstoß = ", Fstoß];

k75 = Eph75 / w75; Print["k75 = ", k75, " kN/m"];
```

```
Tstoß = 3.939

Fstoß = 20 000

TsMax = 1

FsMax = 1

α = 1

ρ = 2

φ = 30°

δ = 15°

θ = 20.6538°

2ah = 0.12

mw = 23.3145

MBmax = 787.909

ka0=0.5

E_0= 1485. kN

δs = 0°

RsBeiwert = 0

Gemax = 7879.09
```

$Ephmax = 14276.6kN$

$\{\{w \to 0.0585076\}, \{w \to 0.197977\}\}$

$Eph_{75} = 10707.4\ kN$

0.0585076

$w_{75} = 0.0585076\ m$

$v_{75} = 0.0547472\ m$

$\{\{w \to 0.128242 - 0.0883069\ i\}, \{w \to 0.128242 + 0.0883069\ i\}\}$

$w_s = Min[0.128242 - 0.0883069\ i,\ 0.128242 + 0.0883069\ i]\ m$

$$v_s = \frac{Min[0.128242 - 0.0883069\ i,\ 0.128242 + 0.0883069\ i]}{\sqrt{1 + \frac{1}{\left(1+\sqrt{1+\sqrt{3}}\right)^2}}}\ m$$

$G_{75} = 5810.11\ kN$

0.737408

$m_{75} = 578.247\ t$

$T_{75} = 0.353183\ s$

$Tstoß = 3.939$

$Fstoß = 20000$

$k_{75} = 183009.\ kN/m$

```
(*-------------------------------------------------------------------------------------------
                                                        --------*)
pinterp = Interpolation[kt, InterpolationOrder -> 1];
W[t_] := Evaluate[pinterp[t]];
Z[t_] := Evaluate[t];
imax = 1000; dt = Tstoß/imax; (*inainte era tmax in loc de Tstoss*)
fvvekt = {}; fwvekt = {};
Do[fvvekt = Append[fvvekt, W[j dt]];
  fwvekt = Append[fwvekt, Z[j dt]],
  {j, 0, imax}];
imax = Length[kraft];

(*Print["fvvekt = ",fvvekt];
Print["fwvekt = ",fwvekt];*)

(*---------- Incepe bucla dupa toate valorile -----------------*)
For[iTS = 1, iTS <= TsMax, iTS++,
```

```
For[iFS = 1, iFS <= FsMax, iFS++,

  Print["Fstoßj = ", Fstoßj];

  tmax = Tstoßj * 2; Print["tmax = ", tmax]; (*---- valoarea "10" este aleatoare iar
    tmax este limita pana unde se cauta solutia ecuatiei diferentiale----------*)

  Print["Calcul ", iFS + (iTS - 1) * FsMax, " din ", TsMax * FsMax,
   "  ***   Tstoßj = ", TsVect[[iTS]], ",  Fstoßj = ", FsVect[[iFS]]];

  p1[t_] := Which[t <= 0, 0, 0 < t <= Tstoßj,
    pinterp[t / TsVect[[iTS]]] * FsVect[[iFS]], t >= Tstoßj, 0];

  (*------- p1 este forta in functie de t in forma "pura" --------*)

  (*---- Find max p1[t] -> pMax ---si tMax*)
  i = 0; iMax = Tstoßj;
  tMax = 0; pMax = p1[0];
  For[ i = 0 , i <= iMax , i += 0.001 * Tstoßj;
   If [pMax < p1[i],
    pMax = p1[i] ; tMax = i;
   ];
  ];
  Print["pMax = ", pMax];
  Print["tMax = ", tMax];
  (*---- valoarea "0.001" este aleatoare -
   este rezolutia de cautare a maximului lui p1[t],
  pMax si tMax sunt coordonatele maximului lui p1[t] iar iMax = Tstoßj este
     limita pana unde merge i iar 0.0001*Tstoßj este pasul lui i ----------*)
  (*---- End Find max ( iMax si Tmax pt p1[t] ------------*)
  ee0 = 1/2 (ρ g h^2 b) ka0;
  (*+MBmax* g Tan[θ+φ]       Print[" Error p[t] ! ! !"]*)
  p[t_] := If[t >= 0 && t < tMax && p1[t] < ee0 * Cos[δ]/(Cos[δ] - Sin[δ] Tan[θ + φ]),
    ee0 * Cos[δ]/(Cos[δ] - Sin[δ] Tan[θ + φ]), p1[t]];
  (*------- p[t] este forta care tine sa nu cada peretele cand forta de
   impact nu invinge presiunea pamnatului in stare de repaus --------*)
  Print["TsVect[[iTS]] = ", TsVect[[iTS]]];
  Print["FsVect[[iFS]] = ", FsVect[[iFS]]];
  Print["-----------------------------------------------------------------"];
  Tstoßj = Tstoß * TsVect[[iTS]]; Print["Tstoßj = ", Tstoßj];
  Fstoßj = Fstoß * FsVect[[iFS]];

  SolS = NSolve[Eph[s] == Fstoßj, s];
```

```
Print["SolS = ", SolS];
ws = Min[N[Part[SolS, 1, 1, 2]], N[Part[SolS, 2, 1, 2]]];
Print["ws = ", ws, " m"];
Print["vs = ", ws * Cos[θ], " m"];

If[ws * Cos[θ] < w75 * Cos[θ], Print["static stabil"], Print["static INSTABIL!!!"]];

Print["Tstoßj = ", Tstoßj];
Print["Fstoßj = ", Fstoßj];

Print[
 "-------------------------------------------------------------------------------
   ----------------------"];
(*------- p[t] este forta in functie de t in forma "modificata" --------*)
m[t_] := Which[w[t] <= 0, 0, 0 < w[t] < 2 a h / Cos[θ],
   MBmax * (2 (w[t] Cos[θ] / (2 a h))^(1/α) - (w[t] Cos[θ] / (2 a h))^(2/α)), w[t] >= 2 a h / Cos[θ], MBmax]; (*------- m[t]
   este masa intr-o functie analoga celei pentru Eph[w] din DIN4085--------*)
eee[t_] := Which[w[t] <= 0, MBmax g Tan[θ] ka0, 0 < w[t] < 2 a h / Cos[θ],
   MBmax g Tan[θ] ka0 * (1 - (w[t] Cos[θ] / (2 a h))^(1/α))^2, w[t] >= 2 a h / Cos[θ], 0];
k[t_] := Which[w[t] <= 0, 0, 0 < w[t] <= w75, k75, w75 < w[t], k75 * w75 / w[t]];
(* functia de elasticitate *)
tm[t_] := D[m[t], w[t]]; (* derivata masei in functie de w *)
w0 = 0;
Print["Incep ec."];
T = NDSolve[{mw (w''[t]) Cos[θ] + (m[t] g Tan[θ + φ] * Cos[δ] / (Cos[δ] - Sin[δ] Tan[θ + φ]) +
        eee[t] Cos[δ] / (Cos[δ] - Sin[δ] Tan[θ + φ])) + (m[t] (w''[t]) + tm[t] (w'[t])^2)
       (Cos[θ] + Sin[θ] Tan[θ + φ]) Cos[δ] / (Cos[δ] - Sin[δ] Tan[θ + φ]) -
     p[t] == 0, w[0] == 0, w'[0] == 0}, w, {t, 0, 5}];
Print["Gata ec."];
(* "t-ul" din solutie nu este o functie ci o regula de inlocuire*)
W[t_] := Evaluate[(Cos[θ] w[t]) /. T];
(* (Cos[θ] w[t])/.T inseamna ca inlocuiesc
  w[t] cu solutia ecuatiei T si apoi il inmultesc cu Cos[θ] *)
wSol[z_] := w[x] /. T /. x -> z;
```

```
(*  "w[x]/.T"inseamna ca lui w[x] ii aplic regula "T" sau alfel spus
 il inlocuiesc pe  w[x] in "T" si apoi x devine z, adica am T(w[z]) *)
(*  astfel am obtinut functia aproape adevarata,
nu mai este numai o regula de inlocuire *)

(*---- Find max al solutiei and plot until max + eps ------------*)

i = 0; iMax = 0;
wMax = First[wSol[0]];

(*"First" alege valoarea primului element dintr-
 o lista de elemente - in cazul nostru solutia ecuatiei dif. *)

thr = -10^10;
(* definesc pragul pentru care consider ca w <
 0 pentru a nu se bloca calculul la primii pasi, inainte sa inceapa*)

(* conditia cu i <=
 "ceva" din While are rostul de a opri cautarea in cazul in care functia
  e monoton crescatoare (pana peste "5"), deci nu mai revine prin "0"*)
i = 0;

While[First[wSol[i]] >= thr && i <= 5,
 i += 0.0001 ;
 If[wMax < First[wSol[i]],
  wMax = First[wSol[i]]; tMaxW = i;
 ]; (* se gaseste maximul lui wMax intre 0 si 1 *)

 If[First[wSol[i]] > 0 && i >= Tstoß / 2,
  thr = 0;
 ];
];
Print["wMax = ", wMax];
Print["h = ", h];
Print["vMax = ", wMax Cos[θ]];
(*---- i este un pas de timp iar cand lßam gasit il inlocuim cu t;
"First" alege prima solotie din multimea de solutii,
in cazul nostru pt o ec dif Cauchy exista numai o singura solutie -----------*)
(*---- valoarea 10 este aleatoare si este limita superioara
  unde se opreste cautarea maximului -----------*)
(*---- valoarea "\""(0 0.00001) "\"" este o rezolutie
  aleatoare pt cautarea maximului-----------*)
(*---- daca solutia a trecut de zero atunci limita inferioara
  pentru oprire "thr" devine 0 -----------*)

If[i >= 5, Print["w nu are solutie pana in 1"]];

(* Bag datele in matrici*)
```

```
    WArray[[iTS, iFS]] = wMax / w75;
    TArray[[iTS, iFS]] = tMaxW / T75;
    (* End bagare de date*)
    Print["pMax = ", pMax];
    Print["tMaxW = ", tMaxW];
   ];
 ];
iTS = 1;
iFS = 1;

Plot[Evaluate[p1[t] /. T], {t, 0, tMaxW 1.5}, Frame -> True,
 GridLines -> Automatic, AxesLabel -> {"t [s]", "F_dyn [kN]"},
 AxesOrigin -> {tMaxW 0.25, 1000}, PlotStyle -> {{Thickness[0.0001], RGBColor[1, 0, 0]}},
 BaseStyle -> {FontSize -> 12}, PlotRange -> All]
Plot[Evaluate[Cos[θ] w[t] /. T], {t, 0., tMaxW 1.5}, Frame -> True, GridLines -> Automatic,
 AxesLabel -> {"t [s]", "v [m]"}, AxesOrigin -> {tMaxW 0.25, 0.01},
 PlotStyle -> {{Thickness[0.005], RGBColor[0, 0, 1], Dashing[{0.002, 0.01, 0.02, 0.01}]}},
 BaseStyle -> {FontSize -> 12}, PlotRange -> All]
Plot[Evaluate[mw * w''[t] Cos[θ] /. T], {t, 0., tMaxW 1.5},
 Frame -> True, GridLines -> Automatic,
 AxesLabel -> {"t [s]", "T1-inertia peretelui"}, AxesOrigin -> {tMaxW 0.25, 0.01},
 PlotStyle -> {{Thickness[0.005`], RGBColor[0, 0, 1], Dashing[{0.002, 0.01, 0.02, 0.01}]}},
 BaseStyle -> {FontSize -> 12}, PlotRange -> All]
Plot[Evaluate[m[t] g Tan[θ + φ] * Cos[δ] / (Cos[δ] - Sin[δ] Tan[θ + φ]) /. T],
 {t, 0., tMaxW 1.5}, Frame -> True, GridLines -> Automatic,
 AxesLabel -> {"t [s]", "T2-frecarea prismului"}, AxesOrigin -> {tMaxW 0.25, 0.01},
 PlotStyle -> {{Thickness[0.005], RGBColor[0, 0, 1], Dashing[{0.002, 0.01, 0.02, 0.01}]}},
 BaseStyle -> {FontSize -> 12}, PlotRange -> All]
Plot[Evaluate[eee[t] Cos[δ] / (Cos[δ] - Sin[δ] Tan[θ + φ]) /. T], {t, 0., tMaxW 1.5}, Frame -> True,
 GridLines -> Automatic, AxesLabel -> {"t [s]", "T3-presiunea in stare de repaus"},
 AxesOrigin -> {tMaxW 0.25, 0.01},
 PlotStyle -> {{Thickness[0.005], RGBColor[0, 0, 1], Dashing[{0.002, 0.01, 0.02, 0.01}]}},
 BaseStyle -> {FontSize -> 12}, PlotRange -> All]
Plot[Evaluate[(m[t] (w''[t]) + tm[t] (w'[t])^2) (Cos[θ] + Sin[θ] Tan[θ + φ])
    Cos[δ] / (Cos[δ] - Sin[δ] Tan[θ + φ]) /. T], {t, 0., tMaxW 1.5}, Frame -> True,
 GridLines -> Automatic, AxesLabel -> {"t [s]", "T4-inertia prismului"},
 AxesOrigin -> {tMaxW 0.25, 0.01},
 PlotStyle -> {{Thickness[0.005], RGBColor[0, 0, 1], Dashing[{0.002, 0.01, 0.02, 0.01}]}},
 BaseStyle -> {FontSize -> 12}, PlotRange -> All]
```

```
Plot[Evaluate[(m[t] (w''[t])) (Cos[θ] + Sin[θ] Tan[θ + φ]) Cos[δ] / (Cos[δ] - Sin[δ] Tan[θ + φ]) /. T],
 {t, 0., tMaxW 1.5}, Frame -> True, GridLines -> Automatic,
 AxesLabel -> {"t [s]", "T4/1-inertia prismului din acceleratie"},
 AxesOrigin -> {tMaxW 0.25, 0.01},
 PlotStyle -> {{Thickness[0.005], RGBColor[0, 0, 1], Dashing[{0.002, 0.01, 0.02, 0.01}]}},
 BaseStyle -> {FontSize -> 12}, PlotRange -> All]
Plot[Evaluate[(tm[t] * (w'[t])^2) (Cos[θ] + Sin[θ] Tan[θ + φ]) Cos[δ] / (Cos[δ] - Sin[δ] Tan[θ + φ]) /.
   T], {t, 0., tMaxW 1.5}, Frame -> True, GridLines -> Automatic,
 AxesLabel -> {"t [s]", "T4/2-inertia prismului din variatia masei"},
 AxesOrigin -> {tMaxW 0.25, 0.01},
 PlotStyle -> {{Thickness[0.005], RGBColor[0, 0, 1], Dashing[{0.002, 0.01, 0.02, 0.01}]}},
 BaseStyle -> {FontSize -> 12}, PlotRange -> All]
Fstoßj = 20000
tmax = 7.878
Calcul 1 din 1  ***   Tstoßj = 1,  Fstoßj = 1
pMax = 19999.8
tMax = 3.03303
TsVect[[iTS]] = 1
FsVect[[iFS]] = 1
------------------------------------------------------------------
Tstoßj = 3.939
SolS = {{s → 0.128242 - 0.0883069 i}, {s → 0.128242 + 0.0883069 i}}
Tstoßj = 3.939
Fstoßj = 20000
-------------------------------------------------------------------------------------------------
  -----------
11111111111111
222222222222222
3333333333333333
444444444444444
555555555555555555
777777777777777
888888888888888888
Incep ec.
Gata ec.
wMax = 5.02303
h = 3
vMax = 4.70019
w nu are solutie pana in 1
pMax = 19999.8
tMaxW = 4.069
```

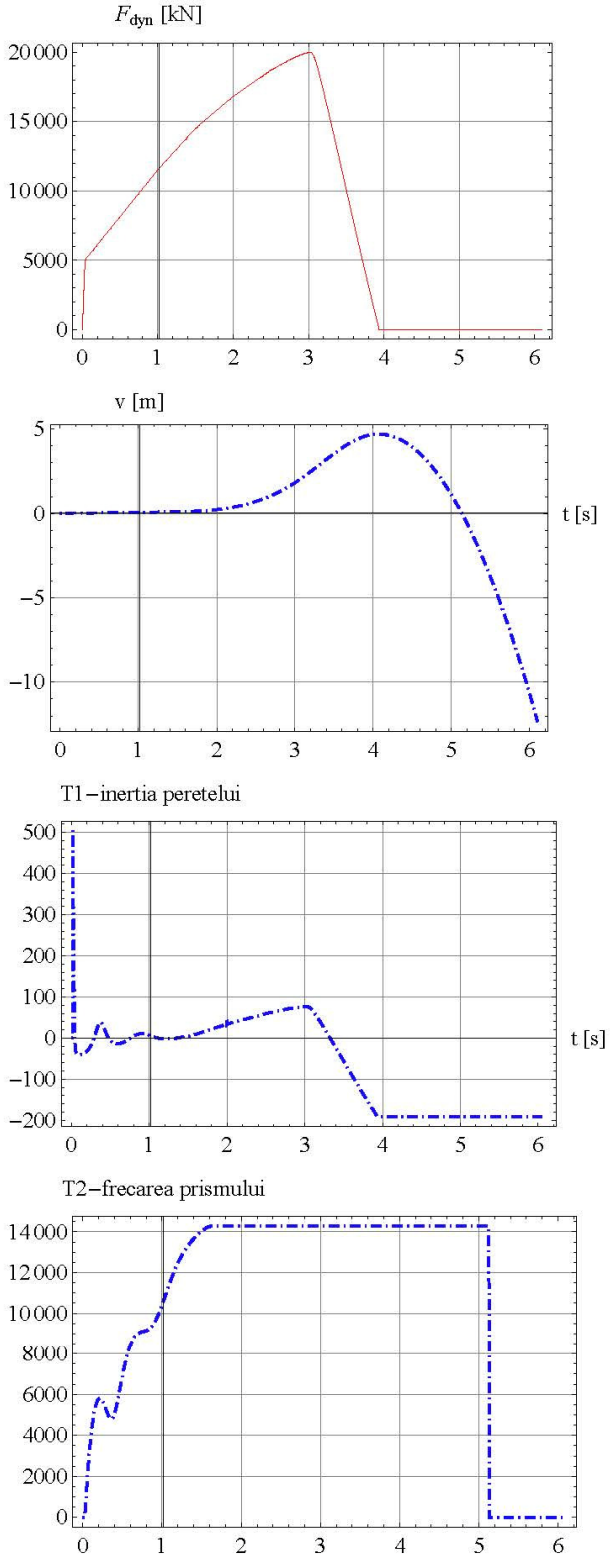
F_{dyn} [kN]
20000
15000
10000
5000
0
0 1 2 3 4 5 6
v [m]
5
0
−5
−10
t [s]
0 1 2 3 4 5 6
T1−inertia peretelui
500
400
300
200
100
0
−100
−200
t [s]
0 1 2 3 4 5 6
T2−frecarea prismului
14000
12000
10000
8000
6000
4000
2000
0
0 1 2 3 4 5 6

T3–presiunea in stare de repaus

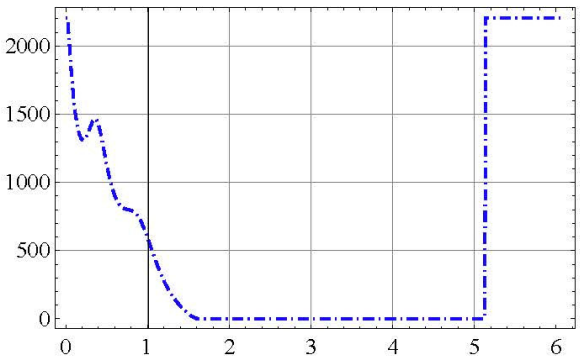

T4–inertia prismului

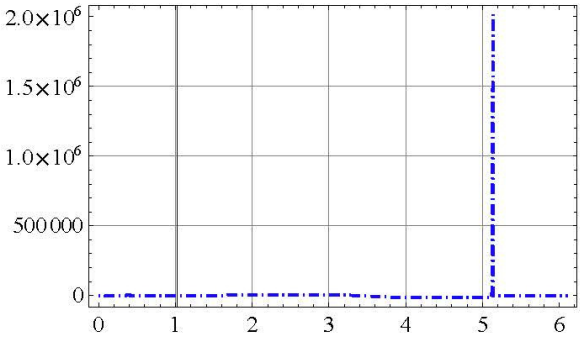

T4/1–inertia prismului din acceleratie

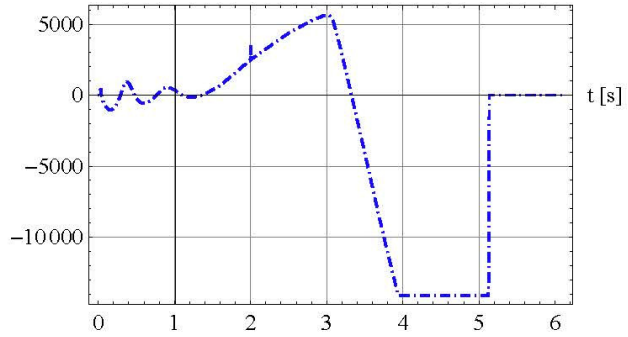

T4/2–inertia prismului din variatia masei

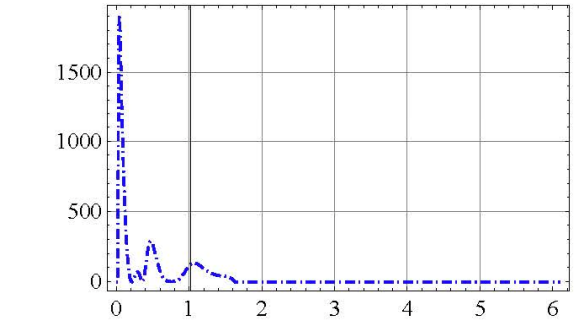

```
Plot[Evaluate[Cos[θ] w[t] /. T], {t, 0., tMaxW * 1.1 },
 Frame -> True, GridLines -> Automatic, AxesOrigin -> {0.05, 0.01},
 PlotStyle -> {{Thickness[0.005], RGBColor[0, 0, 1], Dashing[{0.002, 0.01, 0.02, 0.01}]}},
 BaseStyle -> {FontSize -> 12}, PlotRange -> All]
```

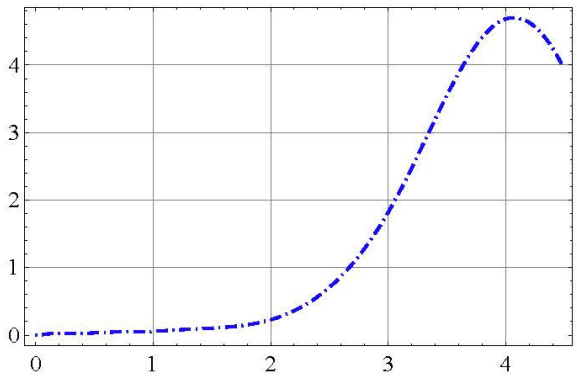

Annex 4 Summary table of the dynamic tests performed on physical models under shock-type loads

Nr.	Denumire	Data	Lățime perete mobil b	Inaltime perete h	Grad îndesare D	Masa pendu-lului	Lungi-mea pendu-lului	Devierea inițială pendul	Înălți-mea inițială pendul	Amplit. forță impact	Durată forță impact	Im-puls	Deplasare maximă perete	Accelerație maximă	Înregis-trare distribuție presiune	Înregis-trare video	Observații
			[cm]	[cm]	[-]	[kg]	[m]	[cm]	[m]	[kN]	[s]	[kNs]	[cm]	[m/s²]			
D1	TS_DynBr_09_24	8/22/2001	32	24	0.9	12.75	0.8	orizontal		3.96	0.075	0.277	0.8		da		
D2	TS_DynBr_07_24	8/20/2001	32	24	0.7	12.75	0.8	orizontal		3.33	0.078	0.27	1.8		da		
D3	TS_DynBr_05_24	8/19/2001	32	24	0.5	12.75	0.8	orizontal		3.16	0.078	0.256	3.3		da		
D4	TS_DynBr_6_8	4/5/2001	32	8	0.9	7.937	0.8	60°		0.76	0.08	0.096	1.6		da		
D5	TS_DynBr_5_12	4/5/2001	32	12	0.9	7.937	0.8	orizontal		1.7	0.071	0.17	1		da		
D6	TS_DynBr_4_16	4/2/2001	32	16	0.9	12.75	0.8	orizontal		3.9	0.076	0.273	1.46		da		
D7	TS_DynBr_3_24	4/2/2001	32	24	0.9	12.75	0.8	vertical		9.79	0.06	0.35	1.44		da		
D8	TS_DynBr_2_24	4/2/2001	32	24	0.9	12.75	0.8	vertical		9.79	0.06	0.35	1.34		da		
D9	TS_DynBr_1_24	4/2/2001	32	24	0.9	12.75	0.8	orizontal		3.13	0.078	0.272	0.57		da		
D10	DynamEngH24_2	1/31/2001	16	24	0.9	5.4	0.8	vertical							da		
D11	DynamEngH24_1	1/31/2001	16	24	0.9	5.4	0.8	vertical							da		
D12	DynamEngH16_2	1/30/2001	16	16	0.9	5.4	0.8	orizontal							da		
D13	DynamEngH16_1	1/30/2001	16	16	0.9	5.4	0.8	orizontal							da		
D14	DynamEngH12_3	1/29/2001	16	12	0.9	5.4	0.8	vertical							da		Masurătoare de probă
D15	DynamEngH12_2	1/29/2001	16	12	0.9	5.4	0.8	100							da		
D16	DynamEngH12_1	1/28/2001	16	12	0.9	5.4	0.8	90							da		
D17	DynamBreit_8	11/13/2000	32	32	0.9	12.75	0.8	50							da		
D18	DynamBreit_6	11/13/2000	32	32	0.9	12.75	0.8	50							da		
D19	DynamBreit_5	11/13/2000	32	32	0.9	12.75	0.8	50							da		
D20	DynamBreit_4	11/13/2000	32	32	0.9	12.75	0.8	70							da		
D21	DynamBreit_3	11/10/2000	32	32	0.9	12.75	0.8	vertical	1.5	20	0.062	0.7	0.5		da		
D22	DynamBreit_2	11/10/2000	32	32	0.9	12.75	0.8	orizontal	0.8	7.68	0.075	0.562	0.27		da		
D23	DynamBreit_1	11/10/2000	32	32	0.9	12.75	0.8	orizontal	0.8	6.61	0.077	0.55	0.3	15	nu		
D24	DynamV-25	4/24/2000	16	24	0.9	5.4	0.8	40cm A.								da	
D25	DynamV-24	4/24/2000	16	24	0.9	5.4	0.8	50cm A.								da	
D26	DynamV-23	4/24/2000	16	24	0.9	5.4	0.8	50cm A.								da	
D27	**DynamV-22**	4/24/2000	16	24	0.9	5.4	0.8	70cm A. ~45°								da	
D28	DynamV-21	4/24/2000	16	24	0.7	5.4	0.8	orizontal								da	
D29	DynamV-20	4/24/2000	16	24	0.5	5.4	0.8	orizontal								nu	
D30	DynamV-19	4/24/2000	16	24	0.9	5.4	0.8	vertical	1.5							da	
D31	DynamV-18	4/24/2000	16	24	0.9	5.4	0.8	vertical	1.5							da	
D32	DynamV-17	4/24/2000	16	24	0.9	5.4	0.8	orizontal								da	
D33	DynamV-16	4/24/2000	16	24	0.9	5.4	0.8	90								da	
D34	DynamV-15	4/24/2000	16	24	0.9	5.4	0.8	orizontal								da	
D35	DynamV-14	4/24/2000	16	24	0.9	5.4	0.8	vertical	1.5							da	
D36	DynamV-13	4/24/2000	16	24	0.9	5.4	0.8	vertical	1.5							da	
D37	DynamV-12	4/24/2000	16	24	0.9	5.4	0.8	vertical	1.5							da	
D38	DynamV-11	4/24/2000	16	24	0.9	5.4	0.8	vertical	1.5							da	
D39	DynamV-10	4/24/2000	16	24	0.9	5.4	0.8	vertical	1.5							da	
D40	DynamV-09	4/24/2000	16	24	0.9	5.4	0.8	orizontal								da	
D41	DynamV-08	4/24/2000	16	24	0.9	5.9	1.13	100								da	
D42	DynamV-07	4/24/2000	16	12	0.9	5.9	1.13	vertical	2.2							da	
D43	DynamV-06	4/24/2000				5.9	1.13									da	Fără măsurători

Nr.	Denumire	Data	Lățime perete mobil b	Inaltime perete h	Grad îndesare D	Masa pendu-lului	Lungi-mea pendu-lului	Devierea inițială pendul	Înălți-mea inițială pendul	Amplit. forță impact	Durată forță impact	Im-puls	Deplasare maximă perete	Accelerație maximă	Înregis-trare distribuție presiune	Înregis-trare video	Observații
			[cm]	[cm]	[-]	[kg]	[m]	[cm]	[m]	[kN]	[s]	[kNs]	[cm]	[m/s^2]			
D44	**DynamV-05**	4/24/2000	16	12	0.9	5.9	1.13	vertical	2.2							da	selecționată pentru prezentare
D45	DynamV-04	4/24/2000	16	12	0.9	5.9	1.13	vertical	2.2							da	
D46	DynamV-03	4/24/2000	16	12	0.9	5.9	1.13	vertical	2.2							da	doza de forță a căzut
D47	DynamV-02	4/24/2000	16	12	0.9	5.9	1.13	70								da	
D48	DynamV-01	4/24/2000	16	12	0.9	5.9	1.13	orizontal		0.5			0.4			da	
D49	VideoV-41	4/9/2000	16	24	0.9	5.4	0.8	vertical	1.5							da	Înregistrare video
D50	VideoV-40	4/9/2000	16	24	0.9	5.4	0.8	vertical	1.5							da	Înregistrare video
D51	VideoV-39	4/9/2000	16	24	0.9	5.4	0.8	vertical	1.5							da	Înregistrare video
D52	VideoV-38	4/9/2000	16	24	0.9	5.4	0.8	orizontal								nu	nu s-au salvat înregistrarile
D53	VideoV-37	4/9/2000	16	24	0.9	5.4	0.8	100								da	Înregistrare video
D54	VideoV-36	4/9/2000	16	24	0.9	5.4	0.8	70								da	Înregistrare video
D55	VideoV-35	4/9/2000	16	24	0.9	5.4	0.8	60								da	Înregistrare video
D56	VideoV-34	4/9/2000	16	24	0.9	5.4	0.8	50								da	Înregistrare video
D57	VideoV-33	4/9/2000	16	24	0.9	5.4	0.8	40								da	
D58	VideoV-32	4/9/2000	16	24		5.4	0.8	100								da	Înregistrare video
D59	VideoV-31	4/9/2000	16	24	0.9	5.4	0.8	100								da	Înregistrare video
D60	VideoV-30	4/9/2000	16	24	0.7	5.4	0.8	vertical	1.5	3	58		4			da	Eroare după deplasarea de 3 cm
D61	VideoV-29	4/8/2000	16	24	0.5	5.4	0.8	vertical	1.5							da	Eroare după deplasarea de 2,5 cm
D62	VideoV-28	4/8/2000	16	24	0.9	5.4	0.8									da	Înregistrare video
D63	VideoV-27	4/8/2000	16	24	0.9	5.4	0.8	vertical	1.5							da	Înregistrare video
D64	VideoV-26	4/8/2000	16	24	0.9	5.4	0.8	orizontal								da	Înregistrare video
D65	VideoV-25	4/8/2000	16	24	0.9	5.4	0.8	orizontal								da	Înregistrare video
D66	VideoV-24	4/8/2000	16	24	0.9	5.4	0.8	orizontal								da	Înregistrare video
D67	VideoV-23	4/8/2000	16	24	0.9	5.4	0.8	orizontal								da	Înregistrare video
D68	VideoV-22	4/8/2000	16	24	0.9	5.4	0.8	orizontal								da	Înregistrare video
D69	VideoV-21	4/7/2000	16	24	0.9	5.4	0.8	50								da	Înregistrare video

Nr.	Denumire	Data	Lățime perete mobil b	Inaltime perete h	Grad îndesare D	Masa pendu-lului	Lungi-mea pendu-lului	Devierea inițială pendul	Înălți-mea inițială pendul	Amplit. forță impact	Durată forță impact	Im-puls	Deplasare maximă perete	Accelerație maximă	Înregis-trare distribuție presiune	Înregis-trare video	Observații
			[cm]	[cm]	[-]	[kg]	[m]	[cm]	[m]	[kN]	[s]	[kNs]	[cm]	[m/s^2]			
D70	VideoV-20	4/7/2000	16	24	0.9	5.4	0.8	orizontal								da	Înregistrare video
D71	VideoV-19	4/7/2000	16	24	0.9	5.4	0.8	70								da	Înregistrare video
D72	VideoV-18	4/7/2000	16	24	0.9	5.4	0.8	orizontal								da	Înregistrare video
D73	VideoV-17	4/7/2000	16	24	0.9	5.4	0.8	orizontal								da	Eroare
D74	VideoV-16	4/7/2000	16	24	0.9	5.4	0.8	~45°								da	Înregistrare video
D75	VideoV-15	4/6/2000	16	20	0.9	5.4	0.8	orizontal	0.8							da	Înregistrare video
D76	VideoV-14	4/6/2000	16	24	0.5	5.4	0.8	orizontal	0.8							da	Înregistrare video
D77	VideoV-12-B	4/5/2000	16	24	0.9	5.4	0.8	orizontal ?	0.8	3.4	28		1.04	80		da	Înregistrare video
D78	VideoV-10-B	4/4/2000	16	24	0.9	5.4	0.8	orizontal ?	0.8							da	Înregistrare video
D79	VideoV-09-B	4/4/2000	16	24	0.9	5.4	0.8	orizontal ?	0.8	1.5			460mV	0.8		da	Înregistrare video
D80	VideoV-06	4/4/2000	16	24	0.9	5.4	0.8	orizontal	0.8	1.54			250mV->0,125	0.6		da	Înregistrare video
D81	VideoV-05	4/4/2000	16	24	0.9	5.4	0.8	orizontal	0.8	1.36	59		0.1			da	Înregistrare video
D82	VideoV-04	4/3/2000	16	24	0.9	5.4	0.8	orizontal	0.8	1.54	58		0.14	0,9V=9		da	Înregistrare video
D83	VideoV-03	4/3/2000	16	24	0.9	5.4	0.8	orizontal	0.8	1.6	58		0.2	1V=10?		da	Înregistrare video
D84	VideoV-02	4/3/2000	16	24	0.9	5.4	0.8	orizontal	0.8	1.55	58		0.5	1,6V=16		da	Înregistrare video
D85	VideoV-01	4/3/2000	16	24	0.5	5.4	0.8	orizontal	0.8	1.3	60		2.05	300mV=30		da	Înregistrare video
D86	V63	12/17/1999	16	24	0.9	5.4	0.8	70		3.8	11		0.325	190			
D87	V62	12/17/1999	16	24	0.9	5.4	0.8	60									
D88	V61	12/17/1999	16	24	0.9	5.4	0.8	50									
D89	V59	12/17/1999	16	24	0.9	5.4	0.8	40		1.58	14		0.32	100			
D90	V58	12/17/1999	16	24	0.9	5.4	0.8	30									
D91	V57	12/17/1999	16	24	0.9	5.4	0.8	20									
D92	V56	12/17/1999	16	24	0.9	9.7	0.8	vertical	1.5	7.06			1.33	100			
D93	V54	12/17/1999	16	24	0.9	9.7	0.8	orizontal		3.9			8.6	36			
D94	V53	12/17/1999	16	24	0.9	9.7	0.8	70		1.02			0.3	17.6			
D95	V52	12/17/1999	16	24	0.9	9.7	0.8	50		0.6			0.164	12.5			
D96	V51	12/17/1999	16	24	0.9	9.7	0.8	40									
D97	V50	12/17/1999	16	24	0.9	9.7	0.8	30									
D98	V49	12/17/1999	16	24	0.9	5.7	0.8	vertical	1.5	2.68			0.408	40			
D99	V47	12/17/1999	16	24	0.9	5.7	0.8	orizontal		1.58			0.287	32			
D100	V46	12/17/1999	16	24	0.9	5.7	0.8	100		1.1			0.18	20			
D101	V45	12/17/1999	16	24	0.9	5.7	0.8	70		0.54	70		0.079	10			
D102	V43	12/17/1999	16	24	0.9	5.7	0.8	60									
D103	V42	12/17/1999	16	24	0.9	5.7	0.8	50									
D104	V41	12/17/1999	16	24	0.9	5.7	0.8	40									

Nr.	Denumire	Data	Lățime perete mobil b	Inaltime perete h	Grad îndesare D	Masa pendu-lului	Lungi-mea pendu-lului	Devierea inițială pendul	Înălți-mea inițială pendul	Amplit. forță impact	Durată forță impact	Im-puls	Deplasare maximă perete	Accelerație maximă	Înregis-trare distribuție presiune	Înregis-trare video	Observații
			[cm]	[cm]	[-]	[kg]	[m]	[cm]	[m]	[kN]	[s]	[kNs]	[cm]	[m/s^2]			
D105	V40	12/17/1999	16	24	0.9	5.7	0.8	30									
D106	V39	12/17/1999	16	24	0.9	5.7	0.8	20									
D107	V37	12/17/1999	16	24	0.9	2.5	1.13	vertical	2.2	1.1			0.2	40			
D108	V36	12/17/1999	16	24	0.9	2.5	1.13	vertical	2.2	1.1			0.175	40			
D109	V35	12/17/1999	16	24	0.9	2.5	1.13	vertical	2.2	1.1			0.126	60			
D110	V33	12/17/1999	16	24	0.9	2.5	1.13	orizontal		0.61			0.0504	33			
D111	V32	12/17/1999	16	24	0.9	2.5	1.13	70									
D112	V31	12/17/1999	16	24	0.9	2.5	1.13	100		0.34			0.023	17.5			
D113	V29	12/17/1999	16	24	0.9	2.5	1.13	60		0.235			0.012	9.5			
D114	V28	12/17/1999	16	24	0.9	2.5	1.13	50		0.22			0.011	7.8			
D115	V27	12/17/1999	16	24	0.9	2.5	1.13	40									
D116	V26	12/17/1999	16	24	0.9	2.5	1.13	30									
D117	V25	12/17/1999	16	24	0.9	2.5	1.13	20									
D118	V09	12/15/1999	16	24	0.9	2.5	1.13	60									
D119	V08	12/15/1999	16	24	0.9	2.5	1.13	50									
D120	V07	12/15/1999	16	24	0.9	2.5	1.13	40									
D121	V06	12/15/1999	16	24	0.9	2.5	1.13	30									
D122	V05	12/15/1999	16	24	0.9	2.5	1.13	20									
D123	V04	12/15/1999	16	24	0.9	1.5	1.13	vertical	2.2								
D124	V03	12/15/1999	16	24	0.9	1.5	1.13	vertical	2.2								
D125	V24	12/15/1999	16	24	0.9	3.5	1.13	vertical	2.2	2.1	36		0.46				
D126	V23	12/15/1999	16	24	0.9	3.5	1.13	orizontal		1	43		0.33				
D127	V22	12/15/1999	16	24	0.9	3.5	1.13	orizontal		1.84	50		0.46				
D128	V20	12/15/1999	16	24	0.9	3.5	1.13	100									
D129	V19	12/15/1999	16	24	0.9	3.5	1.13	70									
D130	V17	12/15/1999	16	24	0.9	3.5	1.13	60									
D131	V16	12/15/1999	16	24	0.9	3.5	1.13	50									
D132	V15	12/15/1999	16	24	0.9	3.5	1.13	40									
D133	V14	12/15/1999	16	24	0.9	3.5	1.13	30									
D134	V13	12/15/1999	16	24	0.9	3.5	1.13	20									
D135	V11	12/15/1999	16	24	0.9	2.5	1.13	100									
D136	V10	12/15/1999	16	24	0.9	2.5	1.13	70									

A - amortizor din neopren
MS - masă suplimentară
SC - strat compresibil

Annex 5 Bibliography

Bartl, U., 1995: Untersuchungen zum Erdwiderstand auf ebene Wände am Beispiel von 1g-Modellversuchen mit Kopfpunktdrehung. In: Institut für Geotechnik, Technische Universität Dresden, Mitteilungen Heft 3, Dresden 1995

Bartl, U., Franke, D.: Ergebnisse von Modellversuchen zur Untersuchung der Abhängigkeit des stützenden Erddrucks von Wandbewegungen-am Beispiel von Zentrifugenversuchen mit Kopfpunktdrehung; In: Franke, D. (Hrsg.): *Ohde-Kolloquium an der TU Dresden*, Mitteilungen Institut für Geotechnik, TU Dresden, Heft 4, S. 1-27, 1997

Bauer, E.: Zum mechanischen Verhalten granularer Stoffe unter vorviegend ödometrischer Beanspruchung. *Veröffentl. des Institutes für Bodenmechanik und Felsmechanik der Universität Karlsruhe*, Heft 130, 1992

Bauer, E.: Calibration of a compressive constitutive equation, *Soils and Foundations*, 1995

Bauer, J., Foros, P., und Schwarz, R.: Studie zum Lastfall Flugzeugabsturz auf Kernkraftwerke (Phase II). Schriftenreihe Reaktorsicherheit und Strahlenschutz, GRM, Merkel-Verlag 1989

Biggs, J. M.: Introduction to structural dynamics, 1964

Block, K.: Der harte Querstoß-Impact auf Balken aus Stahl, Holz und Stahlbeton, Dissertation, Abteilung Bauwesen der Universität Dortmund, 1982

Brinkgreve, R. B. J., Vermeer, P. A.: Plaxis Version 7, Finite Element Code for Soil and Rock Analyses. A.A. Balkema/Rotterdam/Brookfield, 1998

Chiapella, R.L., Costello, J.F.: Automobile Impact Forces on Concrete Walls, Transactions of the 6th International Conference on Structural Mechanics in Reactor Technology, Vol. J(b), Paris, 1981

Chopra, A. K.: Dynamics Of Structures; Theory and Applications to Earthquake Engineering, Second Edition, Prentice Hall, New Jeresey, 2001

Chugh, A. K.: A Unified Procedure for Earth Pressure Calculations, Third International Conference on Recent Advances in Geotechnical Earthquake Engineering and Soil Dynamics, Volume III, St. Louis, Missouri 1995

Coulomb, C. A.: Essai sur une application des regles des maximis et minimis a quelques problemes de statique relatifs a l'architecture. Memoires de l'Academie Royale Pres Divers-Savants, Vol. 7, Paris 1776

DIN 1054 Ground – Verification of the safety of earthworks and foundations, 2005

DIN 1072 Straßen - und Wegbrücken: Lastannahmen, 1985

DIN 4014 Bohrpfähle: Herstellung, Bemessung und Tragverhalten, 1990

DIN 4085: Baugrund, Berechnung des Erddrucks + Beiblatt 1: Erleuterungen, 1987

DIN 4085:2011-05: Baugrund, Berechnung des Erddrucks, 2011

DIN 4085 Bbl 1:2011-12: Baugrund, Berechnung des Erddrucks – Beiblatt 1: Berechnungsbeispiele, 2011

DIN V 4085-100: Baugrund, Berechnung des Erddrucks - Teil 100: Berechnung nach dem Konzept mit Teilsicherheitbeiwerten, 1996

E DIN 4085-100: Baugrund, Berechnung des Erddrucks, 2002

DIN 18123: Soil, investigation and testing - Determination of grain-size distribution, 2011

DIN 18124: Soil, investigation and testing - Determination of density of solid particles - Capillary pycnometer, wide mouth pycnometer, gas pycnometer, 2011

DIN 18125-1: Laboratory tests for determination of soil density, 1997

DIN 18126: Soil, investigation and testing - Determination of density of non-cohesive soils for maximum and minimum compactness. 1996

DIN 18137-3: Soil, investigation and testing - Determination of shear strength - Part 3: Direct shear test, 2002

EAU 2004: Empfehlungen des Arbeitsausschusses „Ufereinfassungen", Häfen und Wasserstrassen. 10. Auflage, 2009

Empfehlungen des Arbeitskreises „Baugruben" EAB, 4. Auflage, herausgegeben von der Deutschen Gesellschaft für Geotechnik e.V., Ernst & Sohn, 2006

ENV 1991-1-7: Background document to ENV 1991-1-7 Accidental actions due to impact and explosions, 2005

Franke, D., 1981: Erddruck auf Querflügelmauem. Bauplanung - Bautechnik, Berlin, 1981 H. 2, S. 85-88

Franke, D., 1982: Beiträge zur praktischen Erddruckberechnung. Von der Fakultät für Bau-, Wasser- und Forstwesen der Technischen Universität Dresden genehmigte Habilitationsschrift

Franke, D., 1984: Verbesserte Berechnung der Erddruckgrenzwerte bei bindigem Lockergestein. Bauplanung-Bautechnik, Berlin, 1984, S. 27-31

Franke, D., 1988: Erddruck auf unnachgiebige Wände - Auswertung von Modellversuchen. Geotechnik, Essen, 1988, S. 20-26

Franke, E.: Grundbau - Taschenbuch, Teil 3 Grundbauwerke, Kapitel 3.3 Pfähle, Ernst & Sohn, Verlag für Architektur und technische Wissenschaften, Berlin 1997

Griffiths, D. V., Hicks, M. A. und Li, C. O.: Transient passive earth pressure analyses. Geotechnique 41, Nr. 4, S. 615–620, 1991

Grundhoff, T.: Horizontal impact on large bored single piles in sand, Offshore and Polar Engineering Conference, Paper No. 97-JSC-272, Honolulu, Hawaii, USA 1997

Grundhoff, T., Latolzke, J., Laue, J.: Investigations of vertical piles under horizontal impact, International Conference Centrifuge 98, Paper No. 97-JSC-272, Tokyo, Japan 1998

Gudehus, G.: *Bodenmechanik.* Enke - Verlag, Stuttgart, 1981

Gudehus, G.: Erddruckermittlung: im Grundbautaschenbuch, Teil 1, 6. Auflage, Ernst und Sohn, S. 401–430, 2001

Haupt, W: Bodendynamik, Vieweg Verlag, Braunschweig 1986

Hettler, A.: Verschiebungen starrer und elastischer Gründungskörper in Sand bei monotoner und zyklischer Belastung. *Veröffentl. des Institutes für Bodenmechanik und Felsmechanik der Universität Karlsruhe*, Heft 90, 1981

Hettler, A.: Maßstabseffekte beim Erddruck in Sand, *Ohde-Kolloquium an der TU Dresden*, 49-71, 1997

Herten, M.: Räumlicher Erddruck auf Schachtbauwerke in Abhängigkeit von der Wandverformung. *Veröffentl. des Institutes für Bodenmechanik und Grundbau der Bergischen Universität - GH Wuppertal*, Bericht Nr. 22, 1999

Holzlöhner, U: Einfluß des Bodens beim Schiffsstoß auf Bauwerke, BAM, *nepublicat*, Berlin 1994

Holzlöhner, U: Einfluß des Bodens beim Schiffsstoß auf Bauwerke, Mitteilungsblatt der Bundesanstalt für Wasserbau Nr. 72, Berlin 1995

Jessberger, H. L, Latolzke, J.: Tragverhalten von vertikalen Bohrpfählen unter horizontalen Anprallasten. Forschungsbericht 98-3, Institut für Grundbau und Bodenmechanik, Ruhruniversität Bochum 1998

Jaeger, E.: Erdwiderstand unter dem Einfluß von Seitenwänden, Mitteilungen aus dem Gebiete des Wasserbaues und der Baugrundforschung Heft 5, Verlag von Wilhelm Ernst & Sohn, Berlin 1931

James, R. G. und Bransby, P. L.: Experimental and Theoretical Investigations of a Passive Earth Pressure Problem. *Geotechnique 20,* Nr. 1, S. 17–37, 1970

Keane R. D. and Adrian R. J.: Theory of cross correlation Analysis of PIV images. *Applied Scientific Researc*h, 49, 191-215, 1992.

Klapperich, H.: Untersuchungen zum dynamischen Erddruck, Veröffentlichung des Grundbauinstitutes der Technischen Universität Berlin, Heft Nr. 14, 1983

Kolymbas, D.: Pfahlgründungen, Springer-Verlag, 1989

Kotthaus, M.: Zum Tragverhalten von horizontal belasteten Pfahlreihen aus langen Pfählen in Sand, Schriftreihe des Instituts für Grundbau, Bochum 1992

Krepki R., Pu Y., Meng H. and Obermayer K.: A New Algorithm for the Interrogation of 3D HPIV Data Based on Deterministic Annealing and EM-Optimization; *Experiments in Fluid*s, in review, 99-107, Springer-Verlag, Berlin 2000

Loewenstein, R. M., Clemence, S. P. (1984): Study of Impact Loads on Retaining Walls, *Proc. Fourth Australia - New Zealand Conference on Geomechanics*, Perth, 39-43.

Mao, P.: Erdwiderstand von Sand in Abhängigkeit von Wandbewegungsart und Sättigungsgrad. Dissertation Universität Dortmund 1993

Mononobe, N., and Matsuo, H.: On the determination of earth pressures during earthquakes, *Proc. World Engineering Conference*, 274-280 (1929)

Morrison Jr., E. E., Ebeling, R. M.: Limit equilibrum computation of dynamic passive earth pressure, *Can. Geotech. J.* 32, 481-487 (1995)

Müller-Breslau, H.: Erddruck auf Stützmauern, Alfred Kröner Verlag, Stuttgart 1947

NP 113:2004: Normativ privind proiectarea, execuția, monitorizarea și recepția pereților îngropați, 2004

NP 120:2014: Normativ privind cerințele de proiectare, execuție și monitorizare a excavațiilor adânci în zone urbane, 2014

Okabe, S.: General theory of earth pressure, J. Japanese Soc. Civil Eng., Vol. 12, No. 1, 1926

ÖNORM B 4434 Erd- und Grundbau - Erddruckberechnung 1993

Paikowsky, S., G., Xi, F.: Particle Motion Tracking Utilizing a High-Resolution Digital CCD Camera, *Geotechnical Testing Journal,* GTJODJ, Vol. 23, No. 1, S. 123-134, 2000

Popp, C.: Untersuchungen über den Querstoß beim Aufprall von Kfz auf Gründungspfähle aus Stahlbeton und Stahl, Deutscher Ausschuß für Stahlbeton, H. 246, W. Ernst & Sohn, Berlin 1974

Popp, Camillo: Der Querstoss beim Aufprall (in German), Forschungshefte aus dem Gebiete des Stahlbaues, Deutschen Stahlbau Verband, Köln am Rhein, 1961

Raffel, M., Willert, C., Kompenhans, J.: *Particle image velocimetry - a practical guid*e. Springer: Berlin 1998

Rankine, W.: On the Stability of Loose Earth, Proceedings of the Royal Society of London, Philosophical Transactions of the Royal Society, 1857

Resolution No. 92/2 on New Classification of Inland Waterways (Report), European Conference of Ministers of Transport, 12 June 1992

Riera, J. D., Zorn, N. F: Risk due to accidental aircraft crash against nuclear power plants – on the definition of the excitation due to engin impact, Caderno

Technico CT 28/81, Curso de Pos Graduaco em Engenharia Civil, UFRGS, Porto Alegre, Brasil 1981

Saidel, T., Savidis, S.: Passiver Erddruck auf Stützkonstruktionen bei stoßartiger Belastung, Fraunhofer IRB Verlag, T 2918, 2000

Savidis, S., Klapperich, H. und Abdel Karim, M.: Klassische Verfahren zur Berechnung des seismischen Erddruckes, Veröffentlichung des Grundbauinstitutes der Technischen Universität Berlin, Heft Nr. 8, 1980

Savidis, S.: Beiträge zur Modellversuchstechnik in der Geotechnik, Veröffentlichung des Grundbauinstitutes der Technischen Universität Berlin, Heft Nr. 18, 1988

Sokolovski, V.: Statics of Granular Media, London, New York: Pergamon Press 1965

SR EN 1991-1-7:2007: Acțiuni asupra structurilor. Partea 1-7: Acțiuni generale – Acțiuni accidentale

SR EN 1997-1:2004: Eurocod 7 – Proiectarea geotehnică. Partea 1: Reguli generale

Stanciu, A., Lungu, I.: Fundații. Fizica și Mecanica Pământurilor, București, 2006

Terzaghi, K., Jelinek,R.:Theoretische Bodenmechanik, Springer-Verlag, Berlin, 1959

Vermeer, P.A., Schanz, T.: Die Steifigkeit des Bodens und ihr Einfluß auf die Fußeinspannung einer Stützwand. OHDE-Kolloquium ’97, *Mitteilungen des Institutes für Geotechnik der Technischen Universität Dresden,* Heft 4, S. 247-264, TU Dresden, 1997

Vogt, N.: Erdwiderstandsermittlung bei monotonen und wiederholten Wandbewegungen in Sand, Mitteilung 22, Baugrundinstitut der Universität Stuttgart 1984

Vrouwenvelder, Ton: Eurocode 1, Part 1.7, Accidental actions, Proceedings ICOSSAR 2005, Safety and Reliability of Engineering Systems and Structures, paginile 3311-3317, Millpress, Rotterdam, ISBN 90 5966 040 4, 2005

Weißenbach, A.: Der Erdwiderstand vor schmalen Druckflächen. *Mitteilungen des Franzius-Instituts für Grund- und Wasserbau der Technischen Hochschule Hannover*, Heft 19, 1961

Weißenbach, A.: Beitrag zur Ermittlung des Erdwiderstandes. *Bauingenieur* 58, 161–173, 1983

Weißenbach, A.: Baugruben, Teil II: Berechnungsgrundlagen, Verlag Ernst & Sohn, Berlin-München-Düsseldorf 1975

Walz, B., Schober, H.-D. und Diekmann, N.: Untersuchungen zum lagenweisen Einbau von Sandvolumina für bodenmechanische Modellversuche. *Aus Theorie und Praxis des Grundbaus und der Bodenmechanik*, S.A. Savidis, H. Müller-Kirchenbauer, B. Walz (Hrsg.), TU Berlin, 219-247, 1975

Walz, B., K. Hock: Berechnung des räumlich aktiven Erddrucks mit der modifizierten Elementscheibentheorie. In: Bergische Universität Gesamthochschule Wuppertal, Fachbereich Bautechnik, Grundbau, Bodenmechanik und Unterirdisches Bauen. Bericht-Nr. 6, März 1987

Walz, B., Kremer, A.: Diskussion zum Beitrag: „Maßstabeffekte beim Erddruck in Sand", *Ohde-Kolloquium an der TU Dresden*, 73-82, 1997

Winkler, A.: Ermittlung des Erddrucks im Bruchzustand bei Drehung einer Wand um den Kopfpunkt. Dissertation, TU Dresden, 2001

Wu, W.:Hypoplastizität als mathematisches Modell zum mechanischen Verhalten granularer Stoffe. *Veröffentl. des Institutes für Bodenmechanik und Felsmechanik der Universität Karlsruhe*, Heft 129, 1992

Zambelli, C., di Prisco, C.: DEPENDENCY OF THE MECHANICAL BEHAVIOUR OF GRANULAR SOILS ON LOADING FREQUENCY: EXPERIMENTAL RESULTS AND CONSTITUTIVE MODELLING, Soil Stress-Strain Behavior: Measurement, Modeling and Analysis Geotechnical Symposium in Roma, March 16 & 17, 2006

Ziegler, M.: Berechnung des verschiebungsabhängigen Erddrucks in Sand. *Veröffentl. des Institutes für Bodenmechanik und Felsmechanik der Universität Karlsruhe*, Heft 101, 1987